ABSTRACT

PBM AND DEM SIMULATIONS OF LARGE-SCALE CLOSED-CIRCUIT CONTINUOUS BALL MILLING OF CEMENT CLINKER

by
Nontawat Muanpaopong

Cement milling is known to be inefficient and energy-intensive. Thus, even small improvements in cement milling's performance could significantly reduce operation costs. This dissertation aims to develop a simulation tool for dry milling and generate a fundamental process understanding, which enables process optimization. To this end, a true unsteady-state simulator (TUSSIM) for continuous dry milling is developed and applied to model various processes: (a) open circuit continuous mills, (b) closed-circuit continuous mills, and (c) vertical roller mills. TUSSIM is based on the solution of the cell-based population balance model (PBM) for continuous milling, which consists of a set of differential algebraic equations (DAEs). Moreover, air classifier parameters and ball size distribution for the closed-circuit operation are tailored to maximize production capacity while achieving desirable cement product qualities. Discrete element method (DEM) and PBM are coupled to simulate lab-scale batch milling of cement clinker to gain fundamental understanding of the roles of ball size and material (steel vs. alumina).

First, dynamic simulations are performed to investigate the impact of ball mill operation parameters on the full-scale *open-circuit* ball milling of cement clinker without an external air classifier. Parameters for the simulation are taken from the literature. Simulation results suggest that a single-compartment mill produces the desired cement size, but it requires pre-milled fresh feed. Depending on the ball sizes used, a two-

compartment mill produces cement sizes similar to those produced by a three-compartment mill. A uniform mass of balls achieves an 8% higher specific surface area (SSA) compared to a uniform number of balls. The classifying liners have negligibly finer cement products compared to a uniform mass distribution.

TUSSIM is also incorporated with a variable Tromp curve model for classification to simulate full-scale closed-circuit ball milling with an air classifier. The simulation results suggest that a faster rotor speed or lower air flow rate leads to a finer cement product and increases the dust load of the classifier feed. Integrating air classifiers into open-circuit ball milling increases the production rate by 15% or cement SSA by 13%. Operation failure due to overloading of the entire circuit is detected when dust load is too high. Process optimization with a global optimizer–DAE solver is performed to identify either the air classifier's parameters or the ball size distributions that yield desirable cement quality while maximizing production rate. Optimization results show that the production rate can be increased by 7% compared to the baseline process. Unlike open circuits, a two-compartment mill produces a finer cement product than a three-compartment mill. Optimal ball mixtures are identified in a two-compartment mill, suggesting a 14% increase in production rate at a desirable cement quality.

A global optimizer-based back-calculation method, based on PBM, is used to determine the breakage kinetics parameters of cement clinker in a lab-scale ball mill loaded with steel or alumina balls of three single ball sizes and their mixtures. The motion of the balls in the mill is simulated via the DEM. The results show that steel balls achieve faster breakage of clinker than alumina balls, which is explained by the higher total–mean energy dissipation rates of the steel balls. The particle size distribution (PSD) becomes finer as

smaller balls are used. The ball mixture is the most effective overall. Significant energy can be saved if steel balls are replaced with alumina balls, but the slower breakage with the alumina balls needs to be accounted for.

Finally, steady-state cement PSD obtained from a full-scale vertical roller mill is fitted with TUSSIM. The fitted results show good agreement compared to the experimental PSD. Overall, this dissertation has provided a novel process simulator, TUSSIM, and many fundamental insights into the continuous milling of cement clinker and its optimization.

PBM AND DEM SIMULATIONS OF LARGE-SCALE CLOSED-CIRCUIT CONTINUOUS BALL MILL OF CEMENT CLINKER

by
Nontawat Muanpaopong

A Dissertation
Submitted to the Faculty of
New Jersey Institute of Technology
in Partial Fulfillment of the Requirements for the Degree of
Doctor of Philosophy in Chemical Engineering

Otto H. York Department of
Chemical and Materials Engineering

May 2023

APPROVAL PAGE

PBM AND DEM SIMULATIONS OF LARGE-SCALE CLOSED-CIRCUIT CONTINUOUS BALL MILL OF CEMENT CLINKER

Nontawat Muanpaopong

Dr. Ecevit Bilgili, Dissertation Advisor — Date
Professor of Chemical and Materials Engineering, NJIT

Dr. Rajesh Davé, Dissertation Co-Advisor — Date
Distinguished Professor of Chemical and Materials Engineering, NJIT

Dr. Lisa Axe, Committee Member — Date
Professor and Chair of Chemical and Materials Engineering, NJIT

Dr. Roman Voronov, Committee Member — Date
Associate Professor of Chemical and Materials Engineering, NJIT

Dr. R. Bertrum Diemer, Committee Member — Date
Professor, Affiliated Faculty of Chemical and Biomolecular Engineering,
University of Delaware, Wilmington, Delaware

BIOGRAPHICAL SKETCH

Author: Nontawat Muanpaopong

Degree: Doctor of Philosophy

Date: May 2023

Undergraduate and Graduate Education:

- Doctor of Philosophy in Chemical Engineering,
  New Jersey Institute of Technology, Newark, NJ, 2023

- Bachelor of Engineering in Mechanical Engineering,
  Chulalongkorn University, Bangkok, Thailand, 2013

Major: Chemical Engineering

Presentations and Publications:

Journal Articles:

N. Muanpaopong, R. Davé, E. Bilgili, PBM simulation and optimization of closed-circuit cement mills with various compartments and ball size distributions, Under review.

N. Muanpaopong, R. Davé, E. Bilgili, Modeling of closed-circuit ball milling of cement clinker via a PBM with a variable Tromp curve for classification, Under review.

N. Muanpaopong, R. Davé, E. Bilgili, A comparative analysis of steel and alumina balls in fine milling of cement clinker via PBM and DEM, Powder Technology, 421 (2023) 118454.

N. Muanpaopong, R. Davé, E. Bilgili, Impact of ball size distribution, compartment configuration, and classifying liner on cement particle size in a size in a continuous ball mill, Minerals Engineering, 189 (2022) 107912.

N. Muanpaopong, R. Davé, E. Bilgili, A cell-based PBM for continuous open-circuit dry milling: impact of axial mixing, nonlinear breakage, and screen size, Powder Technology, 397 (2022) 117099.

Conference Proceedings:

E. Bilgili, N. Muanpaopong, R. Dave, Dry ball milling of a pre-milled cement clinker: elucidating the impact of the ball material type and size of grinding balls, Presented at the 2022 American Institute of Chemical Engineers (AIChE) Annual Meeting, Paper No: 333b, Phoenix, AZ, 13–18 November 2022.

R. Dave, N. Muanpaopong, E. Bilgili, Modeling the impact of ball size–material on the fineness of cement clinker particles prepared by dry ball milling, Keynote Speech, Presented at the 9th World Congress on Particle Technology (WCPT9), Madrid, Spain, 18–22 September 2022.

N. Muanpaopong, R. Dave, E. Bilgili, Unsteady-state simulation of cement milling in closed-circuit operation: a fully coupled ball mill–air classifier model, Presented at the 2021 American Institute of Chemical Engineers (AIChE) Annual Meeting, Paper No: 724e, Virtual, 13–14 November 2021.

N. Muanpaopong, R. Dave, E. Bilgili, Simulation of full-scale open-circuit, multi-compartment cement ball mills: a new true unsteady-state simulator, Presented at the 2021 American Institute of Chemical Engineers (AIChE) Annual Meeting, Paper No: 325c, Boston, MA, 5–8 November 2021.

N. Muanpaopong, R. Dave, E. Bilgili, Modeling of full-scale cement ball milling using a new simulator: TUSSIM-BM, Presented at the 12th International Comminutuin Symposium (Comminution ’21), Virtual, 19–22 April 2021.

N. Muanpaopong, R. Dave, E. Bilgili, Mathematical modeling of continuous milling processes using a cell-based PBM approach: a parametric study, Presented at the 2020 Virtual American Institute of Chemical Engineers (AIChE) Annual Meeting, Paper No: 261h, Virtual, 16–20 November 2020.

To my family

ACKNOWLEDGMENTS

My gratitude goes to my advisor, Professor Ecevit Bilgili, for his teaching and training me in population balance modeling and computer simulations, revising and editing manuscripts for publication, and helping with various personal issues over the past five years. An equal amount of my gratitude goes to my co-advisor, Professor Rajesh Dave.

Special thanks go to Professors Lisa Axe, Roman Voronov, and Bertrum Diemer for their serving on my committee for proposal and PhD dissertation defenses.

My gratitude also goes to Research and Innovation, as part of Siam Cement Group, for their research funding support through the Research & Development Service Agreement "Improvement of Cement Milling Processes via Advanced Process Modeling" (grant number G2714L0). I am greatly thankful to Mr. Banjong Witayatawornwong, the director of the Center of Excellence, for choosing me over other employees to complete this project.

Last but not least, I am very much thankful to Sangah Kim and her mother for all their help during my stay in NJ.

TABLE OF CONTENTS

TABLE OF CONTENTS
(Continued)

Chapter **Page**

TABLE OF CONTENTS
(Continued)

Chapter **Page**

TABLE OF CONTENTS
(Continued)

Chapter **Page**

TABLE OF CONTENTS
(Continued)

Chapter **Page**

TABLE OF CONTENTS
(Continued)

Chapter **Page**

TABLE OF CONTENTS
(Continued)

Chapter **Page**

LIST OF TABLES

LIST OF TABLES
(Continued)

Table **Page**

LIST OF TABLES
(Continued)

Table **Page**

LIST OF FIGURES

LIST OF FIGURES
(Continued)

Figure **Page**

LIST OF FIGURES
(Continued)

Figure **Page**

LIST OF FIGURES
(Continued)

Figure **Page**

LIST OF FIGURES
(Continued)

Figure **Page**

LIST OF FIGURES
(Continued)

Figure **Page**

LIST OF FIGURES
(Continued)

Figure **Page**

LIST OF FIGURES
(Continued)

Figure **Page**

LIST OF FIGURES
(Continued)

Figure **Page**

LIST OF FIGURES
(Continued)

Figure **Page**

CHAPTER 1

INTRODUCTION

1.1 Background Information

Cement is a fundamental building material; it is an essential binder in concrete production. Concrete consists of cement, aggregate, and water. It can be cast in desired shapes and becomes a structure once hardened. The growing construction industry has continuously increased global cement production. International Energy Agency forecasted that it will reach 4.40 billion metric tons by 2050 (IEA and WBCSD, 2009). As shown in **Figure 1.1**, the cement manufacturing process consists of three main processes: raw material preparation (e.g., quarrying raw material, crushing raw material, milling raw meal), clinker burning, and cement milling. Different raw materials (e.g., limestone and clay) are mixed and milled into a homogeneous powder and placed in high-temperature kiln to produce clinker. The clinker is then milled with gypsum and admixtures to produce cement. The strength of cement mainly depends on cement size: the higher the strength class needed, the finer the cement product size should be.

The average energy consumption in cement manufacturing is 111 kWh per metric ton of cement (IEA and WBCSD, 2009). The cement milling department consumes about 40% of all energy in the manufacturing process (IEA and WBCSD, 2009; Su et al., 2013). Although there are other milling technologies, such as the vertical roller mill (VRM), the conventional ball mill is still the most widely used milling technology because it is easier to operate, and it produces smaller product at a lower capital expense. Ball milling can be performed under batch, continuous open-circuit, and continuous closed-circuit grinding

modes. While batch milling is used in laboratories, continuous processes are used at industrial scale to achieve the high production rates (King, 2001).

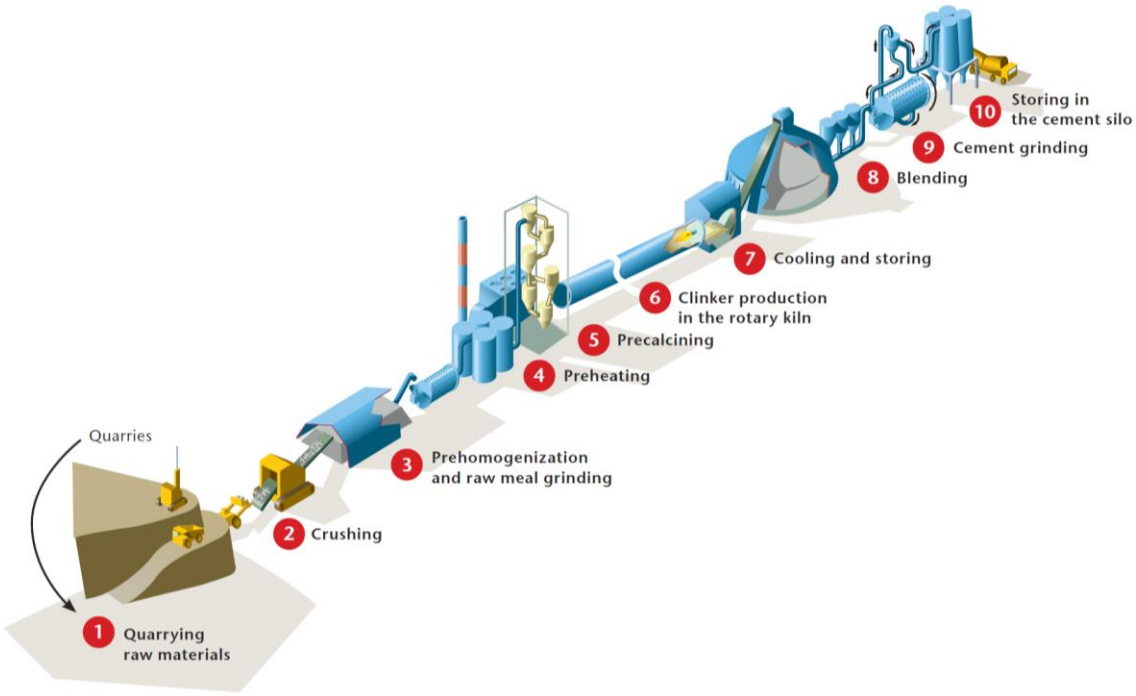

Figure 1.1 A schematic of the cement manufacturing process, from raw material preparation to cement storage.

Source: IEA and WBCSD (2009)

A ball mill is a type of comminution equipment that has a rotating, horizontal tube. The tube is filled with grinding balls and, when the mill is operated, these balls break down particles (Napier-Munn et al., 1996; King, 2001). The mill shell is protected by liners. In continuous open-circuit milling, materials are fed at the inlet and ground inside the mill. Particles are air-swept and ground products are discharged at the end of the mill. The diaphragms (partitions) are located inside and at the discharge of the mill. While the intermediate diaphragm separates two milling processes (coarse milling and fine milling)

into different compartments, the discharge diaphragm mainly prevents the grinding balls from leaving the mill.

Continuous ball milling can also be performed as a closed-circuit operation, in which ground materials are fed through an external classifier. Although open-circuit operation is easier to handle than the closed-circuit operation, it produces over-milling of fine particles as a result of consuming more energy (FLSmidth, 2014). This over-milling causes wider product particle size distribution (PSD), which severely affects product quality (i.e., lower cement strength). To achieve the desired fineness of product size when using an open-circuit mill, the mill needs to be long, with multiple compartments. This limits the open-circuit ball mill's production rate. For that reason, the closed-circuit ball mill operation is widely used in the cement manufacturing process (Shimoide, 2016). While **Figure 1.2** presents a flow diagram of the closed-circuit ball milling process, **Figure 1.3** presents a detailed view of the ball mill and the air classifier used in closed-circuit operations. Particles are transported by an air stream generated by a mill fan. This air stream pulls particles through the compartments toward the discharge end. The mill collector (see **Figure 1.2**) is used to clean exhausted gases to prevent drastic wear of the collector fan's impellers because of the dust. An air classifier is equipped with a rotor (the rotating part), driven by a separate motor, and guide vanes (which are stationary). The separation area of the air classifier is the space between the rotor cage and the guide vanes. Particles are subjected to drag, centrifugal, and gravitational forces. Depending on the magnitude and direction of these forces, particles move along different trajectories. The desired product size can be adjusted by changing the airflow rate and/or the rotor speed. The higher the airflow rate, the coarser the product size; the slower the rotor speed, the

coarser the product size (Gao et al., 2013; Shimoide, 2016). Fine product is collected at a filter, while the coarse reject is combined with feed material and then re-milled.

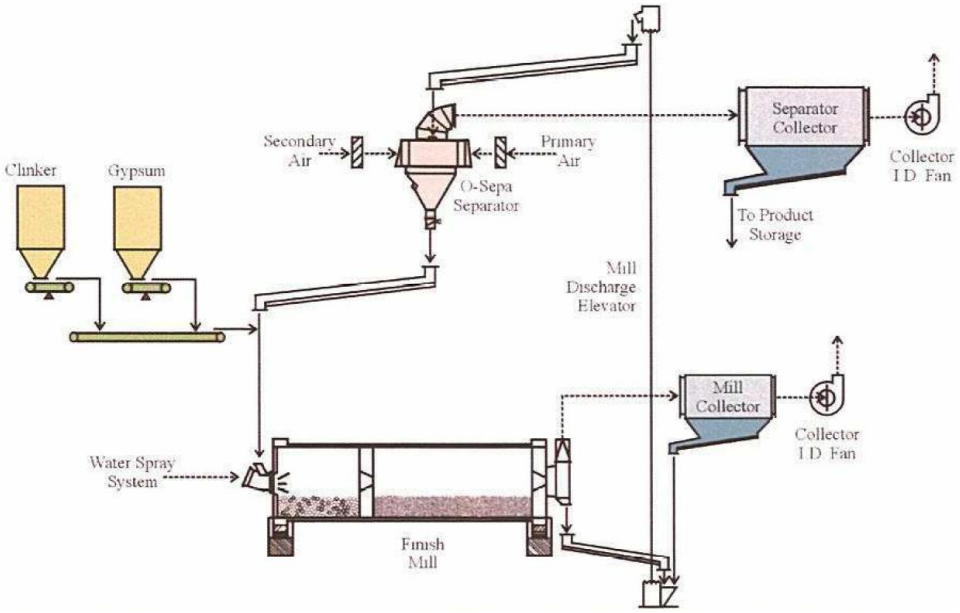

Figure 1.2 A general schematic of closed-circuit ball milling; it consists of a ball mill and an external air classifier.

Source: FLSmidth (2014)

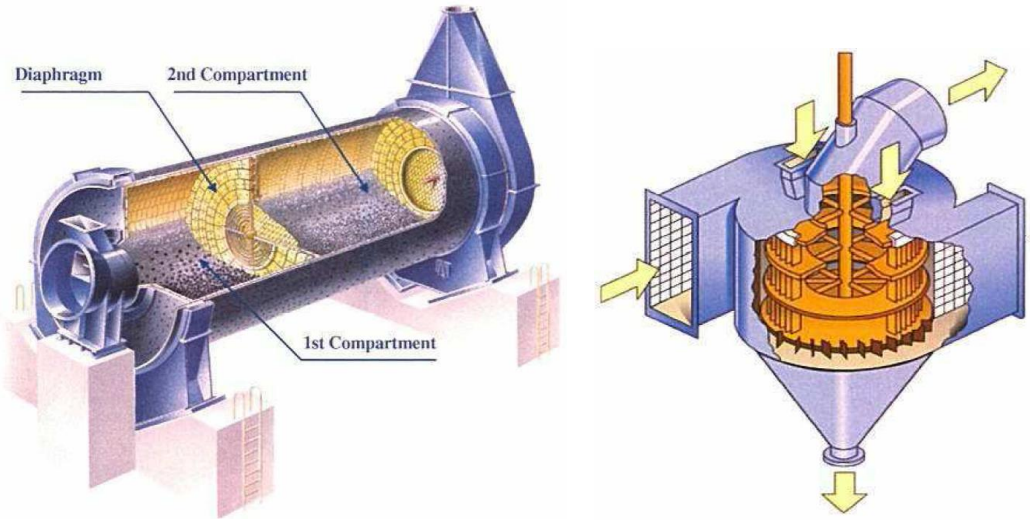

Figure 1.3 A general view of a ball mill (left) and an air classifier (right). The ball mill has two compartments and intermediate and discharge diaphragms.

Source: FLSmidth (2014)

Milling performance is affected by several factors, including process operation parameters, mill geometry, and shape of milling media. There is extensive experimental research on the impact on dry ball milling performance of process parameters such as ball filling ratio J, rotation speed, and ball size distribution (BSD) (e.g., Deniz and Onur, 2002; Deniz, 2003; Deniz, 2004; Kiangi and Moys, 2008; Deniz, 2011; Deniz, 2012). Rotation speed is typically reported as a percentage of critical speed N_c, where critical speed is defined as the speed of rotation when centrifugal and gravitational forces are equal. At that critical speed, the balls do not fall away from the mill shell. Critical speed N_c (expressed in rpm) and ball filling ratio J are given by

$$N_c = \frac{42.3}{\sqrt{D_M - d_B}} \tag{1.1}$$

$$J = \frac{m_B}{\rho_B (1-\varepsilon_B) V_M} \tag{1.2}$$

where D_M is ball mill diameter, d_B is ball size, m_B is ball mass, V_M is mill volume, ρ_B is ball density, ε_B is void fraction of grinding balls at rest. In general, product size is evaluated on the basis of specific surface area (SSA), median size (d_{50}), and 80% passing size (d_{80}) of cumulative PSD. SSA is calculated as

$$\text{SSA} = \frac{6}{\rho_p d_{32}} \tag{1.3}$$

where ρ_p is particle density and d_{32} is Sauter mean diameter, which in turn is calculated as

$$d_{32} = \frac{1}{\sum_{i=1}^{N} \frac{M_i}{x_i}} \tag{1.4}$$

Here, M_i is mass fraction of particles in size class i, and x_i is size of particles in class i. Size class i extends from size class 1, representing the coarsest particles, to size class N, representing the finest particles.

Using a lab-scale batch mill (diameter 200 mm), Cayirli (2018) thoroughly investigated the impact of various operational parameters in batch dry ball milling. The material he used was calcite (poly-dispersed feed with d_{50} = 0.6 mm), with stainless steel cylpebs as milling media and a milling time of 10 min. To begin, the impact of rotation speed on products was experimentally investigated. The results showed that the product became finer (smaller d_{50}, smaller d_{80}, and higher SSA) when rotation speed was increased from 60% of N_c to 70% of N_c. Rotation speeds faster than 70% of N_c led to coarser product in terms of d_{50} and d_{80} but did not affect product SSA. Note that unlike d_{50} and d_{80}, SSA takes account of effects on all size classes. Cayirli's finding can be explained by the fact that increasing rotation speed beyond a certain level causes the milling media (in this case, stainless steel tapered cylindrical media, also known as cylpebs) to be centrifuged inside the mill, so reducing milling action. In a ball mill study using steel ball media for cement clinker milling, Deniz (2004) investigated the impact of rotation speed on breakage kinetics and identified an optimum rotation speed of 85% of N_c.

In his batch milling study, Cayirli (2018) also investigated the impact of ball filling. Based on the optimum identified in his previous experiment, rotation speed was set at 70% of N_c. A change of ball filling from 0.20 to 0.35 was observed to produce finer products, but a further increase in ball filling to 0.40–0.45 adversely affected product size—that is, product sizes became coarser. Cayirli's explanation for these results was that in conditions of underfilling (low ball filling), the cushioning action of the material powder contributed to inefficient collisions between the balls. At optimum ball filling, however, the collision spaces between balls were properly filled, leading to efficient breakage. Overfilling of balls increased mill hold-up, but the collision zone was saturated, leading to lower breakages. Similarly, Deniz's (2012) observations indicated that the optimum ball filling for barite is 0.35.

Experimental studies of continuous milling commonly examine the extent of particle mixing in terms of the Péclet number N_{Pe}, which is defined as the significance of particle transport by convection relative to dispersion. As the Péclet number decreases, mixing converges to perfect mixing. In their experimental study of material transport in a ball mill, Swaroop at al. (1981) observed that N_{Pe} increased as feed rate increased. They also investigated ball filling ratio. Their results showed that N_{Pe} decreased as ball filling increased. However, N_{Pe} became saturated at about 40% ball filling, as the interaction between particle and ball did not increase for higher levels of ball filling. Unlike ball filling ratio, rotation speed did not significantly affect mixing degree. As rotation speed increased from 25% to 50% of N_c, N_{Pe} decreased from 11 to 7. Note that their results were based on open-end discharge. Their results also showed that, for a given feed rate, material hold-up increased as ball filling increased. The continuous increase in material hold-up can be

explained by an increase of resistance due to the ball media. It was also observed that for a given ball filling, increased feed rate led to higher hold-up.

Ball size is known to have an important effect on milling performance. In the milling literature, the impact of ball size on product size has been extensively studied using batch ball milling at laboratory scale (e.g., Erdem and Ergun, 2009). For application to industrial-scale continuous ball milling operations, experimental results for small batch mill process operations were augmented using the scale-up rule (Austin et al., 1984; Morrell and Man, 1997; Chimwani et al., 2014; Mulenga, 2017). The impacts of ball size and BSD are briefly detailed here. In an experiment investigating ball size in a batch mill (diameter 120 cm, length 60 cm), Erdem and Ergun (2009) used six single ball sizes (d_B = 70, 60, 50, 40, 30, and 20 mm). Samples were taken from the batch mill at milling times of 2, 5, 10, 15, 20, 30, 45, and 60 min; the cement clinker feed size had a d_{80} of 1.7 mm. Their results showed that, for a given single ball size, the product size became finer as milling time increased. While a bigger ball size was more efficient for breakage into coarser particles, a smaller ball size was better for breakage into smaller particles. They also found that the particle size at which maximum breakage occurs related to ball size. It should be noted that the correlation between mono-dispersed feed size and single ball size have been widely reported (e.g., Napier-Munn et al., 1996; Kanda et al., 1999; Kotake et al. 2002, Deniz 2003). Cayirli (2018) also studied the impact of BSD. Using ball sizes of 40, 32, 20, and 12 mm, six selected BSDs were assessed. Cayirli found that while a coarser BSD is not effective for particle breakage, a finer BSD produces higher product SSA (finer product) but is not effective for breaking coarser particles. The experiment indicated that the best BSD was a combination of coarse and fine ball sizes.

In closed-circuit operation, the classifier's operation parameters have a significant influence on product size (e.g., Gao et al., 2013; Yu et al., 2014). Classifier cut size, which is defined as the particle size that has an equal probability of being collected as fine product or classified as coarse reject, directly affects product size. In their classification experiments involving calcium carbonate, Yu et al. (2014) observed that classifier cut size is process-dependent. They investigated the impacts of rotor speed, feed rate, and air inlet velocity on cut size using an air classifier with a rotor radius of 106 mm. Their experimental results were as follows. (i) For a given rotor speed and feed rate to classifier, cut size became smaller with lower air inlet velocity. (ii) For a given air inlet velocity and feed rate to classifier, cut size became smaller as rotor speed increased. (iii) For a given air inlet velocity and rotor speed, cut size became smaller as feed rate to classifier decreased. These results clearly show the significance of air classification operation parameters for cut size.

Despite its importance and overwhelming experimental studies mentioned, dry ball milling process, especially continuous dry ball milling process, is not fully understood and requires high level of empiricism in process development and scale-up. As the ball milling is energy-inefficient (Fuerstenau and Abouzeid, 2002), any optimization of the existing mills could significantly reduce energy consumption for a given throughput or increase the product for a given energy consumption. The development of advanced simulation tools could help engineers gain fundamental insights about the ball milling and enable them to optimize the process. For example, optimal operational conditions that achieve maximum production rate at a desired product fineness, considering production cost, for the closed-circuit ball mills can be identified by simulating the cement mills and elucidating the impact of different ball size distribution/ configurations and air-classifier parameters.

Hence, in the subsequent sections, various facets of the modeling tools used for ball milling are introduced.

1.2 Population Balance Modeling (PBM)

1.2.1 PBM for batch ball milling

1.2.1.1 Linear PBM for batch ball milling. Particles are broken by application of mechanical forces that induce deformation–stresses in a mill. Although breakage of individual particles is regarded as "events," the breakage of multi-trillion particles can be regarded as a "rate process," akin to the rate of chemical processes. The population balance model (PBM) is used to simulate the spatio-temporal evolution of the PSD during milling processes (Varinot, 1997; Hounslow, 1998; Hennart et al., 2009), and it can also reveal breakage mechanisms. Material properties, process parameters, mill type/geometry, etc. affect the breakage kinetics. A common assumption in the PBM for batch milling is perfect mixing. This assumption is accurate for mills with small mill length to mill diameter ratios (Yildirim et al., 1999; Weedon, 2001). The size-discrete continuous-time PBM for a batch milling process is given by

$$\frac{dM_i(t)}{dt} = -S_i M_i(t) + \sum_{j=1}^{i-1} b_{ij} S_j M_j(t) \tag{1.5}$$

where $N \geq i \geq j \geq 1$ and $M_i(0) = M_{i0}$. The size class indices *i* and *j* extend from size class 1, which represents the coarsest particles, to size class *N*, which represents the finest particles in a mill. M_i is the mass fraction in size class *i* and *t* is the milling time. S_i

represents the specific breakage rate of particle size x_i. The breakage distribution parameter, b_{ij}, describes the fraction of broken particles in size class j that appears in size class i. Due to the conservation of mass, the specific breakage rate and the breakage distribution parameter have the following constraints:

$$S_N = 0,\ \sum_{i=j+1}^{N} b_{ij} = 1, \text{ and } b_{ii} = 0 \tag{1.6}$$

On the right-hand side of Equation (1.5), the first term represents the disappearance rate at which particles in size class i are broken into smaller particles, while the second term represents summed rate at which particles in all j size classes ($j < i$) are broken into size class i. First-order breakage kinetics are assumed in traditional linear PBMs, which means that the specific breakage rate S_i is time-invariant and dependent only on size x_i during milling. In view of this, Equation (1.5) is referred to as the linear, time-invariant or shortly linear PBM.

Clearly, both S_i and b_{ij}, are size-dependent functions. Smaller particles are more difficult to break due to the fact that less flaws (e.g., cracks) are affected by an impact. For example, the following expressions have been commonly used to describe the first-order specific breakage rate $S_i = k_i$ and the cumulative breakage distribution parameter B_{ij} (Austin and Luckie, 1972; Klimpel and Austin, 1977):

$$k_i = A\left(\frac{x_i}{x_0}\right)^m,\ B_{i,j} = \phi\left(\frac{x_{i-1}}{x_j}\right)^\mu + (1-\phi)\left(\frac{x_{i-1}}{x_j}\right)^\nu \text{ where } b_{i,j} = B_{i,j} - B_{i+1,j} \tag{1.7}$$

Readers are referred to Prasher (1987) and Diemer and Olson (2002) for other k_i and b_{ij} functions. The specific breakage rate and the breakage distribution parameters can be experimentally determined using the procedure proposed by Austin and Bhatia (1972) for batch mill processes. This method requires tedious milling experiments on numerous mono-dispersed feeds (narrow sieve cuts). In addition, Austin and Luckie (1972) outlined the BI, BII, and BIII methods to determine the breakage distribution parameters. These methods involve many assumptions such as the small extent of re-breakage of particles during a short milling period. Another major approach is the so-called back-calculation method based on coupled use of Equation (1.5) along with an optimizer to estimate the parameters (see Klimpel and Austin, 1970; Capece et al., 2011b). The optimization-based back-calculation method is fast and efficient and it does not require the preparation of mono-dispersed feeds in experiments.

Regarding ball milling, two major models for the first-order specific breakage rate k_i were used: the Austin model (Austin et al., 1984) and the Kotake–Kanda model (Kotake et al., 2002). Both models successfully capture the physics in that there exists an optimal ball size for a given feed size or vice versa. Finer particles are more difficult to break due to the fact that fewer internal flaws are affected by an impact, while coarser particles are more difficult to efficiently nip between grinding balls. The Austin model, in which the impact of the process parameters (ball filling J, powder filling ratio U, and ball size d_B) are involved, is given by

$$k_i\left(x_i, d_{\mathrm{B}}\right)=a_0 \frac{\left(x_i / x_0\right)^\alpha}{d_{\mathrm{B}}{}^{A_1}\left[1+\left(\frac{x_i}{\mu d_{\mathrm{B}}{}^{A_2}}\right)^\Lambda\right]} \frac{\exp\left(-1.2U\right)}{1+6.6J^{2.3}} \frac{\phi_{\mathrm{c}}-0.1}{\left\{1+\exp\left[15.7\left(\phi_{\mathrm{c}}-0.94\right)\right]\right\}} \tag{1.8}$$

Here, a_0, μ, α, and $\wedge$ are specific breakage rate parameters. A_1 and A_2 are correction factors. ϕ_{c} is the ratio of the operating rotation speed to the critical speed N_{c}. While ball filling J can be determined using $J=\frac{m_{\mathrm{B}}}{\rho_{\mathrm{B}}\left(1-\varepsilon_{\mathrm{B}}\right)V_{\mathrm{M}}}$ in Equation (1.2), the interstitial filling ratio can be calculated by

$$U=\frac{m_{\mathrm{p}}}{\rho_{\mathrm{p}} V_{\mathrm{M}} J\left(1-\varepsilon_{\mathrm{B}}\right)\varepsilon_{\mathrm{B}}} \tag{1.9}$$

where m_{p} is the mass of the powder, ρ_{p} is the powder density, V_{M} is the mill volume, and ε_{B} is the void fraction of grinding balls at rest.

In the ball milling of various materials (silica glass, limestone, and gypsum) performed by Kotake et al. (2002), various feed particle sizes (narrow sieve cuts) and grinding ball sizes were investigated to experimentally determine their effect on the specific breakage rate parameter. The Kotake–Kanda model is given by

$$k_1=A_3 d_{\mathrm{B}}{}^{A_4} x_{\mathrm{f}}{}^{A_5} \exp\left(-A_6 \frac{x_{\mathrm{f}}}{d_{\mathrm{B}}{}^{A_7}}\right) \tag{1.10}$$

Here, k_1 is the specific breakage rate for a given mono-dispersed feed x_f, and d_B is a single ball size. The coefficients A_3–A_7 are fitting parameters. **Figure 1.4** shows the specific breakage rate parameter as determined by an empirical equation that Kotake et al. (2002) developed specifically to describe the influence of feed and ball sizes for this set of experiments. Note that k_1 in the Equation (1.10) is K_1 in **Figure 1.4**. As Kotake et al.'s experimental result show, a maximum of the specific breakage rate parameter is obtained at about 3 mm for this particular milling condition using a 30-mm ball size. Particle sizes finer than and coarser than 3 mm have a lower specific breakage rate corresponding to slower breakage rates.

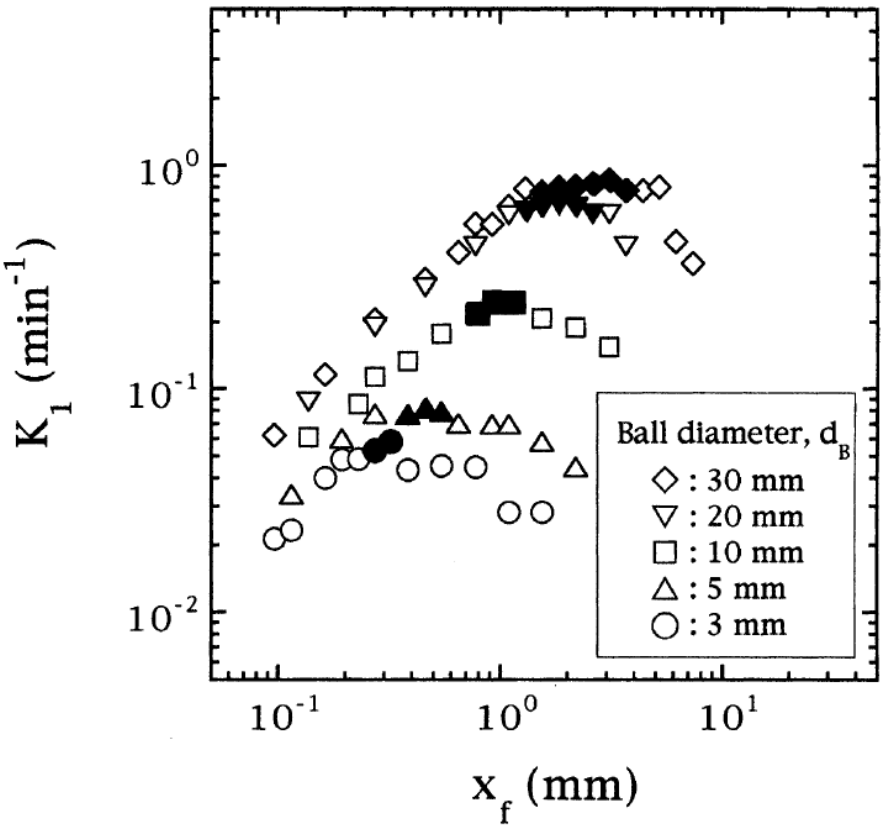

Figure 1.4 Experimental specific breakage rate of silica glass for various feed and ball sizes. K_1 refers to the specific breakage rate for mono-dispersed feed x_f.

Source: Kotake et al. (2002)

In the milling literature, the specific breakage rates for various materials were determined using lab-scale mills. However, these specific breakage rates cannot be applied directly to commercial mills due to the different breakage capabilities of mills of different sizes. Therefore, the specific breakage rates need to be scaled up. The rule for scaling up models to determine specific breakage rates, which was developed by Austin et al. (1984), is given by

$$k_i\left(x_i\right) = a_{\mathrm{T}} \frac{\left(x_i / x_0\right)^{\alpha}}{\left[1+\left(\frac{x_i}{C_1 \mu_{\mathrm{T}}}\right)^{\Lambda}\right]} C_2 C_3 C_4 C_5 \tag{1.11}$$

$$C_1 = \left(\frac{D}{D_{\mathrm{T}}}\right)^{N_2} \left(\frac{d_{\mathrm{B}}}{d_{\mathrm{B,T}}}\right)^{N_3} \tag{1.12}$$

$$C_2 = \left(\frac{d_{\mathrm{B,T}}}{d_{\mathrm{B}}}\right)^{N_0} \tag{1.13}$$

$$C_3 = \begin{cases} \left(\frac{D}{D_{\mathrm{T}}}\right)^{N_1} & \text{if } D \le 3.81\,\mathrm{m} \\ \left(\frac{3.81}{D_{\mathrm{T}}}\right)^{N_1} \left(\frac{D}{3.81}\right)^{N_1 - N_4} & \text{if } D > 3.81\,\mathrm{m} \end{cases} \tag{1.14}$$

$$C_4 = \frac{1+6.6 J_{\mathrm{T}}^{2.3}}{1+6.6 J^{2.3}} \exp\left[-c\left(U - U_{\mathrm{T}}\right)\right] \tag{1.15}$$

$$C_5 = \left(\frac{\phi_C - 0.1}{\phi_{C,T} - 0.1} \right) \left\{ \frac{1 + \exp\left[15.7\left(\phi_{C,T} - 0.94 \right) \right]}{1 + \exp\left[15.7\left(\phi_C - 0.94 \right) \right]} \right\} \tag{1.16}$$

where a_T and μ_T are specific breakage rate parameters in which experiments were performed in a mill diameter D_T with a ball size $d_{B,T}$, a ball filling ratio J_T, a powder filling ratio U_T, and a rotation speed $\phi_{C,T}$, which is expressed as a fraction of the critical speed. Parameters N_0–N_4 are correction factors. Then, the specific breakage rate for the ball mill (diameter D) operating with ball size d_B, ball filling ratio J, powder filling ratio U, and rotation speed ϕ_c can be determined using the scale-up rule in Equations (1.11)–(1.16). In Equation (1.15), c = 1.2 for dry ball milling.

1.2.1.2 Nonlinear PBM for batch milling processes. Unfortunately, the predictive capability of the linear, time-invariant model, i.e., Equation (1.5), for the evolution of PSD deteriorates for prolonged milling during which significant amounts of fines are produced in a dense particle bed (Austin and Bagga, 1981; Austin et al., 1981a; Gutsche and Fuerstenau, 1999), typical of ball milling processes. **Figure 1.5** displays three types of deviations from the linear PBM. Note that m in **Figure 1.5** is mass fraction. Type I deviation occurs during the milling of a mono-dispersed feed. Considering only topmost size class (i = 1), solution of Equation (1.5) for the topmost size class is given by

$$M_1(t) = M_{10} \exp(-S_1 t) \tag{1.17}$$

With a semi-log plot (horizontal axis is m_1/m_{10} and vertical axis is t), the constant slope is equal to $-S_1/2.3$. The slope is invariant to the initial mass fraction for topmost size

class (i = 1) for linear breakage kinetics (single curve for any M_{10}). For a short milling of mono-sized feed ($t < t^*$), the specific breakage rate is constant, which is compliant with the first-order breakage kinetics. However, for prolonged milling time ($t > t^*$), the specific breakage accelerates or decelerates (Type I deviation). The time, t^*, after which the deviation becomes significant, depends on the mode of operation, milling conditions, and properties of the material being ground. Type II and III deviations occur when a binary feed, comprising coarse and fine particles, is ground. The specific breakage rate of the coarse particles may increase (Type II) or decrease (Type III) upon the initial addition of fine particles, unlike linear breakage kinetics. These deviations from linear breakage kinetics were experimentally observed by Fuerstenau and Abozeid (1991) (Type II deviation) and Austin and Bagga (1981) (Type III deviation). Both deviations reveal the significant impact of the initial feed mixture or PSD on the specific breakage rate, which is a manifestation of complex nonlinear effects.

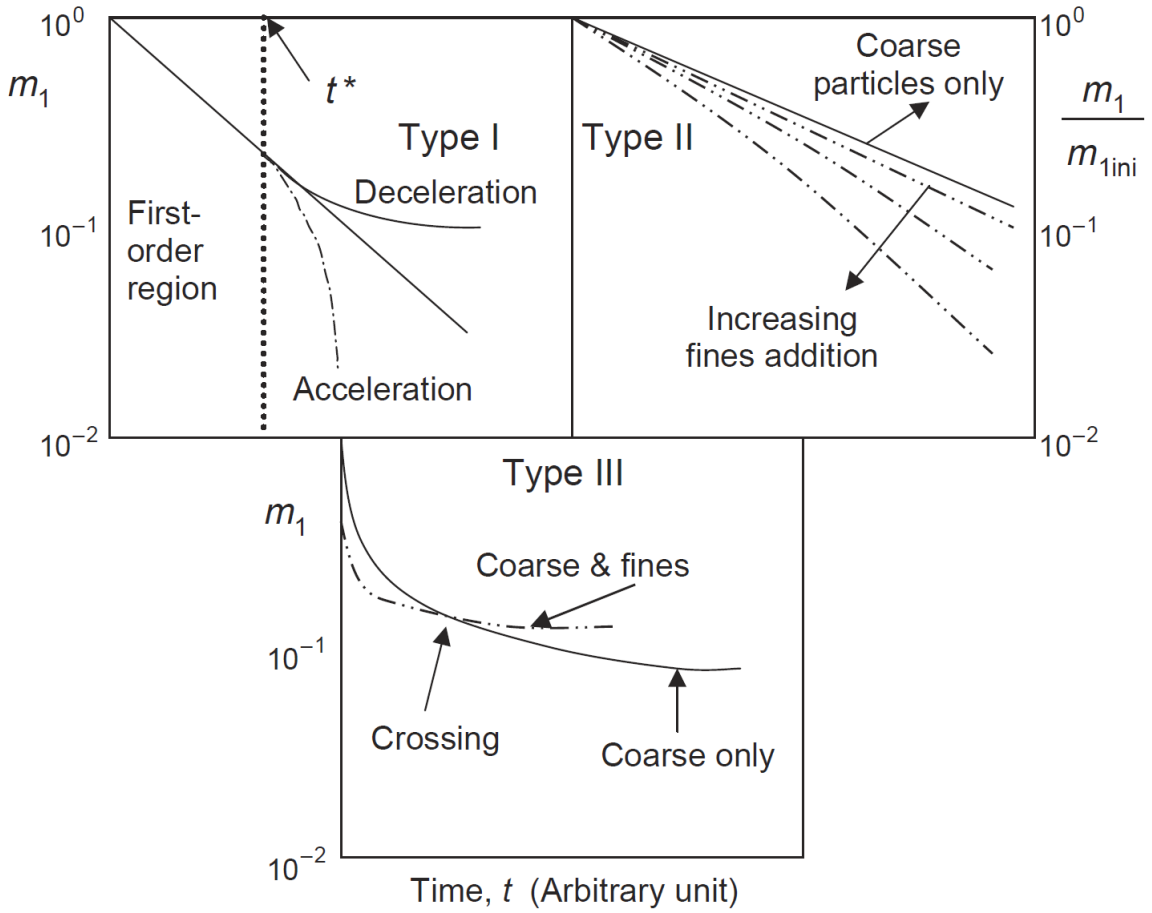

Figure 1.5 A schematic demonstrating the following characteristic deviations from linear PBM: breakage of a mono-dispersed feed (Type I deviation) and breakage of a binary feed comprising coarse and fine particles (Type II and Type III deviation).

Source: Bilgili and Scarlett (2005a)

To address this complex milling behavior, a linear, time-variant (LTVAR) model was proposed (Austin and Bagga, 1981; Austin et al., 1981a). According to the model, the specific breakage rate was time-dependent and modulated by an appropriate acceleration–deceleration function of time, $\kappa(t)$. The specific breakage rate for all size classes was assumed to vary in the same way as the milling environment changed according to the acceleration–deceleration function. The LTVAR model is expressed by the following equation:

$$\frac{dM_i(t)}{\kappa(t)dt} = -k_i(0)M_i(t) + \sum_{j=1}^{i-1} b_{ij}k_j(0)M_j(t) \tag{1.18}$$

where $N \geq i \geq j \geq 1$ and $M_i(0) = M_{i0}$. Here, $\kappa(t) = 1$, $\kappa(t) > 1$, and $\kappa(t) < 1$ refer to the constant specific breakage rate, acceleration, and deceleration, respectively. Also, by defining a transformed time θ as an effective first order milling time via $\theta = \int_0^t \kappa(t)dt$ and $d\theta/dt = \kappa(t)$ with $\theta(0) = 0$, t can be replaced with θ and solved it in the domain of θ, as expressed by

$$\frac{dM_i(\theta)}{d\theta} = -k_i(0)M_i(\theta) + \sum_{j=1}^{i-1} b_{ij}k_j(0)M_j(\theta) \tag{1.19}$$

Although the LTVAR model can explain the acceleration or deceleration of the breakage, it cannot explain nonlinear effects associated with a wide, evolving PSD during milling or different feed PSDs (Type II and Type III deviations) because it assumes that $\kappa(0) = 1$ by definition. In other words, it cannot account for nonlinearities that arise from multi-particle interactions in a wide feed/initial PSD. Hence, a general nonlinear PBM theory is needed to describe the complex nonlinear effects in ball milling.

The complex nonlinear breakage behavior observed in batch milling experiments was successfully described by a nonlinear PBM framework formulated by Bilgili and Scarlett (2005a). Their nonlinear framework was also extended to continuous milling (Bilgili and Scarlett, 2005b), which is detailed in the next section. In their approach, the specific breakage rate of particles of size *x* is affected by the surrounding population with

generic particle size $z \neq x$. The specific breakage rate S is dependent on the particle population density; therefore, it can phenomenologically account for the impact of evolving PSD and mechanical multi-particle interactions. With these considerations, the specific breakage rate was composed of the first-order specific breakage rate function $k(x)$ and the nonlinear function $F\left[\int_0^\infty W(x,z)M(z)dz\right]$, a.k.a., the effectiveness factor, which expresses the contribution of generic size z particles to the disappearance rate of size x particles due to multi-particle interactions. Note that both $F[\ ]$and $k(x)$ depend on the mill type, design variables, operation mode, operating variables, and material properties. The size-discrete continuous-time PBM for batch milling is represented by the following equation:

$$\frac{dM_i(t)}{dt} = -k_i F_i\left[\sum_{q=1}^{N} W_{iq} M_q(t)\right] M_i(t) + \sum_{j=1}^{i-1} b_{ij} k_j F_j\left[\sum_{q=1}^{N} W_{jq} M_q(t)\right] M_j(t) \qquad (1.20)$$

where $N \geq i \geq j \geq 1$ and $M_i(0) = M_{i0}$.

The set of coupled nonlinear ordinary differential equations (ODEs) in Equation (1.20) can account for occasional accelerated ($F_i[\ ] > 1$) and decelerated ($F_i[\ ] < 1$) breakage depending on the instantaneous PSD. This equation can also be simplified by assuming that the specific breakage rate of size x particles is primarily affected by the mass fraction of particles of size $z \leq x$, which can be written as

$$\frac{dM_i(t)}{dt} = -k_i F_i \left[\sum_{q=j}^{N} W_{iq} M_q(t) \right] M_i(t) + \sum_{j=1}^{i-1} b_{ij} k_j F_j \left[\sum_{q=j}^{N} W_{jq} M_q(t) \right] M_j(t) \tag{1.21}$$

Bilgili et al. (2015) discriminated different PBMs in their capability to fit the experimental data from Austin et al. (1990) on the fine, dry ball milling of quartz. Various PBMs were used in the fitting: time-continuous linear PBM (TCL-PBM, Equation (1.5)), linear time-variant PBM (LTVAR-PBM, Equation (1.19), and time-continuous nonlinear PBM (TCNL-PBM, Equation (1.21)) with two different effectiveness factors F (refer to EF1 and EF2 in Equations (1.22) and (1.23), respectively). In all PBMs, k_i and B_{ij} were assumed to follow Equation (1.7).

$$F_i[\ ] = \left[1 + \lambda \sum_{q=i}^{N} \left(1 - x_q / x_i \right)^{\alpha} M_q \right]^{-1} \tag{1.22}$$

$$F_i[\ ] = \frac{1}{1 + \left[\lambda \sum_{q=i}^{N} \left(1/x_q - 1/x_i \right)^{\alpha} M_q \right]^2} \tag{1.23}$$

In the context of LTVAR PBM (Equation (1.19)), various forms of $k_i(t)$ can be used; the following specific function has been used to account for the deceleration of breakage rate due to presence of fines (Austin et al., 1984):

$$k_i(t) = \kappa(t) k_i = \left[\kappa_0 + \frac{1-\kappa_0}{1+\left(x_{80} / x_{80}^* \right)^{-\Delta}} \right] k_i \tag{1.24}$$

where k_i is the (time-independent) specific breakage rate parameter, $\kappa(t)$ is a time-dependent deceleration factor, x_{80} is the temporally evolving 80%-passing size of the cumulative PSD, and κ_0, x_{80}^*, and Δ are model parameters to be estimated. The slowing-down factor κ_0 ($0 < \kappa_0 < 1$) scales the overall deceleration of the breakage rate, while x_{80}^* and Δ modulate the change of $\kappa(t)$ with x_{80}.

Figure 1.6 illustrates the fit of all models to the experimental data, while **Table 1.1** presents the fitted parameters, sum of squared residuals (*SSR*), standard error of the residuals (*SER*), and standard error of the parameter (*SEP*). The coefficient of variation (*COV*) and p-value for each parameter were calculated (not shown for brevity). After 15 min milling, the most commonly used form of the PBM, TCL-PBM, exhibits marked deviation from the cumulative PSD data (**Figure 1.6**), which can also be inferred from the relatively high *SSR* and *SER*. Note that even the slightest systematic deviation from experimental data in cumulative representation of the PSD is regarded significant because cumulative PSDs tend to mask random noise (Das, 2001). TCL-PBM was the least capable of fitting the experimental data among all models. The best fit, i.e., the lowest *SSR* and *SER* with all statistically significant parameters ($p < 0.05$), was achieved with the nonlinear PBM, TCNL-PBM with EF2 (see **Table 1.1**). If 99% confidence level ($p < 0.01$) is intended for the fitted parameters, only the nonlinear PBMs are capable of achieving that objective among all models. The LTVAR-PBM with $\kappa_0 = 0$ also performed well with similar fitting capability to that of TCNL-PBM2. This is not very surprising as the LTVAR-PBM with

Equation (1.19) is actually a specific form of the nonlinear PBM with the lumped kinetics assumption (see Bilgili et al., 2006). Overall, these results clearly demonstrate the superiority of the nonlinear framework over the traditional TCL-PBM for dense-phase fine milling of materials. Recent multi-scale modeling efforts (Capece et al., 2014; Capece et al., 2015), which will be detailed in the next section, have provided a mechanistic basis for the superiority of the TCNL-PBM for modeling dense-phase dry milling.

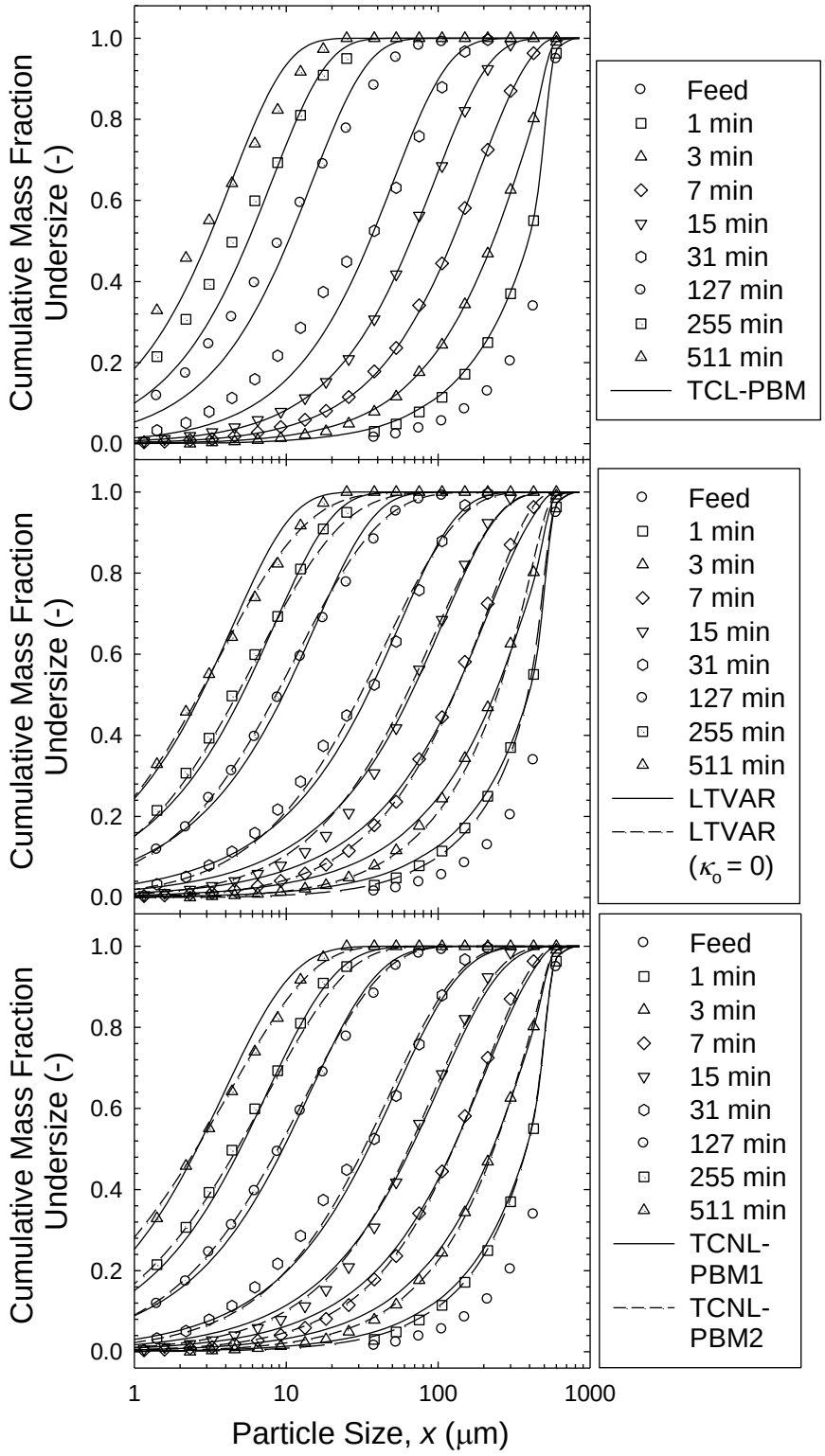

Figure 1.6 Fitting of the experimental ball milling data via various population balance models. Fitted parameters are presented in **Table 1.1**. TCNL-PBM1 and TCNL-PBM2 uses the effectiveness factors EF1 (Equation (1.22)) and EF2 (Equation (1.23)), respectively.

Source: Experimental data (Austin et al., 1990) and fitted parameters (Bilgili et al., 2015)

Table 1.1 Estimated Parameters for Various Models Fit to the Batch Milling Data

Parameter	TCL-PBM		LTVAR-PBM		LTVAR-PBM[b]		TCNL-PBM1		TCNL-PBM2	
	Estimated Value	*SEP*	Estimated Value	*SEP*	Estimated Value	*SEP*	Estimated Value	*SEP*	Estimated Value	*SEP*
A (min^{-1})	1.082	0.342	5.482	1.173	2.551	0.099	1.369	0.277	1.200	0.089
m	1.136	0.012	1.118	0.015	0.316	0.128	1.091	0.015	0.812	0.027
ϕ	0.737	0.267	0.615	0.138	0.313	0.132	0.522	0.187	0.395	0.099
μ	1.053	0.094	0.779	0.074	1.327	0.081	0.816	0.085	0.979	0.031
v	5.122	2.348	3.151	0.641	7.400	0.202	3.195	0.500	3.768	0.124
α	—	—	—	—	—	—	7.327	2.763	0.320	0.073
λ[a]	—	—	—	—	—	—	3.382	1.307	3.604	0.064
κ_o	—	—	0.155	1.121	—	—	—	—	—	—
Δ	—	—	7.635	1.188	0.969	0.059	—	—	—	—
$x_{80}^{*}(\mu\text{m})$	—	—	824.193	0.369	792.580	0.244	—	—	—	—
SSR	1.405×10^{-1}		6.780×10^{-2}		3.477×10^{-2}		5.768×10^{-2}		2.842×10^{-2}	
SER	3.180×10^{-2}		2.233×10^{-2}		1.593×10^{-2}		2.052×10^{-2}		1.440×10^{-2}	

[a] λ is dimensionless for TCNL-PBM1 (with EF1) and has units of μm^{α} for TCNL-PBM2 (with EF2)

[b] with $\kappa_o = 0$

Source: Batch milling data of Austin et al. (1990) and table 1.1 was excerpted from Bilgili et al. (2015)

1.2.2 PBM for open-circuit continuous ball milling

Similar to batch mill, perfect mixing was usually assumed to describe mixing degree in continuous milling (e.g., Whiten 1974; Weedon, 2001). The linear PBM for continuous mill operated at steady state is given by

$$0 = M_{i,\text{in}} - M_{i,\text{out}} - \tau S_i M_i + \tau \sum_{j=1}^{i-1} b_{ij} S_j M_j \tag{1.25}$$

where $M_{i,\text{in}}$ and $M_{i,\text{out}}$ represents mass fraction in size class i at inlet and outlet, respectively. τ is the space-time or average residence time defined as the ratio of total mass hold-up to the mass flow rate of the feed. Weedon (2001) stated that perfect mixing model was assumed to avoid the consideration of residence time distribution in the mill and it seems to be adequate for ball mill having appropriate length.

Bilgili and Scarlett (2005b) investigated the impact of nonlinear breakage kinetics in continuous open-circuit milling in which the mixing degrees were ideal (i.e., perfect mixing and plug flow (no axial back-mixing)). It should be noted that unsteady state operations and internal separations that occurred in the mill were not considered in their study. For steady-state continuous milling operation, the size-discrete form of the nonlinear PBM assuming perfect mixing and plug flow are expressed in the following equations, respectively:

$$M_{i,\text{in}} - M_i - \tau k_i F_i \left[\sum_{q=1}^{N} W_{iq} M_q \right] M_i + \tau \sum_{j=1}^{i-1} b_{ij} k_j F_j \left[\sum_{q=1}^{N} W_{jq} M_q \right] M_j = 0 \qquad (1.26)$$

$$\frac{dM_i(\bar{\eta})}{d\bar{\eta}} = -\tau k_i F_i \left[\sum_{q=1}^{N} W_{iq} M_q(\bar{\eta}) \right] M_i(\bar{\eta}) + \tau \sum_{j=1}^{i-1} b_{ij} k_j F_j \left[\sum_{q=1}^{N} W_{jq} M_q(\bar{\eta}) \right] M_j(\bar{\eta}) \qquad (1.27)$$

In Equation (1.27), $\bar{\eta} = \eta / L$ where η is the axial position from the inlet and L is the total length of the mill. Solutions to Equations (1.26) and (1.27) yield steady-state product PSDs. **Figure 1.7** compares the product PSDs for the two idealized mixing regimes, i.e., perfect mixing and plug flow with otherwise identical conditions: the same τ and inlet PSD; Gaussian mean = 600 μm, standard deviation = 100 μm. Bilgili and Scarlett (2005b) used nonlinear function $F_i[\ ] = \left[1 + \lambda \sum_{q=i}^{N} \left(1 - \frac{x_q}{x_i} \right)^{\alpha} M_q \right]^{-1}$ in their study. A higher λ signifies that the fine particles have a more significant deceleration effect on the coarse particles. For any given λ, the size distribution shifts monotonically toward finer sizes with an increase in average residence time τ. For any given τ, the PSD becomes coarser with increased λ (16 vs. 0). For a given λ and τ, the plug flow produces a finer PSD than perfect mixing for sizes ranging from 100 to 800 μm due to the absence of axial back-mixing.

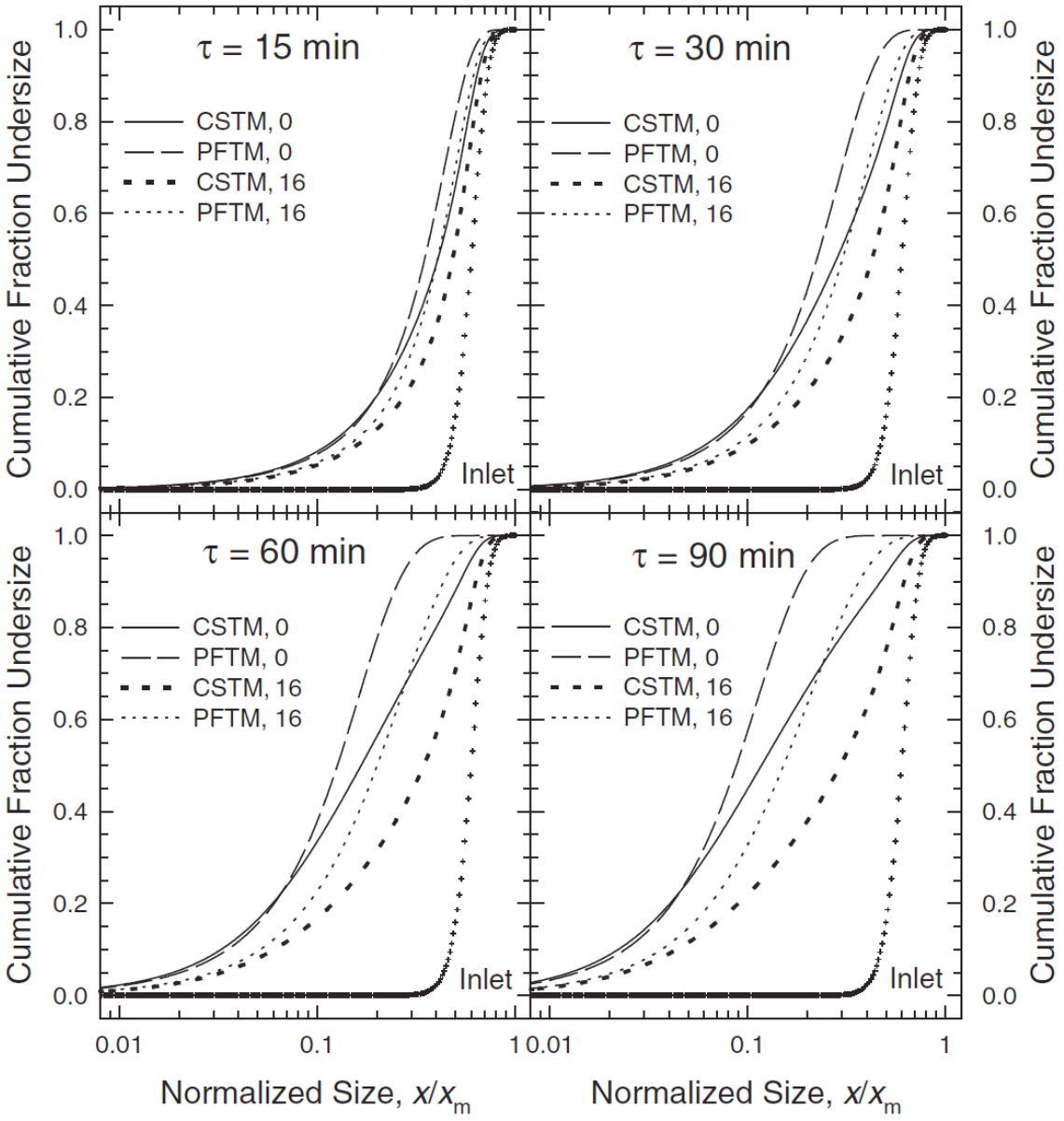

Figure 1.7 A comparison of the PSDs for perfect mixing (CSTM) and plug flow (PFTM) for various values of average residence time τ and multi-particle interaction parameter λ.

Source: Bilgili and Scarlett (2005b)

The above models did not consider non-ideal mixing regimes in the mill. Experimental studies based on tracer studies in the mills suggest that finite axial back-mixing takes place. In these studies, residence time distribution (RTD) was measured. Analogous to the determination of conversions in chemical reactors, the degree of the particles' mixedness in the mill can be quantifiably assessed using RTD function, which can be experimentally obtained from the pulse injection of an inert chemical (i.e., tracer) (Austin et al., 1971; Shoji et al., 1973; Fuerstenau et al., 1986). The tracer pulse is injected at the mill inlet and the concentration of the tracer is measured at the mill outlet. The RTD function can be determined as expressed in Equation (1.28).

$$E(t) = \frac{C(t)}{\int_0^\infty C(t)\mathrm{d}t} \tag{1.28}$$

where $E(t)$ and $C(t)$ are the RTD function and the concentration of tracer leaving the mill between time t and $t+dt$, respectively. **Figure 1.8** compared experimental RTD and computed RTD using convective-dispersion model, showing a good agreement. In **Figure 1.8**, α refers to inverse of Peclect number which describes particle transport by convection relative to dispersion.

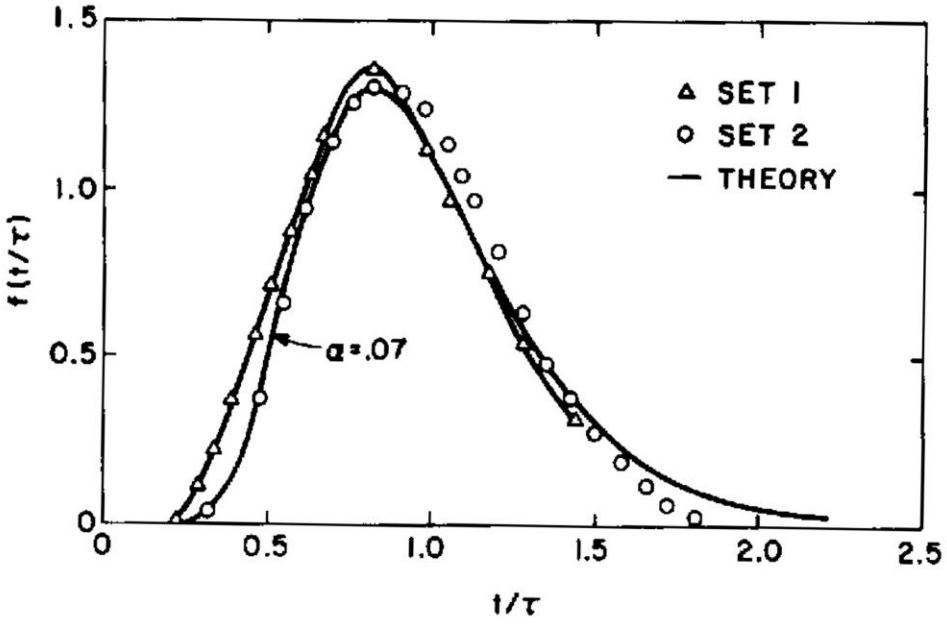

Figure 1.8 Comparison of dimensionless RTDs between experimental and convective-dispersion model.

Source: Austin et al. (1971)

The convection-dispersion model assumes that particles are well-mixed in the radial direction and that the hold-up did not significantly change throughout the length of the mill. The size- and time-continuous convective dispersion PBM proposed by Mihalyko et al. (1998) is expressed by the following equation:

$$\frac{\partial M_{\mathrm{d}}(x,y,t)}{\partial t} = -k(x)M_{\mathrm{d}}(x,y,t) + \int_{x}^{x_{\mathrm{m}}} k(l)b(x,l)M_{\mathrm{d}}(l,y,t)dl + D\frac{\partial^2 M_{\mathrm{d}}(x,y,t)}{\partial y^2} - u\frac{\partial M_{\mathrm{d}}(x,y,t)}{\partial y} \tag{1.29}$$

$M_{\mathrm{d}}(x,y,0) = M_{\mathrm{d},0}(x,y)$, $uM'_{\mathrm{d}}(x,t) = uM_{\mathrm{d}}(x,0,t) - D\frac{\partial M_{\mathrm{d}}(x,0,t)}{\partial y}$, and $\frac{\partial M_{\mathrm{d}}(x,L,t)}{\partial y} = 0$.

$M_d(x,y,t)$ is the mass density of size x particles at longitudinal location y and time t. Moreover, D and u denote the dispersion coefficient and the average velocity. Mihalyko et al. (1998) demonstrated the impact of the extent of mixing on the PSD; however, they did not consider the complex nonlinear kinetics effects observed in the literature. Their result showed that lower uL/D led to coarser product size. Also, the impact of internal classification within the mill was not modeled. Bilgili and Scarlett (2005b), however, did account for this. Unfortunately, neither theoretical study validated their simulations with any experimental results in continuous open-circuit ball milling.

The tanks-in-series model, which assumes perfect mixing in each tank (cell), accounts for finite axial mixing effects in both open- (Genc, 2016) and closed-circuit ball milling (Austin et al., 1975; Benzer, 2005). In this model, there is no back-flow of materials between the tanks. While this class of PBMs shows promising results in accounting for the finite axial mixing effects and fitted experimental data for a given set of process conditions well, there are many caveats and unresolved issues. Before delving into such issues, it should be mentioned that the tanks-in-series model is the reduced form of the cell-based PBM, which does consider axial back-flow between adjacent cells. The schematic of cell-based model for the open-circuit continuous milling equipped with discharge screen is showed in **Figure 1.9**.

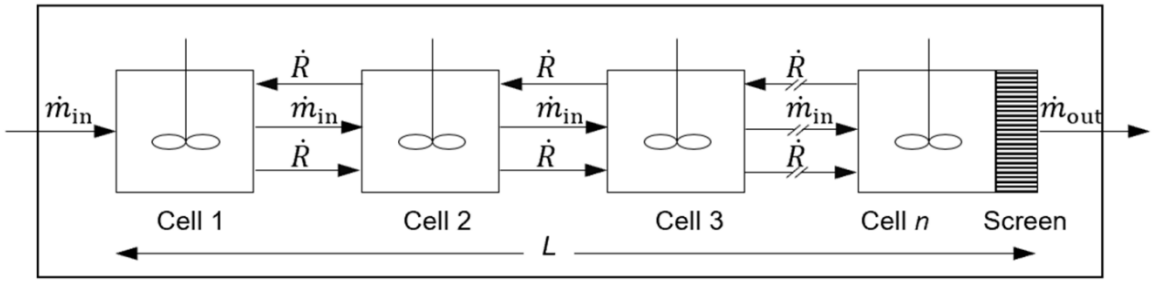

Figure 1.9 Schematic model of a continuous mill represented as a series of *n* well-mixed cells with a discharge screen at the end. Cells exchange particles at the rate $\dot{R}$ (axial back-flow rate). The mill has the effective length *L*. $\dot{m}_{in}$ and $\dot{m}_{out}$ refer to feed and production rates, respectively.

Source: Adapted from Kwade and Schwedes (2007)

In addition, Kwade and Schwedes (2007) demonstrated that the cell-based model could be more accurate than the convection-dispersion model when describing the mixing degree in a wet stirred media mill. It is critical to note that no cell-based PBM approach has been applied dry ball milling yet. Finally, all of the PBMs mentioned considered steady-state operation. Hence, they do not allow for the analysis of unsteady-state operation and impact of various disturbances. None of these studies considered nonlinear breakage kinetics commonly observed in dry ball milling; they all assumed traditional linear breakage kinetics in their models.

1.2.3 Classification modeling

An air classifier is an important machine in the cement milling process. In a cement plant, closed-circuit ball milling is a conventional milling system. The performance of an air classifier can be examined using a Tromp curve, which is defined as the fraction of the classifier's feed stream sent to the classifier's reject stream. Austin and Klimpel (1981) proposed a three-parameter Tromp curve, which is expressed as:

$$T_i = \delta + (1-\delta)\left[\frac{1}{1+\left(x_i/d_{50c}\right)^{-\Lambda}}\right] \tag{1.30}$$

where T_i is the mass fraction of particles in size class i in the classifier's feed sent to the reject stream. d_{50c}, δ, and Λ are parameters describing the corrected cut size, bypass fraction, and sharpness. It is critical to note that the classification model in Equation (1.30) cannot explain the fish-hook phenomenon which has been observed experimentally.

Napier-Munn et al. (1996) formulated a classification model in terms of an efficiency curve. They defined the efficiency curve $E_{oa,i}$ as the mass fraction of particles in size class i in the classifier's feed sent to the product stream, i.e., $E_{oa,i} = 1 - T_i$. The five-parameter efficiency curve (Napier-Munn et al., 1996) is given by

$$E_{oa,i} = C\left\{\frac{\left(1+\beta'\beta^*\frac{x_i}{d_{50c}}\right)\left[\exp(\alpha')-1\right]}{\exp\left(\alpha'\beta^*\frac{x_i}{d_{50c}}\right)+\exp(\alpha')-2}\right\} \tag{1.31}$$

where C is defined as 1–bypass fraction, i.e., $1-\delta$; α' is the sharpness parameter, and β' is the fish-hook parameter. β^* is a parameter that ensures $E_{oa,i} = C/2$ for $x_i = d_{50c}$, thus preserving the definition of d_{50c}. The classification model in Equation (1.31) accounts for the bypass fraction, sharpness, and the fish-hook phenomenon. It should be noted that the classification model in Equation (1.31) was also applied to account for air-sweeping action, i.e., internal separation, (Benzer, 2005; Genc, 2016).

Besides fitting Tromp parameters using experimental data (Ergun at al., 2004; Benzer, 2005; Altun, 2018), there have been a few attempts to correlate the parameters in Equation (1.31) with the operation parameters in closed-circuit ball milling. Those efforts can be divided into two groups: (i) fixed classification models according to which the classification function (Tromp curve or efficiency curve) of an air classifier depends solely on the classifier parameter (Altun et al., 2016), and (ii) variable classification models according to which the classification function also depends on the incoming PSD and dust loading (Altun and Benzer, 2014). Altun et al. (2016) performed a lab-scale experiment with the Alpine 100 MZR. This classifier can be operated with rotor speeds in the range of 1,000–15,000 rpm and airflow rates of 5–50 m^3/h. They reported the following correlations between the parameters of the classification model and the classifier operation parameters for a cement clinker:

$$\alpha' = 274.95\left(AF/RS_{\text{rpm}}\right)^{0.9165} \tag{1.32}$$

$$\beta' = -136.5\left(AF/RS_{\text{rpm}}\right) + 1.4362 \tag{1.33}$$

$$C = 23.8\ln\left(AF/RS_{\text{rpm}}\right) + 199.21 \tag{1.34}$$

$$d_{50c} = 2727\left(AF/RS_{\text{rpm}}\right) - 1.7929 \tag{1.35}$$

where AF is airflow in m^3/h, RS_{rpm} is rotor speed in rpm, d_{50c} is corrected cut size in μm. It should be mentioned that the classification model using the correlations in Equations (1.32)–(1.35) have not been applied to closed-circuit ball milling. Experiments have been performed to find only the correlation between the classifier's operation parameters (airflow rate and rotor speed) and the parameters for an efficiency curve in the lab-scale experiments.

While Altun et al. (2016) studied a fixed classification model based on a lab-scale classifier, Altun and Benzer (2014) proposed a variable classification model considering the large-scale operation parameters of the classifier and the separator feed properties. Their correlations for cement clinker are expressed as follows:

$$\alpha' = 0.905\left(D/DL\right)^{1.2679} \tag{1.36}$$

$$\beta' = 0.4417DL^{1.4171} - 0.1293 \tag{1.37}$$

$$\beta^* = 0.4365DL^{1.4171} + 0.7224 \tag{1.38}$$

$$C = 1 - 0.10467DL^{1.4171} \tag{1.39}$$

$$d_{50c} = \frac{1}{2.47}\left(\frac{AF}{RSF'}\right)^{0.7775} \tag{1.40}$$

where *D* is the diameter of the classifier's chamber in m. *DL* is dust loading in m^3/kg, which is defined as the ratio of the mass flow rate at the mill outlet to *AF*. *RS* is rotor speed in m/h, and F' is the mass flow rate at the mill outlet having sizes between 3 μm and 36 μm in kg/h. Interestingly, the variable classification models (Equations (1.36)–(1.40)) have not been coupled with a PBM to predict the PSD from a closed-circuit ball mill operating under milling conditions that are different from those used to estimate the parameters in the classifier model.

1.2.4 PBMs for closed-circuit continuous ball milling

There have not been many studies of simulations of closed-circuit cement clinker ball milling. While perfect mixing was generally assumed to describe the mixedness degree of particles in the mill (e.g., Jankovic et al., 2004), some researchers applied the tanks-in-series model to account for the mixing degree in the mill (Austin et al., 1975; Benzer, 2005; Altun, 2018). Austin et al. (1975) concluded that the tanks-in-series model could explain the mixing degree in the mill based on their earlier residence time distribution study (Austin et al., 1971). By fitting the residence time distribution in the large-scale mill with the tanks-in-series model, they showed that the 10-tank model could explain the mixing degree in the mill. A total average residence time τ of 5.58 min was reported. In their study, the classification model in Equation (1.30) was applied. They also used a constant scale-up factor of 2.75 to project the specific breakage rate from the lab mill's diameter of 200 mm to a commercial mill's diameter of 4000 mm. However, their model could examine the influences on the product PSD only during the steady-state operation.

While Austin et al. (1975) did not consider air-sweeping action, Benzer (2005) proposed a fully air-sweeping model for steady-state operation. He used the classification

model in Equation (1.31) and determined the classification parameters by fitting the classification model into existing performances of air classifier (for external separation) and ball mill (for internal separation which is air-sweeping) in a cement plant. He also analyzed the PSDs of samples taken along the axial direction of the mill during a sampling survey. He concluded that the classification model in Equation (1.31) could be used for both air classification and air-sweeping action. The simulation results (i.e., product PSD and reject rate) were validated with plant data, showing good agreement. However, it is critical to mention that the modeling proposed by both Austin et al. (1975) and Benzer (2005) cannot account for (i) unsteady-state operation, (ii) complex nonlinear breakage kinetics, (iii) internal separation by intermediate and discharge screens (mechanical separation), and (iv) classification induced by air-sweeping action in a single, integrated model. Also, the most important gap in their models is that they did not fully couple the ball mill with the classifier, i.e., the classification performance of the air classifier did not depend on the ball mill's performance.

1.2.5 PBMs for vertical roller mill

Vertical roller mills (VRM) have been used for cement milling since the 1980s (Tamashige et al., 1991). It has been reported that the specific energy consumption of VRMs is lower than that of a traditional ball mill (Tamashige et al., 1991; Xu et al., 2015). A VRM combines particle breakage and classification processes into a single-unit operation. **Figure 1.10** presents a general flow diagram of the VRM milling process. **Figure 1.11** presents a detailed view of VRM operations (Strohmeyer, 2013).

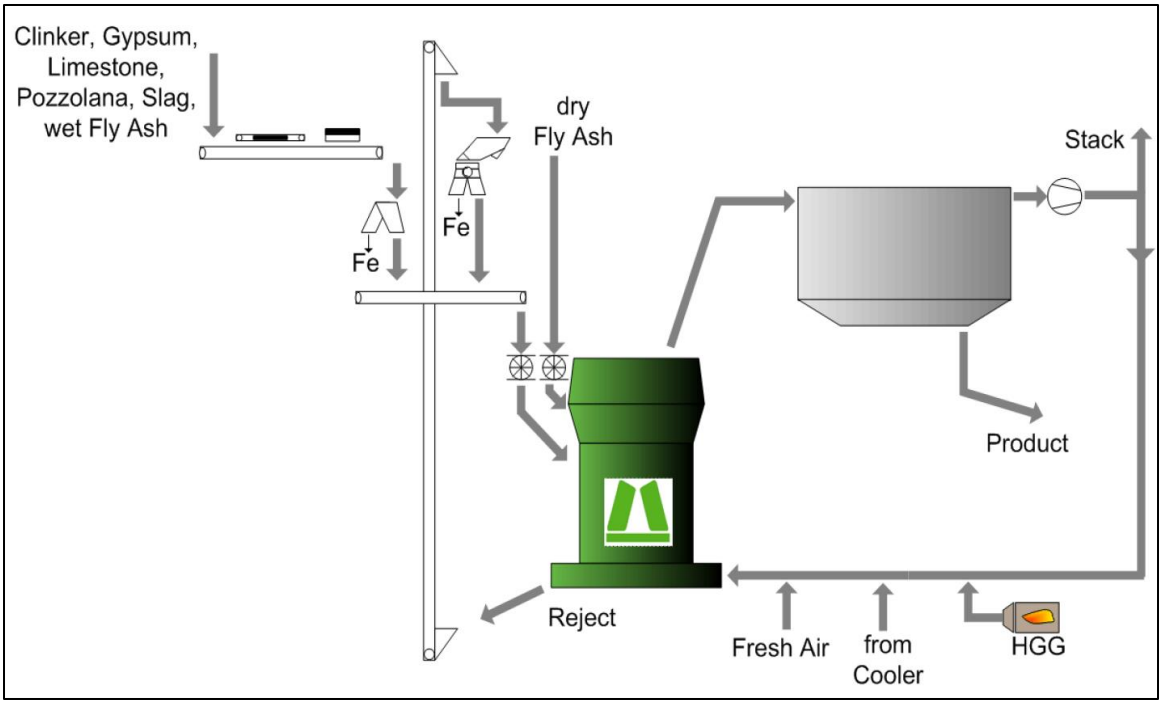

Figure 1.10 A general schematic of VRM operations.

Source: Strohmeyer (2013)

A simplified process operation can be briefly explained as follows. First, fresh particles are continuously fed to the VRM by a feeder. These fresh feed particles are mixed with coarse particles on the milling table, which are recycled from the built-in air classifier on top of the VRM. The milling pressure is transferred from the hydraulic cylinder to rollers for particle breakage. The particles retained on the rotating table due to the dam ring at the table's edge are broken by rollers. The rollers are rotated according to the motion of the rotating table. Therefore, both compression and shear forces from the rollers are applied for particle breakage (Strohmeyer, 2013). Sufficiently fine particles are lifted to the air classifier by air flow induced by an external mill fan, and fine products passing through the air classifier are collected as the final product. Finally, coarse particles are recycled back

to the table and mixed with fresh feed particles. This process takes place continuously inside the VRM.

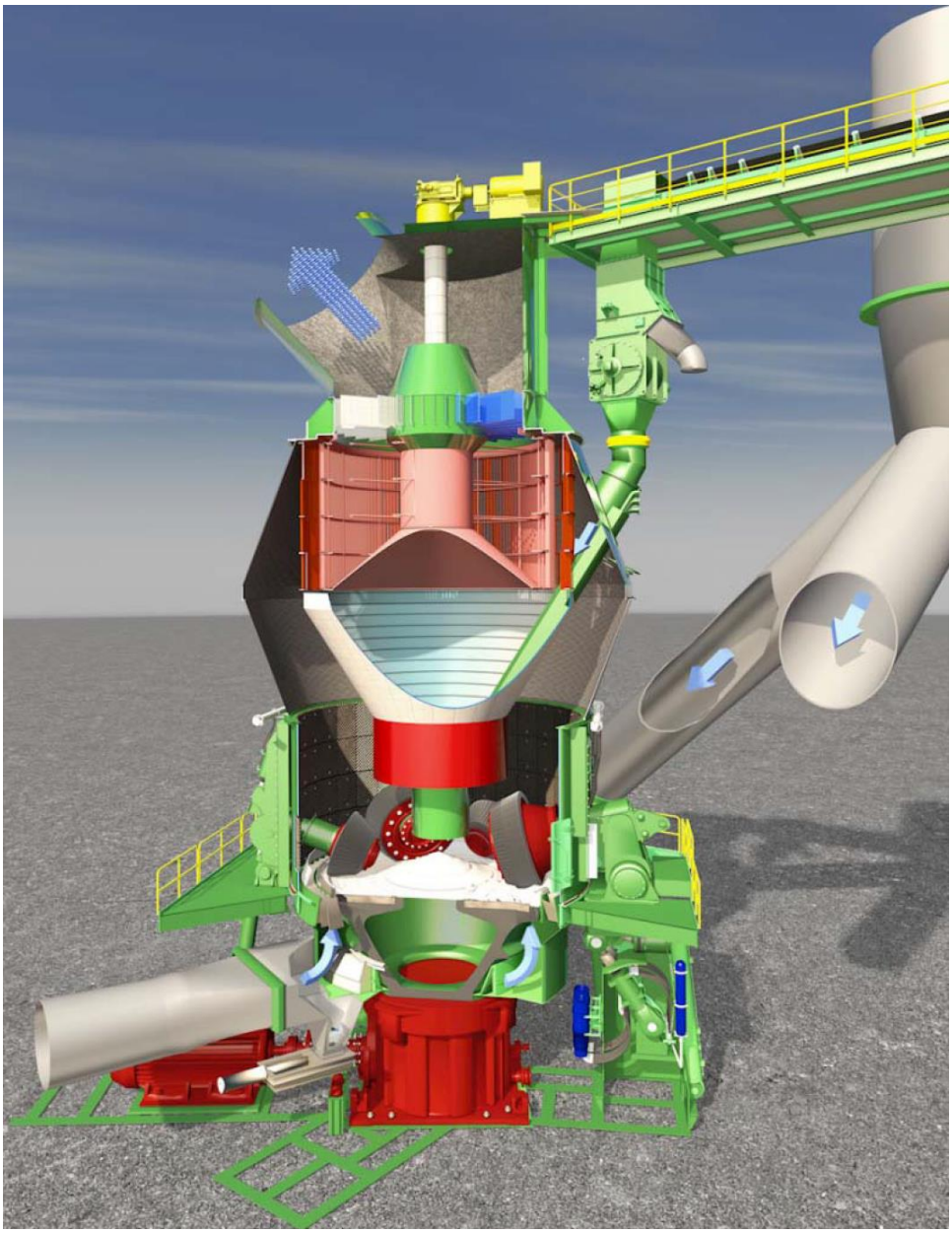

Figure 1.11 A detailed view of VRM operations.

Source: Strohmeyer (2013)

In the context of the PBM, only a limited number of studies on VRM for cement milling (Shahgholi et al., 2017; Fatahi and Barani, 2020; Fatahi et al., 2022) are available in the literature. All these works were conducted by the research group in Iran. The modeling approach from this group can be summarized as follows. Cumulative breakage distribution parameters used in the PBM were obtained from lab-scale data using a compression piston (Shahgholi et al., 2017), where the shear force could not be accounted for. The cumulative breakage distribution parameter was assumed to be material dependent and did not vary with the operation conditions. The experimentally obtained RTD data of full-scale VRM for cement mills was fitted with various RTD models. Their results (Fatahi and Barani, 2020) showed that the 5-tanks-in-series model could be accurately fitted with the experimental RTD of VRM. The average residence time (space time) was reported to be 1.12 min. However, when their PBM simulation was performed, they assumed ideal perfect mixing (i.e., one tank), which contradicts their RTD study (Fatahi and Barani, 2020). These previous modeling studies applied a steady-state, perfect mixing PBM for a continuous mill to fit the experimental cement product PSD at steady state. Their model considered only breakage kinetics while disregarding particle classification in the VRM. Neglecting classification could lead to an erroneous interpretation of the breakage kinetics and erroneous specific breakage rate parameters (falsified kinetics). Given the limitations of prior work, there is a need to develop a robust model of VRM that accounts for particle classification.

1.3 Discrete Element Modeling (DEM)

While the PBM can provide insight into the milling process at the process-length scale, it yields a limited understanding of milling at the particle-length scale. In PBM, the specific breakage rate parameter and the breakage distribution parameters are fitting parameters, which do not model the actual particle breakage. Moreover, most PBMs in the literature do not associate the specific breakage rate to material parameters and machine–process parameters explicitly. To gain further insight into the breakage at the particle ensemble scale, the discrete element method (DEM), developed by Cundall and Strack (1979), which models the mechanical inter-particle interactions, can be used. DEM solves the translational and rotational motion of particles using Newton's law of motion. The particle motion and the force of the contact between particle and particle or particle and geometry are resolved and updated every timestep. The mechanical interaction between particles can be described by various contact models. For the sake of brevity, only the most common model, the Hertz–Mindlin (no-slip) model, is detailed here. The normal force F_n and the tangential force F_t are expressed in Equations (1.41) and (1.42):

$$F_n = \frac{4}{3} E^* \sqrt{R^*} \delta_n^{3/2} - 2\sqrt{\frac{5}{6}} \frac{\ln e}{\sqrt{\ln^2 e + \pi^2}} \sqrt{2E^* m^*} (R^* \delta_n)^{1/4} v_n^{rel} \tag{1.41}$$

$$F_t = -8G^* \sqrt{R^* \delta_n} \delta_t - 2\sqrt{\frac{5}{6}} \frac{\ln e}{\sqrt{\ln^2 e + \pi^2}} \sqrt{8G^* m^*} (R^* \delta_n)^{1/4} v_t^{rel} \tag{1.42}$$

On the right-hand side of Equations (1.41) and (1.42), the first term represents elastic force, and the second term represents the damping force. E^*, G^*, R^*, and m^* are, respectively, the equivalent Young's modulus, equivalent shear modulus, equivalent radius, and equivalent mass. δ_n is normal particle overlap, and δ_t is tangential particle overlap. v_n^{rel} and v_t^{rel} are the normal and tangential components of the relative velocity between two generic particles at contact.

The DEM approach is mechanistic and deterministic, in which the interaction and motion of particles is tracked. Therefore, it is highly computationally expensive, and often unsuitable for industrial applications. DEM was first utilized in the mineral field to simulate the motion of the balls in the mill by Mishra and Rajamani (1992). Initially, DEM was used for qualitative studies; for example, to study granular motion in the mill (Mishra, 2003; Zhu et al., 2008). An application of DEM used in rotating drum as example is showed in **Figure 1.12** as a spatial distribution. Various parameters (e.g., number of collisions and collision velocity) can be tracked by DEM. Since then, the method has been rapidly developed to predict breakage efficiency through the specific breakage rate parameter via simulation of particle interactions obtained by DEM (e.g., Datta and Rajamani, 2002; Tavares and Carvalho, 2009; Wang et al., 2012; Capece et al., 2014).

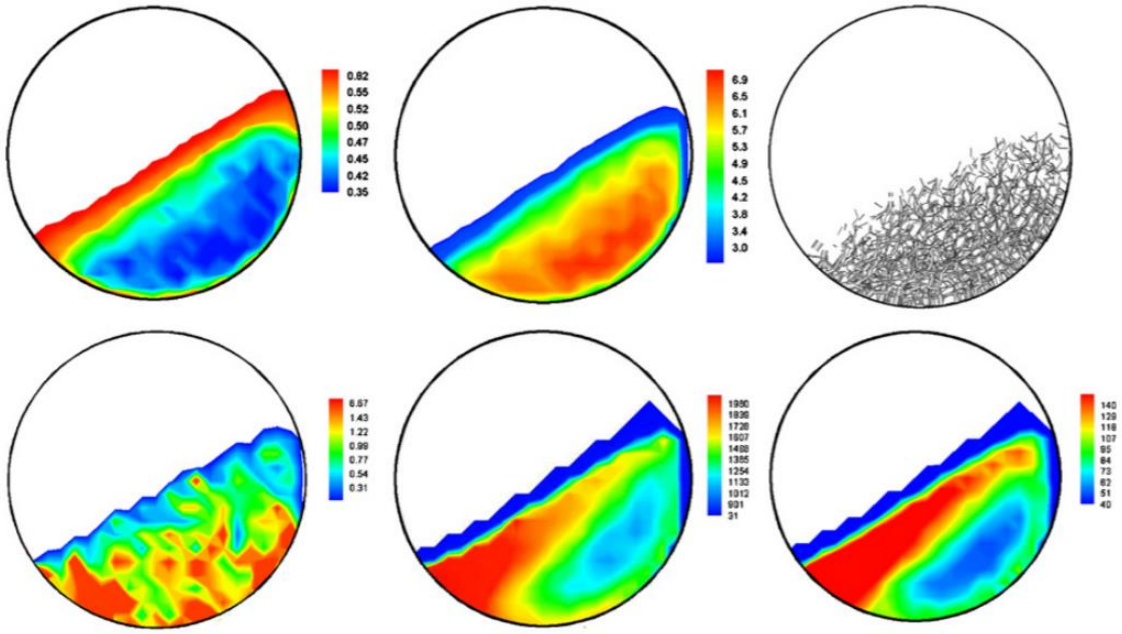

Figure 1.12 Spatial distribution of (from left to right and from top to bottom) porosity, coordination number, force network, total force, collision velocity, and number of collisions in rotating drum at rotation speed of 20 rpm.

Source: Yang et al. (2003) and Zhu et al. (2008)

1.4 Research Gaps and Challenges

This critical review has helped to identify various challenges and knowledge gaps in the modeling of closed-circuit dry ball milling and the need for model-guided process optimization for an industry, i.e., the cement industry, that heavily relies on empirical work and guidance from mill manufacturer's best practices. The need for mechanistic modeling such as PBM, DEM, and their combinations as opposed to statistically-based models is clear; there is great opportunity to optimize existing milling plants via optimization of e.g. ball size distribution and classifier parameters. This literature review revealed that there is not a single, integrated PBM for dry ball milling that can account for (i) unsteady-state operation, (ii) variable classification performance, (iii) finite back-mixing, (iv) internal separations, (v) optimal distribution of multi-sized balls in different compartments of the mill, (vi) optimal operation parameters of the air classifier, and (vii) a scale-up factor of the specific breakage rate. More specifically, the following features in the closed-circuit ball mill have not been addressed in any study, to the best knowledge of the author:

- A PBM approach in which an external air classifier is fully coupled with the performance of a ball mill. No variable classification model has been used along with the PBM for the mill considering dust loading and the amount of fine particles that are fed from the mill to the air classifier.
- Ball size distribution optimization
- Air classifier's operation optimization

To address all these gaps, a more advanced and integrated PBM framework is needed, and that is the primary concern of this dissertation. As a large-scale operation (ball mill and VRM) is in our interest, the challenge is also to formulate an approach that couples PBM and DEM to bring the physics of particle breakage into the models and make the approach more mechanistic.

1.5 Objective and Dissertation Outline

The main goal of this dissertation is to develop a credible simulation tool that can provide fundamental insights into and process understanding of ball milling and, ultimately, suggest manipulated process variables for process optimization. To achieve these goals, a true unsteady-state simulator (TUSSIM), which is based on cell-based PBM, was developed (**Chapter 2**). With TUSSIM, comprehensive parametric studies of ball milling of cement clinker were performed to investigate the impact of various operation parameters on the ball milling of cement clinker operating in open circuit (**Chapter 3**) and closed circuit (**Chapters 4 and 5**). Breakage kinetics parameters of pre-milled cement clinker were determined using data obtained from a lab-scale batch ball mill with traditional steel balls and alternative alumina balls (**Chapter 6**). In the same chapter, DEM was used to simulate ball motion and determine the impact energy spectra of ball–ball collisions to develop mechanistic understanding of collision-induced breakage. Finally, TUSSIM was used in an inverse framework to determine the breakage kinetics of full-scale VRM for cement milling (**Chapter 7**). This dissertation consists of eight chapters, including **Chapter 1: Introduction**.

In **Chapter 2**, the study formulates a cell-based PBM simulator (TUSSIM) that accounts for internal classification due to the discharge screen and the cushioning action of finer particles on coarser ones (nonlinear breakage kinetics) during continuous dry milling. The model is capable of simulating the spatio-temporal evolution of the particle size distribution (PSD) in mill content, total mass hold-up, and product PSD. Moreover, the cell-based PBM realistically accounts for the degree of non-ideal mixing and associated residence time distribution in the continuous mills.

In **Chapter 3**, the TUSSIM developed from **Chapter 2** is utilized to simulate full-scale, multi-compartment cement ball milling to gain fundamental insights into the impacts of ball size distribution (BSD), the number of milling compartments, and classifying liners on cement size distribution during open-circuit continuous ball milling.

Chapter 4 presents the incorporation of a variable Tromp curve model for the air classifier into the TUSSIM to simulate a full-scale closed-circuit cement ball mill and optimize the operation. The impacts of the air flow rate and rotor tip speed on the PSD and mass flow rate in the circuit, as well as the Tromp curve, were examined. Process optimization using a combined global optimizer–differential algebraic equation (DAE) solver was implemented. This approach enables the identification of optimal circuit operation by considering the quality attributes of the cement product and the production rate simultaneously.

Chapter 5 discusses the use of the coupled TUSSIM with the variable Tromp curve model described in Chapter 4 and examines the impact of ball mixture and BSD, sheds light on the selection of the number of compartments, and assesses the impact of ball classification due to the classifying liner. Further, process optimization for BSD was performed to identify the optimal BSD using a combined global optimizer–DAE solver.

Chapter 6 discusses the results of the breakage kinetics of pre-milled cement clinker in a lab-scale batch ball mill loaded with steel or alumina balls, as well as their mixtures. The specific breakage rate and breakage distribution parameters of the cement clinker were determined using a global optimizer-based back-calculation method. DEM simulations were performed to obtain microdynamic behavior of ball–ball collisions and explain the impacts of the ball size–type experimentally observed. Moreover, the findings

are expected to guide the feasibility of the replacement of traditional steel balls with alumina balls in continuous ball milling circuits, which could significantly reduce the energy consumption and cost of manufacturing of cement products.

In **Chapter 7**, the feasibility of modeling a full-scale VRM for cement milling via TUSSIM is examined. Two process configurations (open circuit with internal classification and closed circuit with external classification) were tested.

Chapter 8 provides the conclusions and recommendations for future work.

CHAPTER 2

A CELL-BASED PBM FOR CONTINUOUS OPEN-CIRCUIT DRY MILLING: IMPACT OF AXIAL MIXING, NONLINEAR BREAKAGE, AND SCREEN SIZE

This theoretical study examined the impact of the degree of mixing, nonlinear particle breakage, and screen opening size on the particle size distribution (PSD) and mass hold-up in continuous dry mills with internal classification. A cell-based population balance model (PBM) incorporating a non-ideal screen model was formulated, wherein the back-mixing ratio and number of cells modulated the extent of axial mixing. The set of differential–algebraic equations (DAEs) was solved for the spatio-temporal evolution of the PSD in the mill and the product stream. The simulation results suggest that a smaller screen opening delayed the attainment of the steady state, increased the hold-up, and yielded a finer product PSD. The cushioning action of fines resulted in a coarser product PSD; however, a screen with a smaller opening mitigated this effect. The cell-based PBM predicted various features of experimental milling observations while providing insights into the mixing–nonlinear breakage–classification interplay.

2.1 Introduction

Particles with a higher specific surface area usually exhibit more desirable functional responses, such as higher reactivity (Vikesland et al., 2007), faster dissolution (Kim et al., 2021), better content uniformity (Rohrs et al., 2006), and higher compressive strength (Tsivilis et al., 1990; Zhang and Napier-Munn, 1995) in final products. Milling, which has been commonly used in a multitude of industries (Prasher, 1987), reduces the size of the particles, thereby increasing their specific surface area, for downstream processing or end

use. Practically, milling processes operate in either batch or continuous mode (Prasher, 1987). While batch mode is suited to bench-scale, laboratory or small-scale operation, continuous mode is commonly used in pilot scale and large-scale operations (King, 2001).

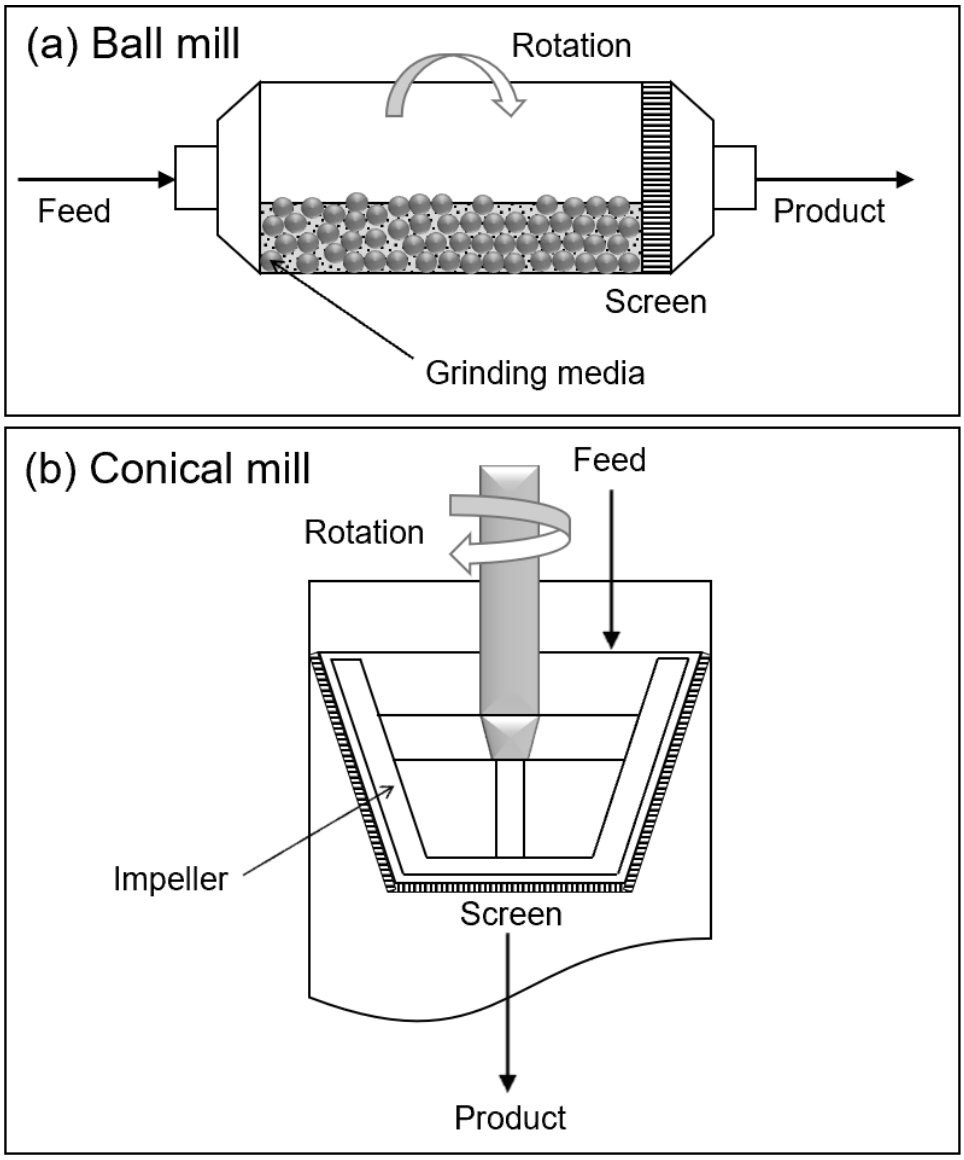

Figure 2.1 Sketches of the continuous dry milling process incorporating an internal discharge screen: (a) ball mill and (b) conical screen mill.

In the continuous mode, coarse feed particles are continuously fed into the inlet and through the mill body and then ground by grinding media or various rotating milling tools. The fine product particles passing through a discharge screen exit at the outlet in the open-circuit operation, where there is no external classifier. Depending on the specific design of the continuous mill, the discharge screen retains the milling media such as balls or rods as well as some oversized particles (**Figure 2.1a**) or restricts the passage of oversized particles completely in the absence of milling media (**Figure 2.1b**). The oversized particles retained in the milling chamber are subjected to further impact–deformation and breakage until they pass through the screen opening and get discharged as product.

Earlier studies (Reid, 1965; Austin, 1971/1972; Marchand et al., 1980; Mihalyko et al., 1998; King, 2001; Cho and Austin, 2002) have revealed that the degree of particle mixing affects the particle size distribution (PSD) of the product. Analogous to the analysis of degree of mixing in chemical reactors (Fogler, 2006), the degree of the particles' mixedness in continuous mills can be quantifiably assessed using a residence time distribution (RTD) function. The RTD can be experimentally obtained from the pulse injection of an inert chemical, i.e., a tracer (Austin et al., 1971; Shoji et al., 1973; Abouzeid et al., 1974; Gardner et al., 1977; Rogers and Gardner, 1979; Swaroop et al., 1981; Austin et al., 1983; Fuerstenau et al., 1986; Rogovin et al., 1988; King, 2001). A tracer pulse is injected at the mill inlet and the concentration of the tracer is measured at the mill outlet. Although the RTD data clearly indicate that finite axial back-mixing takes places in many continuous open-circuit mills (Gardner and Sukanjnajtee, 1973; Gardner et al., 1977; Abouzeid et al., 1980; de Oliveira and Tavares, 2018), many researchers assumed idealized mixing regimes, i.e., perfect mixing (Morrell and Man, 1997; Yildirim et al., 1999,

Weedon, 2001; Jankovic et al., 2004) or plug flow (Reid, 1965; Horst, 1967; Furuya et al., 1971; Luckie and Austin, 1972; King, 2001), for the sake of simplicity in their population balance models (PBMs). Other researchers used the convective dispersion model (Horst, 1967; Austin et al., 1971; Mika, 1976; Austin et al., 1983; Austin et al., 1984; Mihalyko et al., 1998) and the tanks (mixers)-in-series model (Gardner and Sukanjnajtee, 1973; Austin et al., 1975; Austin and Luckie, 1984; Benzer et al., 2001a; Benzer et al., 2001b; Genc et al., 2013; Wang et al., 2015; de Oliveira and Tavares, 2018) to describe the finite mixing in continuous mills and fit the RTD data. The convective dispersion model assumes that particles are well-mixed in the radial direction; the hold-up does not significantly change throughout the length L of the mill, and the axial dispersion coefficient D and average axial velocity u of the powder are constant. Readers are referred to Appendix A.1, where the size- and time-continuous convective dispersion PBM (Mihalyko et al., 1998) for continuous milling is reported. The significance of particle transport by convection relative to dispersion is indicated by the Péclet number N_{Pe}; i.e., $N_{Pe} = uL/D$, which is obtained through fitting of the convection–dispersion model to experimental RTD data. The domains of particle size, axial distance from the feed section, and time in Equation (A.1) were discretized, and the resulting system of equations were solved (Mihalyko et al., 1998). The simulations suggest that the product PSD becomes coarser as the extent of axial mixing increases, i.e., lower N_{Pe}, corresponding to higher D. Although that study (Mihalyko et al., 1998) presented the unsteady-state convective dispersion PBM, the unsteady-state solutions for a continuous open-circuit mill were not provided. Moreover, possible nonlinear breakage kinetics and internal classification effects were not considered either.

In the tanks-in-series PBM approach, the mill content is idealized as a series of well-mixed tanks without any back-mixing between adjacent tanks. The size-discretized form of the tanks-in-series PBM for steady-state operation is described as follows (Austin et al., 1975):

$$0 = -k_i M_{i,z} + \sum_{j=1}^{i-1} b_{i,j} k_j M_{j,z} + \frac{n}{\tau}\left(M_{i,z-1} - M_{i,z}\right) \tag{2.1}$$

with $M_i(0) = M_{i,0}$, where i and j are the size class indices. Size classes 1 and N contain the largest and smallest particles, respectively. z is the index for the tanks; tank 1 represents the first tank at the entrance and n refers to the last tank at the discharge. If only one tank is considered, Equation (2.1) turns into the continuous stirred tank mill (CSTM) model. The first-order specific breakage rate is k_i, while the breakage distribution parameter is denoted as $b_{i,j}$. The mass fraction in size class i is M_i, and τ denotes the space-time or mean residence time (ratio of the total mass hold-up to the mass flow rate). The tanks can have identical average residence time as implied in Equation (2.1) or variable residence time (hold-up) with some modification of Equation (2.1). Gardner and Sukanjnajtee (1973) performed an RTD study using a radioactive tracer in a continuous ball mill sized 12 in in diameter and 12 in in length. Their results showed that a 3-tanks-in-series model can describe the experimental RTD for two feed rates. A similar result was obtained by Oliveira and Tavares, but with different mean residence time in each tank (de Oliveira and Tavares, 2018). Austin et al. (1975) reported that a 10-tank model fit the experimentally measured RTD of industrial dry cement ball mills. Furthermore, based on a sampling survey for commercial mills, Benzer et al. (2001b) applied a 4-tanks-in-series model for a dry ball

mill.

The cell-based PBM approach, which was originally formulated by Whiten (1974), has been used to describe the extent of back-mixing and particle breakage in continuous *wet stirred media milling* (Lira and Kavetsky, 1990; Berthiaux et al., 1996; Kwade and Schwedes, 1997; Fadhel et al., 1999; Varinot et al., 1999; Frances, 2004; Kwade and Schwedes, 2007). In this approach, the mill is idealized to consist of well-mixed cells (**Figure 2.2**). Unlike the tanks-in-series model, an axial recirculation rate $\dot{R}$ of particles between adjacent cells is explicitly considered. The dimensionless form of $\dot{R}$, i.e., the axial back-mixing ratio R is the ratio of the recirculation rate between cells $\dot{R}$ to the mass flow rate through a cell $\dot{m}_{\text{in}}$. The tanks-in-series model is clearly a subset of the cell-based PBM and recovered when R is set to 0. Kwade and Schwedes (2007) found for a wet stirred media mill that the cell-based model accurately describes the mixedness degree of particles in a horizontal wet stirred media mill. In their study, the number of cells was set to be equal to the number of stirrer discs. Therefore, only one parameter—the back-mixing ratio R—was fitted to the measured RTD. Although they estimated R by fitting the cell-based model to the RTD, the evolution of the PSD using the cell-based approach was not reported. Furthermore, Fadhel et al. (1999) and Frances (2004) used the cell-based PBM approach with some modifications to fit experimental *steady-state PSDs in wet stirred media mills*.

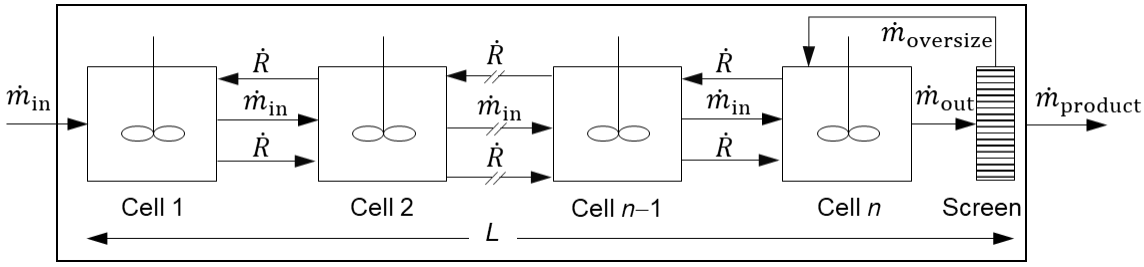

Figure 2.2 Schematic model of a continuous mill represented as a series of n well-mixed cells with a discharge screen at the end. Cells exchange particles at the rate $\dot{R}$. The mill has the effective length L.

Source: Adapted from Kwade and Schwedes (2007)

Besides the degree of mixedness, as one can intuitively expect, the breakage kinetics of particles tremendously affects the product PSD obtained from the continuous mills. Linear (first-order) breakage kinetics is the fundamental assumption in most of the milling studies (Reid, 1965; Mika, 1976; Austin et al., 1983; Mihalyko et al., 1998; Varinot et al., 1999; Weedon, 2001). However, this assumption has been shown to be invalid especially for prolonged fine milling of materials and/or dense-phase milling processes, wherein particles encounter enduring multi-particle mechanical interactions (Bilgili et al., 2006; Bilgili et al., 2017). In fact, since the mid-70s, many researchers (Shoji and Austin, 1974; Austin and Bagga, 1983; Lytle and Prisbrey, 1984; Fuerstenau and Abouzeid, 1991; Verma and Rajamani, 1995; Fuerstenau et al., 2004; Tavares and de Carvalho, 2009) have criticized the linear PBMs because they evidently deviated from the experimental observations. To address such deviations, for example, Austin and Bagga (1981) proposed a time-dependent PBM that was formulated for well-mixed batch milling. Although their proposed model can precisely explain the acceleration or deceleration of the breakage of a mono-dispersed feed, it cannot explain the nonlinear breakage of a binary feed (combination of coarse and fine particles). Bilgili et al. (2006) and Bilgili and Scarlett

(2005a) proposed a nonlinear PBM framework in which the specific breakage rate is the product of the first-order specific breakage rate k_i and the nonlinear functional $F_i[\ ]$, which phenomenologically describes the impact of multi-particle interactions among particles of different sizes. The impact of such multi-particle mechanical interactions on the breakage kinetics in batch dry milling was elucidated via combined PBM–DEM (discrete element method) simulations (Capece et al., 2015; Capece et al., 2018). The nonlinear PBM fitted the experimental PSD evolution of quartz in a laboratory tumbling ball mill (Austin et al., 1990) better than the linear PBM and the time-dependent PBM (Capece et al., 2011a; Bilgili et al., 2017). The PBM–DEM simulations (Capece et al., 2015) elucidated the cushioning action of the finer particles on the slower breakage of the coarser particles in a particle population during dry ball milling. That study (Capece et al., 2015) demonstrated that finer particles in a particle bed increase mechanical energy loss and distribute inter-particle forces more extensively thereby preventing or reducing the breakage of the coarser particles.

Surprisingly, there is limited investigation as to how and to what extent nonlinear particle breakage kinetics affect PSD evolution during continuous dry milling. PBMs with the convection dispersion model and the tanks-in-series model, as well as the abovementioned cell-based PBMs do not consider nonlinear breakage kinetics. Moreover, most of the aforementioned models assume steady state, and others do not consider the process dynamics. Hence, there is a need for a better understanding of the factors that affect the attainment of a steady state milling operation. Bilgili and Scarlett (2005b) extended their nonlinear PBM to open-circuit steady-state continuous milling processes assuming two ideal mixing regimes: well-mixed (perfect or infinite axial back-mixing) and plug flow

(zero axial mixing). Their simulation results for a well-mixed CSTM and a plug flow tube mill (PFTM) revealed that the PFTM produces finer particles than the CSTM. However, they did not consider *finite axial mixing*, the internal separation caused by a discharge screen, and unsteady-state operation. Based on our review of the continuous open-circuit dry milling literature, it is fair to assert that the impacts of finite axial back-mixing, nonlinear breakage kinetics, and internal classification on the spatio-temporal evolution of the PSD inside the mill and the product PSD have not been investigated holistically in a single study before.

The aim of this theoretical study is to gain insights into the impact of finite axial mixing, the nonlinear breakage kinetics, and the opening size of the discharge screen on the product PSD, total mass hold-up, and attainment of steady-state in open-circuit continuous mills via simulations. To achieve this objective, we have formulated a cell-based PBM that accounts for the internal classification due to the discharge screen and the cushioning action of finer particles on the coarser ones (nonlinear kinetics). As another novelty, the cell-based PBM consists of a system of differential–algebraic equations (DAEs), which were solved efficiently and accurately using a variable order–step-size ordinary differential equation (ODE) solver. Our model is capable of simulating the spatio-temporal evolution of the PSD in the mill content, total mass hold-up, and the product PSD. First, the consistency of the cell-based PBM was established theoretically by reproducing the steady-state PSDs in the limiting cases of perfect mixing and plug flow (no axial mixing). Then, simulations were performed to examine the impact of the final axial mixing, as characterized by the number of cells and the back-mixing ratio. Reasonably accurate parameter values were used in the simulations considering the fitting of the experimental

RTD data on various continuous mills. The impact of nonlinear breakage kinetics was also examined by considering the experimentally observed cushioning action of finer particles on the coarser ones during dry ball milling (Austin and Bagga, 1981; Austin et al., 1990; Bilgili et al., 2017). While a screen opening size larger than or equal to 1700 μm was considered to emulate negligible classification action of the screen, other values of the screen opening size (100, 300, and 500 μm) were simulated to discern the impact of the screen size along with that of the nonlinear breakage kinetics. The simulations with the proposed cell-based PBM are expected to provide significant insights into the roles of the mixing–nonlinear breakage–classification and allow us to develop better process understanding of continuous open-circuit mills.

2.2 Theoretical

2.2.1 A size-discrete cell-based PBM

In this study, a PBM was formulated based on the multi-cell mass balance approach (Whiten, 1974; Whiten and Kavetsky, 1984; Lira and Kavetsky, 1990; Kwade and Schwedes, 2007), which considers finite axial mixing/dispersion. Physically, the axial particle mixing/dispersion is caused by the random motion of particles in the longitudinal axis of a mill of effective length L or radial velocity variations. In addition to finite axial mixing and nonlinear breakage kinetics, the model also considers a discharge screen to examine the impact of the internal classification of the particles. A schematic model of a continuous mill with n well-mixed cells is depicted in **Figure 2.2**. The model does not consider particle segregation in the mill; all particles move with a constant bulk velocity u. Limiting cases of zero axial back-mixing (i.e., plug flow) and perfect mixing can be

analyzed by considering the limiting scenarios of a large number of cells and a single well-mixed cell (n = 1), respectively.

The general size-discretized, time-continuous PBM for the first cell (feed), intermediate cells, and the last cell (discharge) without any classification action of the discharge screen are mathematically expressed by Equation (2.2). Readers are referred to Appendix A.2 for details.

$$\frac{dm_{i,z}}{dt} = \begin{cases} -k_i F_{i,z}[\ ]m_{i,z} + \sum_{j=1}^{i-1} b_{i,j} k_j F_{j,z}[\ ]m_{j,z} \\ +\frac{n}{\tau}\left(Rm_{i,z+1} - m_{i,z} - Rm_{i,z}\right) + \dot{m}_{i,\text{in}} & \text{if } z = 1 \\ -k_i F_{i,z}[\ ]m_{i,z} + \sum_{j=1}^{i-1} b_{i,j} k_j F_{j,z}[\ ]m_{j,z} \\ +\frac{n}{\tau}\left(m_{i,z-1} + Rm_{i,z-1} + Rm_{i,z+1} - m_{i,z} - 2Rm_{i,z}\right) & \text{if } 1 < z < n \\ -k_i F_{i,z}[\ ]m_{i,z} + \sum_{j=1}^{i-1} b_{i,j} k_j F_{j,z}[\ ]m_{j,z} \\ +\frac{n}{\tau}\left(m_{i,z-1} + Rm_{i,z-1} - Rm_{i,z}\right) - \dot{m}_{i,\text{out}} & \text{if } z = n \end{cases} \tag{2.2}$$

with $m_{i,z}(0) = 0$. Here, t is milling time. $\dot{m}_{i,\text{in}}$ and $\dot{m}_{i,\text{out}}$ denote the inlet mass flow rate and outlet mass flow rate, respectively, of the particles in size class i. The size classes range from size class 1 (coarsest) to size class N (finest) with a geometric progression of sizes. The particle size in each size class is represented by the upper edge of the size class. The mass fraction in size class i is given by $M_{i,z} = m_{i,z} \Big/ \sum_{i=1}^{N} m_{i,z}$ with m_i denoting the mass of particles in size class i and cell z. On the right-hand side of Equation (2.2), the first term refers to the death rate caused by breakage within size class i. The second term describes

the birth rate in size class i due to the transport of broken particles from all size classes, with $j < i$. The last term accounts for the bulk transport of particles as well as the recirculation between the cells. The number of cells n and the axial back-mixing (recirculation) ratio $R = \dot{R}/\dot{m}_{\text{in}}$ modulate the degree of axial mixedness within the context of the cell-based PBM. They can be determined by an RTD study on the specific continuous mill similar to Austin et al. (1975), Fadhel et al. (1999) and Kwade and Schwedes (2007). Note that the consideration of a small number of cells, similar to that in tanks-in-series models, also introduces axial dispersion. In Equation (2.2), $F_i[\ ]$ is the population-dependent functional for nonlinear breakage kinetics (Bilgili and Scarlett, 2005a; Bilgili et al., 2006), which describes the acceleration–deceleration impact of mechanical multi-particle interactions between all generic size classes q with the particles in size class i; i.e., $F_i\left[\sum_{q=1}^{N} W_{i,q} M_q\right]$. $W_{i,q}$ expresses the influence of each i–q size class interaction on the specific breakage rate of the particles in size class i.

We consider the internal classification during the continuous open-circuit milling by a screen classification function. The product rate equals the rate of discharge through the discharge screen, as modulated by the screen's classification function P_{c}, i.e., $\dot{m}_{i,\text{product}} = \dot{m}_{i,\text{out}} P_{\text{c},i}$. The coarser particles that are prevented from leaving the mill by the discharge screen are recycled to the last cell (King, 2001). This relationship can be mathematically expressed as $\dot{m}_{i,\text{oversize}} = \dot{m}_{i,\text{out}}(1 - P_{\text{c},i})$. Unlike that of the first and intermediate cells, the space time in the last cell is expressed by

$$\tau_n = \frac{m_{\text{hold-up},n}}{\sum_{i=1}^{N} \dot{m}_{i,\text{in}} + \sum_{i=1}^{N} \dot{m}_{i,\text{oversize}}} \tag{2.3}$$

where $m_{\text{hold-up},n}$ is the total mass of material in cell n. The model equation of the last cell ($z = n$) considering the classification action from the discharge screen is expressed as follows:

$$\begin{aligned} \frac{dm_{i,n}}{dt} = &-k_i F_{i,n}\left[\ \right] m_{i,n} + \sum_{j=1}^{i-1} b_{i,j} k_j F_{j,n}\left[\ \right] m_{j,n} + \frac{n}{\tau}\left(m_{i,n-1} + R m_{i,n-1}\right) \\ &- \frac{1}{\tau_n}\left(R m_{i,n} + m_{i,n}\right) + \dot{m}_{i,\text{oversize}} \end{aligned} \tag{2.4}$$

with $m_{i,n}(0) = 0$. The oversized return rate is time-dependent and unknown during the transient period. Hence, the space time of the last cell is unknown and must be solved along with Equations (2.2) and (2.4). In general, Equations (2.2)–(2.4) constitute a set of DAEs. Interestingly, such DAEs have never been solved for continuous open-circuit milling directly, which is yet another novelty of the present work. For continuous open-circuit mills with discharge screens, an iterative solution method for the *steady-state solution* was commonly employed in the literature (King, 2001; de Oliveira and Tavares, 2018).

Experimental observations suggest that the prediction of PSD using a linear PBM is perfectly valid for a mono-dispersed feed, i.e., a feed with a narrow PSD, milled for a short milling time or a poly-dispersed (natural) feed is milled under operating conditions conducive to processing with limited enduring contacts among the particles (Gutsche and Fuerstenau, 1999; Bilgili and Scarlett, 2005a; Bilgili et al., 2006; Capece et al., 2011b). In fact, there are matrix-based analytical solutions to the PBM for various batch and

continuous milling processes (see e.g., Herbst and Fuerstenau, 1980; Diemer, 2021). Note that the analytical solutions are strictly valid when classification functions do not depend on the operating conditions (fixed and linear) and (ii) breakage kinetics is linear. As a general simulator, TUSSIM, was developed in this thesis study for use with all possible breakage kinetics and classification functions, the numerical solution of the cell-based PBM was implemented. In view of the above experimental observations, the following constraints on the nonlinear functional in Equations (2.2) and (2.4) can be imposed (Bilgili et al., 2006):

$$F_i[\ ] \to 1 \text{ as } \forall M_q (q \neq i) \to 0 \tag{2.5}$$

Moreover, the conservation of total mass dictates that the first-order specific breakage rate and the breakage distribution parameter in Equations (2.2) and (2.4) are restricted by the following constraints:

$$k_N = 0, \sum_{i=j+1}^{N} b_{i,j} = 1, b_{i,i} = 0 \tag{2.6}$$

2.2.2 Specific functional forms used in the simulations

Representative values of the breakage parameters for our simulations were based on dry ball milling experiments conducted by Austin et al. (1990). Quartz was milled in a laboratory ball mill measuring 194 mm in diameter and 175 mm in length filled with steel balls in batch mode. Their experimental PSD data after milling were successfully fitted to

the nonlinear PBM for batch mill with the assumption of perfect mixing by Bilgili et al. (2017). The nonlinear optimizer "fmincon" from the optimization toolbox in MATLAB was employed to minimize the sum of squared residuals (*SSR*) between the model predictions (i.e., the PBM solution) and the experimental data. Bilgili et al. (2017) reported the fitted PBM parameters (e.g., k_i and $F_i[\ ]$) for various models. In the present study, the PBM parameters in Equations (2.7) and (2.8) were obtained from the fitting results in Bilgili et al. (2017). A power-law function and a normalized function were selected (see Equation (2.7)) for k_i and the cumulative breakage distribution parameter $B_{i,j}$, respectively. Equation (2.8) expresses the form of $F_i[\ ]$ and $W_{i,q}$ that capture phenomenologically the slowing-down or cushioning action of the finer particles on the coarser particles.

$$k_i = A\left(\frac{x_i}{x_0}\right)^m,\ B_{i,i} = 1,\ B_{i,j} = \phi\left(\frac{x_{i-1}}{x_j}\right)^{\mu} + (1-\phi)\left(\frac{x_{i-1}}{x_j}\right)^{\nu}\ i > j \text{ with}$$
$$b_{i,j} = B_{i,j} - B_{i+1,j} \text{ and } b_{N,j} = B_{N,j} \tag{2.7}$$

$$F_{i,z}[\ ] = \frac{1}{1+\left[\lambda\sum_{q=i}^{N}\left(1/x_q - 1/x_i\right)^{\alpha} M_{q,z}\right]^2} \tag{2.8}$$

The breakage rate constant A, normalizing reference particle size x_0, and the breakage rate exponent m were obtained from Bilgili et al. (2017) as 1.2 min^{-1}, 1000 μm, and 0.812, respectively. The breakage distribution constant ϕ and the breakage distribution exponents μ and ν were 0.395, 0.979, and 3.768, respectively (Bilgili et al., 2017). On the basis of the chosen form of $F_i[\ ]$, the traditional linear PBM was recovered for $\lambda = 0$. The

slowing-down phenomenon (cushioning effect) can be predicted with $\lambda > 0$. A larger λ signifies a greater extent of the retardation effect of the finer particles on the breakage of the coarser ones. $F_i[\ ]$ varies in the range of 0–1. An α value of 0.32 and λ value of 3.604 $\mu m^{0.32}$ were taken from Bilgili et al. (2017).

An ideal screen with opening size d_s will let all particles with size $x_i \leq d_s$ pass. However, such a model is too simplistic. Hence, a non-ideal screen classification function was taken from Barrasso et al. (2013) to describe classification action of the discharge screen. The critical screen size parameter δ was taken as 0.4 based on fitting to experimental data (Barrasso et al., 2013). Note that the internal classification could originate from the physical presence of the screen; however, there are other physical mechanisms such as air-sweeping induced classification (Benzer, 2005) in air-swept mills, which is not explained by Equation (2.9). Of course, more complicated classification functions can be used in such cases (Benzer, 2005); but this is beyond the scope of this theoretical study as our objective is not to model a specific mill type/size.

$$P_{c,i} = \begin{cases} 0 & \text{if } x_i > d_s \\ 1 - \dfrac{x_i - (1-\delta) d_s}{\delta d_s} & \text{if } (1-\delta) d_s \leq x_i \leq d_s \\ 1 & \text{if } x_i < (1-\delta) d_s \end{cases} \tag{2.9}$$

2.2.3 Simulation study

Table 2.1 presents the overall design of the simulation study with 20 runs. Interestingly, the cell-based PBM has not been applied to dry continuous ball milling before. Hence, reasonable values of n and R were obtained by fitting the cell-based PBM to the

experimental RTD data from the literature and estimating R for various cell numbers (n). In Runs 14–20, $n = 5$ was set as a baseline to examine the impact of nonlinear breakage kinetics and screen opening size. The transient operation of continuous dry mills is often neglected in most studies (Austin et al., 1975; Benzer et al., 2001a; Benzer et al., 2001b; Genc et al., 2013). A study of the transient behavior in the continuous open-circuit mills could help predict the time-scale of the attainment of a steady-state and influence of possible process fluctuations such as the feed rate and/or PSD on the fluctuations of the product PSD. Moreover, transient models can be used for process control purposes. Hence, the temporal evolution of the PSD and hold-up was also assessed, and results are presented for selected runs.

To validate the consistency of the cell-based PBM approach, n was varied from 1 to 60 (Runs 1–5), and the solutions were compared with those obtained from PBMs with idealized (extreme) mixing regimes, which corresponded to the CSTM (perfect mixing) and the PFTM (zero axial mixing). In all simulations, we set a τ value of 10 min, which was experimentally obtained in open-circuit continuous ball mills (Mori et al., 1964; Fuerstenau et al., 1986), and the feed mass flow rate of 10 g/min. In Runs 1–5, λ value was set as 0 (linear breakage kinetics). The other parameters were obtained from Bilgili et al. (2017). The solutions of the CSTM model (refer to Equation (2.1) with one tank only) and the PFTM model (Equation (A.4)) were obtained by the steady-state PBM solvers, as described by Bilgili and Scarlett (2005b).

Table 2.1 Cell-based Simulation Parameters Employed in Determining the PSD and the Total Mass Hold-up for the Open-circuit Continuous Mill

Run no.	No. of cells, n	Back-mixing ratio, R	Interactions parameter, λ ($\mu m^{0.32}$)	Screen size, d_s (μm)[a]
1	1	0	0	≥ 1700
2	3	0	0	≥ 1700
3	5	0	0	≥ 1700
4	15	0	0	≥ 1700
5	60	0	0	≥ 1700
6	5	0.1	0	≥ 1700
7	5	0.5	0	≥ 1700
8	5	1	0	≥ 1700
9	5	2.5	0	≥ 1700
10	15	0.1	0	≥ 1700
11	15	0.5	0	≥ 1700
12	15	1	0	≥ 1700
13	15	2.5	0	≥ 1700
14	5	0	3.604	≥ 1700
15	5	0	0	100
16	5	0	0	300
17	5	0	0	500
18	5	0	3.604	100
19	5	0	3.604	300
20	5	0	3.604	500

[a] The screen opening size values of 1700 μm and above lead to identical simulation results as there is no classification for the assumed Gaussian feed PSD with a mean size of 600 μm and a standard deviation (*SD*) of 100 μm.

After the consistency of the cell-based approach was established in view of the numerical solutions for the idealized mixing regimes, the impact of the extent of finite axial mixing, which was characterized by n and R, was examined without considering the nonlinear breakage kinetics and the classification action from the discharge screen ($d_s \geq$ 1700 μm) in Runs 2–13. Based on the selected feed PSD and the screen function in Equation (2.9), $d_s \geq 1700$ μm will not have any classification effect. Furthermore, the cushioning action of the finer particles on the coarser particles on the steady-state product PSD was studied via Runs 3 and 14 (λ = 0 and 3.604 $\mu m^{0.32}$). The milling operation was

assumed to attain a steady-state product PSD when the total absolute deviation, over all 320 size classes, between two subsequent cumulative product PSDs was less than or equal to 10^{-1}. Although the evolution of the PSD was recorded at each minute over 120 min, the simulation results were sampled at various times to demonstrate the evolution of the PSD and the attainment of the steady-state product PSD. With the incorporation of the classification action from the discharge screen, the simulation with the finest screen size (100 μm) was chosen to examine the impact of the screen opening size on the spatio-temporal evolution of the PSD in the mill content and temporal evolution of the product PSD (Run 15). The role and impact of the screen sizes (d_s = 100, 300, and 500 μm) were examined in Runs 15–17. Finally, the impact of the various screen opening sizes (d_s = 100, 300, and 500 μm) with nonlinear breakage kinetics ($\lambda = 3.604\ \mu m^{0.32}$) was studied in Runs 18–20. The temporal evolution of the hold-up from the starting time of operation (t = 0 min) to the steady-state hold-up was also examined. The milling operation was deemed to attain a steady-state hold-up when the percentage deviation of the total mass hold-up between consecutive time steps was less than 0.05%.

In all numerical simulations, the number of size classes N and the geometric progression ratio were set as 320 and $2^{1/16}$, respectively, which yields grid-independent simulation results. The upper edge of the topmost size class was 1000 μm. Both the initial and feed PSDs were taken as Gaussian with a mean size of 600 μm and a standard deviation (*SD*) of 100 μm. The Gaussian PSD was generated using the function "normpdf" in MATLAB version 9.7. The set of nonlinear DAEs in Equations (2.2)–(2.4) with the constraints in Equations (2.5) and (2.6) and the expressions in Equations (2.7)–(2.9) was solved using the function "ode15s" in MATLAB, which is a highly accurate, variable

order–step-size ODE solver that can also handle DAEs (Shampine et al., 2003). The relative error tolerance and the absolute error tolerance were set as 10^{-4} and 10^{-6}, respectively.

2.3 Results and Discussion

2.3.1 Establishing the theoretical consistency of the cell-based PBM

The consistency of the transient cell-based PBM was established by predicting the product PSD at prolonged milling times (steady-state) for two idealized mixing regimes in the continuous mill, namely, perfect mixing (CSTM: $N_{Pe} \rightarrow 0$ as $D \rightarrow \infty$) and plug flow (PFTM: zero axial mixing, $N_{Pe} \rightarrow \infty$ as $D \rightarrow 0$). To this end, the steady-state product PSD (cumulative mass fraction undersize) was determined by solving the cell-based PBM with $n = 1$ (to compare with CSTM solution) and $n = 60$ (to compare with PFTM) for sufficiently long times. These solutions were compared with the CSTM and the PFTM model solutions obtained via the steady-state PBM solvers presented in Bilgili and Scarlett (2005b). In these simulations, R and λ were set as 0, and the classification action of the screen was not considered. The simulations were also performed with various n values to assess the impact of the extent of axial mixing on the product fineness and to demonstrate convergence to the PFTM model's solution with an increase in n (Runs 1–5 in **Table 2.1**).

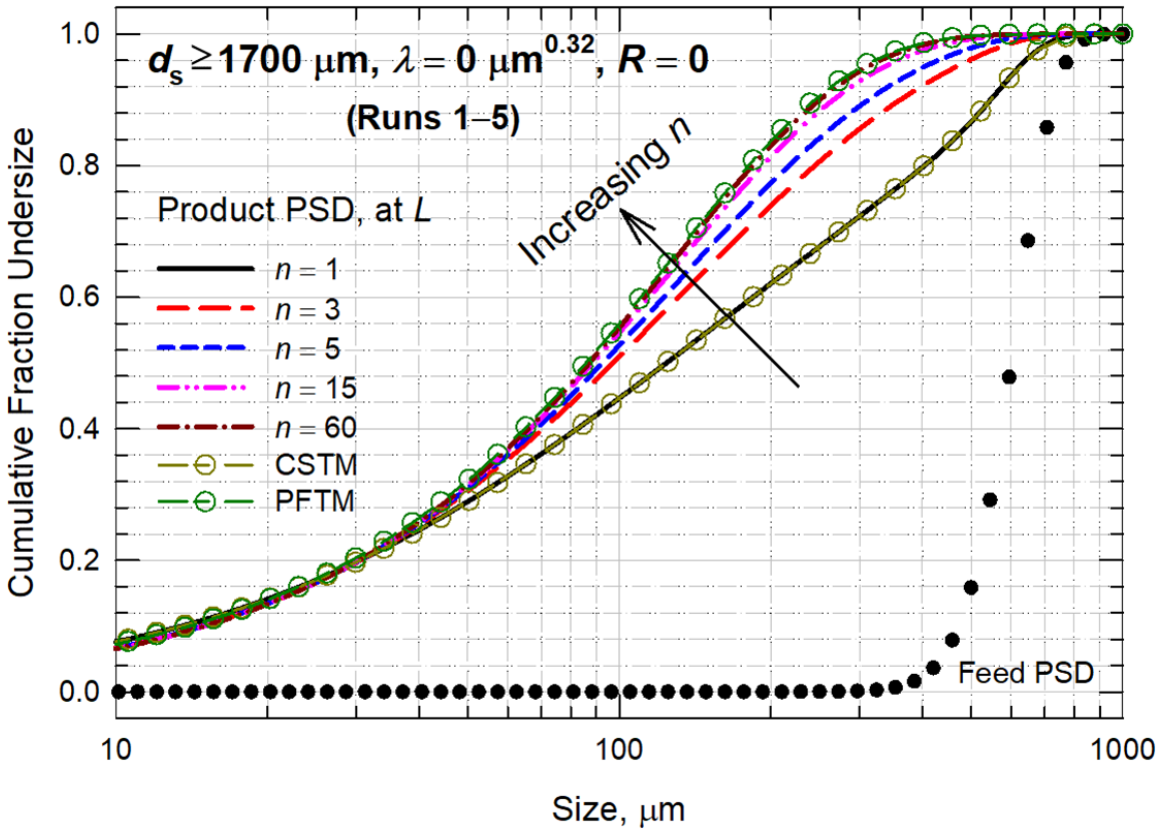

Figure 2.3 Impact of axial mixing, modulated by n (R = 0), on the steady-state cumulative PSD of the product for a continuous milling process (Runs 1–5). There is no classification action of the screen ($d_s \geq 1700$ μm). The cushioning action of the fines was not considered ($\lambda = 0$ μm$^{0.32}$).

A comparison of the current cell-based PBM prediction and the PBM with the two idealized mixing results for a CSTM and a PFTM is illustrated in **Figure 2.3** under identical conditions, namely the same feed PSD (Gaussian distribution, with a mean size of 600 μm and an *SD* of 100 μm) and τ = 10 min. **Figure 2.3** illustrates that, as n increases from 1 to 60, which corresponds to a lower extent of axial back-mixing, the product PSD becomes finer. While the lower tail of the product PSD (<30 μm) is not considerably affected, the effect of n is significant in the particle size domain from 30 to 600 μm. The cell-based PBM with n = 1 reproduces the CSTM model solution without any deviation, justifying

the high temporal numerical accuracy of the solver (ode15s). Although the plug flow (zero axial mixing) solution for the PFTM theoretically entails $n \rightarrow \infty$ in the cell-based PBM, practically, even n = 60 of the cell-based PBM converges to the PFTM solution. These theoretical results establish that the cell-based PBM is a consistent method that reproduces or converges to the steady-state PSDs under idealized mixing regimes. The finite mixing impact on the product PSD is most notable for $n < 15$. As will be shown in Subsection 2.3.2, the cell-based PBM with $n > 1$, but without the breakage terms, accurately captures the RTD data in various continuous tumbling ball mills and stirred media mills. Our simulations and the RTD data in the literature suggest that the finite axial mixing effects must be considered in the PBMs for accurate prediction of product PSD and its evolution. Therefore, the cell-based PBM that factor in the finite mixing effects, as described by the RTD data for a specific continuous mill, will predict any experimentally observed PSD more accurately than the widely used CSTM and PFTM models.

The product PSD obtained from the cell-based PBM with n = 60 deviates by a small percentage from that of the PFTM model solution. Obviously, the use of higher n could allow us to perfectly match the PFTM model solution; however, we have not attempted to do this so for several reasons: (i) the convergence of the cell-based PBM with the increase of n to the PFTM solution is apparent from **Figure 2.3**; (ii) the RTD studies on continuous ball mills suggest that there is always finite axial mixing (Gardner and Sukanjnajtee, 1973; Austin et al., 1975) that would necessitate the use of 3–10 cells (with R = 0); thus, a plug flow solution ($n \rightarrow \infty$) is unrealistic; (iii) $n > 15$ increases the computational effort/time significantly even for simulations (forward problem). If the breakage parameters were to be estimated from the continuous milling data via optimization-based back-calculation

methods (Bilgili et al., 2017) for a specific continuous mill, then the cell-based PBM with $n > 15$ as well as the convection–dispersion model would be computationally expensive. Nonetheless, practically, neither fitting of the RTD nor back-calculation of the breakage parameters would warrant the use of $n > 15$, as will be seen from fits to real experimental RTD data in the next section. This is also why we considered $n = 5$ in most of the simulations.

2.3.2 Impact of *n* and *R* on the spatio-temporal variation of PSD

First, $n = 5$ (Run 3) and $n = 60$ (Run 5), with $R = 0$, were selected to examine the impact of the axial dispersion, as modulated by n, on the PSD of the mill content at $L/5$, $3L/5$, and L in the mill. The classification action of the discharge screen in these simulations was not considered ($d_s \geq 1700$ μm) as all particles of the assumed Gaussian feed PSD pass through this screen size. Therefore, the PSD at the axial location L in the mill is the same as the product PSD at the mill outlet. Cells 1 and 12, Cells 3 and 36, and Cells 5 and 60 correspond to the identical axial locations of $L/5$, $3L/5$, and L in the mill, respectively. The other parameters were kept the same as in the previous simulations ($\lambda = 0$ and $\tau = 10$ min). **Figure 2.4** depicts a comparison of the steady-state PSD at the axial locations of $L/5$, $3L/5$, and L for $n = 5$ and $n = 60$. For a given n, the PSD shifts monotonically toward finer sizes from the inlet to the outlet. The PSD for $n = 60$ is finer than that for $n = 5$ at any axial location in the mill. The higher extent of axial mixing ($n = 5$ vs. 60) leads to a coarser PSD, which is consistent with what Figure 3 depicts.

Figure 2.5 illustrates the temporal evolution of the PSD in Cells 1, 3, and 5 (at the axial locations of $L/5$, $3L/5$, and L) of a continuous mill with $n = 5$ cells and the attainment of the steady-state product PSD. As the milling continues, the PSD shifts to finer particles,

as expected intuitively, and a steady-state PSD emerges within 26 min in all cells. However, the attainment of steady-state PSD takes longer for the cell at the discharge (n = 5, also product PSD) than that at the inlet (n = 1). Both the transient and steady-state PSDs suggest that the extent of size reduction increases monotonically as the particles move along the mill axis from the feeding section to the outlet (Cell 5). This finding agrees with the survey results of PSD at different locations of continuous dry mills (Benzer et al., 2001b; Genc, 2016).

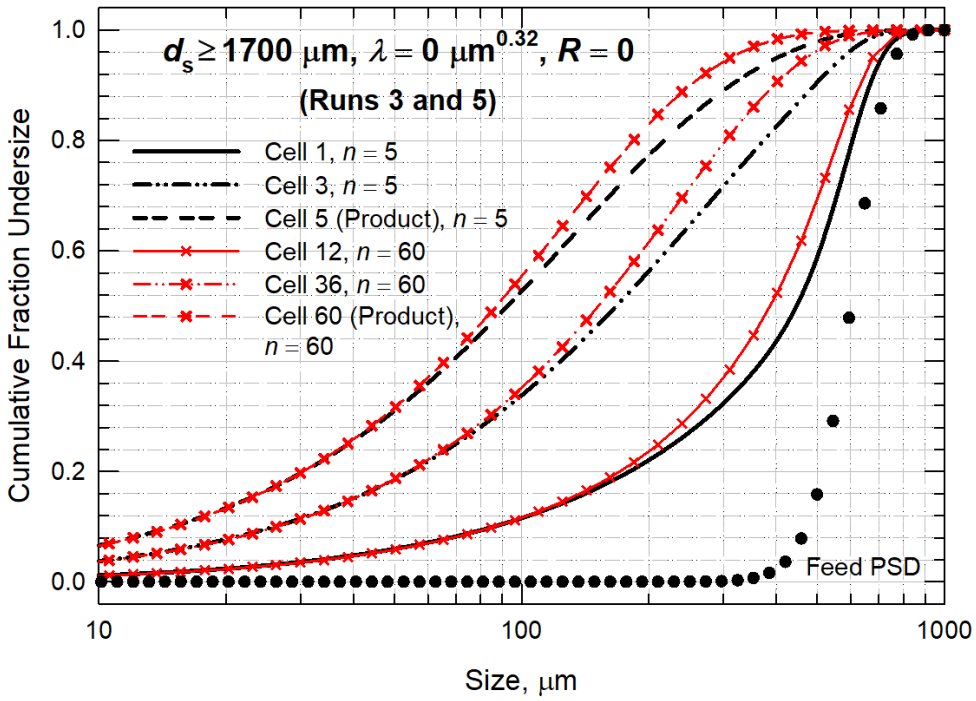

Figure 2.4 Steady-state spatial variation of the cumulative PSD along the axial direction of a continuous mill for n = 5 and n = 60 with R = 0 (Runs 3 and 5). There is no classification action of the screen ($d_s \geq 1700$ μm). The cushioning action of the fines was not considered ($\lambda = 0$ μm$^{0.32}$). Cells 1 and 12, Cells 3 and 36, and Cells 5 and 60, respectively, correspond to the axial location L/5, 3L/5, and L.

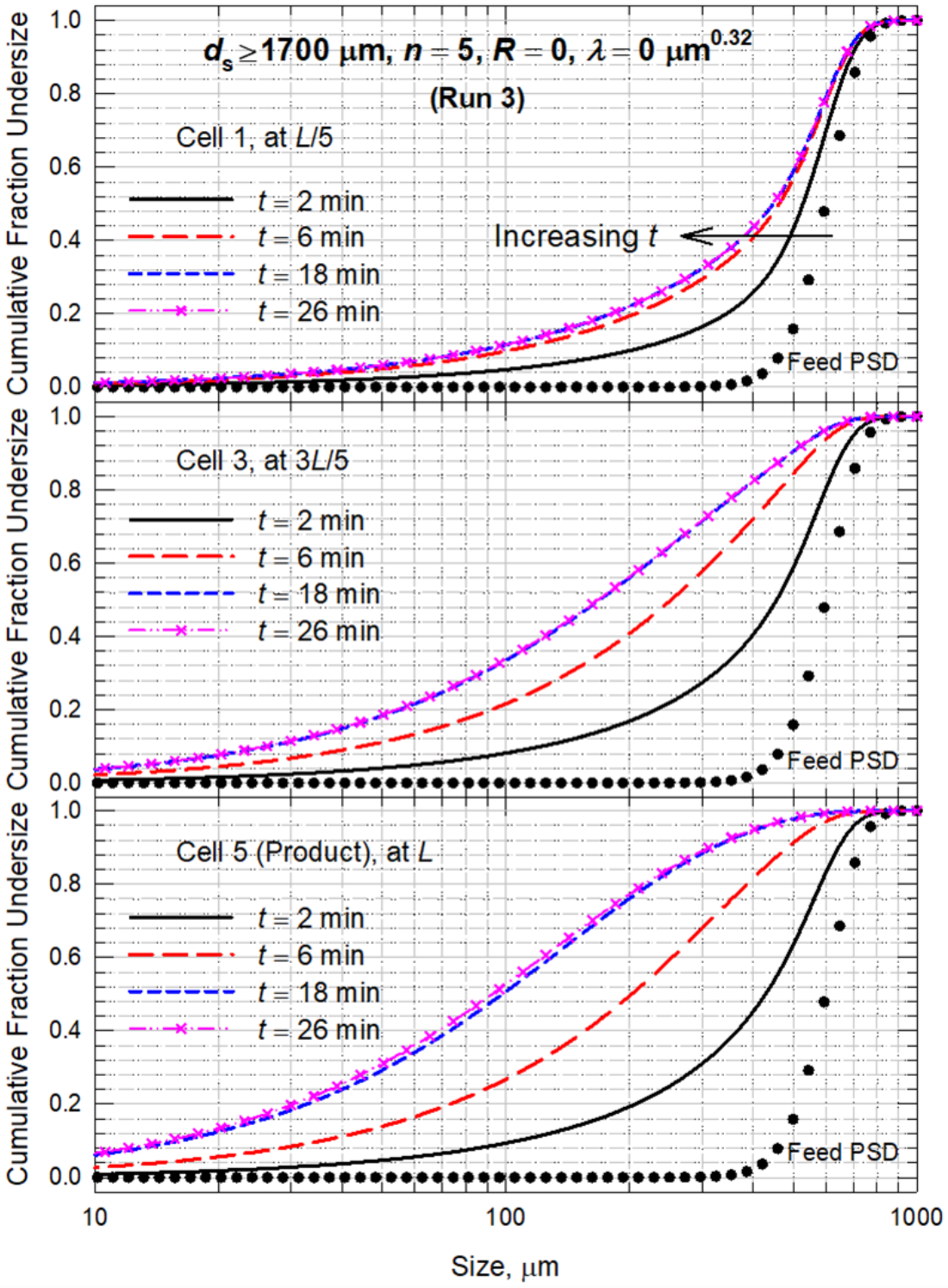

Figure 2.5 Spatio-temporal variation of the cumulative PSD along the axial direction of a continuous mill (Run 3). There is no classification action of the screen ($d_s \geq 1700$ µm). The cushioning action of the fines was not considered ($\lambda = 0$ µm$^{0.32}$). Other parameters used in simulations are $n = 5$ and $R = 0$. Cell 1, Cell 3 and Cell 5, respectively, correspond to the axial location $L/5$, $3L/5$, and L of the mill.

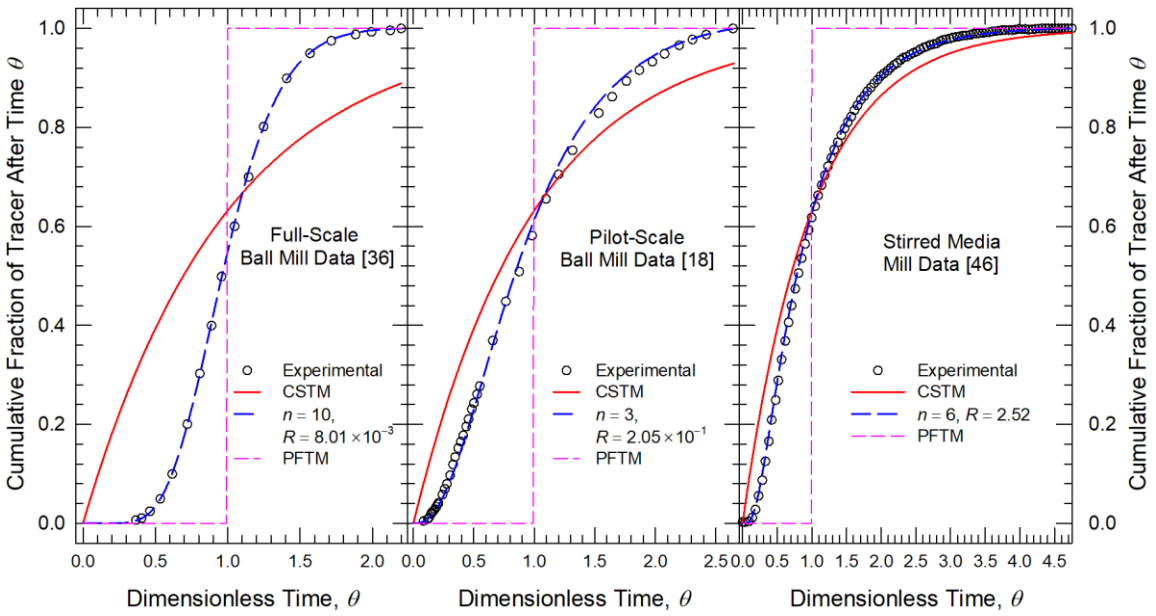

Figure 2.6 Deviation of the prediction by the CSTM model and the PFTM model as well as the fit by the cell-based PBM (without the breakage terms) from the experimentally measured RTD data on two tumbling ball mills and a stirred media mill.

Experimentally measured RTD data on two tumbling ball mills (Austin et al., 1975; Gardner et al., 1977) and a stirred media mill (Kwade and Schwedes, 2007) were fitted by the cell-based PBM (without the breakage terms) with various n and R values that minimized the sum-of-squared residuals (see **Figure 2.6** and **Table 2.2**). The RTD was also predicted using the CSTM model and the PFTM model for the two idealized mixing regimes, i.e., the perfect mixing and the zero axial mixing, respectively (refer to Fogler (2006)). **Figure 2.6** depicts that the cell-based PBM fits the experimental RTD in the mills very well, and indeed the RTD data for the mills notably deviate from those predicted with idealized mixing regimes. A novel insight from these fitting results is that the stirred mill has at least an order of magnitude higher R than the two tumbling ball mills, which can be attributed to the presence of high-speed mixing elements (stirrer discs) in the stirred media mills, which favors recirculation among the cells. The continuous tumbling ball mills do

not have moving, internal mixing elements; so, recirculation rate between adjacent cells is expected to be rather low as compared with the bulk axial transport rate of the material, thus justifying the lower value of the fitted *R*.

Table 2.2 Deviation of the Prediction of the CSTM model and the PFTM Model as well as the Fit by the Cell-based PBM (without the Breakage Terms) from the Experimentally Measured RTD Data on Two Tumbling Ball Mills and a Stirred Media Mill

Source of experimental data	Model	Back-mixing ratio, *R*	Sum of squared residuals, *SSR*
Austin et al. (1975)	CSTM	–	8.68
	10-cell PBM[a]	8.01×10^{-3}	2.92×10^{-3}
	PFTM	–	7.53
Gardner et al. (1977)	CSTM	–	2.03
	3-cell PBM[a]	2.05×10^{-1}	4.89×10^{-2}
	PFTM	–	15.0
Kwade and Schwedes (2007)	CSTM	–	1.34
	6-cell PBM[b]	2.52[a]	1.52×10^{-2}
	PFTM	–	17.1

[a] Value for the lowest *SSR* indicated.
[b] Taken from Kwade and Schwedes (2007) directly as *n* corresponds to the number of impeller elements.

We investigated the impact of the back-mixing (recirculation) ratio *R* from 0 to 2.5 on the product PSD for two different number of cells: $n = 5$ and $n = 15$ (Runs 3, 4, and 6–13) in view of the above RTD fits and associated *R* values. **Figure 2.7** presents the steady-state product PSDs corresponding to several *R* values. For both $n = 5$ and $n = 15$, a higher *R* results in a coarser product PSD. The PSD shifts away from that of the PFTM and gets closer to that of the CSTM at higher *R*. As before, for a given *R*, the product PSD is finer for $n = 15$ than that for $n = 5$. Hence, in the cell-based PBM, the extent of axial back-mixing and the product PSD are modulated by *both n* and *R*. In practice, the range of likely *n* values is determined by prior knowledge on similar mills and/or operational characteristics of a

particular mill (e.g., number/type of stirrer elements on the shaft of a stirred mill) or n is fitted with R to the RTD data of the mill in a sequential manner.

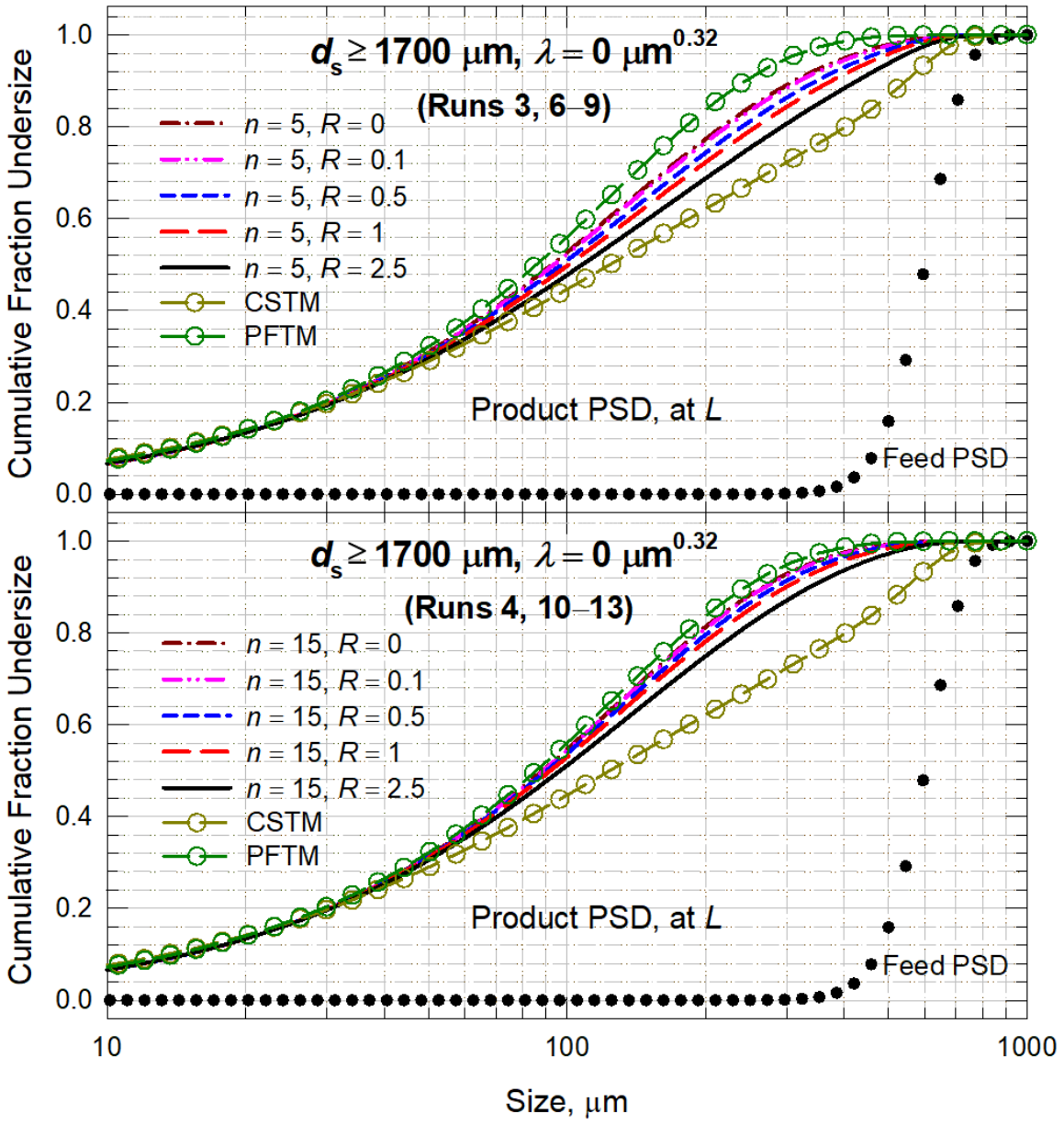

Figure 2.7 Impact of axial mixing, as modulated by the back-mixing ratio R, on the steady-state cumulative PSD of the product for n = 5 and n = 15 (Runs 3, 4, and 6–13). There is no classification action of the screen ($d_s \geq 1700$ µm). The cushioning action of the fines was not considered ($\lambda = 0$ µm$^{0.32}$).

Since n is an integer while R is a real number, the use of R could afford better fitting capability to the RTD data by the cell-based model without the breakage terms, as compared with the tanks-in-series model with n being the sole parameter. Even more interestingly, Kwade and Schwedes (2007) reported that a 6-cell PBM with R = 2.52 fitted their experimental RTD slightly better than the convective dispersion model with the fitted N_{Pe} = 2.33 (Kwade and Schwedes, 2007). But, more importantly, the numerical solution of the convection–dispersion model (see Appendix A.1), upon spatio-temporal discretization (Mihalyko et al., 1998), typically entails a high number of node points and very small time step for accuracy and grid-independence, which renders it much more computationally demanding than the cell-based PBM with n = 3–15. This issue will be exacerbated if the inverse problem of parameter estimation is considered. Hence, the cell-based RTD, with n and R as its two parameters, can capture a wide range of non-ideal mixing regimes between the two idealized mixing regimes and allow for better or similar prediction of the RTD and the product PSD in continuous open-circuit mills, yet most likely at a smaller computational cost than the convection–dispersion model.

2.3.3 Impact of cushioning effect on PSD without the classification action of the discharge screen

As thoroughly discussed for batch milling (Bilgili and Scarlett, 2005a; Bilgili et al., 2006), the specific breakage rate is a function of the evolving PSD through mechanical multi-particle interactions when fine milling of materials in a dense-phase is carried out such as in ball mills. With the form chosen of the nonlinear functional in Equation (2.8), the traditional linear breakage kinetics is recovered when $\lambda = 0$. The impact of the cushioning action of fines on the particle breakage dynamics (λ = 3.604 $\mu m^{0.32}$) and the PSD was examined in comparison with the traditional linear breakage kinetics, which disregards the

experimentally observed cushioning effect of the finer particles on the coarse ones. The 5-cell PBM was chosen to simulate the spatial variation of the PSD of the mill content and the product at the steady state.

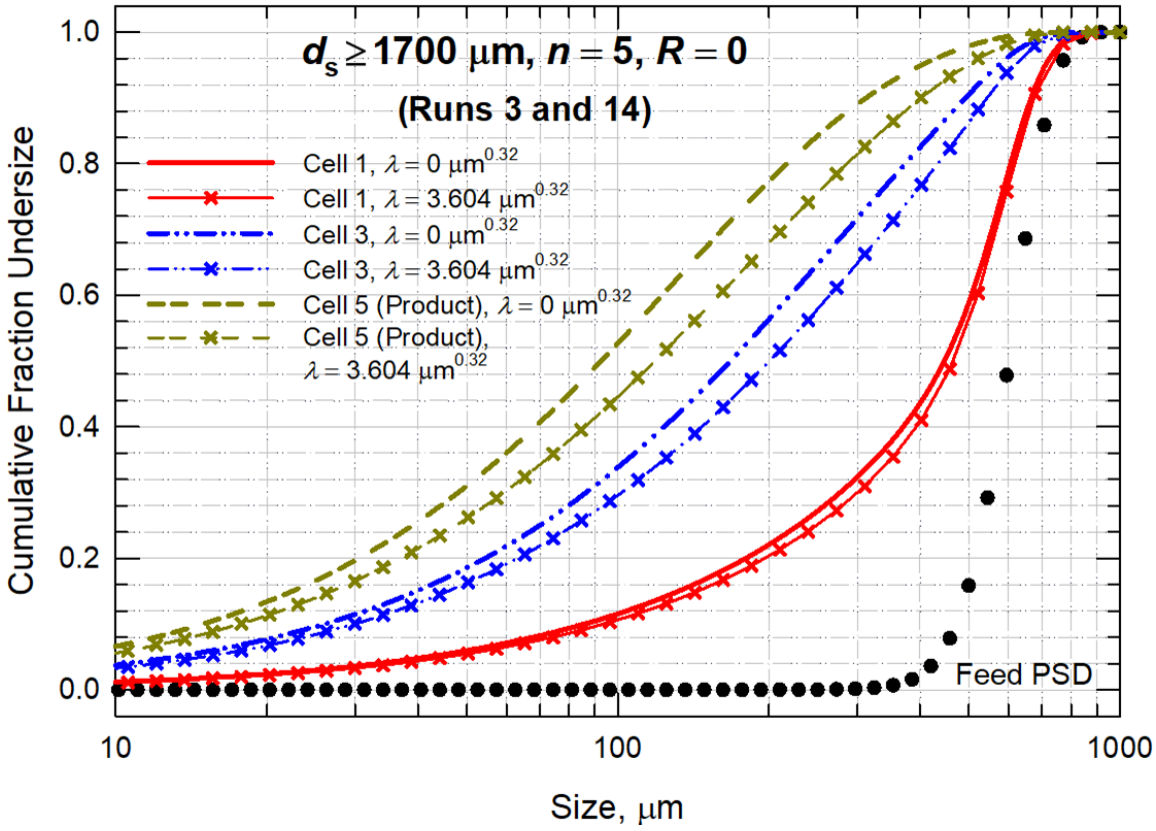

Figure 2.8 The impact of the cushioning action of the fines, as modulated by the multi-particle interaction parameter λ, on the spatial variation of the cumulative PSD along the axial direction of a continuous mill at the steady-state (Runs 3 and 14). There is no classification action of the screen ($d_s \geq 1700$ μm). Other parameter used in simulations are $n = 5$ and $R = 0$. Cell 1, Cell 3 and Cell 5, respectively, correspond to the axial location $L/5$, $3L/5$, and L of the mill.

As can be seen in **Figure 2.8**, for both the traditional linear breakage kinetics (Run 3) and nonlinear breakage kinetics (Run 14), the particle sizes in the mill monotonically decrease and shift to finer sizes from the inlet to the outlet. With the cushioning action of the fines on the breakage of the coarser particles considered in the context of the nonlinear

PBM (λ = 3.604 μm$^{0.32}$), the PSD is coarser at each location in the mill. This nonlinear impact becomes more pronounced as the PSD gets finer along the axial direction and generation of finer particles. This cushioning effect of the finer particles is one reason for the inefficiency in dry fine ball milling processes (Austin and Bagga, 1981; Austin et al., 1990; Gutsche and Fuerstenau, 1999).

2.3.4 Impact of screen opening size on classification and milling

In the previous simulations, we assumed a relatively large screen opening size ($d_s \geq 1700$ μm); this opening size had no classification action at the discharge because all particles were much smaller than $(1–\delta)d_s$ = 1020 μm, in accordance with Equation (2.9). In this section, we consider discharge screens with smaller opening sizes that could significantly impact the classification and milling. To better illustrate the classification effect of the screen, we reported the PSDs in differential form (**Figures 2.9–2.12**) in this section. The impact of d_s was first examined with the assumption of linear breakage kinetics ($\lambda = 0$). In Run 15, the classifying action of a continuous mill incorporating a discharge screen with d_s = 100 μm was simulated using a non-ideal screen function along with the cell-based PBM with n = 5. The spatio-temporal evolution of the PSD at various axial mill locations (L/5, 3L/5, and L) and the mill discharge at the outlet (product PSD) is depicted in **Figure 2.9**. Along the axial direction of the mill from the feed (with the modal/mean size of 600 μm) to Cell 5 and the discharged product, the modal size gets smaller at any given time. The PSD shifts to finer particle sizes as the milling continues; a finer PSD is produced until the steady state is attained.

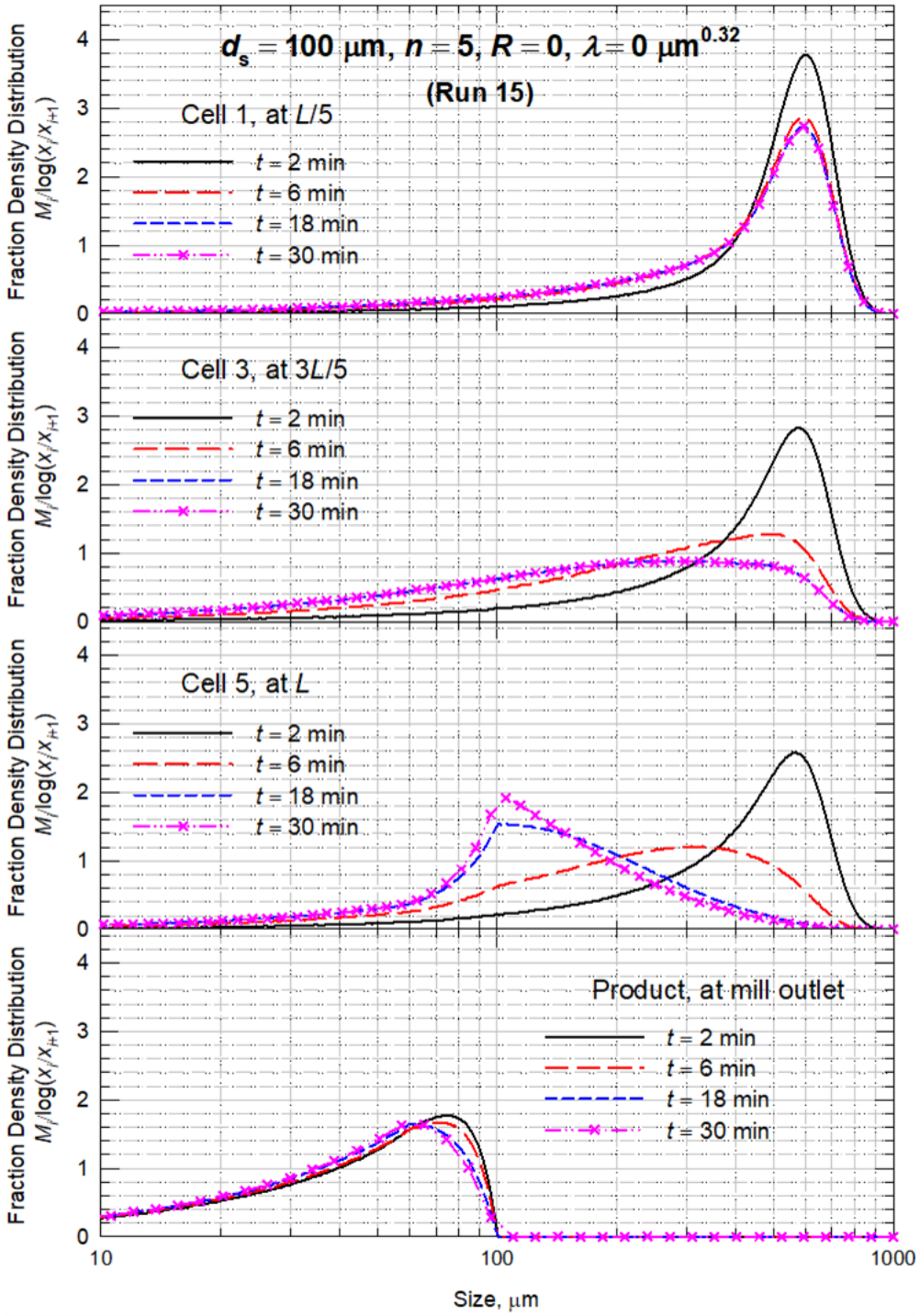

Figure 2.9 Spatio-temporal variation of the differential PSD along the axial direction of a continuous mill with a screen opening size d_s = 100 μm (Run 15). The cushioning action of the fines was not considered (λ = 0 μm$^{0.32}$). Other parameters used in simulations are n = 5 and R = 0. Cell 1, Cell 3 and Cell 5, respectively, correspond to the axial location $L/5$, $3L/5$, and L of the mill.

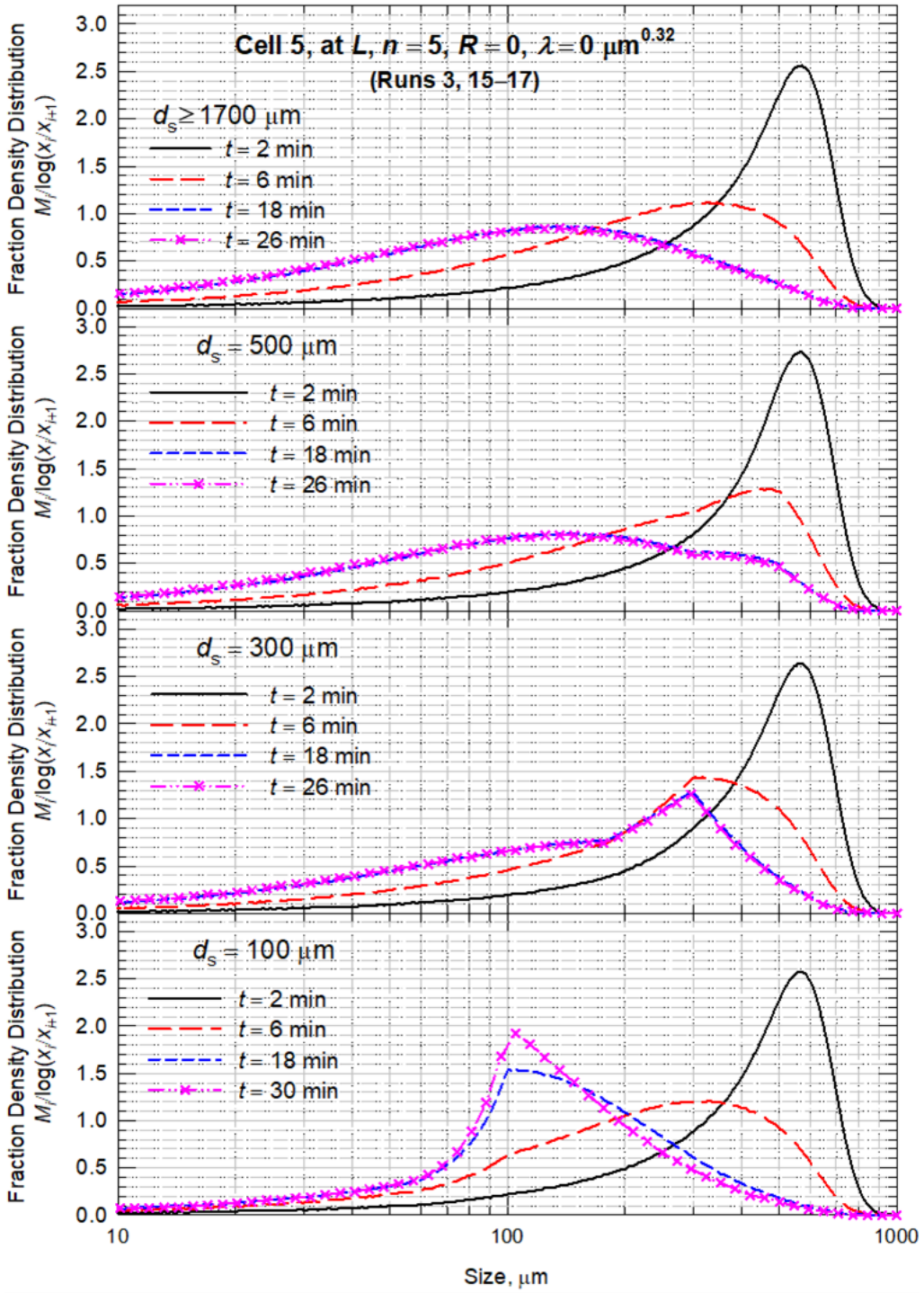

Figure 2.10 Impact of the opening size of the discharge screen d_s on the attainment of a steady-state differential PSD in the last cell of the continuous mill (Runs 3 and 15–17). The cushioning action of the fines was not considered (λ = 0 $\mu m^{0.32}$). Other parameters used in simulations are n = 5 and R = 0.

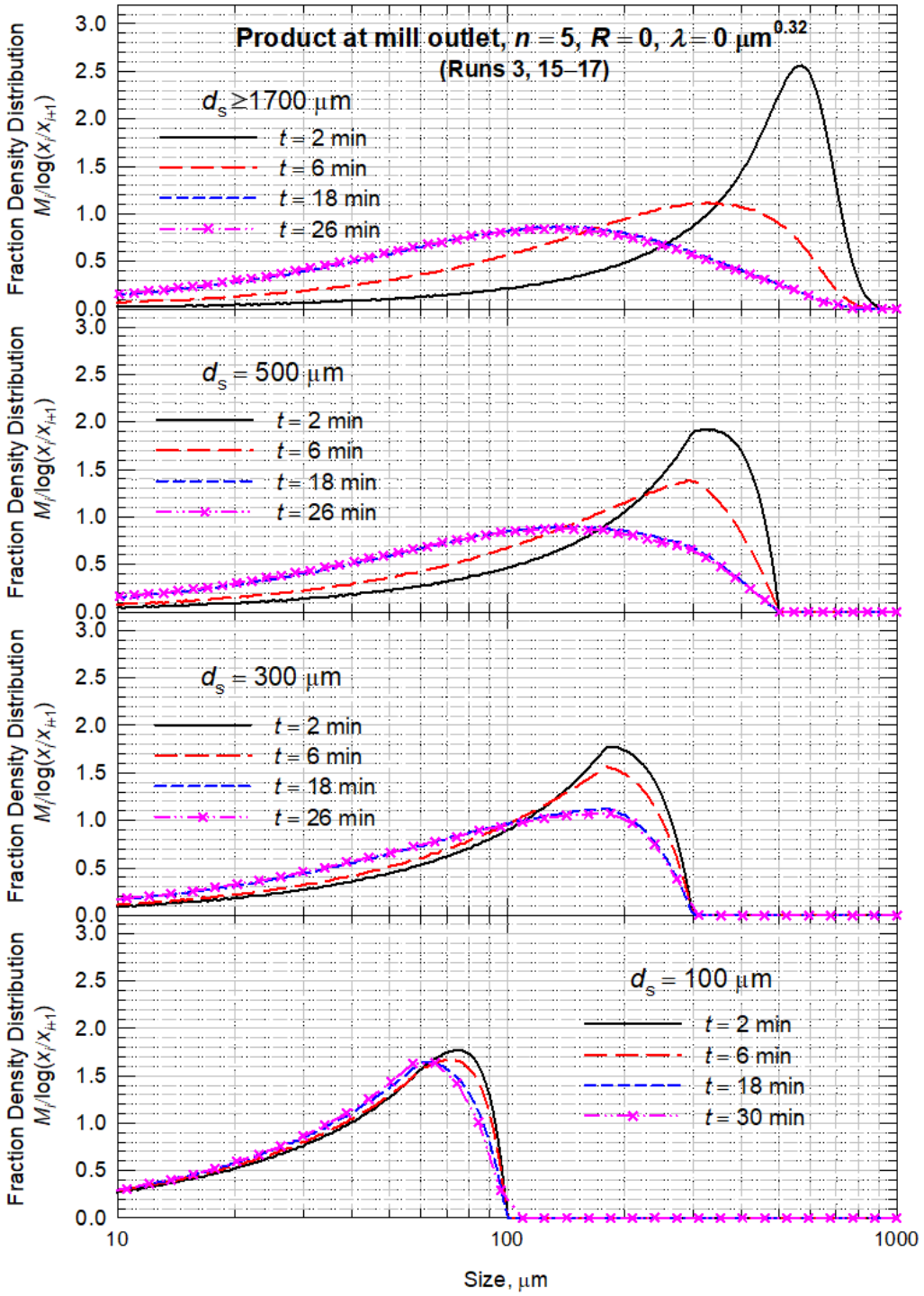

Figure 2.11. Impact of the opening size of the discharge screen d_s on the temporal evolution of the differential PSD of the product (Runs 3 and 15–17). The cushioning action of the fines was not considered (λ = 0 μm$^{0.32}$). Other parameters used in simulations are n = 5 and R = 0.

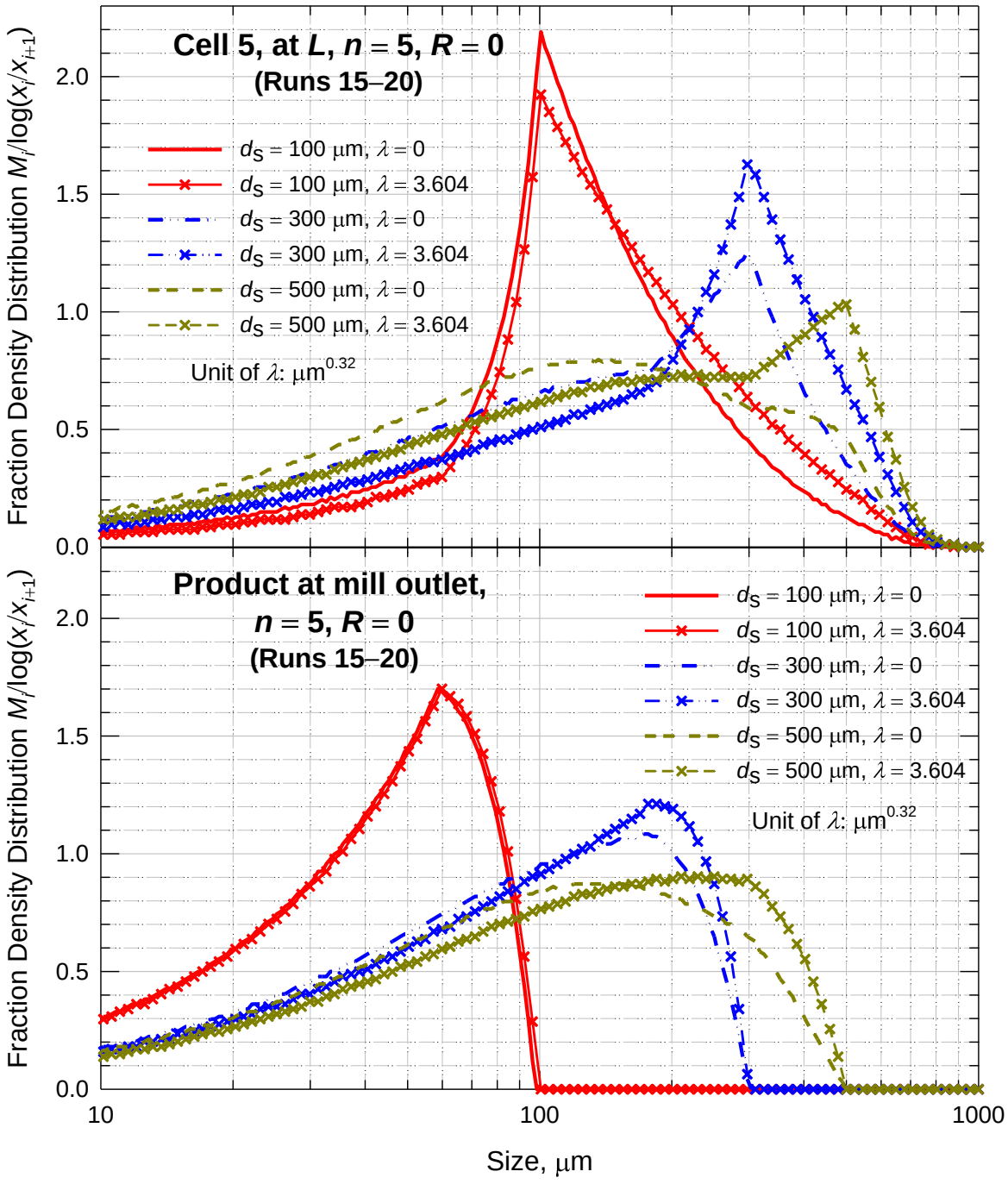

Figure 2.12 Impact of the opening size of the discharge screen d_s and the cushioning action of the fines (λ = 0 and 3.604 $\mu m^{0.32}$) on the differential PSD in Cell 5, corresponding to the axial location L of the mill, and the differential PSD of the product at the steady state (Runs 15–20). Other parameters used in simulations are n = 5 and R = 0.

The classifying action of the discharge screen can be seen by the drastically finer PSD of the product than the PSD in Cell 5. The attainment of steady-state PSD occurs later in Cell 5 (30 min), where the screen resides, than Cell 3 (within 18 min) and Cell 1 (within 18 min). This can be largely attributed to the classification action of the screen and the build-up particles $x_i > (1–\delta)d_s$. Note that the PSD of the mill discharge (product PSD) is somewhat insensitive to the milling time after 18 min, and it is largely controlled by the screen's classification function.

A comparison of **Figure 2.9** (Run 15: d_s = 100 µm) and **Figure 2.5** (Run 3: $d_s \geq$ 1700 µm) reveals that a smaller d_s delays the attainment of a steady-state PSD (30 min vs. 26 min) and leads to a finer PSD in the discharged material, which signifies the criticality of internal classification for continuous fine dry milling. The examination of the screen opening size effect, without nonlinear breakage kinetics, is expanded to 300- and 500-µm-sized screens (Runs 16 and 17). **Figures 2.10 and 2.11** illustrate the impact of d_s on the evolution of the PSD in Cell 5 and in the discharged product, respectively. Both figures show identical PSDs in Cell 5 and in the discharged product for $d_s \geq$ 1700 µm because this screen does not have any classifying action on the mill content. The use of a screen with a lower d_s led to removal of coarse particles with $x_i > (1–\delta)d_s$ and all particles with $x_i > d_s$, which is signified by the drastic reduction of the maximum particle size of the PSD in **Figure 2.11**. A lower d_s also results in longer milling time to attain a steady-state PSD. This can be best explained by the accumulation of particles coarser than $(1–\delta)d_s$ depending on their size and breakage rate. Compared with the screen with $d_s \geq$ 1700 µm, which had no classification action, the screens with smaller opening sizes led to finer product PSDs with a lower fraction of >200 µm particles because the classification action, in view of

Equation (2.9), applies to finer particles in Cell 5 content upon a decrease in d_s and thus $(1–\delta)d_s$. Overall, all these results accord well with the experimentally observed general trends regarding the impact of screen opening size for various continuous conical screen mills and hammer mills with a discharge screen (Barrasso et al., 2013; Vanarase et al., 2015; Capece, 2018). We also note an intriguing interplay between the breakage kinetics and the feed PSD–screen opening size in **Figures 2.10 and 2.11**. When the feed particles (here, with a mean/modal size of 600 μm with SD = 100 μm) are much coarser than the screen size (note the d_s = 100 and 300 μm cases), the steady-state modal size of the mill content in Cell 5 occurs at d_s and that of the product at $(1–\delta)d_s$. Obviously, if the particles break at a rate much faster into size classes with $x_i < d_s$ than what the currently assumed $k_iF_i[\ ]b_{ij}$ values entail and/or if the feed PSD is such that more particles become smaller than d_s in the mill right before Cell 5, then the modal size will occur below d_s. With the same $k_iF_i[\ ]b_{ij}$ values and $F_i[\ ] = 1$ in these simulations (**Figures 2.10 and 2.11**), the latter situation is observed here for the d_s = 500 and ≥ 1700 μm cases, where the modal size occurs at ~140 and 120 μm, respectively, well below d_s.

We hypothesize that there exists an interplay also exists between the nonlinear breakage kinetics stemming from the cushioning action of finer particles and the classification action of the discharge screen, which has not been theoretically investigated in the milling literature. For the discharge screen with no classification action ($d_s \geq 1700$ μm), the cushioning action of the finer particles on the breakage kinetics and the product PSD is quite notable and significant; the product PSD is coarser when such nonlinear breakage occurs (refer to **Figure 2.8**). To examine the impact of the classification action of the screen, new simulations were performed with and without the cushioning action of

the finer particles (λ = 3.604 μm$^{0.32}$ and λ = 0 μm$^{0.32}$, respectively) for various screen opening sizes: 100, 300, and 500 μm (Runs 15–20). As illustrated in **Figure 2.12** in general, the product PSD at the steady-state is finer in the absence of the cushioning effect of the finer particles (λ = 0) than that with the cushioning effect (λ = 3.604 μm$^{0.32}$). Our simulations suggest that the smaller the size of the screen opening, the smaller the impact of the cushioning action on the *product PSD*. The cushioning effect on the product PSD is most remarkable when there is no particle classification in the mill for the largest screen opening size ($d_s \geq$ 1700 μm) (**Figure 2.8**). On the other hand, this does not mean that the cushioning action has no impact on the mill performance when a small screen opening size is used. As seen from **Figure 2.12**, for d_s = 100 μm, while the cushioning action has no impact on the product PSD, the mill content in Cell 5 becomes considerably coarser. Thus, while the nonlinear breakage kinetics does not manifest itself remarkably in the product PSD of a continuous dry milling process due to the classifying action, the PSD of the mill content is still influenced by such nonlinear effects significantly. Finally, **Figure 2.12** highlights confirms the previously observed result for d_s = 100 μm: when the modal size of the mill content right before discharge (Cell 5) occurs at d_s, the modal size of the product occurs at $(1–\delta)d_s$. Interestingly, for the given feed PSD and d_s = 500 μm, the modal sizes of the Cell 5 content and the product occur at d_s = 500 μm and $(1–\delta)d_s$ = 300 μm, respectively, when the cushioning effect of the finer particles is considered (λ = 3.604 μm$^{0.32}$). In the absence of this nonlinear slowing-down effect (λ = 0 μm$^{0.32}$), they both occur at ~150 μm (below d_s and $(1–\delta)d_s$), pointing out to the aforementioned interplay between the breakage kinetics and the feed PSD–screen opening size.

Additional insights can be gained from these simulations: if the inverse problem (identification of the breakage parameters) is to be solved considering the product PSD only, the nonlinear effects will probably be harder to discern; the negligence of nonlinear effects could cause falsified kinetics, as demonstrated earlier in batch milling studies (Klimpel and Austin, 1977; Capece et al., 2011a; Bilgili et al., 2017). To distinguish and separate impacts and possible bias of the nonlinear kinetics vs. classification action of the discharge screen, one could use the existing simulation results with exactly known parameter values as 'simulated experiments' for subsequent parameter estimation. While this approach will expose the extent of bias and confounding of the nonlinear kinetics vs. classification action of the discharge screen, it will not resolve this challenging inverse problem. Our current simulations suggest that the measurement and analysis of the evolving PSD in the mill content or, at least, at the steady-state PSD at various locations besides the evolving product PSD could help to mitigate the bias and confounding because the nonlinear kinetics have a notable impact on the PSD of the mill content, while the product PSD at the steady-state is largely affected by the screen's classification function (refer to **Figure 2.12**). Hence, for elucidating such nonlinear effects in continuous dry milling, ideally, the evolving PSD of the mill content at various locations must be determined. However, either for practical reasons and/or for its laborious/costly nature, this practice has not been generally adopted in the literature although such measurements are quite feasible to perform at the steady-state operation (Benzer, 2005; Genc et al., 2013). In fact, the nonlinear effects have rarely been examined or even mentioned for continuous dry milling processes, with exceptions such as Kolacz and Sandvik (1996) and Yildirim et al. (1999). There are several reasons for this: impact of nonlinear breakage on the PSD may

be genuinely weak depending on the specific mill–discharge screen design, material flow/transport mechanisms inside the mill, and the properties of the material being ground (Bilgili and Scarlett, 2005a; Capece et al., 2015; Capece et al., 2018). However, the nonlinear effects are also likely masked or confounded by the discharge screen action as implied by this study and/or by air sweeping action in the mill (if it is part of the operation) (Kolacz and Sandvik, 1996). Also, in most continuous milling studies, the PSD of the mill content have not been analyzed or reported at all; only product PSDs have been analyzed and reported, e.g., as in (Barrasso et al., 2013; Vanarase et al., 2015; Capece, 2018), which makes the discernment of any nonlinear effects separately from the classification more difficult.

The impact of the various screen sizes and the cushioning action of the fines was also scrutinized in view of the total mass hold-up in the mill. As seen in **Figure 2.13**, as milling proceeds, the total mass hold-up gradually increases from 0 (empty mill) mass at t = 0 min until the attainment of the steady-state hold-up, which is defined as a <0.05% percentage deviation of the total mass hold-up between consecutive time steps. Without classification action from the discharge screen ($d_s \geq 1700$ μm), the total mass hold-up at the steady-state hold-up is 100 g (i.e., no mass accumulation due to the screen), as expected. However, when the classification takes places upon use of a smaller screen opening size (d_s = 100, 300, and 500 μm), accumulation of particles coarser than $(1–\delta)d_s$ becomes evident. The smaller the screen size is, the higher the level of total mass hold-up in the mill is. As experimentally observed (Shoji et al., 1980; Shoji et al., 1982), the breakage kinetics could be affected when the total mass hold-up is higher than a certain level. However, our current model does not include this impact.

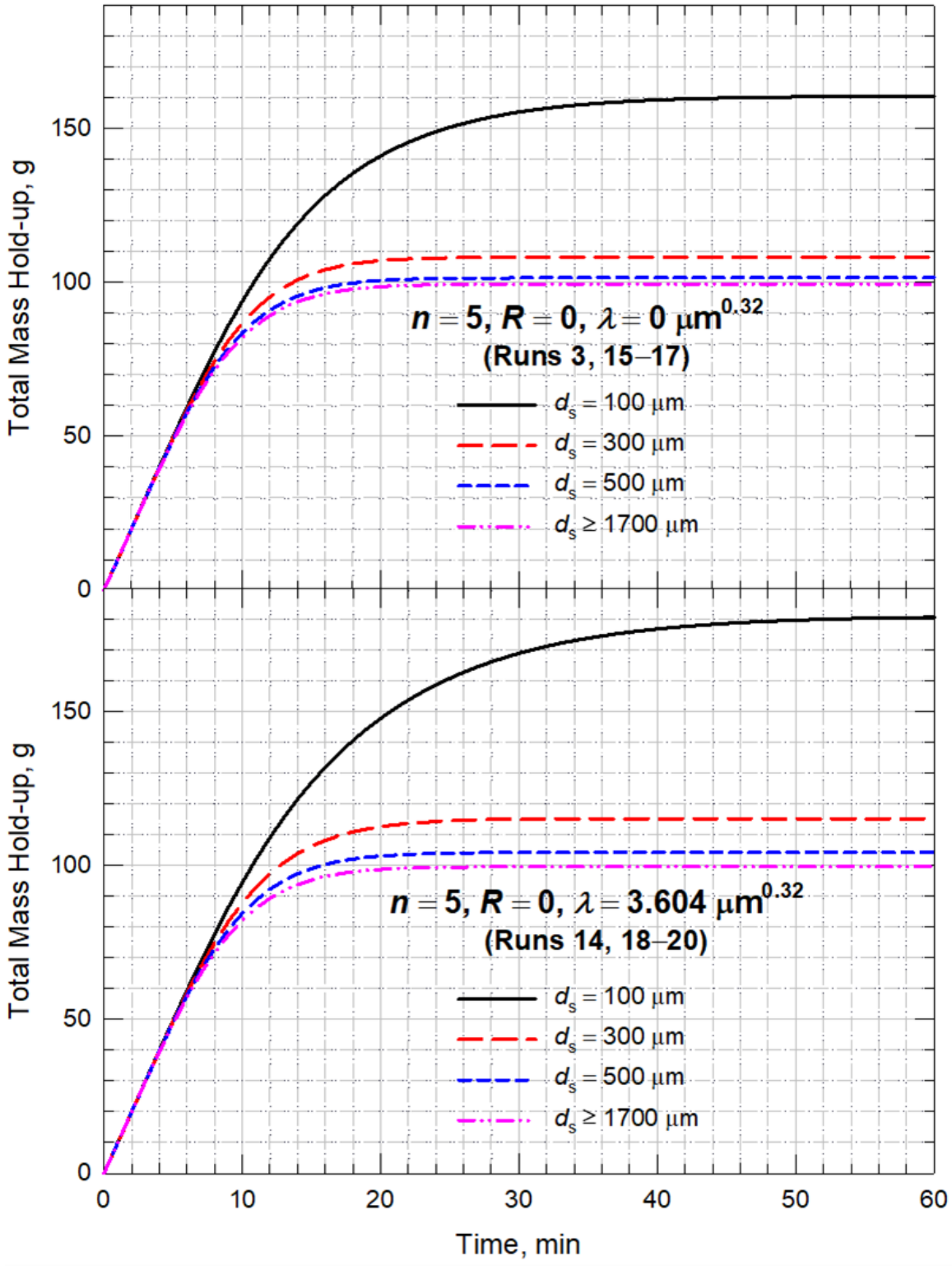

Figure 2.13 Impact of the opening size of the discharge screen d_s and the cushioning action of the fines (λ = 0 and 3.604 $\mu m^{0.32}$) on the attainment of a steady-state hold-up (Runs 3 and 14–20). Other parameters used in simulations are n = 5 and R = 0.

Figure 2.13 clearly shows that the smaller opening size prolongs the attainment of the steady-state hold-up. While the ≥1700 μm screen opening requires 25 min to attain a steady-state hold-up, the screens with 500, 300, and 100 μm opening sizes require 25, 26, and 46 min, respectively. When the cushioning action of the fines is present, the steady-state hold-up is attained at 25, 26, 30, and 55 min, respectively, for ≥1700 μm, 500, 300, and 100 μm opening sizes. Hence, for a given d_s except for $d_s \geq 1700$ μm, the total mass hold-up is higher when the cushioning action of the fine particles is present ($\lambda = 3.604$ $\mu m^{0.32}$) than it is absent ($\lambda = 0$). Finally, we record that the occurrence of the modal size of the product at d_s (**Figure 2.12**) coincides with discernible mass accumulation (deviation from 100 g baseline: >1%) in the mass hold-up at the steady-state.

2.4 Conclusions and Outlook

In this theoretical study, we have developed a cell-based PBM for the transient, open-circuit continuous operation of a dry mill with a discharge screen to study the impact of the extent of axial particle mixing, the cushioning action of fine particles on coarse ones, and the classifying action of a non-ideal discharge screen. Extensive computer simulations have been performed to gain fundamental insights into and enhance our understanding of the classification–milling interplay. The cell-based PBM has been shown to reproduce or converge to the steady-state product PSDs for continuous mills with two idealized mixing regimes: perfect mixing (CSTM) and plug flow (PFTM). Our simulation results suggest that the number of cells n and back-mixing ratio R modulate the extent of axial mixing; a higher n and lower R reduce the extent of axial mixing, leading to a finer product PSD. The fitting of the RTD using the cell-based PBM reveals that stirred media mills have much

higher R, on the order $O(10^0)$, than the continuous tumbling ball mills $O(10^{-3}–10^{-1})$. The cushioning action (nonlinear breakage) of the finer particles leads to a coarser product than that predicted by the traditional linear PBM. A screen with a smaller opening size yields a finer product PSD while taking longer to achieve a steady-state PSD. With the assumed non-ideal classification function for the screen, the modal size of the product and the modal size of the mill content near the discharge may occur at $(1–\delta)d_s$ and d_s, respectively. This occurrence is dependent upon the interplay between the breakage kinetics and the feed PSD–screen opening sizes. For a small screen opening size with respect to the given feed PSD coupled to slow breakage kinetics, a continuous milling process will be more likely to exhibit this occurrence. A small screen size also leads to a higher level of total mass hold-up due to the accumulation of particles coarser than $(1–\delta)d_s$, thus delaying the attainment of a steady-state hold-up. When the cushioning action of the finer particles on the coarser ones is present, the simulations predict a coarser product PSD. While this cushioning impact on the product PSD weakens upon use of a screen with a smaller opening size, the mill content near the discharge becomes coarser due to this impact as well. Overall, this theoretical study demonstrates the versatility of the cell-based PBM in representing a wide range of axial dispersion (RTD data) and the significant interplay between the classifying action of the discharge screen and the impact of nonlinear breakage kinetics on the product PSD and the PSD of the mill content during open-circuit dry milling with an internal classifier. Future research should address various issues associated with the inverse problem considering the interplay between the nonlinear breakage and the classification action.

CHAPTER 3

IMPACT OF BALL SIZE DISTRIBUTION, COMPARTMENT CONFIGURATION, AND CLASSIFYING LINER ON CEMENT PARTICLE SIZE IN A CONTINUOUS BALL MILL

A true unsteady-state simulator (TUSSIM), based on a cell-based Population Balance Model (PBM) with a differential algebraic equation (DAE) solver, was used for modeling a full-scale open-circuit cement ball mill for better understanding the industry best practices of employing number of mill compartments, classifying liners, and ball mixtures. Model parameters for the particle breakage and classification action with/without the classifying liner were obtained from the available literature for cement clinker. Experimental residence time distribution data for a full-scale cement ball mill was fitted by the cell-based PBM to determine the number of cells and axial back-mixing ratio. Dynamic simulations, conducted to determine the temporal evolution of the particle size distribution and mass hold-up, demonstrate that milling with a ball mixture outperforms milling with a single ball size. Single-compartment milling can achieve desirable product fineness if the feed is pre-milled. Having the same length, a two-compartment mill obviates the need for pre-milling and performs similarly or better than a three-compartment mill, depending on the ball sizes used. For a given set of ball sizes, a distribution with uniform mass of balls, as opposed to that with a uniform number of balls, achieves 8% increase in cement specific surface area. The use of a classifying liner achieves a negligibly finer cement product compared to uniformly mixed balls. Overall, these results agree with experimental observations, lending credence to TUSSIM, while providing rationale to best practices in the cement industry, offering various process insights and a toolbox to optimize existing open-circuit continuous ball mills.

3.1 Introduction

Performing controlled, scientific experiments on the impact of process and design parameters on product particle size distribution (PSD) in full-scale continuous ball milling can be quite laborious, expensive, time-consuming, and sometimes infeasible. In fact, it is hard to find any scientific study that examines the impact of number of compartments, ball sizes–distributions, and use of classifying liners on cement fineness in full-scale continuous ball mills in the open literature. In this context, modeling of full-scale continuous balls mills could provide significant insights and help process design (King, 2001). Ball milling, where balls hit and grind particles in a rotating horizontal tube, is reported to be an inefficient unit operation (von Seebach et al., 1996; Fuerstenau and Abouzeid, 2002). Mechanical energy is lost via heat dissipation and sound energy (Duda, 1985). Although more efficient milling technologies such as vertical roller mills have been introduced to the field of cement milling since the 1980s (Tamashige et al., 1991), ball milling is still a dominant technology used by cement manufacturers owing to its legacy status, simple operation, and relatively low investment cost (Xu et al., 2015).

In the open-circuit continuous operation of a ball mill (**Figure 3.1**), raw materials are continuously fed to the mill and continuously discharged from the mill (King, 2001). Feed particles become progressively finer along the axial direction due to repeated breakage by balls hitting the particle bed. Particles are transported by an air stream generated by a mill fan. This air stream pulls particles axially through the milling compartments toward the discharge end, i.e., air sweeping, which also causes the axial dispersion of particles in the mill. Practically, the industrial-scale ball mills consist of multiple compartments separated by partition diaphragms. Multi-compartment mills allow

the use of different ball sizes in each compartment. Diaphragms prevent grinding balls from slipping out of the mill and oversized particles from passing to the next milling compartment, where the particles are subject to further breakage until the particle size is fitted to the diaphragm slot. The fineness of the final cement product discharged from the mill has a specific surface area (SSA) in the range of 300–500 m^2/kg depending on the intended cement quality (Saleh and Rahman, 2018). Specific applications require specific cement sizes. For example, Zhang (2011) stated that the SSA of Portland cement should exceed 300 m^2/kg. Even a small difference in SSA can significantly influence the quality of the cement product. An increase in cement SSA results in an increase of the surface for reaction, leading to higher cement quality (cement strength). Troxell et al. (1968) reported that each percent increase in SSA leads to nearly double the percent increase in cement compressive strength.

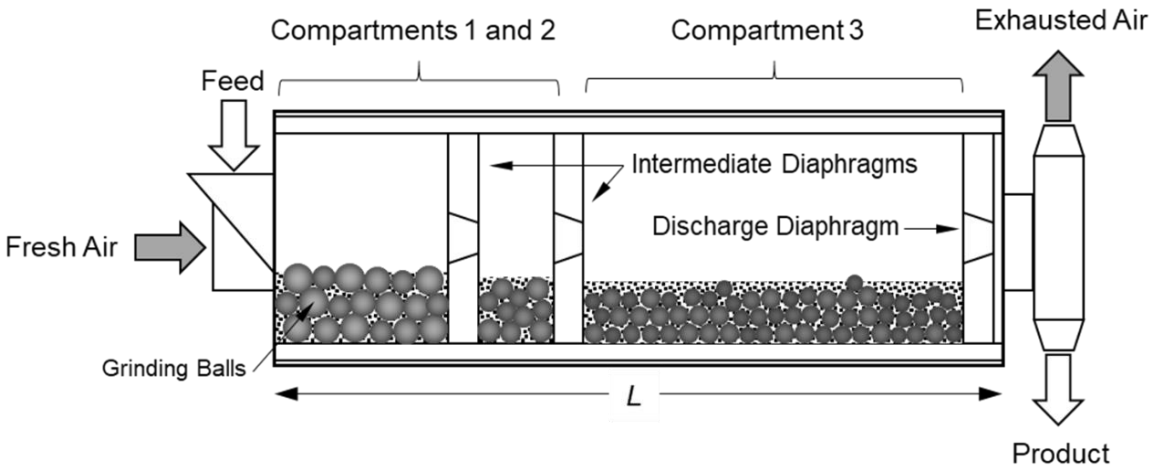

Figure 3.1 Sketch of a continuous three-compartment cement ball mill incorporating two intermediate diaphragms and one discharge diaphragm.

Ball size selection is a general problem encountered in optimizing ball mills. Such selection is a complicated nonlinear problem because it depends on several factors, including the initial feed size, evolution of particles during milling, and required final product fineness. Various efforts have been exerted to investigate the influence of ball size on the particle size distribution (PSD) in laboratory ball mills, but most studies (e.g., Katubilwa et al., 2011; Nava et al., 2020; Camalan, 2021a) used various single-ball sizes to mill multiple mono-dispersed feeds (narrow sieve cuts). Experimental observations (Kotake et al., 2002; Deniz, 2003; Kotake et al., 2004) have shown that an optimal particle size exists for a given ball size because a large ball size effectively breaks coarse particles only, while a small ball size is more effective for fine particle breakage. A power-law correlation relates the optimal mono-dispersed feed size to a given single ball size (Austin et al., 1976; Deniz, 2003; Trumic et al., 2007).

For a natural (poly-dispersed) feed to be ground, where coarse and fine particles coexist, the use of a mixture of ball sizes is the common practice (Austin et al., 1984). A few experimental studies (Erdem and Ergun, 2009; Cayirli, 2018) have considered the impact of ball size distribution (BSD) on the evolution of PSD during milling. For example, using a laboratory batch ball mill, Cayirli (2018) found that an increase in the mass fraction of smaller balls yields a finer product with higher SSA. Moreover, an excessive number of ball sizes does not always yield a finer product. Clearly, the ball selection task becomes more complicated for a natural feed, where fine and coarse particles coexist. It is critical to mention that the above studies of ball size were experimentally performed under batch mode, whereas the industry operates ball mills in continuous mode. In the context of full-scale continuous cement ball milling, there is no exact rule for ball selection; rather, the

cement industry designs the mixture of ball sizes and BSD on the basis of their experience along with recommendations from the mill machine suppliers (e.g., FLSmidth, 2012; FLSmidth, 2014) and (empirical) Bond's approach (Bond, 1958), in which top ball size can be estimated from 80% passing size of mill feed, i.e., whole feed PSD is not considered. Commonly, up to four ball sizes with different mass fractions have been used in industry (Duda, 1985; Deolalkar, 2009). As of now, unfortunately, only rough guidance for ball selection in full-scale ball mills is available. Therefore, there is a need to develop a better understanding of how to properly select BSD in continuous full-scale ball milling operations, which will benefit industry practitioners in optimizing the milling process.

Regarding ball mill design, the full-scale cement mill obviously differs from the laboratory mills in various respects. While the former commonly consists of multiple compartments and multiple diaphragms (Seebach and Schneider, 1987; Ozer et al., 2006; Genc, 2015a), the latter uses a single compartment without partition diaphragms. Thus, experiments performed with a lab mill alone cannot predict the complex milling–internal classification behavior in a full-scale mill. A multi-compartment mill is reasonably expected to provide a finer product because it has the flexibility to contain different mixtures of ball sizes in each compartment. Surprisingly, only one study (Genc, 2016) has attempted to investigate the impact of the number of milling compartments in an open-circuit cement ball mill operation. With a *steady-state* population balance model (PBM), their simulation results (Genc, 2016) suggested that for a given cement product fineness, the two-compartment mill yielded approximately 10% higher mill capacity compared to the three-compartment mill, which contradicts the traditional design in the cement industry of operating three-compartment ball mills in open circuit (Beke, 1981; Lynch and

Rowland, 2005; Deolalkar, 2009). However, it is critical to mention that the number of compartments and BSD were simultaneously adjusted in their simulations (Genc, 2016). The BSD in the two-compartment simulation was much smaller than that of the three-compartment mill, so the interpretation of the results could be somewhat confounded. Clearly, a comprehensive study on the impact of the number of milling compartments using various ball combinations could shed light on the above controversy regarding the number of compartments.

Another obvious difference in design between the full- and lab-scale ball mills is the lining plates, also known as liners. The main role of liners is to protect the mill shell from possible damage resulting from collisions with the balls. Unlike in laboratory ball mills, various designs in liner shape, including lifting and classifying liners, have been developed to increase milling performance in full-scale production mills. For example, a classifying liner provides an appropriate classification of different ball sizes along the axial mill length, i.e., a spatially varying ball mixture. Larger balls are retained at the compartment entrance, and ball sizes become progressively smaller toward the compartment end (Benzer, 2005; Genc, 2015b; Altun, 2018). Since particles become progressively finer along the axial length of the milling compartment, a classifying liner is reasonably expected to lead to more effective particle breakage. However, limited data regarding the comparison of a ball mill's performance with/without classifying liner was available in the literature. Fortsch (2006), based on the actual performance of various full-scale cement ball mills, reported that the specific power consumption of the ball mill process is equal to or higher with a classifying liner than without one; no performance improvement with a classifying liner was observed. Although a classifying liner has been

widely used in cement ball mills (e.g., Duda, 1985; Genc, 2008; Altun, 2018), no attempt within the context of a PBM has been made to quantitatively determine the improvement in product fineness when a specific liner design is used.

Among various simulation approaches, only PBM can describe the spatio-temporal evolution of PSD during milling at the process length scale. Since the 2000s, most PBM simulation studies on a cement ball mill in full-scale production (e.g., Benzer et al., 2001b; Dundar et al., 2011; Genc et al., 2013; Genc, 2016; Altun, 2018) have been carried out using the perfect mixing with discharge function approach developed by Whiten (1974). They only simulated steady-state operation. The major limitation of this approach is that the operation-dependent model parameter, i.e., the ratio of specific breakage rate parameter to discharge rate parameter, must be back-calculated from the measured PSD data obtained from sampling campaigns in actual production-scale mills. Therefore, the model parameters cannot be directly transferred to different operating conditions, limiting the predictive capability of this approach. Extensive data collection from full-scale milling circuits is required to predict PSDs with different process variables including BSD (Dundar et al., 2011). Based on a review of the literature and to the best of our knowledge, no study has explored the impact of BSD, number of milling compartments, and use of a classifying liner on cement product fineness via an unsteady-state PBM holistically.

The aim of this theoretical study is to gain fundamental insights into the impacts of BSD, number of milling compartments, and classifying liner on cement size distribution during open-circuit continuous ball milling. To this end, the recently developed true unsteady-state simulator (TUSSIM) (Muanpaopong et al., 2021; Muanpaopong et al., 2022a), based on a cell-based PBM with a differential algebraic equation (DAE) solver,

was employed for full-scale cement ball milling simulations. A recent strategy for scale-up (Bilgili, 2023) was adopted in which Kotake–Kanda's specific breakage rate model was integrated with the Austin's scale-up methodology. Moreover, experimental residence time distribution (RTD) data for a full-scale cement ball mill was fitted by the cell-based PBM to determine the number of cells and axial back-mixing ratio. Simulations were performed to investigate how the continuous ball milling process attained steady-state operation. First, spatio-temporal evolution of the PSD and the attainment of steady-state operation of a full-scale cement mill were simulated to verify if our methodology could simulate the production of a realistic open-circuit cement production process. Then, simulations for a continuous mill with one, two, and three compartments containing various ball sizes and BSDs were carried out. Finally, the advantage of employing a classifying liner, leading to ball classification along axial mill length, in fine milling compartments was explored, as compared to the case in which different ball sizes are uniformly mixed. The simulation results are expected to provide fundamental insights into the feed size–compartment configuration interplay, resolve the controversy around two- vs. three-compartment mills, elucidate effects of the BSD and classifying liner, and rationalize some of the industry practices.

3.2 Theoretical

3.2.1 Model description of TUSSIM for a three-compartment ball mill

TUSSIM was customized for an open-circuit three-compartment ball mill incorporating two intermediate diaphragms and one discharge diaphragm. Readers are referred to Muanpaopong et al. (2022a) for the derivation and details of the cell-based PBM, which

forms the core of TUSSIM. The essence of the cell-based PBM is presented here (refer to **Figure 3.2**).

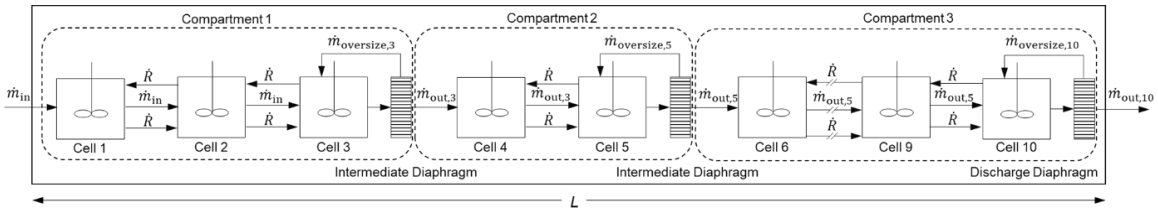

Figure 3.2 Model representation of a continuous ball mill with an effective axial length L consisting of ten well-mixed cells with three diaphragms. The axial exchange between adjacent cells occurs at the rate $\dot{R}$.

Let z be the cell index ranging from 1, which is the first cell located at the mill inlet, running up to n, which refers to the last cell located at the mill outlet. The cell-based PBM was fitted to the experimental RTD data on a full-scale cement ball mill; the total number of well-mixed cells n = 10 and the axial back-mixing ratio $R = 8.01 \times 10^{-3}$ best fitted the data. The RTD data and the cell-based PBM parameters suggest that the mixedness of the mill content is far from the idealized mixing regimes of perfect mixing and plug flow, which are widely used in the literature. Hence, the first, second, and third compartments were modeled using three, two, and five cells, respectively, which were set based on the fraction of mill length for each compartment to the total mill length of the referenced mill (see details of the referenced mill in Subsection 3.2.2). The model equations can be categorized into four groups: (i) cell at the mill inlet receiving fresh feed particles (z = 1); (ii) intermediate cells (z = 2, 7, 8, 9); (iii) cells connecting to the diaphragm, which keeps the balls in the compartment and prevents oversized particles from leaving the compartment (z = 3, 5, 10); and (iv) cells receiving particles passing through the diaphragm

(z = 4, 6). The size-discretized, time-continuous form of the cell-based PBM for n = 10 is given by

$$\frac{dm_{i,z}}{dt}=\begin{cases}-k_{i,z}m_{i,z}+\sum_{j=1}^{i-1}b_{i,j}k_{j,z}m_{j,z} & \\ +\dot{m}_{\text{in},i}+\left[Rm_{i,z+1}-(1+R)m_{i,z}\right]\tau_z^{-1} & \text{for } z=1 \\ -k_{i,z}m_{i,z}+\sum_{j=1}^{i-1}b_{i,j}k_{j,z}m_{j,z} & \\ +\left[(1+R)m_{i,z-1}-(1+2R)m_{i,z}+Rm_{i,z+1}\right]\tau_z^{-1} & \text{for } z=2,7,8,9 \\ -k_{i,z}m_{i,z}+\sum_{j=1}^{i-1}b_{i,j}k_{j,z}m_{j,z} & \\ +\left[(1+R)m_{i,z-1}-Rm_{i,z}\right]\tau_z^{-1}-\dot{m}_{\text{out},i,z} & \text{for } z=3,5,10 \\ -k_{i,z}m_{i,z}+\sum_{j=1}^{i-1}b_{i,j}k_{j,z}m_{j,z} & \\ +\dot{m}_{\text{out},i,z-1}+\left[Rm_{i,z+1}-(1+R)m_{i,z}\right]\tau_z^{-1} & \text{for } z=4,6\end{cases} \tag{3.1}$$

with $m_{i,z}(0) = 0$, $i = 1, 2, \ldots, N$, and $j = 1, 2, \ldots, N$. In Equation (3.1), i and j denote size class indices that extend from size class 1 (the coarsest particles) to size class N (the finest particles) in a geometric progression; t is milling time. Mass of particles of size class i in cell z is denoted as $m_{i,z}$. The first-order specific breakage rate parameter of particles with size x_i in cell z is $k_{i,z}$, which describes how quickly particles of size class i in cell z is broken. The breakage distribution parameter is $b_{i,j}$, representing the mass fraction of particles in size class j broken down to size class i. $\dot{m}_{\text{in},i}$ is the fresh feed rate of particles in size class i into the mill inlet (z = 1). τ_z is the average residence time (space time) of cell z, which is defined as the ratio of total mass hold-up in cell z to mass flow rate through cell z, i.e., $\tau_z = m_{\text{H},z} \Big/ \sum_{i=1}^{N} \dot{m}_{\text{in},i}$ with $m_{\text{H,z}}$ being the total mass hold-up in cell z. Mass flow rate of

particles of size class i passing through the diaphragm connected to cell z is denoted as $\dot{m}_{\text{out},i,z}$. The following constraints were imposed to satisfy the conservation of total mass:

$$k_N = 0, \quad \sum_{i=j+1}^{N} b_{i,j} = 1, \quad b_{i,i} = 0 \tag{3.2}$$

$$\tau_z = m_{\text{H},z} \left(\sum_{i=1}^{N} \dot{m}_{\text{in},i} + \sum_{i=1}^{N} \dot{m}_{\text{oversize},i,z} \right)^{-1} \tag{3.3}$$

where $\dot{m}_{\text{oversize},i,z}$ is the mass flow rate of particles in size class i of cell z that do not pass through the diaphragm, which can be determined by

$$\dot{m}_{\text{oversize},i,z} = \left(1 - P_{i,z}\right) m_{i,z} / \tau_z \tag{3.4}$$

where $P_{i,z}$ is the fraction of particles in size class i passing through the diaphragm connected to cell z due to air-sweeping action. It is critical to mention that $\dot{m}_{\text{oversize},i,z}$ is time-dependent and unknown during unsteady-state operation. Therefore, Equations (3.3) and (3.4) must be solved simultaneously along with Equation (3.1), which forms a set of DAEs.

It should be noted that in this chapter and following chapters, possible nonlinear breakage kinetics have not been considered. First and foremost, largely due to its complexity, nonlinear breakage kinetics have been disregarded in a great majority of the milling studies; no study on cement milling has considered nonlinear breakage. This prevented us from using the nonlinear breakage theory developed by Bilgili and Scarlett

(2005a) and Bilgili et al. (2006) as there was no experimental data for cement milling. Second, elucidation of nonlinear effects in milling entails collecting dense data sets. Even our late-phase and limited experimental batch milling study in Chapter 6 did not have such dense data, and it shows that the linear kinetics assumptions led to a decent fitting/prediction of the data. Hence, we assumed linear breakage kinetics for cement clinker in view of existing literature and our limited study. Whether batch cement milling truly exhibits nonlinear breakage entails a detailed future investigation, and this aspect has been indicated in Future Work of this dissertation report. Finally, air sweeping in continuous ball mills prevents any cushioning action due to accumulation of fines (Austin et al., 1981b; Kolacz and Sandvik, 1996), which is a major reason for nonlinear breakage. In other words, even when some nonlinear effects are present in batch milling of cement clinker (somewhat speculative), such effects are not likely prevalent in full-scale continuous ball milling operations due to air sweeping. No nonlinear effect has been reported for cement milling in either batch or continuous ball milling processes.

3.2.2 Specific functions and parameters used in the simulations

All functions and parameters of cement clinker were taken from the relevant milling literature, as described below. The Kotake–Kanda kinetic model (Kotake et al., 2002; Kotake et al., 2004) was augmented with Austin's scale-up methodology (Austin et al., 1984) to determine the scaled-up specific breakage rate for the full-scale milling simulations:

$$k_i = C_1 d_B^{C_3} x_i^{C_4} \exp\left(-C_2 \frac{x_i}{K_1 d_B^{C_5}} \right) K_2 K_3 K_4 \tag{3.5}$$

where d_B is a single ball size represented by its ball diameter, C_1–C_5 are model parameters, and K_1–K_4 are scaled-up factors (refer to Appendix B.1). Representative values of the specific breakage rate parameters for cement clinker in a laboratory ball milling test (i.e., C_1–C_5) were taken from Deniz (2003), wherein steel balls were used as the grinding media. Density of cement clinker ρ_c was taken from Deniz (2003) as 3000 kg/m^3. The mill had a diameter D_T of 0.2 m and was operated at the speed $\phi_{c,T}$ of 0.75. Ball filling J_T and powder filling U_T were 0.2 and 0.525, respectively. According to Deniz (2003), C_1, C_2, C_3, C_4, and C_5 for the cement clinker were 12.86 min^{-1}·mm$^{-0.274}$, 50 mm$^{0.217}$, –0.736, 1.01, and 1.217, respectively.

The plant scale operation and specification of the referenced industrial cement ball mill were taken from Genc (2016). The full-scale mill had a diameter D of 3.5 m and a length L of 9.3 m, with individual lengths of 2.94, 1.7, and 4.66 m for the compartments 1, 2, and 3, respectively. The fresh feed rate to the mill $\dot{m}_{in}$ was set to 640 kg/min, corresponding to a mass flow rate of cement clinker of 38.42 t/h, taken from Genc (2016). The mass flow rates of gypsum and admixture were neglected. This minor adjustment resulted in a more realistic cement product size distribution in the Run 1 simulation (base case) in comparison with the actual cement reported by Genc (2016). Natural feed PSD was taken from Genc (2016) for all simulations, unless stated otherwise. The mill with a top ball size of 90 mm was rotated at the speed of 16.55 rpm. The ball filling ratios J for compartments 1, 2, and 3 were 0.318, 0.318, and 0.290, respectively. The total average residence time without classification action τ was taken from Austin et al. (1975) as 14 min.

When a mixture of ball sizes was used, the specific breakage rate was determined by the weighted average from the individual specific breakage rate of a single ball size and its mass fraction M_B (Austin et al., 1976). Let Q be the number of different single ball sizes and q the ball size index ranging from 1 to Q. The specific breakage rate parameter for the mixture of Q different ball sizes is given by

$$k_{i,z} = \sum_{q=1}^{Q} M_{B,q} k_{i,z,q} \tag{3.6}$$

Three different BSDs were considered for a given set of Q ball sizes: uniform mass (UM) of balls, uniform number (UN) of balls, and uniform surface area (USA) of balls. The mass fraction of ball size index q ($M_{B,q}$) based on UM, UN, and USA were calculated respectively by

$$M_{B,q} = 1/Q,\ M_{B,q} = d_{B,q}{}^3 \Big/ \sum_{q=1}^{Q} d_{B,q}{}^3, \text{ and } M_{B,q} = d_{B,q} \Big/ \sum_{q=1}^{Q} d_{B,q} \tag{3.7}$$

Unlike the specific breakage rate parameter, the breakage distribution parameter is assumed to be material-dependent (Fuerstenau et al., 1991; Ozkan et al., 2009), and it does not largely depend on the operational parameters. Hence, the breakage distribution parameter obtained in a lab-scale experiment was directly used at the large scale (similar to Chimwani et al., 2014). An expression for the non-normalizable cumulative breakage distribution parameter $B_{i,j}$ is given by (Austin and Luckie, 1972):

$$B_{i,j} = \phi_0 \left(\frac{x_0}{x_j} \right)^{\theta} \left(\frac{x_{i-1}}{x_j} \right)^{\mu} + \left[1 - \phi_0 \left(\frac{x_0}{x_j} \right)^{\theta} \right] \left(\frac{x_{i-1}}{x_j} \right)^{\nu} \tag{3.8}$$

By definition, $b_{i,j}$ can then be determined from $b_{i,j} = B_{i,j} - B_{i+1,j}$ and $b_{N,j} = B_{N,j}$. The model parameters x_0, ϕ_0, θ, μ, and ν for the cement clinker ground in a ball mill were taken from Austin et al. (1975) as 26.9 mm, 0.1755, 0.15, 0.84, and 4.5, respectively.

The function used for internal classification (air-sweeping action) is based on the efficiency curve model (Napier-Munn et al., 1996), which has been commonly used in the literature for internal classification due to diaphragms in cement ball mills (Benzer et al., 2001b; Farzanegan et al., 2014; Altun, 2018). The fraction of particles in size class *i* passing through the diaphragm connected to cell *z* is given by

$$P_{i,z} = \left(1 - \delta_z\right) \left(1 + \beta_z \beta_z^* \frac{x_i}{d_{50c,z}} \right) \left[\exp\left(\alpha_z\right) - 1 \right] \left\{ \exp\left(\alpha_z \beta_z^* \frac{x_i}{d_{50c,z}} \right) + \exp\left(\alpha_z\right) - 2 \right\}^{-1} \tag{3.9}$$

Here, δ is the bypass fraction, α is the sharpness parameter, and β is the fish-hook parameter. d_{50c} is the corrected cut size, which is defined as the particle size that has equal probability to pass through or be recycled from the diaphragm. β^* is a parameter conserving the definition of the corrected cut size. As presented in **Table 3.1**, the model parameters for each diaphragm for the full-scale mill were based on Genc (2016). These parameters were assumed to be invariant with the milling operation conditions. The details of the size-discretization and the numerical method used to solve the DAEs are covered in Appendix B.2.

Table 3.1 Parameters of the Classifier Model for the Intermediate and Discharge Diaphragms in Full-scale Cement Ball Milling Operation

Cell index, z	Bypass fraction, δ (–)	Sharpness parameter, α (–)	Fish-hook parameter, β (–)	Corrected cut size, d_{50c} (mm)
3	0	3	0	0.70
5	0	3	0	0.16
10	0	2	0	0.15

By definition, parameter β^* was calculated using Equation (3.9).
Source: Genc (2016)

3.2.3 Some practical caveats considered in the simulations

The simulation studies were restricted with some practical rules of thumb that consider industry limitations and concerns. Fortsch (2006) stated that, as a rule of thumb in the cement industry, the smallest ball sizes are limited by the opening slot of the diaphragm, and ball sizes smaller than twice the diaphragm's slot are not typically selected. As the opening slot of the diaphragm is between 6 and 8 mm (Ozer et al., 2006), the smallest ball size in each ball mixture in the current work was set to be greater than or equal to 15 mm, which is in line with industry practice. Practically, the difference in size between the maximum and minimum ball sizes varies in certain ranges. In numerous cement ball mill operations (Genc, 2008; Tsakalakis and Stamboltzis, 2008; Altun, 2018; Ghalandari and Iranmanesh, 2020), the ratio of maximum ball size to minimum ball size for coarse milling compartments lies between 1.3 and 2.0, while a wider range has been indicated for the fine milling compartments. In most of the cases, we restricted the ball size ratio to 2.0 for all milling compartments. The largest ball size was selected as 90 mm in line with the referenced mill (Genc, 2016) and the size of the next largest ball size was reduced by 10–20

mm based on the available commercial ball sizes. These considerations were used as the basic rationale for the selection of the ball sizes presented in **Table 3.2**.

3.3 Results and Discussion

3.3.1 Spatio-temporal variation of cumulative PSD in a three-compartment ball mill

We first simulated the spatio-temporal evolution of PSD along the axial direction and product cement PSD to determine whether the product can attain typical cement particle sizes, as a base case (Run 1). A quaternary ball mixture, which is also considered an overlapping mixture, was selected. The first, second, and third compartments contained 90–60, 60–30, and 30–15 mm size range of four balls, respectively (see Run 1 in **Table 3.2**). A steady state in terms of product PSD is reached at 33 min. **Figure 3.3** demonstrates the temporal evolution of cumulative PSD in cells 3, 5, and 10, corresponding to axial lengths 3*L*/10, *L*/2, and *L*, respectively, and attainment of steady-state product PSD. These three cells were connected to diaphragms (see schematic in **Figure 3.2**) and were selected to demonstrate the possible accumulation of particles due to internal classification action. **Figure 3.3** illustrates that the PSD becomes progressively finer and narrower along the axial length from the first compartment (cell 3) to the last compartment (cell 10) and are discharged as a product at the mill outlet.

Table 3.2 Ball Mixtures and Compartment Configurations Investigated in the Simulations. All Simulation Scenarios were Based on Uniform Mass (UM) of Balls except for the Compartments with a Classifying Liner

Run no.	Designation of the balls	Number of compartments[a]	Ball size, d_B (mm)		
			First compartment	Second compartment	Third compartment
1	Quaternary mixture	Three	90, 80, 70, 60	60, 50, 40, 30	30, 25, 20, 15
2	Single ball size	One	90	–	–
3	Single ball size	One	50	–	–
4	Single ball size	One	15	–	–
5	Ternary mixture	One	90, 50, 15	–	–
6	Ternary mixture	One	90, 70, 50	–	–
7	Ternary mixture	One	50, 30, 20	–	–
8[b]	Ternary mixture	One	50, 30, 20	–	–
9	Ternary mixture	Two	90, 70, 50	50, 30, 20	–
10	Ternary mixture	Three	90, 80, 70	70, 60, 50	40, 30, 20
11	VNBS[c]	Three	90, 80, 70, 60	50, 40, 30	20, 15
12	Ternary mixture	Three	90, 80, 70	60, 50, 40	30, 20, 15
13	Binary mixture	Three	90, 60	60, 30	30, 15
14	Single ball size	Three	90	60	30
15	Quaternary mixture	Two	90, 80, 70, 50	30, 25, 20, 15	–
16	VNBS–I[c]	Two	90, 80, 70, 50	40, 30, 20	–
17	VNBS–II[c]	Two	90, 80, 70, 50	30, 20, 15	–
18	Ternary mixture–I	Two	90, 70, 50	40, 30, 20	–
19	Ternary mixture–II	Two	90, 70, 50	30, 20, 15	–
20	Binary mixture–I	Two	90, 50	40, 20	–
21	Binary mixture–II	Two	90, 50	30, 15	–
22	Single ball size	Two	90	30	–
23	Quaternary–Binary	Three	90, 80, 70, 60	60, 50, 40, 30	Class. liner[d]
24	Quaternary–Binary	Two	90, 80, 70, 50	Class. liner[d]	–
25	Quaternary–Binary	Three	90, 80, 70, 60	60, 50, 40, 30	30, 15
26	Quaternary–Binary	Two	90, 80, 70, 50	30, 15	–

[a] All compartment configurations have the same total length; [b] Pre-milled feed; [c] VNBS: variable number of ball sizes in different compartments; [d] Ball pattern was determined using Equation (3.10) with $d_{B,Max}$ of 30 mm and $d_{B,Min}$ of 15 mm.

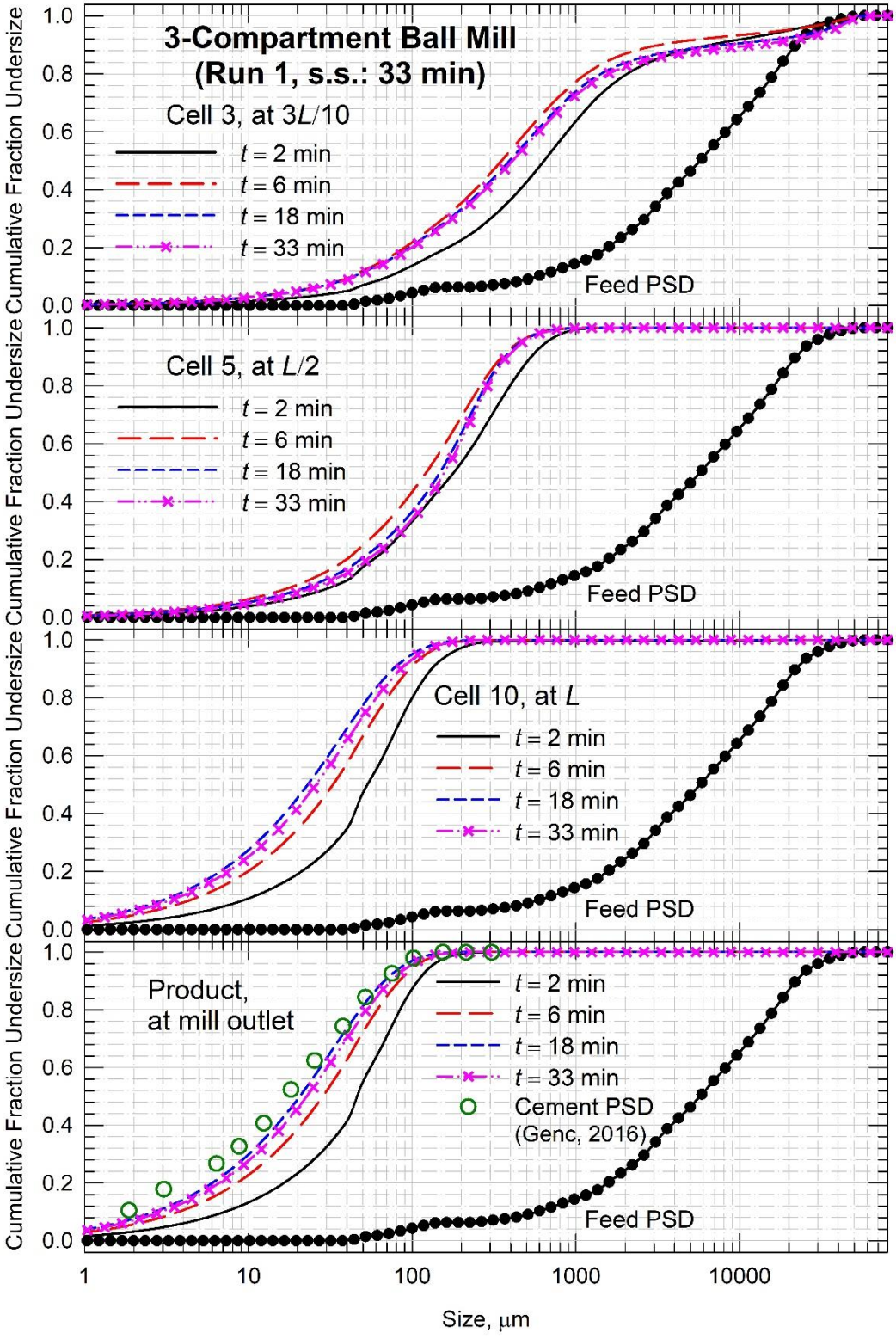

Figure 3.3 Spatio-temporal evolution of cumulative PSD along the axial direction and product PSD in a full-scale continuous cement ball mill (Run 1). Cells 3, 5, and 10 correspond to axial positions 3*L*/10, *L*/2, and *L* of the mill.

This is in agreement with the actual cement ball milling operation observed in Dundar et al. (2011), Genc et al. (2013), Genc et al. (2015a), and Altun (2018). Similar PSDs between cell 10 and cement product were observed, which is in line with experimental observation in full-scale ball mills (Benzer et al., 2001b). This finding suggests that the internal classification (air-sweeping) action from the discharge diaphragm was weaker than from that of the intermediate diaphragms.

At each axial length (cell), as milling proceeds, the PSD first shifts to a finer size initially. However, PSD becomes coarser after a certain milling time as particles continue to accumulate in each cell. In fact, total mass hold-up inside the mill increases as milling time increases until a steady state is reached within 33 min. The general trend of attainment of the steady-state mass hold-up inside the mill can be seen in **Figure 3.4a**. As we factor in the impact of powder filling U on the specific breakage rate parameter in the simulations (see scale-up factor K_3 in Equation (B.2)), the specific breakage rate becomes lower when U exceeds U_T and the PSD thus becomes coarser until a steady-state operation is reached. This explanation accords well with the experimental observations by Shoji et al. (1980, 1982) in that once total mass hold-up goes beyond a certain limit (i.e., powder filling $U > U_T$), the specific breakage rate drops. In comparison with an actual cement PSD obtained from the referenced mill (**Figure 3.3**), although simulated cement product PSD at steady-state operation (t = 33 min) does not exactly match with actual cement PSD in Turkey (Genc, 2016), it is still in the common range of cement size. It is critical to mention that the model parameters used in the simulations were taken from multiple sources from the cement milling literature (Austin et al., 1975; Deniz, 2003; Genc, 2016). Hence, the

simulations were not expected to predict the exact product PSD of the referenced mill taken from Genc (2016).

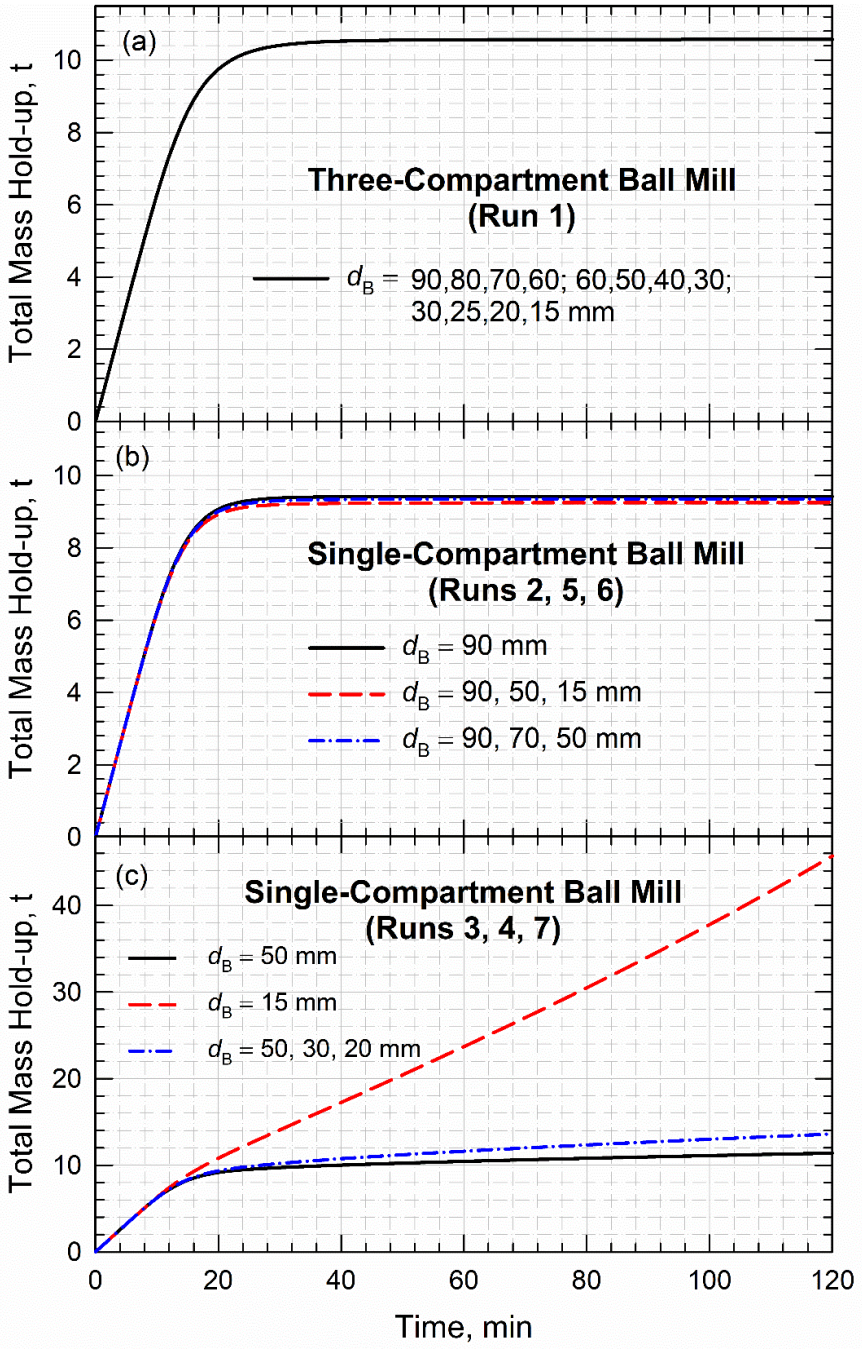

Figure 3.4 Temporal evolution of total mass hold-up during continuous operation of (a) a three-compartment ball mill with a quaternary ball mixture and a single-compartment ball mill with (b) top ball size of 90 mm and (c) top ball sizes of 50 and 15 mm.

Experimental data of Genc (2016) also suggest that the extent of size reduction of particles in the last few meters inside the ball mill became smaller, compared to the front section of the mill. Specifically, the percent decrease of median particle size d_{50} at 4.64 m (in front of intermediate diaphragm) to that at 7.64 m was 46%, while the percent decrease of d_{50} was 10% when the PSD data was compared between 7.64 m to 9.3 m. A similar trend was observed in this simulation study. For example, based on Run 1 simulation at steady state, the percent decrease of simulated d_{50} from cell 5 (L = 4.65 m, in front of intermediate diaphragm) to cell 8 (L = 7.44 m) was 78%, while that from cell 8 (L = 7.44 m) to cell 10 (L = 9.3 m) was 26%. Based on the simulation results of product PSD, it is fair to assert that the recently developed TUSSIM, a PBM-based simulator (Muanpaopong et al., 2021; Muanpaopong et al., 2022a), is reasonably accurate for predicting general trends observed during full-scale cement ball milling.

3.3.2 Advantages of ball mixtures and multi-compartment mill configurations

Studies of BSDs can be categorized into two groups: (i) mixture of different ball sizes based on UM, hereafter known as "study of ball mixture," and (ii) mixture of different mass fraction (UM, UN, and USA) of a selected ball mixture, hereafter referred to as "study of BSD." To explore any advantages of ball mixtures along with the use of multi-compartment configurations, simulations with a single ball size, a ball mixture with natural cement feed, and a ball mixture with pre-milled feed were performed in one-, two-, and three-compartment mills (Runs 2–10). For a direct comparison, the total effective length of the mill for three configurations (one, two, and three compartments) was kept the same. Two intermediate diaphragms were eliminated in the one-compartment mill, while the second diaphragm was eliminated in the two-compartment mill.

3.3.2.1 Advantages of ball mixtures vs. single size balls. For direct comparison of the impact of ball mixture without the influence of multi-compartment configuration, simulations were performed considering single ball sizes (Runs 2–4) as well as mixtures of different ball sizes (Runs 5–7) in a single-compartment mill. **Figures 3.4(b) and (c)** illustrate the total mass hold-up as a function of time. When only a large ball size (90 mm) is used, total mass inside the mill gradually builds up and attains a steady state (**Figure 3.4b**). The profile is similar when 90 mm is used in a mixture with two other ball sizes. On the other hand, in operations with smaller ball sizes, i.e., 50 mm, 15 mm, or a mixture of 50–30–20 mm, for both single balls and the ball mixture, total mass in the mill gradually builds up without limit (**Figure 3.4c**), and steady-state operation could not be attained during the 120 min milling time simulated. The smaller the top ball size is, the higher the level of total mass hold-up in the mill is. In actual operation, a ball mill cannot function continuously with the operational features shown in **Figure 3.4c**, as it will have to be shut down. **Table 3.3** reports details of cement product fineness in terms of characteristic sizes (10% passing size d_{10}, median size d_{50}, and 90% passing size d_{90}), span of product PSD, and SSA for the single-compartment mill. Even though a single ball size of 90 mm (Run 2) attains steady-state operation, the product is too coarse (SSA = 182 m^2/kg) and it thus does not satisfy general cement specifications (Saleh and Rahman, 2018). A ball mixture of 90, 50, and 15 mm balls (Run 5) may not be practically used in actual operation because the smallest balls (15 mm) can be damaged /worn out significantly by the largest balls (90 mm). Regardless, this mixture of ball sizes is effective for breaking both coarse and fine particles in the feed, and thus it yields wider (larger span value of PSD) and finer product size compared to both the single ball size (Run 2: d_B = 90 mm) and the coarse ball mixture

(Run 6: d_B = 90, 70, and 50 mm). In short, all three operations mentioned above are unlikely to satisfy cement specifications (Saleh and Rahman, 2018).

Table 3.3 Characteristic Particle Sizes d_{10}, d_{50}, and d_{90}, Span of the PSD, and Specific Surface Area SSA for a Single-Compartment Mill with Single Ball Size and Ternary Mixtures of Different Ball Sizes

Run no.	Simulated product in single-compartment mill at steady state				
	10% passing size, d_{10} (μm)	Median size, d_{50} (μm)	90% passing size, d_{90} (μm)	Span (–)	Specific surface area, SSA (m^2/kg)
2	6.84	51.4	153	2.85	182
3[a]	–	–	–	–	–
4[a]	–	–	–	–	–
5	3.67	29.2	103	3.42	291
6	5.62	43.3	135	2.99	211
7[a]	–	–	–	–	–
8[b]	2.69	20.6	141	3.41	359

[a] Steady-state operation was not attained during 120 min milling; [b] Pre-milled feed.

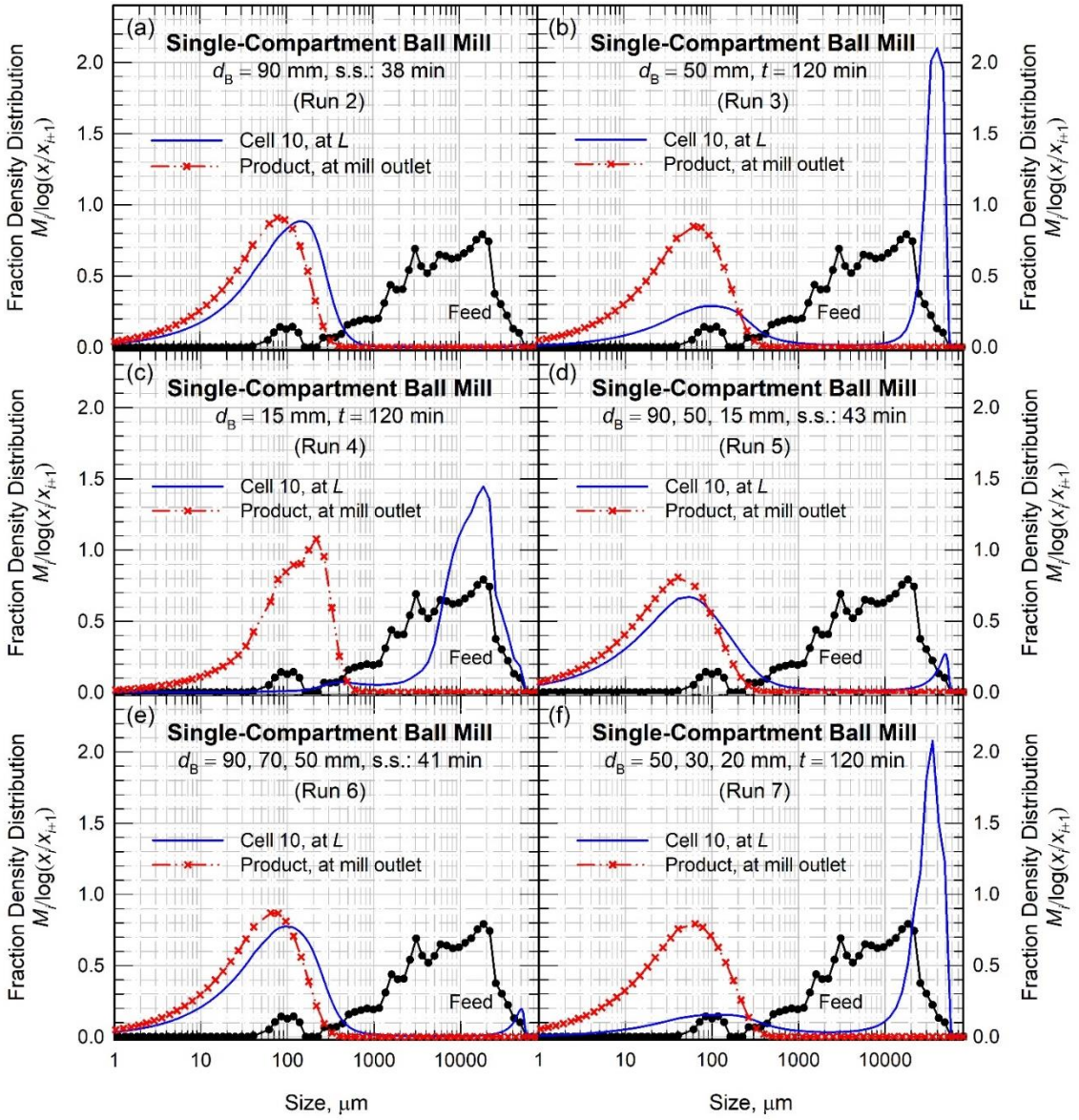

Figure 3.5 Differential PSD at cell 10 corresponding to axial length L and product at mill outlet in a continuous, single-compartment ball mill: (a) d_B = 90 mm, (b) d_B = 50 mm, (c) d_B = 15 mm, (d) d_B = 90, 50, and 15 mm, (e) d_B = 90, 70, and 50 mm, and (f) d_B = 50, 30, and 20 mm.

Figure 3.5, illustrating differential PSD of cell 10 at axial length *L* and product at mill outlet, suggests why small top ball sizes could not attain a steady-state operation in a single-compartment mill. Note that the PSD for Runs 2, 5, and 6 is for the steady-state operation, whereas the PSD for Runs 3, 4, and 7 corresponds to a PSD at t = 120 min (the final milling time) because a steady state operation is not reached. The runs that do not attain a steady state (Runs 3, 4, and 7) are associated with a strong bi-modal distribution and a significant fraction of coarse particles when the maximum ball size is 50 mm. For example, a bimodal PSD with peaks at ~40 mm and ~0.1 mm is observed in cell 10 at *L* when a top ball size of 50 mm is used alone. It is clear that a small top ball size cannot effectively break coarse particles, and they accumulate in the mill; therefore, a large portion of coarse particles remain in the mill, which is consistent with experimental observations from Erdem and Ergun (2009). The modality at the coarse particle domain disappears or gets drastically depressed when 90 mm balls are used alone (Run 2) or in two different mixtures (Runs 5 and 6).

In cement industry, single-compartment mills have been commonly used in cement ball milling circuits with fine feed particles, i.e., a pre-milled feed. **Figure 3.6** compares differential PSD at cell 10 and product PSD at mill outlet when a ternary ball mixture of 50, 30, and 20 mm is used to mill two different feed PSDs: natural or raw feed (Run 7) and pre-milled feed (Run 8). The pre-milled feed data from a hydraulic roller press was taken from Genc and Benzer (2016). Unlike with a raw feed, milling with a pre-milled feed leads to much finer particles in cell 10 and small fraction of coarse particles accumulating inside the mill, and thus, product fineness is satisfactory for cement specifications; see Run 8 in Table 3 for characteristic product sizes and SSA. This is in line with industry practice: by

incorporating full-scale hydraulic roller press for pre-milling, ball mills are commonly modified from two-compartment to single-compartment mills (Strasser, 2002).

3.3.2.2 Advantages of multi-compartment mills vs. single-compartment mills. To investigate the advantages of using multiple versus single compartments, additional simulations with ternary ball mixtures having a 90-mm top ball size in two compartments (Run 9) and three compartments (Run 10) were performed. In the two-compartment mill, the first compartment contained a large ball mixture (90–50 mm) and the second compartment contained a small ball mixture (50–20 mm). **Figure 3.7** depicts that a two-compartment mill yields a much finer product compared to a single-compartment mill, and no particles coarser than 0.5 mm were observed inside the mill in cell 10. A two-compartment mill enables engineers to fully benefit from the diverse ball sizes needed for fine milling of cement clinker: coarser balls in compartment 1 and smaller balls in compartment 2. This wide variation of balls sizes is not feasible in a single-compartment mill as 90 mm balls could cause dramatic damage on the smaller, e.g., 20 mm balls.

In the three-compartment mill, the first compartment contained a large ball mixture (90–70 mm), the second compartment contained an intermediate ball mixture (70–50 mm), and the last compartment contained a small ball mixture (i.e., 40–20 mm). Interestingly, as shown in **Figure 3.8**, significant improvements (both cell 10 and product) for the three-compartment mill compared to the two-compartment mills are not observed. The main notable difference in **Figure 3.8** is that either mill configuration leads to finer particles when 15 mm balls vs. 20 mm balls is used in the last compartment; that is, 14.8% and 16.8% increase in SSA for the three-compartment (Runs 1 and 10) and the two-compartment mills (Runs 9 and 15), respectively. The upshot of the results presented in

Figures 3.6–3.8 is the notable improvement of product fineness when a two-compartment mill is used as opposed to a single-compartment mill. Although a three-compartment mill could provide more flexibility in using more ball sizes/combinations, there is no improvement when switching from a two-compartment mill to a three-compartment mill for the specific set of ball sizes used here. Obviously, the simulations also imply that there is no need for a four-compartment mill from a product fineness perspective.

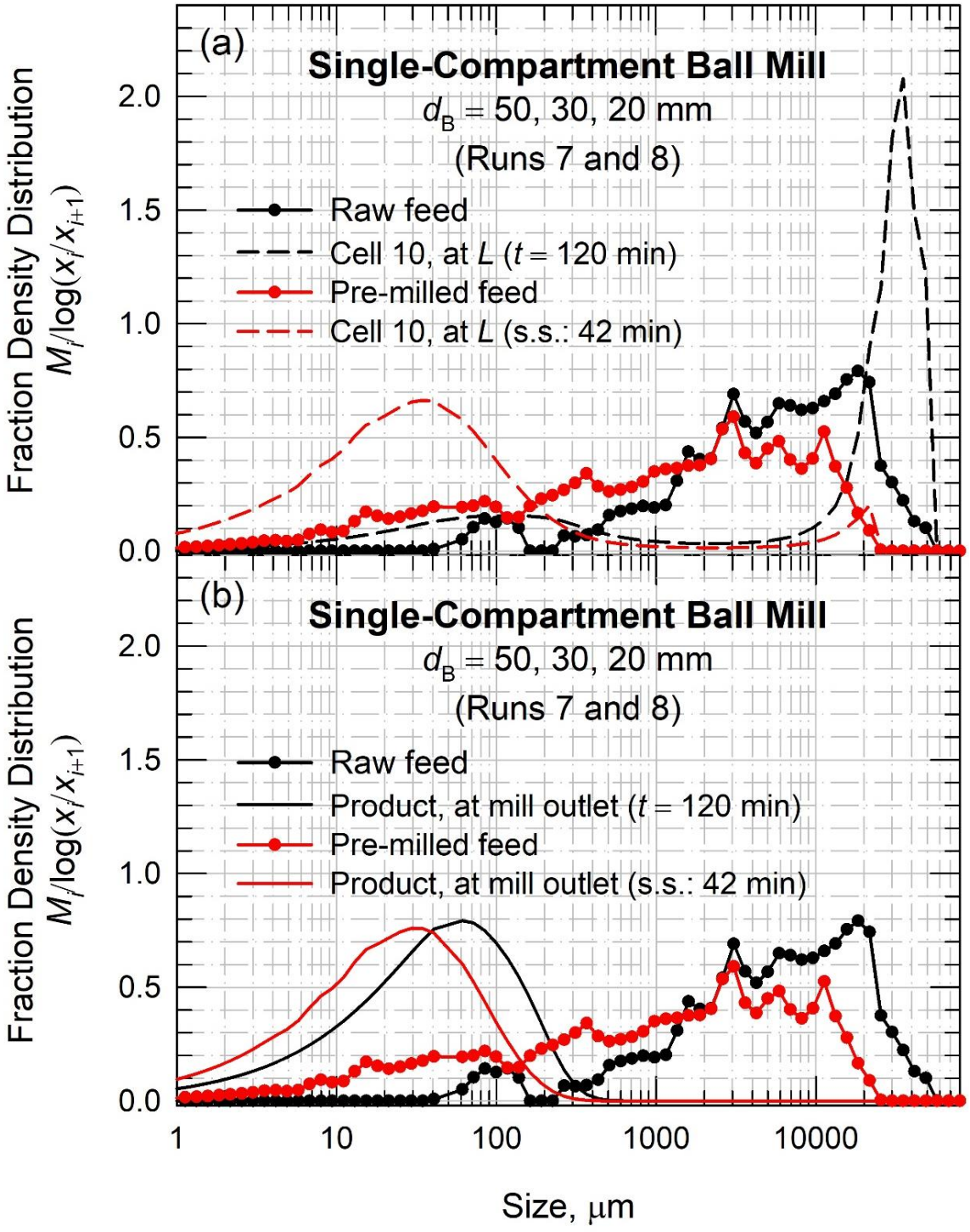

Figure 3.6 Differential PSD in a continuous, single-compartment ball mill with natural and pre-milled feed: (a) cell 10 corresponding to axial length L and (b) product at mill outlet.

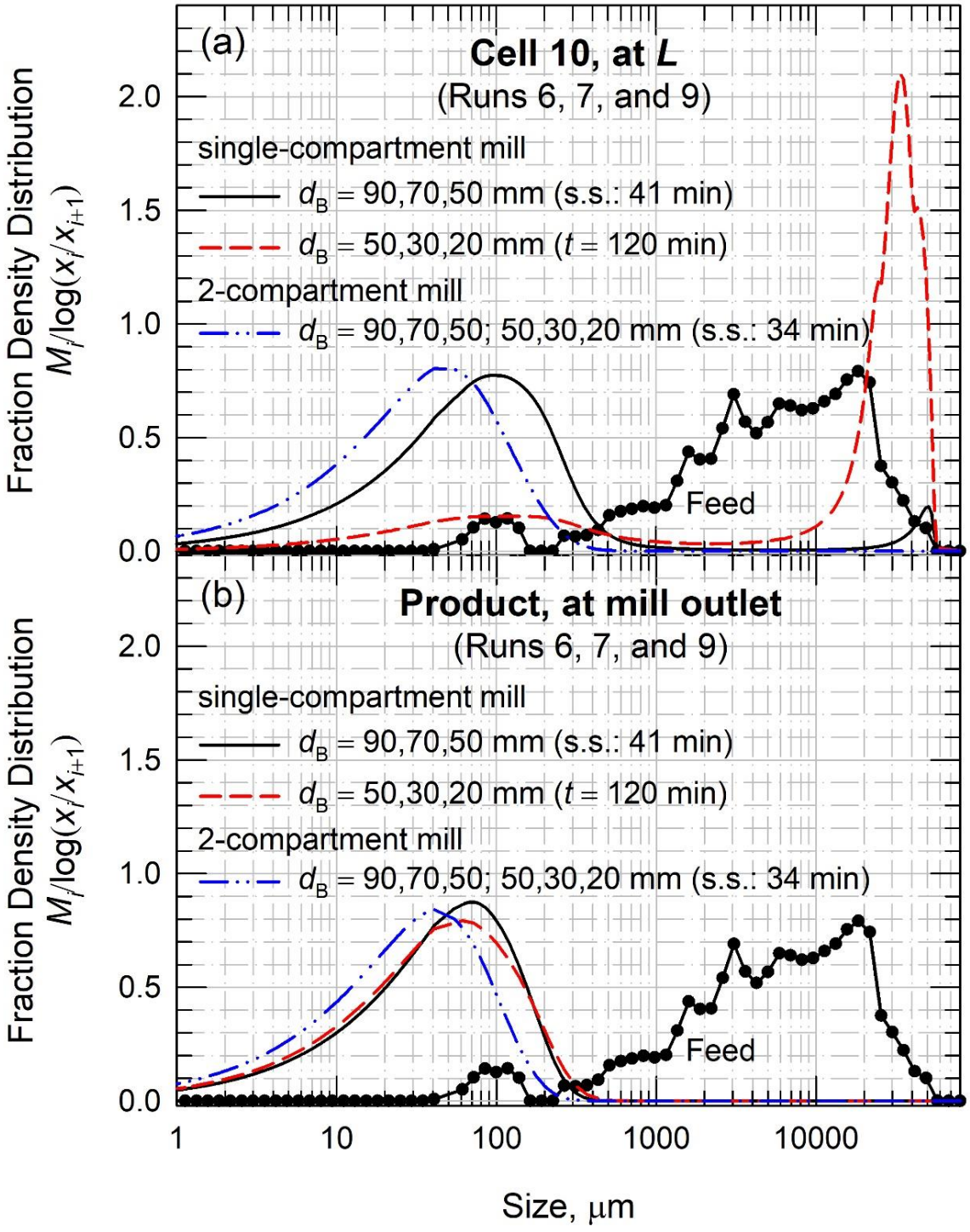

Figure 3.7 Differential PSD in a continuous ball mill with a single compartment and two-compartments: (a) cell 10 corresponding to axial length *L* and (b) product at mill outlet.

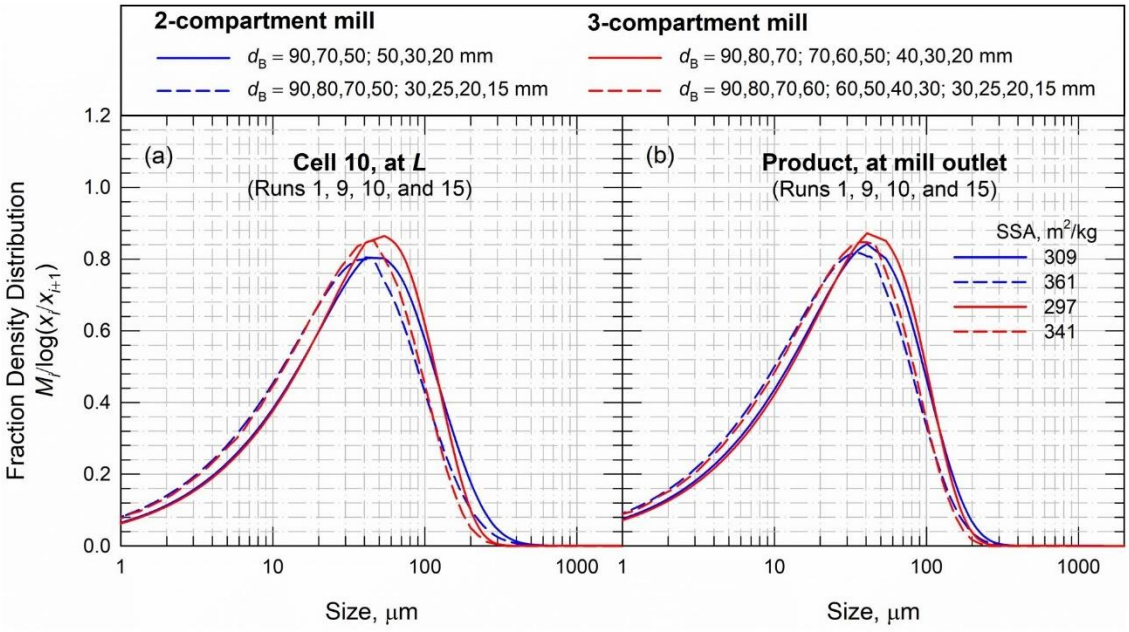

Figure 3.8 Differential PSD in a continuous two-compartment and three-compartment mills with ternary–quaternary ball mixtures: (a) cell 10 corresponding to axial length *L*, and (b) product at mill outlet. The initial PSD is not shown for proper discernment of difference.

3.3.3 Impact of various ball mixtures in multi-compartment ball mills

The next set of simulations was performed to investigate the impact of various ball mixtures such as quaternary, ternary, and binary ball mixtures and variable number of ball sizes (VNBS) along with single ball size in a three-compartment mill (Runs 1, 10–14) and two-compartment mill (Runs 15–22) (see **Table 3.2**). In general, we factored in the constraint of the ratio between the biggest and smallest balls, which was set to less than or equal to 2.0. All simulations were performed under the BSD with uniform mass (UM); that is, the mass fraction of each ball size is equal. Unlike the quaternary ball mixture, VNBS is considered a non-overlapping ball mixture because it does not have common ball sizes in different compartments (**Table 3.2**). Furthermore, the number of ball sizes is reduced by one in the next milling compartment. To cover the same range of ball sizes between two

different configurations, the ball combinations of VNBS, ternary mixture, and binary mixture in the two-compartment mill are considered in two scenarios: with the smallest ball sizes of 20 and 15 mm for scenarios I and II, respectively. The only difference between these scenarios was that ball sizes in the last compartment in scenario I were between 20 and 40 mm, while scenario II contained ball sizes between 15 and 30 mm (smaller balls).

Figure 3.9 illustrates the impact of various types of ball mixtures on the cement product fineness in a three-compartment ball mill. A single ball size in each compartment (Run 14) produces a much coarser cement product than the binary ball mixture: 22.4%, 22.1%, 17.7% higher d_{10}, d_{50}, d_{90} and 21.4% lower SSA. The binary ball mixture yields a slightly finer product than the quaternary and ternary ball mixtures. Among the quaternary, ternary, and binary ball mixtures, the differences between the best scenario (binary mixture) and worst scenario (quaternary mixture) were 2.8%, 2.8%, 2.1%, and 2.1% with respect to d_{10}, d_{50}, d_{90}, and SSA. As stated earlier, the choice of ball mixture is infinite, and a credible simulator can be customized for any ball combination to find the optimum condition of ball selection. Here, VNBS ball mixture was shown to be more effective compared to other mixtures. VNBS yielded the finest final product, which had a ~7% higher SSA than the product of the binary ball mixture, which could lead to significant improvement in cement strength (Troxell et al., 1968). This result points to a need for a comprehensive BSD optimization using a simulator like TUSSIM, which is out of the scope of this study.

It is inferred from the binary vs. ternary/quaternary ball mixture simulation results that an excessive number of ball sizes does not always yield a finer product, which is in line with past experimental results (Cayirli, 2018). However, this outcome contradicts

common industry practice wherein the combination of up to four ball sizes is commonly used (Duda, 1985; Deolalkar, 2009). Although binary mixtures perform slightly better than other mixtures in terms of breakage kinetics, a caveat to the use of binary mixtures (large and small ball sizes) is that smaller balls may break or wear due to their collisions with the much larger balls (Meulendyke and Purdue, 1989; Chenje, 2007). The wear rate of balls may also be a potential issue that needs to be considered, which is largely disregarded in small-scale, laboratory ball milling studies. While the breakage kinetics of the binary mixture is slightly higher than that of the ternary and quaternary mixtures, it may not be practical in terms of ball wear. This may explain why a mixture of three or four ball sizes is commonly used. The simulations were also performed for ball mixtures in a continuous two-compartment mill; the details for each ball combination are shown in Runs 15–22 (**Table 3.2**). **Figure 3.10** illustrates a result similar to the simulation result with the three-compartment mill, where the single ball size produced the coarsest product. Among the ball mixture scenarios, ternary mixture–II yielded the finest product, producing a finer product than the single ball size (the worst-case scenario), as signified by 23.0%, 23.0%, and 19.1% lower d_{10}, d_{50}, and d_{90}, respectively. Figure 10 also depicts that for a given ball mixture, the operation containing 15 mm balls (scenario II) yielded a finer product size compared with the operation that contained the minimum ball size of 20 mm (scenario I), with the difference in SSA reaching approximately 50 m^2/kg. It is asserted that with the proper selection of ball sizes for the two-compartment mill, the product can be slightly coarser than the best scenario of the three-compartment mill (VNBS in Run 11). However, it should be kept in mind that the product fineness is sensitive to ball selection in the two-compartment mill and ball wear must also be considered.

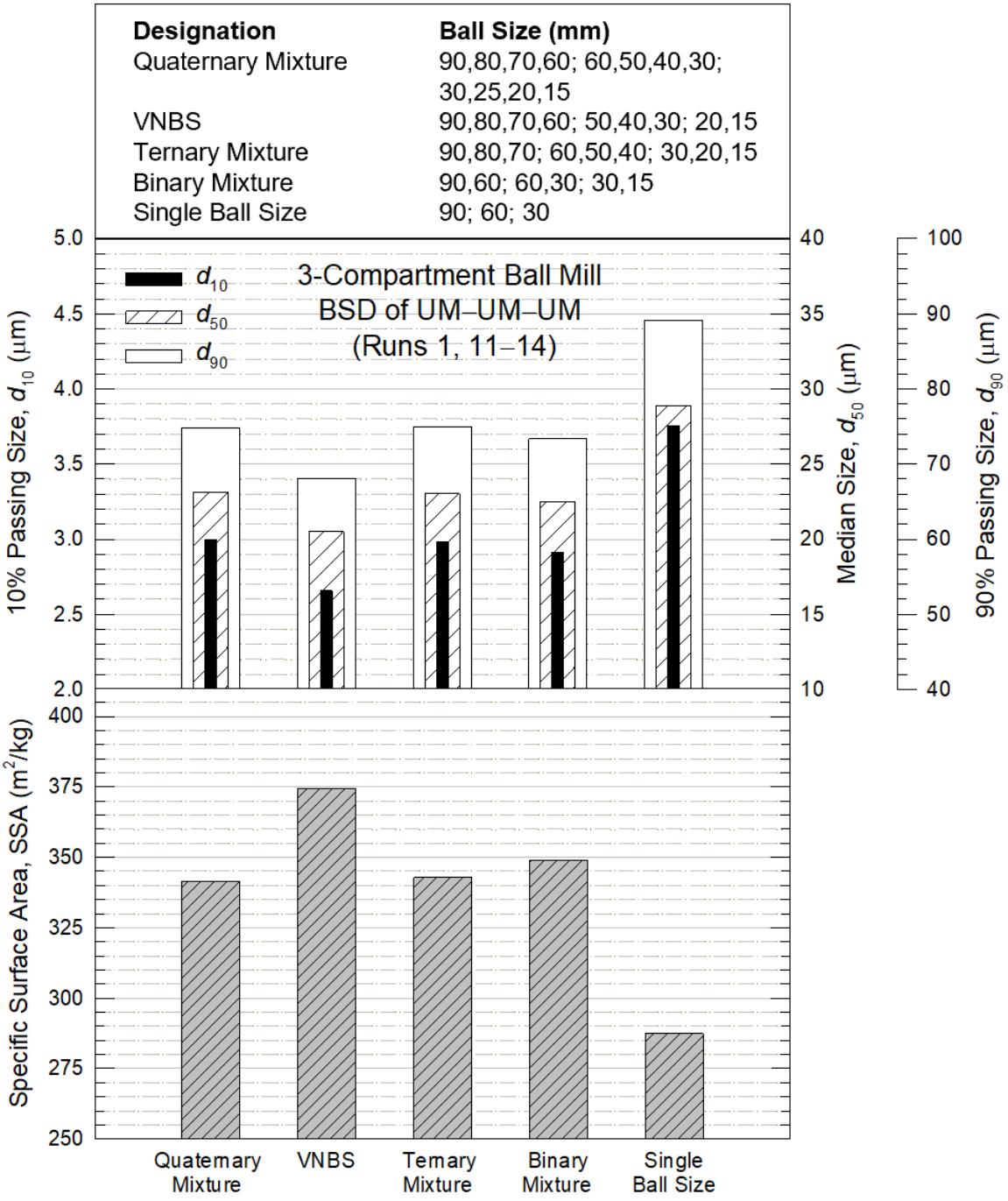

Figure 3.9 Simulated product fineness reported as characteristic sizes and specific surface area for various ball mixtures along with the use of single ball size in a three-compartment ball mill. Ball size distribution is based on the uniform mass (UM) of balls for all simulation runs.

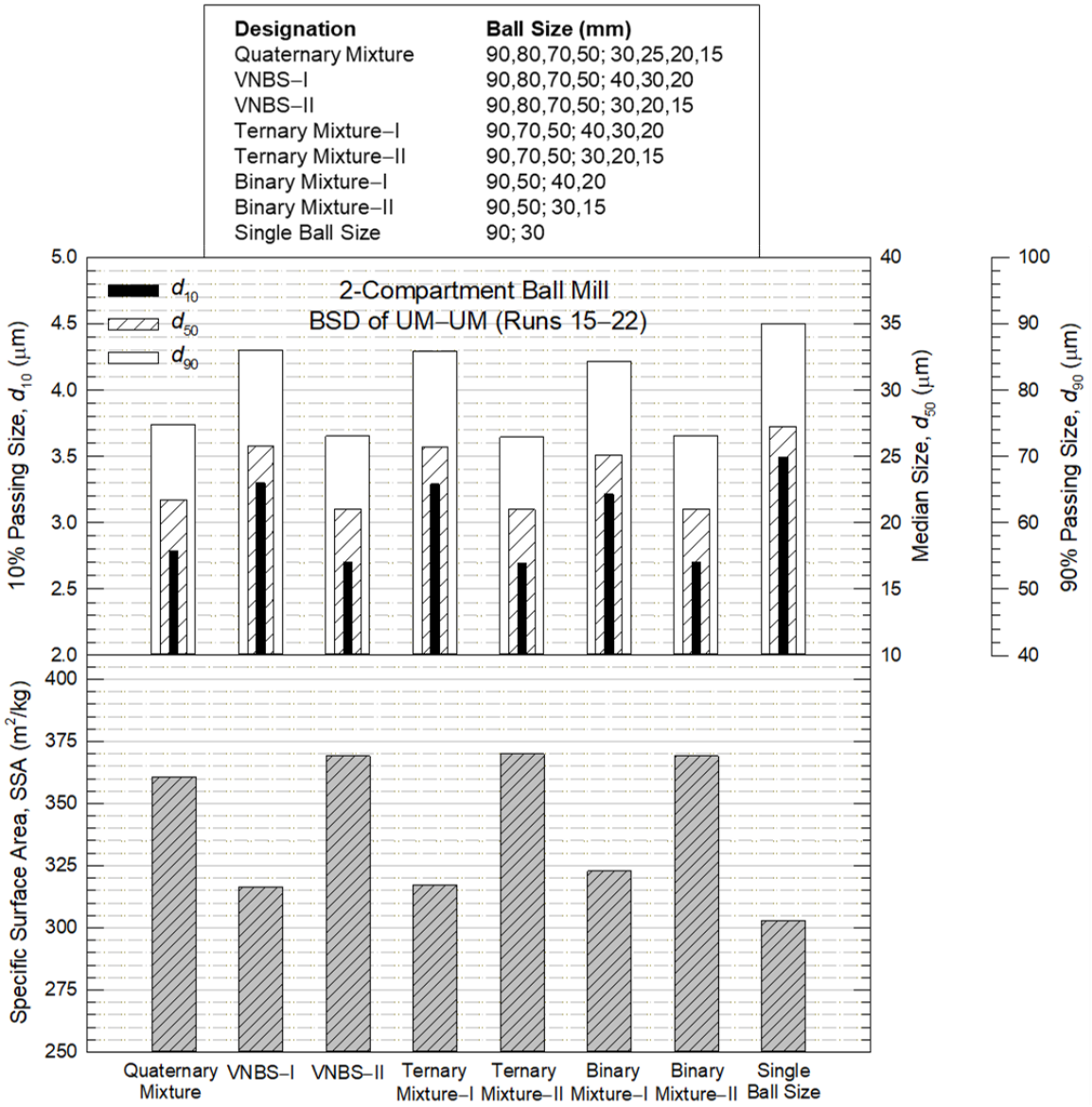

Figure 3.10 Simulated product fineness reported as characteristic sizes and specific surface area for various ball mixtures along with the use of single ball size in a two-compartment ball mill. Ball size distribution is based on the uniform mass (UM) of balls for all simulation runs.

Although the ball mill configuration with a higher number of compartments yields a finer product and provides more flexibility in the designation of ball sizes, resulting in less sensitivity to ball selection, using an excessive number of diaphragms leads to several concerns in actual operation. A caveat is that using a higher number of diaphragms increases the possibility that worn balls will block the diaphragm's slot, and thus, particles cannot be transported properly to the next compartment. In practice, a higher number of diaphragms leads to a higher pressure drop across the mill, due to longer mill (~300 mm longer per diaphragm) (Duda, 1985), and heavier weight of the total ball mill unit. This outcome leads to higher capital costs as well as higher operating costs in terms of specific power consumption when more compartments are used. For these reasons, the use of an excessive number of diaphragms (and compartments) may not be practical besides the fact that a fourth compartment is not expected to yield a much finer product, in view of the discussion in Subsection 3.3.2 Overall, the controversial finding of Genc (2016) in that a two-compartment mill outperforms as compared to a three-compartment mill is shown to be feasible by our simulation study; but, as also implemented by Genc (2016), the two mills would have to use different ball sizes. One major difference between a three-compartment mill and a two-compartment mill appears to be the specific ball sizes used. The performance of the mills is also closely related to the screening efficiency of the intermediate diaphragms, which is modeled by the internal classification function, and this could also contribute to the above-mentioned findings.

Table 3.4 Simulations in which Various Quaternary Mixtures of Balls were Distributed based on UM, UN, and USA Approaches

Run no.	Ball size distribution and mean ball size (mm)		
	First compartment	Second compartment	Third compartment
27	UM (75.0)	UN (52.3)	UM (22.5)
28	UM (75.0)	USA (47.8)	UM (22.5)
29	UN (79.7)	UM (45.0)	UM (22.5)
30	UN (79.7)	UN (52.3)	UM (22.5)
31	UN (79.7)	USA (47.8)	UM (22.5)
32	USA (76.7)	UM (45.0)	UM (22.5)
33	USA (76.7)	UN (52.3)	UM (22.5)
34	USA (76.7)	USA (47.8)	UM (22.5)
35	UM (75.0)	UM (45.0)	UN (26.1)
36	UM (75.0)	UM (45.0)	USA (23.9)
37	UN (79.7)	UN (52.3)	UN (26.1)

UM: uniform mass, UN: uniform number, and USA: uniform surface.
Compartment 1: 90, 80, 70, and 60 mm balls; compartment 2: 60, 50, 40, and 30 mm balls; compartment 3: 30, 25, 20, and 15 mm balls.

3.3.4 Impact of ball size distribution in three-compartment ball mills

A quaternary ball mixture was chosen to examine the impact of BSD, namely, UM, UN, and USA distribution of the four balls (see Run 1 in **Table 3.2** and Runs 27–37 in **Table 3.4**). The mass fraction for each ball size, based on UM, UN, and USA, was calculated using Equation (3.7). Generally, for a given set of ball sizes, the UM-BSD contains a higher mass fraction of the smaller balls compared to the UN-BSD and the USA-BSD. A comparison of simulated product fineness in terms of characteristic sizes obtained from all ball combinations is shown in **Figure 3.11**, where the last compartment was based on UM (Runs 1, and 27–34). In general, the different distributions of the 4 ball sizes (UM, UN, USA) in the first two compartments do not affect product fineness significantly. The impact

of three BSDs in the last compartment, where compartments 1 and 2 were assigned with UM-BSD, was also investigated.

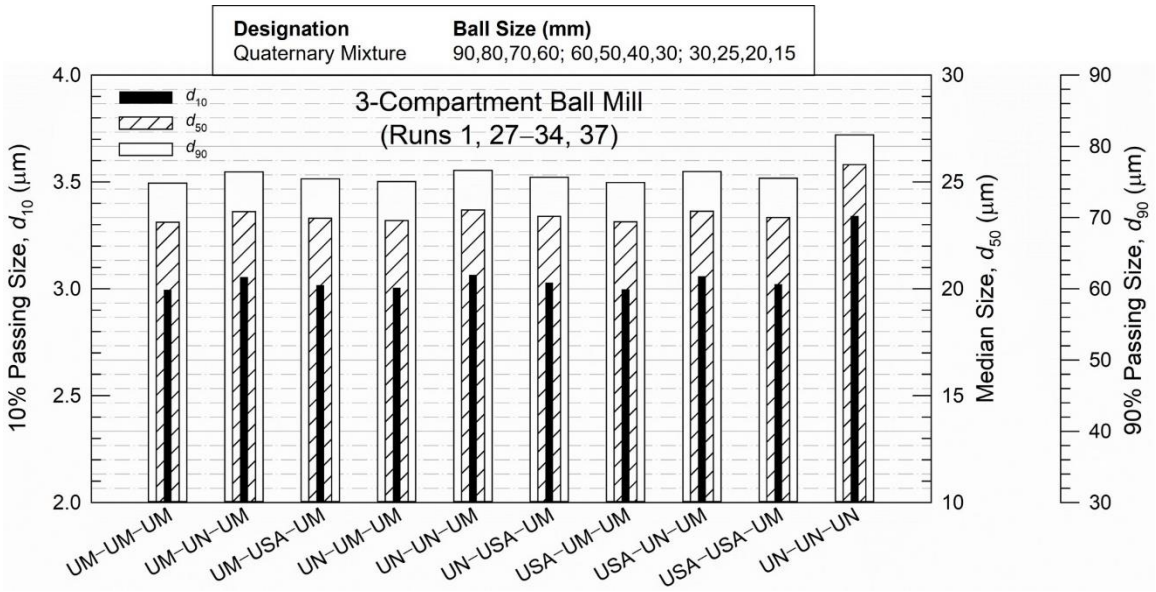

Figure 3.11 Impact of ball size distribution on characteristic particle sizes of the product. Ball size distribution (BSD) in the first two compartments is based on uniform mass (UM), uniform number (UN), and uniform surface area (USA) of the balls, whereas the last compartment is based on UM except Run 37 (UN-BSD). A quaternary ball mixture is used in each compartment.

Simulation results suggest that the combination ending in UM (Run 1) yields the finest product (SSA = 341 m^2/kg), while the BSDs ending in UN (Run 35) and ending in USA (Run 36) yielded SSAs of 320 and 333 m^2/kg, respectively. Among the BSD scenarios (Runs 1, 27–37), the difference in terms of SSA between the best scenario (Run 1: UM–UM–UM, SSA = 341 m^2/kg) and worst scenario (Run 37: UN–UN–UN, SSA = 314 m^2/kg) was ~8%, which could significantly impact cement quality (Troxell et al., 1968). These simulation results agree well with those of past experimental studies (Lynch et al., 2000; Cayirli, 2018), where the higher fraction of the smallest ball yielded a finer

final product. In addition, Katubilwa and Moys (2009) suggested that a full-scale ball mill should be operated with UM-BSD, which in their study is referred to as the original equipment manufacturer recommended BSD.

3.3.5 Ball classification action by classifying liner in fine milling compartment

In the final set of simulations, the impact of ball classification, owing to the presence of a classifying liner along the axial mill length in the last compartment, was investigated in the context of a PBM. Both three- and two-compartment configurations were studied. A classifying liner, which leads to spatially varying balls along the axial length, was used in the last compartment: the third compartment in the three-compartment mill and the second compartment in the two-compartment mill. For both configurations, the maximum and minimum ball sizes of 30 mm and 15 mm, respectively, were used in the compartment fitted with classifying lining plates (see Runs 23 and 24 in **Table 3.2**).

A simple empirical model was developed to describe the mean ball size $d_{\mathrm{B,Mean}}$ as a function of axial location l by fitting it to the ball distribution pattern obtained experimentally by Altun (2018). In this simple analysis, we have not considered the impact of the width of the BSD, mainly because such detailed experimental data were not available. In the simulations, a quaternary ball mixture based on UM was used for all compartments, except the compartment with the classifying liner. The proposed model is given by

$$d_{\mathrm{B,Mean}} = \frac{d_{\mathrm{B,Min}}}{A_3} + \left(\frac{d_{\mathrm{B,Max}}}{A_1} - \frac{d_{\mathrm{B,Min}}}{A_3} \right) \exp\left(-A_2 l\right) \tag{3.10}$$

Here, A_1, A_2, and A_3 are model parameters that characterize the pattern of ball classification, with $d_{B,Max}$ and $d_{B,Min}$ denoting the maximum and minimum ball sizes used in the ball mixture, respectively. The axial location is l, ranging from 0 (inlet of the classifying liner's compartment) to L_F (outlet of the classifying liner's compartment).

Table 3.5 shows the parameters used to predict the mean ball size in the simulations. Indeed, the variation of the mean ball size along the axial position in Altun's study (**Figure 3.12(a)**) and that in the simulations (Runs 23 and 24) was kept similar. The simulations (Runs 23 and 24) were designed for a direct comparison with the case of uniformly mixed balls based on UM-BSD in Runs 25 and 26 for three- and two-compartment mills, respectively, where the last compartment contained binary mixtures of 30 mm and 15 mm balls. When a classifying liner was considered, the mean ball size $d_{B,Mean}$ in the last compartment was calculated for each cell using Equation (3.10). After $d_{B,Mean}$ was calculated, the mass fraction of each ball size at any axial length (cell) was determined, which allowed us to estimate the ball mixture's specific breakage rate parameter via Equation (3.6).

Table 3.5 Estimated Parameters of the Empirical Model, Equation (3.10), that Describe the Ball Classification Pattern Resulting from a Classifying Liner

Source of experimental data and simulation descriptor (Run no.)	Classifying liner's compartment length, L_F (m)	Max. ball size, $d_{B,Max}$ (mm)	Min. ball size, $d_{B,Min}$ (mm)	Parameter in Equation (3.10)		
				A_1 (–)	A_2 (m^{-1})	A_3 (–)
Full-scale ball mill data (Altun, 2018)	8.40	50	17	1.35	0.163	1.11
3-compartment ball mill (Run 23)	4.66	30	15	1.10	0.294	0.899
2-compartment ball mill (Run 24)	6.36	30	15	1.10	0.215	0.899

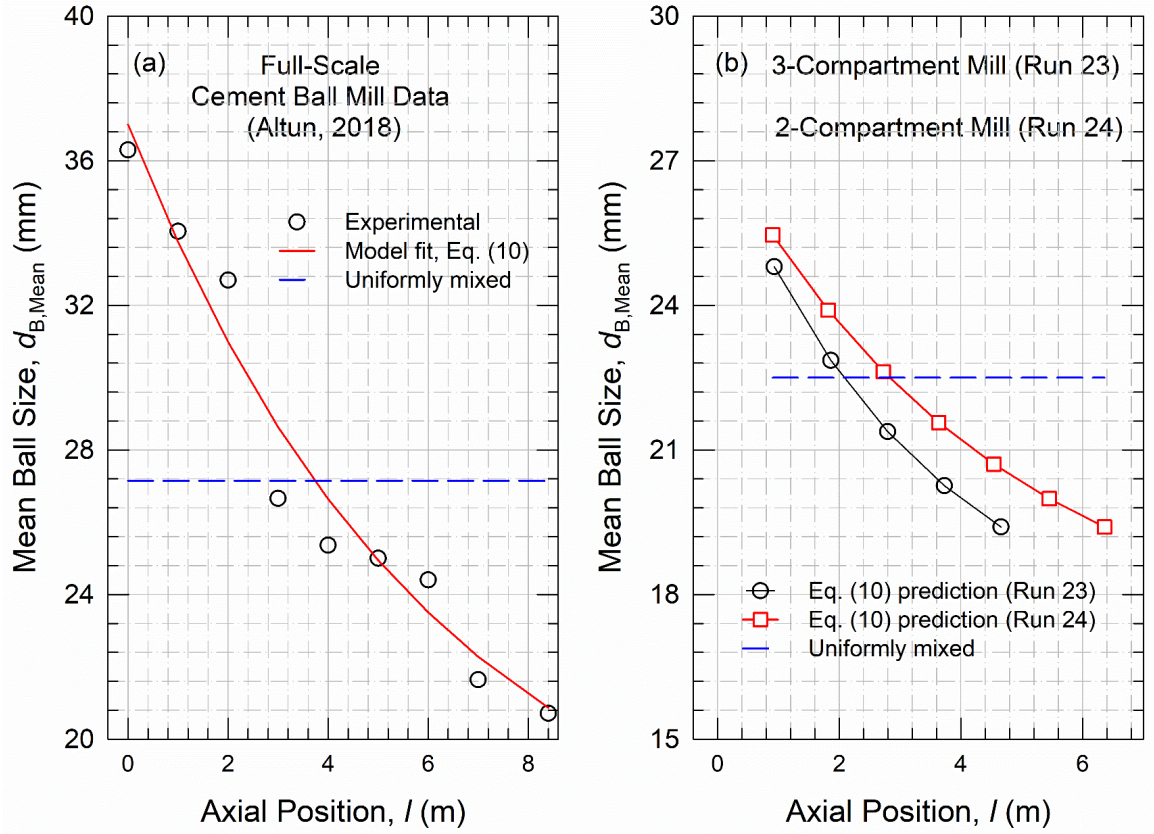

Figure 3.12 Mean ball size variation along the axial position in the compartment with the classifying liner: (a) experimental data and model fit by Equation (3.10) and (b) predicted mean ball size for three- and two-compartment configurations.
Source: Experimental data (Altun, 2018)

As **Figure 3.13** illustrates, the use of the classifying liner (Run 23) increased the product SSA by 1.5% over the SSA of 347 m^2/kg (Run 25) of the uniform BSD based on UM. The same simulation approach was repeated for the two-compartment mill, where the last compartment was modeled with seven cells. **Figure 3.13** also shows that the product SSA increased to 373 m^2/kg with ball classification (Run 24) compared to the SSA of 368 m^2/kg (Run 26) of the uniform BSD. Specifically, product SSA increased by 1.5%. Overall, compared to the spatially uniform distribution of the ball mixture, significant improvement was not observed when using a classifying liner in both three-compartment and two-

compartment mills. These results agree with those in Fortsch (2006), who reported no performance improvement with a classifying liner.

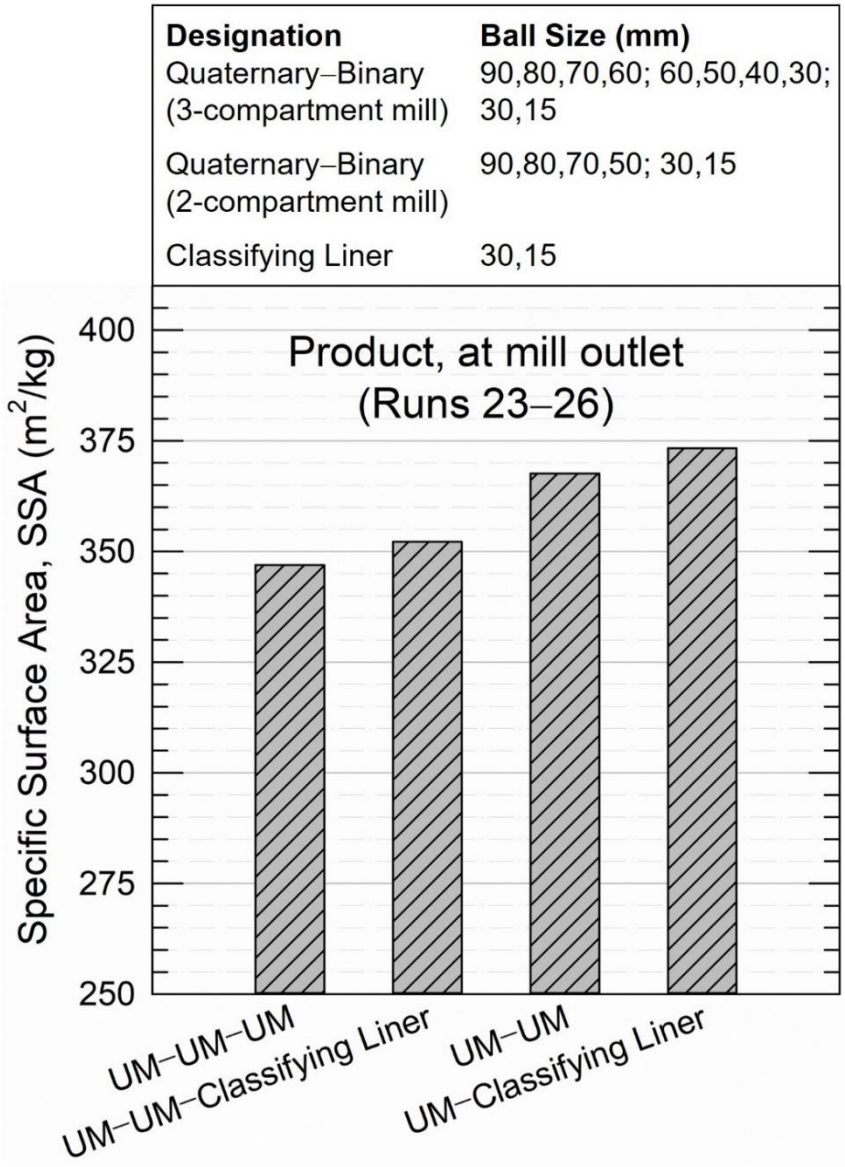

Figure 3.13 Impact of the use of a classifying liner in the last compartment for different compartment numbers (three- vs. two-compartment configurations) on specific surface area (SSA) of the cement product. For the other compartments, the ball size distribution is based on the uniform mass (UM) of balls, and the ball mixture is based on a quaternary ball mixture.

3.3.6 Limitations of TUSSIM and future improvements

Chemical grinding aids help reduce the agglomeration of fine particles in cement ball mills (Sottili and Padovani, 2000). Previous experimental studies (Toprak et al., 2014; Toprak et al., 2020) reported improvements in milling when a grinding aid was used. For example, Toprak et al. (2020) demonstrated that the cement products in a continuous cement ball mill became finer as the dosage of the grinding aid increased. They also reported that the average residence time, which is one of the input parameters of the PBM, decreased with an increase in the dosage of the grinding aid. The current study does not investigate the impact of the grinding aids. In fact, currently, there is no unsteady-state PBM-based simulator that takes into account rheological effects directly. In the future, the impact of grinding aids on the rheology could be simulated when TUSSIM and other simulators integrate the Nomura model (Nomura, 2013; de Oliveira and Tavares, 2018) for modeling of material transport and calibration of relevant parameters. Such coupling will also enable realistic simulation of the impact of fresh feed rates on the open- and closed-circuit operation. Moreover, the impact of grinding aid on internal classification action (and external classification action in the case of closed-circuit operation) must be described by the respective classification functions. Besides the rheological effects of the grinding aids, TUSSIM does not currently consider the breakage of multicomponent mixtures, temperature effects on milling, media wear as well as power consumption–energy expenditures.

3.4 Conclusions

In this study, the recently developed TUSSIM, an unsteady-state PBM-based simulator with a DAE solver, was utilized to model full-scale continuous cement ball milling in an open-circuit operation. The simulations of the spatio-temporal variation of PSD in a three-compartment ball mill with a typical quaternary ball mixture demonstrated the attainment of a steady-state operation and acceptable range of cement particle size. The simulation results with TUSSIM rationalized various practices in the cement industry; and they are also supported by past experimental studies on dry ball milling, giving credence to TUSSIM as a simulation tool. The main conclusions are as follows:

- The use of a single ball size is not desirable: A large single ball size leads to unsatisfactory cement size, while a small single ball size leads to the accumulation of unbroken coarse particles, thus preventing the attainment of a feasible steady-state operation.

- For a natural feed PSD, a mixture of ball sizes produces a finer product than a single ball size in a single-compartment mill; however, the cement product is still coarser than standard, desirable cement size.

- Pre-milling of the feed is required to attain a steady-state operation in a single-compartment mill to produce desirable cement products with acceptable fineness.

- While an increase in the number of compartments from one to two yields a significantly finer product and obviates the need for pre-milling of the feed, switching to a three-compartment mill has diminished value. Both two-compartment and three-compartment mills could perform similarly depending on the ball sizes selected. The difference between these configurations is likely due to differences in the ball sizes and their distribution as well as the internal classification of the diaphragms.

- In a ball mixture, an increase in the fraction of smaller balls, especially in the last compartment, yields a higher product fineness.

- For a quaternary mixture, UM/USA/UN distributions of ball sizes in the first two compartment do not affect product PSD significantly, while those in the third compartment have a notable impact on the product PSD.

- The binary ball mixture yields a finer product than the ternary and quaternary mixtures, but it may not be practical for use when the ball wear rate is considered.

- The use of a classifying liner results in spatially varying BSD and yields a negligibly finer product (approximately 1.5%) in comparison with the spatially uniform BSD in the last compartment.

TUSSIM can help engineers to optimize the existing, specific full-scale open-circuit continuous ball mills besides providing various processing insights. For example, TUSSIM can be coupled to a global optimizer to determine the composition of various ball sizes in each compartment of multi-compartment ball mills for a given feed PSD and desired cement product fineness.

CHAPTER 4

MODELING OF CLOSED-CIRCUIT BALL MILLING OF CEMENT CLINKER VIA A PBM WITH A VARIABLE TROMP CURVE FOR CLASSIFICATION

Full-scale closed-circuit cement ball milling was modeled using a true unsteady-state simulator (TUSSIM), based on a transient cell-based population balance model (PBM) with a set of differential algebraic equations (DAEs). As a major novelty, the PBM for the mill was coupled with a dust load-dependent, variable Tromp curve for the air classifier. Results from the dynamic simulations suggest that lower air flow rate or higher rotor speed of the classifier not only led to a finer product but also increased the dust load of the classifier feed. When the dust load was too high, operational failure due to overloading of the whole circuit was detected. Finally, TUSSIM was used for process optimization with a global optimizer–DAE solver to identify the air classifier's parameters that yielded desirable cement quality while maximizing production rate. We have demonstrated that the optimization could increase production rate by 7% compared to the baseline process.

4.1 Introduction

Improving the performance of a closed-circuit ball mill for cement milling, where a tumbling ball mill is integrated with a dynamic air classifier, is a complicated task because of the fully coupled interplay between the two unit operations. In cement plants, process parameters are usually set based on operators' experience gained from trial and error, along with suggestions from credible engineering companies (FLSmidth, 2012; Shimoide, 2016). It seems that the existing knowhow largely resides within the expertise of the engineering companies, the equipment vendors, and the cement manufactures. Such knowhow is not

easily accessible in the public domain, or the limited information shared does not allow for reproducibility (e.g., Fernandez and Hui (2017)). Even an empirical understanding of the impact of process–design parameters of a full-scale continuous ball mill on product quality attributes entails performing well-controlled, scientific experiments that are quite laborious, expensive, time-consuming, and sometimes infeasible (Muanpaopong et al., 2022b). In general, without thorough process understanding, trial and error must be repeatedly performed with changes in the operating conditions. In view of these considerations, a credible population balance model (PBM) and computer simulations could yield fundamental insights about the process and ultimately provide operational guidance for process optimization (Napier-Munn et al., 1996; Muanpaopong et al., 2022a; Muanpaopong et al., 2022b).

Closed-circuit ball mills have been operated for cement milling for decades (Austin et al., 1975; Brugan, 1988; Yardi, 2005). **Figure 4.1** shows the process flow of a closed-circuit, two-compartment cement ball mill. The closed-circuit operation helped to reduce overmilling of particles (Duda, 1985), resulting in lower specific power consumption (Genc, 2008) in comparison with open-circuit operation, where the ball mill is operated without the external air classifier. For the sake of brevity, only a brief introduction to the operation and key parts of the dynamic air classifier are described here, while the detailed operational aspects of the ball mill can be found elsewhere (Labahn and Kohlhaas, 1983; Duda, 1985). The dynamic air classifier is specifically referred to as a cage wheel classifier with guide vanes, also known as the third-generation high-efficiency air classifier. An air classifier continuously receives milled particles discharged from the ball mill. The air flow generated by an external fan pulls particles through guide vanes and a rotating cage (rotor),

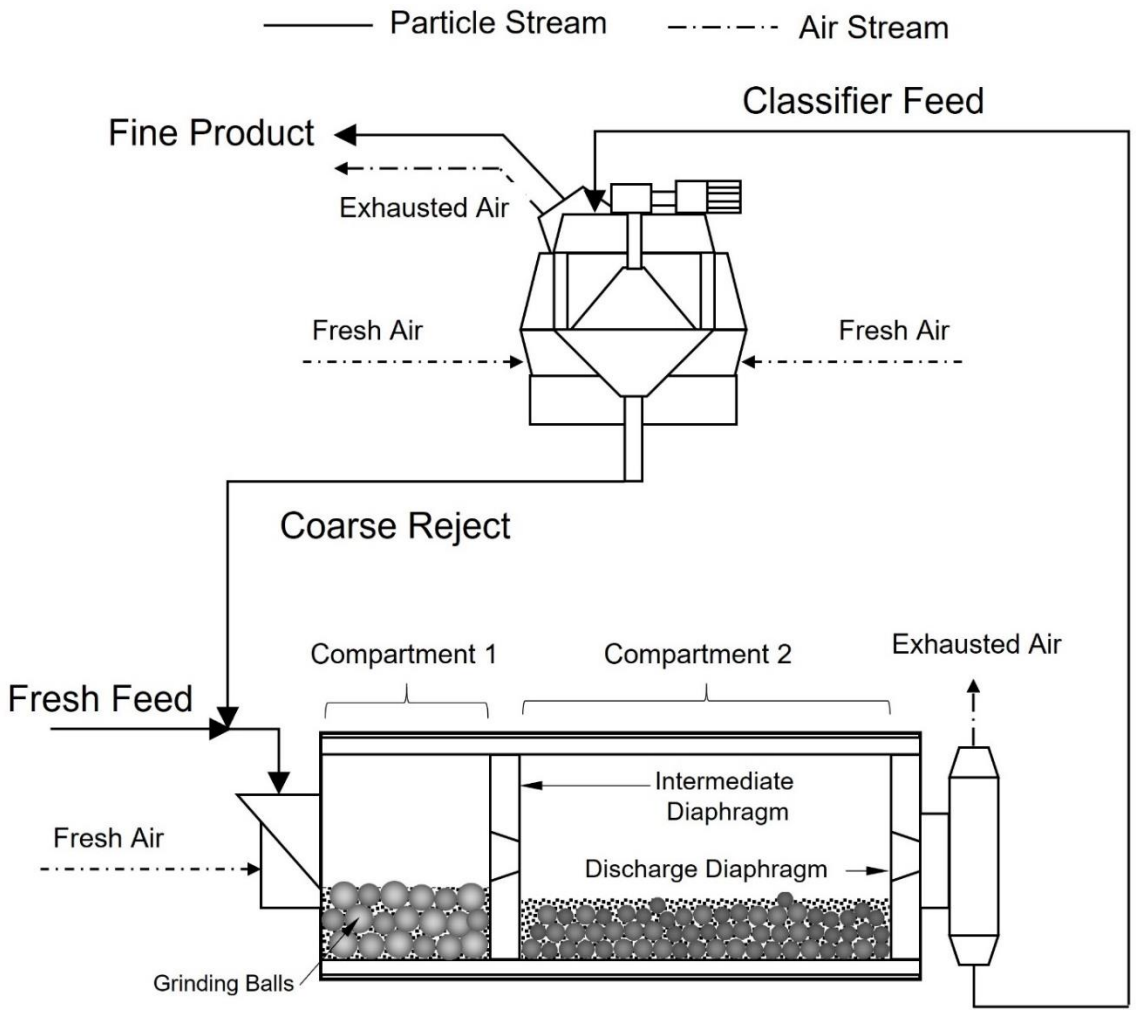

Figure 4.1 Sketch of a two-compartment continuous ball mill integrated with an air classifier in a closed-circuit operation.

where the classification of particles takes place. Fine particles passing through the rotor are collected by the dust collector as the final product, whereas coarse particles are rejected and recycled back to the ball mill for further milling. The balance between the centrifugal force acting on the particles and the drag force imposed by air determines the cut size of classification (Sander and Droop, 2019). Hence, during air classification, product fineness can be changed by adjusting the air flow rate (Yardi, 2005; Altun and Benzer, 2014) and the rotor speed (Brugan, 1988; Yardi, 2005; Altun and Benzer, 2014).

Air classification performance can be described by a Tromp curve (Brugan, 1988), a.k.a. the selectivity curve (Austin and Klimpel, 1981; Klumpar, 1992). The Tromp curve represents the fraction of particles in the classifier feed that reports to the coarse reject stream. Analysis of the Tromp curve provides information about the particle classification, such as bypass fraction (Brugan, 1988; Klumpar, 1992; Onuma, 1995), wherein classification does not take place (Klumpar, 1992), and sharpness of classification (Klumpar, 1992; Onuma, 1995). Ample experimental data on full-scale closed-circuit cement ball mills reported by Altun and Benzer (2014) indicated that classification performance worsened when an air classifier had to deal with a higher dust load of classifier feed, defined as the ratio of the mass flow rate in the classifier feed stream to the air flow rate.

Tromp curve models can be broadly categorized into (i) a fixed Tromp curve model (e.g., Altun, 2018; Lynch et al., 2000; Boulvin et al., 2003; Huusom et al., 2005; Farzanegan et al., 2014) and (ii) a variable Tromp curve model (Zhang et al., 1988; Benzer et al., 2001a; Altun and Benzer, 2014). A fixed Tromp curve is typically developed for a standard set of operational parameters of the closed-circuit ball mill at the steady-state; hence, it has fixed parameters. Unlike the fixed Tromp curve, model parameters of the variable Tromp curve are correlated with a wide variety of the operational parameters of the air classifier at steady state. Therefore, it is capable of capturing the impact of variable dust load of the classifier feed (or mass flow rate fed to the classifier) on classification performance. In this paper, the variable Tromp curve specifically refers to the Altun and Benzer model (2014). Their model parameters characterizing air classification performance are explicitly connected to the operational parameters and dust load. It is

superior to earlier models (Zhang et al., 1988; Benzer et al., 2001a) that assume the invariance of the classification parameters such as the sharpness parameter with the operation parameters.

PBM has been used to simulate the evolution of particle size distribution (PSD) during milling (Austin, 1971/1972). A majority of PBM studies in the context of full-scale cement ball mills have considered only *steady-state operation* (Austin et al., 1975; Zhang et al., 1988; Genc, 2008; Dundar et al., 2011; Farzanegan et al., 2014; Altun, 2018), while only a few research groups have developed an elaborate unsteady-state PBM (Boulvin et al., 2003; Huusom et al., 2005; Muanpaopong et al., 2022b). The latter group performed a perturbation analysis (Boulvin et al., 2003; Huusom et al., 2005) and elucidated the evolution of the PSD and mass hold-up to attain steady state (Muanpaopong et al., 2022b), which could also be useful for process control. All PBM simulations for closed-circuit cement ball mills have used the *fixed Tromp curve*. Although fitting a PBM incorporating a fixed Tromp curve for the external air classification could provide good fitting results (Farzanegan et al., 2014; Altun, 2018), such a coupled PBM offers little to no predictive capability. When such a PBM is used either for a different set of operating conditions within the context of optimization or for simulation of the transient operation, it would give erroneous predictions because whenever dust loading and feed rate vary, the classification performance would vary, but the fixed Tromp is not able to capture these effects. Based on the literature review, and to the best of our knowledge, an unsteady-state PBM for continuous ball milling has never been coupled with a *variable Tromp curve* (Altun and Benzer, 2014) for simulating the closed-circuit ball mill operation and its optimization.

One of the ultimate goals of any modeling study is to develop fundamental process insights and reliable simulation capability to optimize existing milling operations, thus helping industry practitioners. In the dry milling literature, studies focusing on process optimization using a PBM with an optimization algorithm have been limited (Austin et al., 1975; Kis et al., 2005). For example, an unsteady-state convective dispersion PBM was augmented with a *fixed Tromp curve* to simulate (Kis et al., 2002; Kis et al., 2005) and optimize (Kis et al., 2005) a closed-circuit continuous mill. Although their model is mathematically rigorous and numerically correct simulations are presented, the model is for a generic continuous mill that has low fidelity to closed-circuit ball milling. They used a power-law specific breakage rate function for ball milling, disregarded internal classification in the ball mill, and used a jump function for the external classification. All these choices for the specific functional forms of the PBM are not applicable to dry ball milling and internal–external classification. As importantly, no realistic model parameter was used because the simulations did not consider a specific material. Their optimization did not suggest how adjustable operation parameters should be set to achieve the optimal conditions, which is a barrier for practitioners in optimizing actual ball mills. A similar issue was found in optimization work using the steady-state PBM with a fixed classification function (Austin et al., 1975). The cut size of the air classifier was used as the variable of optimization; however, it is unclear how this cut size would translate into manipulated variables such as the rotor speed and the air flow rate of the air classifier. It is important to mention that previous studies (Austin et al., 1975; Kis et al., 2005) that focused on the optimization of the closed-circuit ball milling disregarded the variable nature of the Tromp curve. Therefore, in the context of PBM, there is a need to develop a process optimization

scheme with an explicit connection between model parameters and process operation parameters that allows one to achieve the targeted product size, improve product quality, and maximize the production rate of the circuit by changing the operation parameters.

The aim of this theoretical study is to better understand the complex interplay between ball milling and air classification in full-scale two-compartment ball mills for cement clinker milling. To this end, we modified the true unsteady-state simulator (TUSSIM) for a full-scale open-circuit cement ball mill (Muanpaopong et al., 2022b) by coupling the PBM for the mill with a *variable Tromp curve* for the air classifier (Altun and Benzer, 2014). The cell-based PBM for the mill can address realistic mixedness degree of particles and internal classification caused by possible accumulation of coarse particles due to presence of diaphragms (refer to **Figure 4.1**) (Muanpaopong et al., 2022a; Muanpaopong et al., 2022b). The combined ball mill–air classifier model, consisting of a set of differential algebraic equations (DAEs), poses a challenging numerical problem as the variable Tromp curve increases the degree of two-way coupling and the nonlinearity. The model parameters were obtained from the relevant experimental cement milling literature. To justify the simulation approach along with selected model parameters, simulation of a baseline process was performed to investigate whether the evolution of PSD in the circuit could attain a steady state and provide a realistic cement PSD. Other metrics, such as the PSDs around the air classifier and characteristic information of the Tromp curve at steady state, were also examined. Subsequently, the impacts of the air flow rate and rotor tip speed on the PSD and mass flow rate in the circuit, as well as the Tromp curve, were examined. Yet another novel contribution of this work is that process optimization using a combined global optimizer–DAE solver was implemented. This approach, despite its computational

burden and complexity, enables identification of optimal circuit operation by considering the quality attributes of the cement product and the production rate simultaneously.

4.2 Theoretical

4.2.1 Model description

A recently developed process simulator, TUSSIM, for a full-scale cement ball mill (Muanpaopong et al., 2022b) was augmented with a variable Tromp curve model (Altun and Benzer, 2014) for simulating closed-circuit ball milling. For the sake of brevity, only key aspects of the model are described here. The readers are referred to (Muanpaopong et al., 2022a) for derivation of the cell-based PBM within TUSSIM (Muanpaopong et al., 2022a). Briefly, TUSSIM is based on the solution of a cell-based PBM; the mixedness degree of particles in the ball mill is modulated by two dimensionless parameters: number of cells n and axial back-mixing ratio R, defined as the ratio of the axial recirculation rate $\dot{R}$ between adjacent cells to the mass flow rate through the cell. Values of n = 10 and R = 8.01×10^{-3} were taken from (Muanpaopong et al., 2022b), where the residence time distribution data on the full-scale two-compartment cement ball mill reported in Austin et al. (1975) were fitted by a cell-based PBM without breakage terms. **Figure 4.2** shows the schematic of the mill model with compartments 1 and 2 consisting of 3 and 7 cells, respectively. The number of cells for each milling compartment was estimated according to the ratio of the individual compartment length to the mill length (Gelpe et al., 1985; Muanpaopong et al., 2022b).

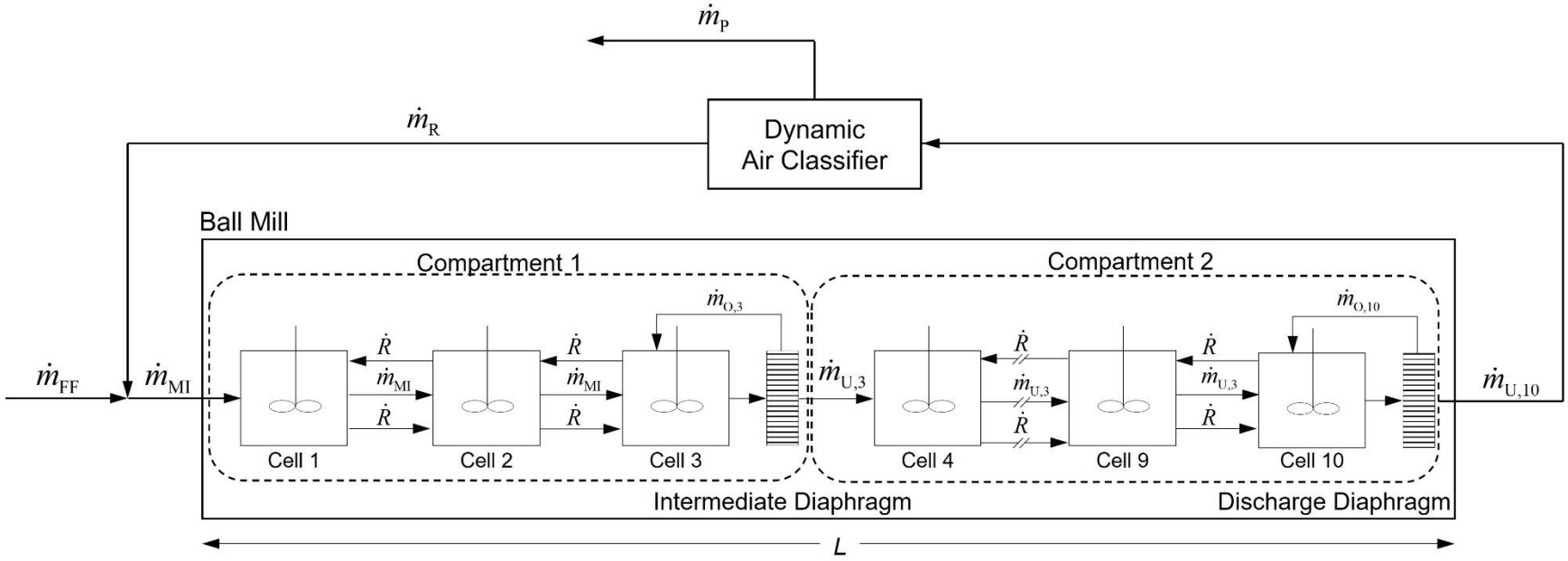

Figure 4.2 Schematic model of a continuous ball mill of length L, with two diaphragms, represented by 10 perfect mixing cells in series. The axial recirculation rate $\dot{R}$ is exchanged between adjacent cells. The coarse particles rejected from the dynamic air classifier is returned to the mill, whereas the fines are taken as the product.

The size-discrete time-continuous form of a cell-based PBM for $n = 10$ is expressed by the following equation:

$$\frac{dm_{i,z}}{dt} = \begin{cases} -S_{i,z}m_{i,z} + \sum_{j=1}^{i-1} b_{i,j}S_{j,z}m_{j,z} \\ +\dot{m}_{\mathrm{MI},i} + \left[Rm_{i,z+1} - (1+R)m_{i,z} \right]\tau_z^{-1} & \text{for } z = 1 \\ -S_{i,z}m_{i,z} + \sum_{j=1}^{i-1} b_{i,j}S_{j,z}m_{j,z} \\ +\left[(1+R)m_{i,z-1} - (1+2R)m_{i,z} + Rm_{i,z+1} \right]\tau_z^{-1} & \text{for } z = 2,5-9 \\ -S_{i,z}m_{i,z} + \sum_{j=1}^{i-1} b_{i,j}S_{j,z}m_{j,z} \\ +\left[(1+R)m_{i,z-1} - Rm_{i,z} \right]\tau_z^{-1} - \dot{m}_{\mathrm{U},i,z} & \text{for } z = 3,10 \\ -S_{i,z}m_{i,z} + \sum_{j=1}^{i-1} b_{i,j}S_{j,z}m_{j,z} \\ +\dot{m}_{\mathrm{U},i,z-1} + \left[Rm_{i,z+1} - (1+R)m_{i,z} \right]\tau_z^{-1} & \text{for } z = 4 \end{cases} \tag{4.1}$$

$m_{i,z}(0) = 0$ with $i, j = 1, 2, \ldots, N$. In Equation (4.1), i and j are size class indices extending from size class 1 containing the coarsest particles of size x_1 to size class N containing the finest particles of size x_N with geometric progression. t is the milling time. $m_{i,z}$ is the mass of particles in size class i in cell z, ranging from cell 1 (ball mill inlet) to cell n (ball mill outlet). $S_{i,z}$ is the specific breakage rate parameter of particle size x_i in cell z. $b_{i,j}$ is breakage distribution parameter with its cumulative counterpart $B_{i,j}$. The constraints in Equation (4.2) were applied to satisfy mass conservation:

$$S_{N,z} = 0, \quad \sum_{i=j+1}^{N} b_{i,j} = 1, \quad b_{i,i} = 0 \tag{4.2}$$

The mass flow rate of particles in size class *i* feeding the ball mill inlet is denoted by $\dot{m}_{\mathrm{MI},i}$. Based on a mass balance, it is calculated from $\dot{m}_{\mathrm{MI},i} = \dot{m}_{\mathrm{FF},i} + \dot{m}_{\mathrm{R},i}$, where $\dot{m}_{\mathrm{FF},i}$ and $\dot{m}_{\mathrm{R},i}$ are the mass flow rates of particles in size class *i* in the fresh feed stream and the coarse reject stream, respectively. The mass flow rate of particles in size class *i* passing through the diaphragm connected to cell *z* =3 and 10 is denoted by $\dot{m}_{\mathrm{U},i,z}$. In correlation with the value of the Tromp curve value T_i for size class *i*, the mass flow rate of particles in size class *i* in the coarse reject stream $\dot{m}_{\mathrm{R},i}$ and fine product stream $\dot{m}_{\mathrm{P},i}$ can be determined by $\dot{m}_{\mathrm{R},i} = \dot{m}_{\mathrm{U},i,10} T_i$ and $\dot{m}_{\mathrm{P},i} = \dot{m}_{\mathrm{U},i,10}(1-T_i)$, respectively.

The average residence time in cell *z* (τ_z), defined as the ratio of the mass in cell *z* ($m_{\mathrm{H},z}$) to the total mass flow rate through that cell, i.e., $\tau_z = m_{\mathrm{H},z} \Big/ \sum_{i=1}^{N} \dot{m}_{\mathrm{MI},i}$, can be determined from $\tau_z = \tau/n$. Here, τ is the average residence time in the mill without considering the accumulation of coarse particles due to diaphragms, and it was taken from Austin et al. (1975) as τ = 14 min. When the possible accumulation of particles in cells connected to the diaphragms, i.e., cells *z* = 3 and 10, is considered, the definition of τ_z for these cells is defined by the following expression (King, 2001):

$$\tau_z = m_{\mathrm{H},z} \left(\sum_{i=1}^{N} \dot{m}_{\mathrm{MI},i} + \sum_{i=1}^{N} \dot{m}_{\mathrm{O},i,z} \right)^{-1} \tag{4.3}$$

Here, $\dot{m}_{\mathrm{O},i,z}$ is the mass flow rate of particles in size class *i* of cell *z* that does not pass through the diaphragm, and it was calculated using the following equation:

$$\dot{m}_{\mathrm{O},i,z} = \left(1 - P_i\right) m_{i,z} / \tau_z \tag{4.4}$$

where $0 \leq P_i \leq 1$ is the fraction of particles in size class i passing through the diaphragm. It is important to mention that $\dot{m}_{\mathrm{R},i}$ and $\dot{m}_{\mathrm{O},i,z}$ are time-dependent, and they are unknown during a transient operation. Therefore, Equations (4.3) and (4.4) must be solved simultaneously with Equation (4.1), which forms a set of DAEs. A steady state was deemed to be attained when the sum of the absolute difference between the cumulative PSDs of subsequent time steps for all N size classes was equal to or less than 10^{-2} (Muanpaopong et al., 2022b). Cumulative PSDs in each stream around the air classifier (classifier feed, fine product, and coarse reject streams) and inside the ball mill (cells 3 and 10) must satisfy this criterion for the steady state. Readers are referred to Appendix C.1 for size discretization and details of the PBM simulations.

4.2.2 Specific functional forms and model parameters used in the PBM

This theoretical study did not attempt to model a specific cement ball mill; therefore, the model parameters for simulations were taken from available and relevant cement milling studies. For the referenced full-scale cement mill, operation data (e.g., ball size distribution) and mill dimensions were taken from Altun (2018) because they reported sufficient operation data and model parameters for the internal classification of the diaphragm. Briefly, the ball mill consists of two compartments, with a mill length L of 12.3 m. Ball sizes of 60–90 mm and 17–50 mm were used in the first and second compartments, respectively. The fresh feed rate $\dot{m}_{\mathrm{FF}}$ was 1723 kg/min. Readers are referred to Appendix C.2 for all details of the referenced full-scale mill (Altun, 2018).

4.2.2.1 Breakage kinetics model of ball milling. Altun (2018) directly fitted the PBM with the perfect mixing assumption along with a discharge function (Whiten, 1974) to the actual industrial-scale data, which is a common practice for cement milling simulations (Lynch et al., 2000; Benzer et al., 2001a; Dundar et al., 2011). Only the operation-dependent lump parameter, i.e., the ratio of the specific breakage rate to the discharge rate from the mill was reported. In other words, breakage parameters (S_i and $B_{i,j}$) were not calculated separately. For this reason, the breakage kinetic parameters for the ball milling of cement clinker were obtained from small-scale ball milling of cement clinker (Deniz, 2003; Dave et al., 2022; Muanpaopong et al., 2023). We applied the Austin's celebrated and well-established scale-up rules (Austin et al., 1984), to scale up S_i obtained from a laboratory ball mill to the full-scale ball mill considered in Section 2.2 (similar to Muanpaopong et al. (2022b)). It is well-known that S_i varies significantly with the operation conditions (Austin et al., 1984; de Carvalho and Tavares, 2013) and mill size (Rogers et al., 1986). The methodology to represent the full-scale S_i was taken from Bilgili (2023): S_i obtained from a lab-scale ball mill using the Kotake–Kanda (KK) model (Bilgili, 2023) was scaled up by the Austin scale-up factors K_1, K_2, K_3, and K_4 (Austin et al., 1984) to represent S_i of industrial-scale ball mills, as expressed by the following equation:

$$S_{i,z} = C_1 d_{\mathrm{B},z}^{C_3} x_i^{C_4} \exp\left(-C_2 \frac{x_i}{K_1 d_{\mathrm{B},z}^{C_5}} \right) K_2 K_3 K_4 \tag{4.5}$$

In Equation (4.5), $d_{\mathrm{B},z}$ is a single ball size represented by its ball diameter in cell z. Since our approach does not consider the breakage of multicomponent mixtures, it was

assumed that breakage parameters for cement milling were based solely on cement clinker (similar to Austin et al. (1975)). Note that cement clinker is the main component of ordinary Portland cement (Vuk et al., 2001; Zhang, 2011). For the lab-scale ball milling of the cement clinker, the model parameters C_1, C_2, C_3, C_4, and C_5 in the KK model were taken from Deniz (2003) as 12.86 $\text{mm}^{-0.274}$/min, 50 $\text{mm}^{0.217}$, –0.736, 1.01, and 1.217, respectively. All details of the lab-scale ball mill (Deniz, 2003) and its scale-up can be found in Appendix C.2.

The specific breakage rate parameter in Equation (4.5) applies to a single ball size. When the ball mill is operated with a mixture of different ball sizes, which is the prevalent industry practice, the specific breakage rate parameter $S_{i,z}$ is replaced by $\bar{S}_{i,z}$. The latter is determined by the weighted average of individual $S_{i,z,g}$ of single ball sizes, indexed by g ranging from 1 to G, with their corresponding ball mass fractions $M_{\text{B},g}$ (Austin et al., 1976) as follows:

$$\bar{S}_{i,z} = \sum_{g=1}^{G} M_{\text{B},g} S_{i,z,g} \tag{4.6}$$

Unlike the specific breakage rate parameter, the cumulative breakage distribution parameter $B_{i,j}$ was assumed to be invariant to the operating conditions (similar to Chimwani et al. (2014)). The normalized, single-term $B_{i,j}$ expressed in Equation (4.7) with breakage distribution exponent $\mu = 8.097 \times 10^{-1}$ was used to simulate cement clinker milling in a ball mill (Dave et al., 2022; Muanpaopong et al., 2023).

$$B_{i,j} = \left(\frac{x_{i-1}}{x_j} \right)^{\mu} \tag{4.7}$$

Using Equation (4.7), $b_{i,j}$ can be determined from B_{ij} through $b_{i,j} = B_{i,j} - B_{i+1,j}$.

4.2.2.2 External particle classification model of the air classifier. Among the available models for particle classification (Austin and Klimpel, 1981; Finch, 1983; Zhang et al., 1988; Napier-Munn et al., 1996), the Whiten model (Napier-Munn et al., 1996) has been widely used in cement milling simulations (e.g., Altun and Benzer, 2014; Altun, 2018) to represent external classification action due to the dynamic air classifier. The Whiten model can be written in the form of a variable Tromp curve (Altun and Benzer, 2014), as expressed by the following equation:

$$T_i = 1 - (1 - \delta_a) \left(1 + \beta_a \beta_a^* \frac{x_i}{x_{50c,a}} \right) \left[\exp(\alpha_a) - 1 \right] \left\{ \exp\left(\alpha_a \beta_a^* \frac{x_i}{x_{50c,a}} \right) + \exp(\alpha_a) - 2 \right\}^{-1} \tag{4.8}$$

where α_a is sharpness parameter, β_a is fish-hook parameter, δ_a is bypass parameter, and $x_{50c,a}$ is corrected cut size. β_a^* is a parameter that preserves the definition of $x_{50c,a}$. Model parameters α_a, β_a, δ_a, and $x_{50c,a}$ were correlated to the air classifier's operational parameters (i.e., rotor tip speed v and air flow rate Q), the classifier's chamber diameter D_c, ball mill performance (i.e., mass flow rate of classifier feed at 3–36 μm range F_{CF}), and particle dust loading of the classifier feed (DL_{CF}) (Altun and Benzer, 2014). Using the Tromp curve approach, classification performance can be evaluated by bypass fraction δ^* and sharpness of classification κ. The former parameter is defined as the minimum value of the Tromp

curve (Klumpar, 1992) and the latter one is defined as the ratio of x_i at T_i = 0.25 to x_i at T_i = 0.75 (Klumpar, 1992). The ideal classification corresponds to $\delta^* = 0$ and $\kappa = 1$. Readers are referred to Appendix C.3 for the details of the variable Tromp curve model taken from Altun and Benzer (2014). Note from Equations (C.3) and (C.4) that α_a, β_a, δ_a, and $x_{50c,a}$ vary with DL_{CF}, F_{CF}, v, and Q; hence, our PBM with the variable Tromp curve is capable of predicting the transient behavior of the circuit and enabling process optimization based on classifier parameters.

An operation setting with a higher air flow rate may require a larger air classifier size (Altun and Benzer, 2014). The air classifier's chamber diameter (D_c) affects a variable Tromp curve via sharpness parameter α_a. For this reason, we formulated the following step function to determine D_c for each interval value of Q based on data available from the air classifier manufacturer (FLSmidth, 2021).

$$D_c = \begin{cases} 3.55 \text{ m if } Q \le 135700 \text{ m}^3/\text{h} \\ 3.75 \text{ m if } 135700 < Q \le 154400 \text{ m}^3/\text{h} \\ 4.00 \text{ m if } 154400 < Q \le 179600 \text{ m}^3/\text{h} \\ 4.25 \text{ m if } 179600 < Q \le 206600 \text{ m}^3/\text{h} \end{cases} \tag{4.9}$$

4.2.2.3 Internal particle classification model of diaphragms. The Whiten model has also been used to model the internal classification action caused by diaphragms (Ozer et al., 2006; Farzanegan et al., 2014; Altun, 2018). The fraction of particles in size class i passing through diaphragm P_i is expressed by the following equation:

$$P_i = \left(1-\delta_{\mathrm{d}}\right)\left(1+\beta_{\mathrm{d}}\beta_{\mathrm{d}}^{*}\frac{x_i}{x_{50\mathrm{c,d}}}\right)\left[\exp\left(\alpha_{\mathrm{d}}\right)-1\right]\left\{\exp\left(\alpha_{\mathrm{d}}\beta_{\mathrm{d}}^{*}\frac{x_i}{x_{50\mathrm{c,d}}}\right)+\exp\left(\alpha_{\mathrm{d}}\right)-2\right\}^{-1} \quad (4.10)$$

The model parameters for the internal classification were taken from Altun (2018). Specifically, the parameters were as follows: sharpness parameter α_{d} = 0.1, fish-hook parameter β_{d} = 0.1, bypass parameter δ_{d} = 0.05, the corrected cut size $x_{50\mathrm{c,d}}$ = 0.5 mm, and the parameter β_{d}^{*} = 1.23. It was assumed that the internal classification actions for the intermediate diaphragm and the discharge diaphragm were identical and invariant to the mass flow rate through the diaphragms.

4.2.3 Process optimization

Our objective was to identify the operation conditions of the air classifier to yield desirable cement quality with a maximum production rate. Therefore, air flow rate Q, rotor tip speed v, and fresh feed rate $\dot{m}_{\mathrm{FF}}$ were variables of optimization. Unlike the earlier optimization studies, where variables of optimization cannot be directly manipulated (Austin et al., 1975; Kis et al., 2005), these variables can be directly manipulated in an actual milling plant. Rather than controlling the full PSD of cement products, mill operators have practically adjusted cement quality based on cement Blaine surface area (Touil et al., 2008), as measured by the Blaine air-permeability apparatus (ASTM C-204, 2019). An approximation of Blaine surface area f_{B} is referred to in Appendix C.4. It is well established that the PSD of the cement product also affects the development of compressive strength (Tsivilis et al., 1990; Tsakalakis and Stamboltzis, 2008; Celik, 2009). For example, Tsivilis et al. (1990) showed that, at the same cement Baine fineness, a higher mass fraction of 3–32 μm ($M_{3\text{–}32}$) of cement led to higher 28-day cement strength. A similar observation

was made in Celik (2009). Considering the factors impacting the cement quality, i.e., f_B and M_{3-32}, and the operational aspects, the following objective function (OF) was formulated for process optimization (minimization):

$$\mathrm{OF} = w_1 \left| f_B^{\mathrm{Mod}} - f_B^{\mathrm{Tar}} \right| + w_2 \left| 1 - M_{3-32}^{\mathrm{Mod}} \right| + w_3 / \dot{m}_{\mathrm{FF}} \tag{4.11}$$

Here, the weighting factors w_1 = 1 g/cm^2, w_2 = 1, and w_3 = 1000 kg/min were set to properly scale the impact of each of the three terms on the objective function value. Superscripts Mod and Tar refer to the model predicted value at the steady state and the targeted value, respectively. The first term on the right-hand side is to minimize the difference in Blaine surface area between the model prediction at steady state and the targeted value f_B^{Tar} of the cement product. The second and the last terms are introduced to achieve maximal values of the cement product's mass fraction of 3–32 μm in size and production rate at the steady state, respectively. Another important point to mention is that we assumed that the mass hold-up at the steady state was invariant to the fresh feed rate (Austin et al., 1975). Nomura's transport model (Nomura, 2013; de Oliveira and Tavares, 2018) correlates feed rate with the mass hold-up, and it could be integrated with TUSSIM and other simulators in the future. However, its model parameters must be obtained by fitting to mass holdup data, and such information is not available for the full-scale cement ball mills (Nomura, 2020).

The OF in Equation (4.11) was minimized using a coupled global optimizer–DAE solver. Although a global optimization scheme in MATLAB (The MathWorks, 2022) was employed, it did not guarantee that the global minimum of objective function could be

obtained. This approach required the number of trial points N_T as one of the inputs, affecting the solutions obtained from the optimizer. Our previous studies (Dave et al., 2022; Muanpaopong et al., 2023) demonstrated that a global minimum could be attained at a sufficiently high N_T value. Therefore, we performed process optimization with three variables (Q, v, and $\dot{m}_{FF}$) for various N_T values to determine whether an N_T-independent solution could be obtained from the optimizer. Solution was deemed to be N_T-independent when the percent relative error of each variable and objective function value between two subsequent N_T values was less than or equal to 10^{-1}. Such a solution was deemed to be the global minimum within the context of this study. Readers are referred to Appendix C.1 for all the details of the process optimization, including the functions used and the tolerances set.

Table 4.1 Design of a Full-factorial Simulation Study on the Impact of Rotor Tip Speed v and Air flow Rate of Q on the Steady-state Values of Mass Flow Rate of the Reject Stream $\dot{m}_R$, Dust Load of the Classifier Feed DL_{CF}, Blaine Surface Area of the Product f_B, Bypass Fraction δ^*, Sharpness of Classification κ, and Cut Size x_{50a}

Run no.	Air classifier operation			Simulation result at the steady state					
	v (m/s)	Q (m^3/h)	D_c (m)	$\dot{m}_R$ (kg/min)	DL_{CF} (kg/m^3)	f_B (cm^2/g)	δ^* (–)	κ (–)	x_{50a} (μm)
1	17.0	103978	3.55	602	1.34	3528	7.86×10^{-2}	5.80×10^{-1}	52.0
2	17.0	114376	3.55	436	1.13	3465	5.67×10^{-2}	6.26×10^{-1}	59.7
3	17.0	98779	3.55	734	1.49	3567	9.41×10^{-2}	5.52×10^{-1}	47.5
4	17.0	88381	3.55	1366	2.10	3722	1.47×10^{-1}	4.72×10^{-1}	35.0
5	17.0	83182	3.55	–[a]	–[a]	–[a]	–[a]	–[a]	–[a]
6	23.8	114376	3.55	945	1.40	3707	8.51×10^{-2}	5.68×10^{-1}	39.8
7	23.8	103978	3.55	–[a]	–[a]	–[a]	–[a]	–[a]	–[a]
8	23.8	98779	3.55	–[a]	–[a]	–[a]	–[a]	–[a]	–[a]
9	23.8	88381	3.55	–[a]	–[a]	–[a]	–[a]	–[a]	–[a]
10	23.8	83182	3.55	–[a]	–[a]	–[a]	–[a]	–[a]	–[a]
11	22.1	114376	3.55	762	1.30	3622	7.49×10^{-2}	5.88×10^{-1}	44.4
12	22.1	103978	3.55	1264	1.72	3773	1.16×10^{-1}	5.15×10^{-1}	35.1
13	22.1	98779	3.55	–[a]	–[a]	–[a]	–[a]	–[a]	–[a]
14	22.1	88381	3.55	–[a]	–[a]	–[a]	–[a]	–[a]	–[a]
15	22.1	83182	3.55	–[a]	–[a]	–[a]	–[a]	–[a]	–[a]
16	18.7	114376	3.55	521	1.18	3518	6.14×10^{-2}	6.15×10^{-1}	54.1
17	18.7	103978	3.55	743	1.42	3590	8.72×10^{-2}	5.65×10^{-1}	46.3
18	18.7	98779	3.55	937	1.62	3636	1.06×10^{-1}	5.32×10^{-1}	41.5
19	18.7	88381	3.55	–[a]	–[a]	–[a]	–[a]	–[a]	–[a]
20	18.7	83182	3.55	–[a]	–[a]	–[a]	–[a]	–[a]	–[a]
21	13.6	114376	3.55	308	1.07	3363	4.97×10^{-2}	6.43×10^{-1}	73.8
22	13.6	103978	3.55	407	1.23	3410	6.67×10^{-2}	6.04×10^{-1}	65.6
23	13.6	98779	3.55	480	1.34	3438	7.81×10^{-2}	5.81×10^{-1}	61.1
24	13.6	88381	3.55	714	1.65	3513	1.09×10^{-1}	5.26×10^{-1}	50.8
25	13.6	83182	3.55	935	1.92	3568	1.32×10^{-1}	4.93×10^{-1}	44.4
26[b]	23.8	124774	3.55	651	1.14	3608	5.79×10^{-2}	6.23×10^{-1}	46.8
27[b]	23.8	135171	3.55	495	9.84×10^{-1}	3548	4.22×10^{-2}	6.64×10^{-1}	52.5
28[b]	25.5	135171	3.55	577	1.02	3593	4.57×10^{-2}	6.54×10^{-1}	48.7
29[b]	25.5	145569	3.75	438	8.91×10^{-1}	3535	2.72×10^{-2}	7.08×10^{-1}	54.0
30[c]	21.8	126752	3.55	818	1.26	3528	7.07×10^{-2}	5.96×10^{-1}	47.4

[a] Operational failure was detected.
[b] Additional runs for high rotor speed and high air flow rate outside the domain of the original design of simulations.
[c] Optimal operation with an $\dot{m}_{FF}$ = 1847 kg/min. All other runs had $\dot{m}_{FF}$ = 1723 kg/m

4.3 Results and Discussion

4.3.1 Spatio-temporal evolution of PSDs and mass hold-up: baseline process

We first simulated a full-scale closed-circuit cement milling process considering a set of baseline conditions: v = 17 m/s and Q = 103978 m^3/h (see Run 1 in **Table 4.1**). This will provide us a basis of comparison with actual cement PSDs and help to validate the simulation approach indirectly. Note that the value of baseline v = 17 m/s was in the middle of the tip speed range of the air classifier (Altun and Benzer, 2014), while baseline Q = 103978 m^3/h was also taken from Altun and Benzer (2014) on the condition that the air classifier in Altun and Benzer (2014) had a similar production rate to the referenced ball mill from Altun (2018). **Figure 4.3** demonstrates the simulated temporal evolution of PSD inside the ball mill for three axial positions: mill inlet, in front of the intermediate diaphragm, and in front of the discharge diaphragm. Although the PBM simulation was run for 120 min milling with data logged every minute, only selected simulation results at t = 10, 20, and 30 min and steady-state PSD are shown. Run 1 attained a steady state at t = 47 min. **Figure 4.3** clearly shows that the PSD inside the ball mill progressively became finer along the mill length, starting from cell 1 (mill inlet) to cell 3 (in front of the intermediate diaphragm) until cell 10 (in front of the discharge diaphragm), corresponding to axial positions L/10, 3L/10, and L, respectively. This is consistent with experimental observations reported in Dundar et al. (2011) and Altun (2018).

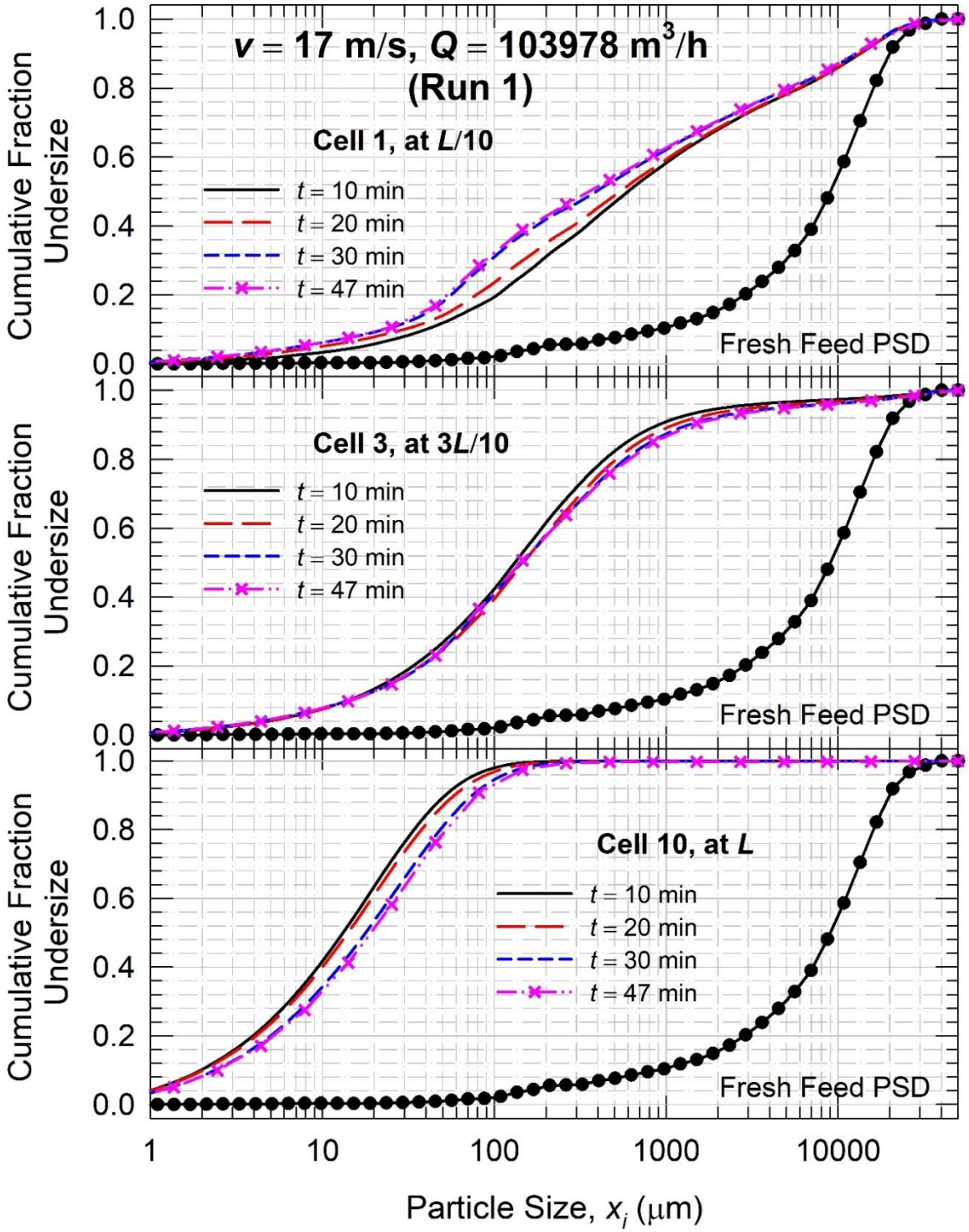

Figure 4.3 Temporal evolution of the cumulative PSD at various axial positions inside the ball mill (Run 1). A steady state was attained at t = 47 min. Cells 1 (mill inlet), 3 (in front of intermediate diaphragm), and 10 (in front of discharge diaphragm) correspond to axial positions L/10, 3L/10, and L, respectively.

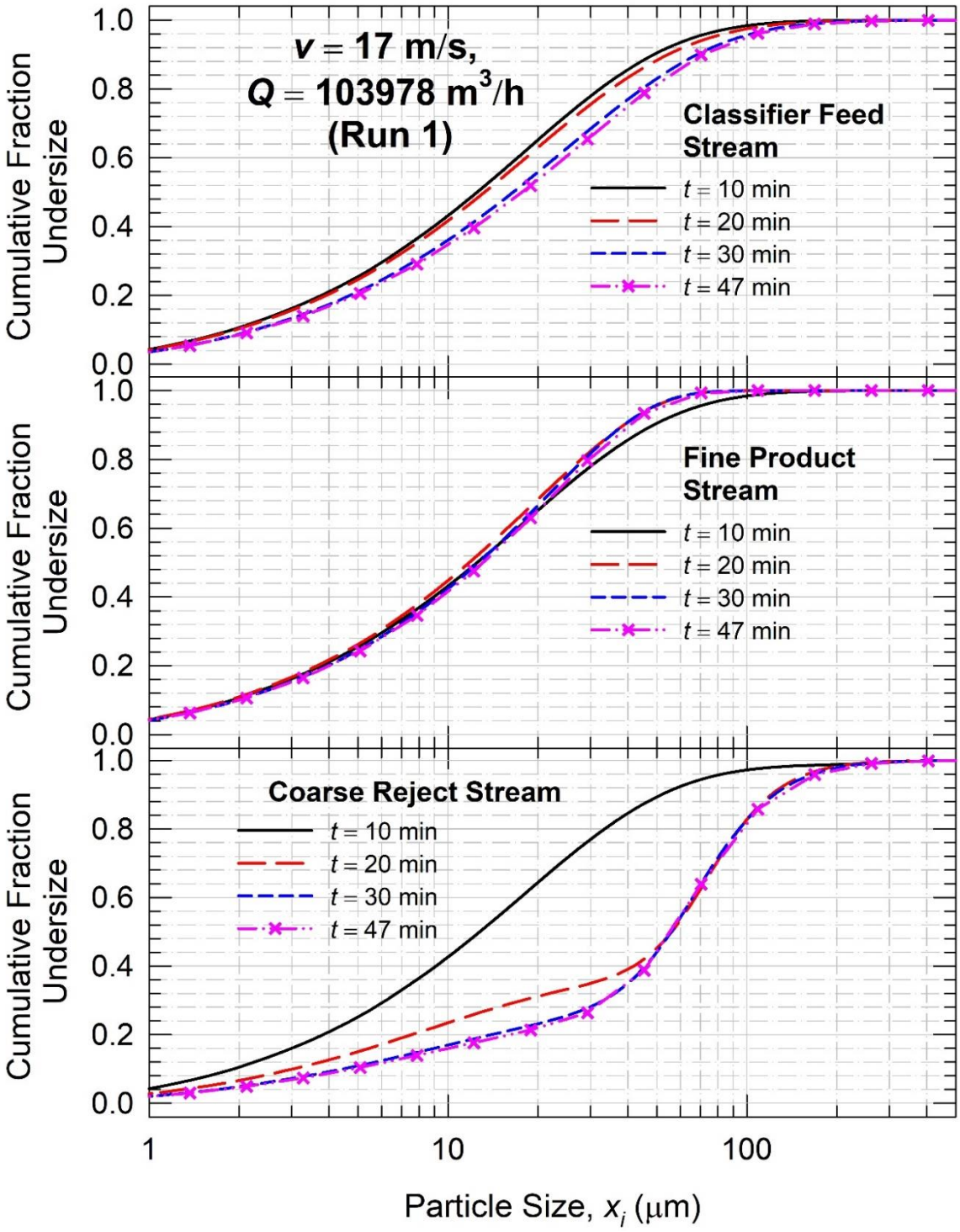

Figure 4.4 Temporal evolution of the cumulative PSD in various streams around the air classifier (Run 1). A steady state was attained at t = 47 min.

While the PSD in cell 1 (mill inlet) became finer over time, the PSDs in cells 3 and 10 became coarser. This can be explained by the fact that the mill inlet receives milled particles from a coarse rejected stream, which is much finer than the fresh feed PSD. Unlike PSD at the mill inlet, PSDs at cells 3 and 10 connecting to the diaphragms become coarser because of the accumulation of coarse particles through the classification action by the two diaphragms.

Figure 4.4 shows the temporal evolution of the PSDs in the classifier feed, fine product, and coarse reject streams around the air classifier. The classifier feed PSD, i.e., the mill discharge, was slightly finer than PSD in cell 10 (before discharge diaphragm), consistent with experimental observations in Altun (2018). Until a steady state was attained, as the classifier feed got coarser, the reject stream also got coarser while the product PSD did not change significantly except a notable reduction in 90% passing size x_{90}. Although the parameters used in this study were not taken from a specific mill, the simulated cement median size (~13 μm) is in the range of typical cement median size (Lynch et al., 2000; Altun et al., 2011; Dundar et al., 2011). Our baseline simulation results at steady state (t = 47 min) revealed an almost identical shape of PSDs for all three main streams around the air classifier compared to the actual PSDs of the full-scale ball mill circuit reported in Altun et al. (2020). **Table 4.1** also shows the simulated results for the mass flow rate of the coarse reject stream, the dust load of classifier feed, and the product Blaine surface area at steady-state operation (t = 47 min). As a measure of cement product fineness, the Blaine surface area was calculated to be 3528 cm^2/g (refer to Equation (C.5)), which also falls in the typical range of cement Blaine values (Bentz et al., 2008; Touil et al., 2008; Deolalkar, 2009). The cement's mass fraction of 3–32 μm M_{3-32} was 0.6769,

which is similar to that of the actual cement reported by Tsakalakis and Stamboltzis (2008) as M_{3-32} = 0.693. The dust load of the classifier feed DL_{CF} = 1.34 kg/m^3 was also in line with actual operations (DL_{CF} = 1.06–2.68 kg/m^3) reported in Altun and Benzer (2014). The dust load of product, defined as the ratio of the mass flow rate in the product stream to the air flow rate, was 0.99 kg/m^3 falling in the actual operation range of 0.49–1.00 kg/m^3 (Altun and Benzer, 2014).

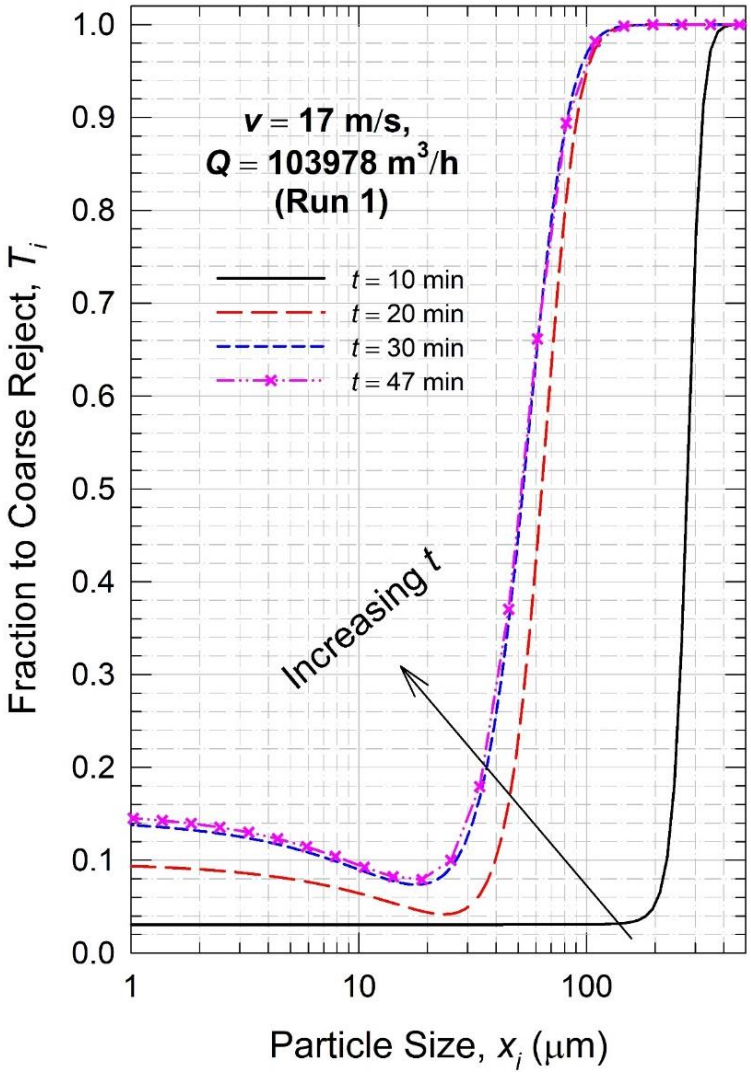

Figure 4.5 Temporal evolution of the air classification performance (Tromp curve, Run 1). A steady state was attained at t = 47 min.

As can be seen from the Tromp curve in **Figure 4.5**, the air classifier initially exhibited a relatively sharp classification (δ^* = 0.03 and κ = 0.84) at t = 10 min. The simulated classification performance worsened (higher δ^* and lower κ values) as the mass flow rate of the classifier feed stream and the dust load of the classifier feed increased over time until a steady state was attained in terms of the PSDs (refer to **Figure 4.4**), the mass flow rates in the streams around the classifier, and the mass hold-up in the mill (see **Figure 4.6**). The temporal evolution of the Tromp curve in **Figure 4.5** is consistent with experimental observations from the actual full-scale cement mills: a higher classifier feed rate led to (i) a higher bypass fraction of the air classifier (Boulvin et al., 2003; Altun et al., 2017), (ii) worse sharpness of classification (Boulvin et al., 2003), and (iii) a smaller cut size of classification x_{50a} (Boulvin et al., 2003), which is x_i at T_i = 0.5. These consistencies between simulated and experimentally observed Tromp curves demonstrated the variable Tromp curve model's ability to capture experimental observations when it was integrated with our unsteady-state PBM simulator (TUSSIM). At the steady state (t = 47 min), the air classification parameters δ^* = 0.08 and κ = 0.58 are in the normal operational range—δ^* = 0.05–0.15 and κ = 0.50–0.60—as reported by the air classifier manufacturer (FLSmidth, 2012). **Table 4.2** lists the variable Tromp curve's model parameters for air classification in Equation (4.8) obtained from the simulation during the steady state in comparison to the normal ranges reported by Altun and Benzer (2014), with all simulated Tromp curve parameters (α_a, β_a, β_a^*, δ_a, and $x_{50c,a}$) falling in the normal operating ranges. **Figure 4.6(b)** shows the temporal evolution of the mass hold-up from t = 0 to t = 120 min. The mass hold-up increased (m_H = 0 at t = 0) and reached a plateau at 25.4 t, corresponding to the

ball-to-cement ratio of 8.3 (assumed ball density ρ_B = 7800 kg/m^3 and porosity ε = 0.4), which falls within a normal range of 8.1–10.1 (Duda, 1985).

Overall, our baseline simulation results provide evidence that our simulation approach, along with the selected models and parameters of breakage kinetics, scaled-up factors, and classification actions (internal and external classifications), are capable of realistically simulating a closed-circuit cement ball mill in a full-scale operation. Extending the baseline simulation, the impact of air flow rate and rotor speed on PSDs in the circuit and Tromp curve is discussed next.

Table 4.2 Tromp Curve Parameters at the Steady State of the Baseline Process (Run 1)

Parameter	Parameter value at steady state	Operating range[a]	
		Minimum	Maximum
α_a	3.22	1.14	6.74
β_a	5.13×10^{-1}	1.00×10^{-3}	1.69
β_a^*	1.25	1.00	2.70
δ_a	1.52×10^{-1}	6.00×10^{-2}	4.40×10^{-1}
$x_{50c,a}$ (mm)	5.59×10^{-2}	4.00×10^{-2}	1.10×10^{-1}

[a] reported by Altun and Benzer (2014) for the classifier with a chamber diameter D_c of 3.55 m

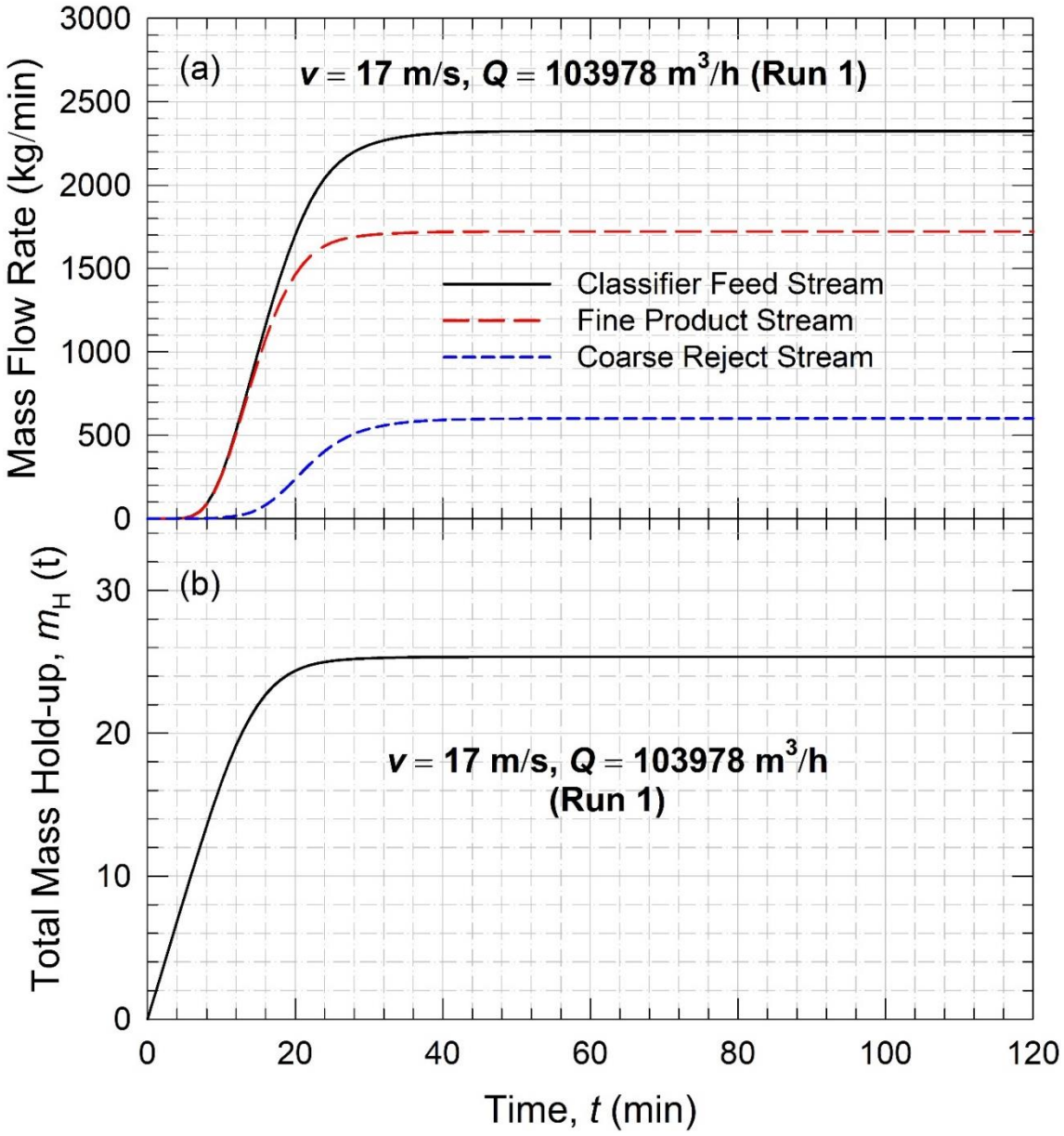

Figure 4.6 Temporal evolution of (a) the mass flow rate of streams around the air classifier and (b) the total mass hold-up (Run 1).

4.3.2 Impact of dynamic air classifier operation on cement size

Table 4.1 lists the operation conditions simulated for the air classifier. A full factorial simulation design involving five conditions of air flow rate and rotor speed was used (Runs 1–25). The air flow rate varied from 83182 to 114376 m^3/h, corresponding to 80–110% of

baseline Q = 103978 m^3/h. Furthermore, five conditions of rotor tip speed ranging from 13.6 to 23.8 m/s, corresponding to 80–140% of baseline v = 17 m/s, were used in the simulations (Runs 1–25). Note that the air flow rate and rotor speed can be practically adjusted in a cement plant. For example, air flow rate can be set to an appropriate level by adjusting the damper position (i.e., modulating pressure drop in the circuit) or the classifier fan speed via a variable speed drive. All conditions of Q and v in **Table 4.1** were in the normal range of the full-scale closed-circuit ball mill operation (Altun and Benzer, 2014).

Figure 4.7(a) presents the impact of the air flow rate, at a fixed rotor tip speed of v = 17 m/s, on the PSDs of three streams around the air classifier: classifier feed, fine product, and coarse reject. A decrease in air flow rate made product PSD slightly finer, as expected. A clear trend can be seen from **Figure 4.8** and **Table 4.1** data (Runs 1–4): a lower air flow rate resulted in a higher reject flow rate and ensuing higher dust load of the classifier feed because of the smaller cut size of classification (see the Tromp curve in **Figure 4.7(b)**), which is consistent with the simulation results of the full-scale cement ball mill in Austin et al. (1975). For this reason, the average residence time in the mill with a higher mass flow rate of the reject stream shortened. Hence, the PSD at the mill outlet stream, i.e., the classifier feed, became coarser (**Figure 4.7(a)**), which is the opposite trend to the product and reject PSDs. When the air flow rate was reduced from 114376 to 88381 m^3/h, the bypass fraction δ^* increased from 0.06 to 0.15 and the sharpness of classification κ decreased from 0.63 to 0.47 (**Table 4.1**). Hence, a consequence of a higher mass flow rate in the classifier feed stream is that air classification performance worsened due to the higher dust load of the classifier feed. This simulation observation is in line with the experimental observations in Brugan (1988), Ito (2000), and Yardi (2005).

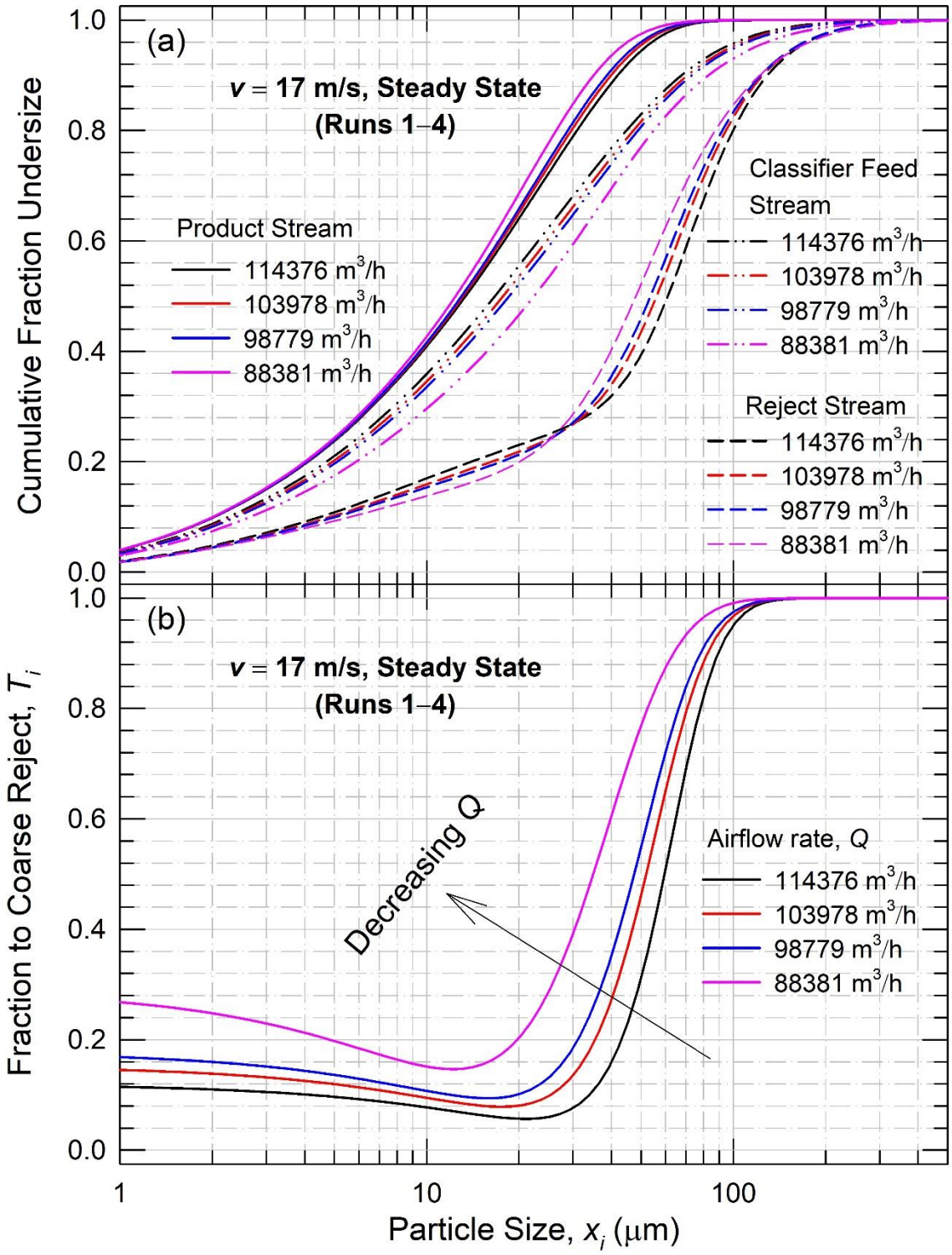

Figure 4.7 Impact of air flow rate through air classifier with fixed value of rotor tip speed on (a) the cumulative PSD in the streams around the air classifier and (b) air classification performance (Tromp curve) at the steady state.

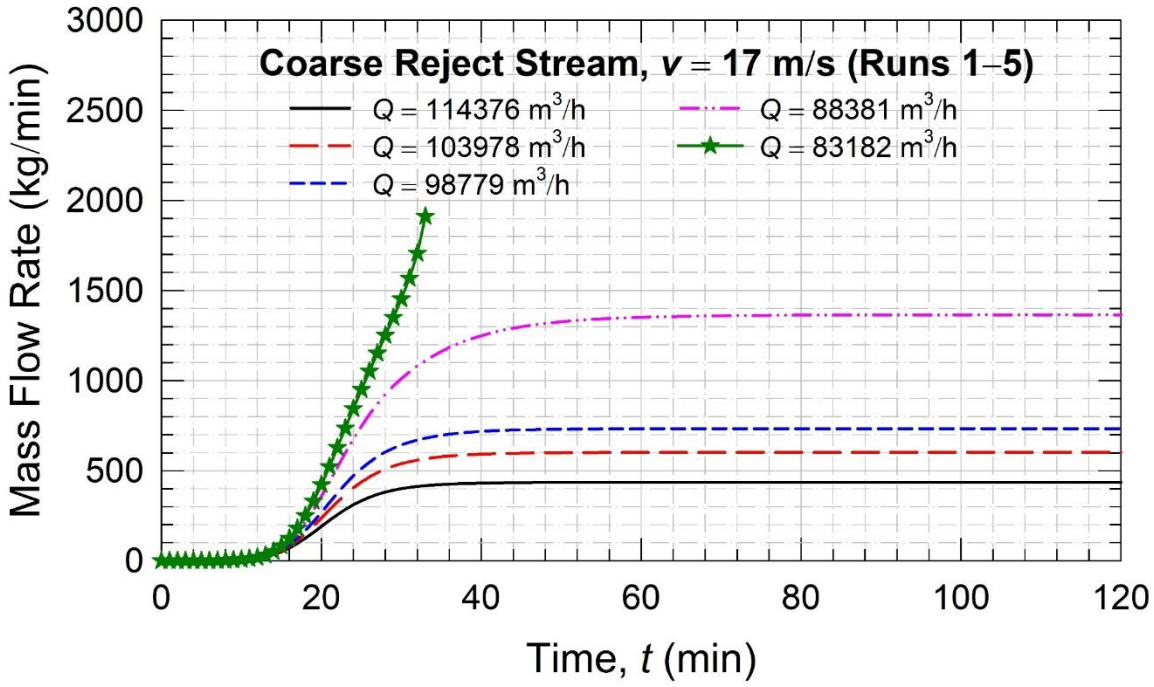

Figure 4.8 Temporal evolution of the mass flow rate of the coarse reject stream from the air classifier. For Q = 83,182 m^3/h, operational failure was detected at 33 min.

As can be seen in **Figure 4.8**, the reject flow rate increased as the air flow rate decreased. A drastic change was observed when Q was reduced from 98779 to 88381 m^3/h. With further reduction to Q = 83182 m^3/h, the reject flow rate increased sharply, and the simulator stopped at t = 33 min, without yielding a steady state solution. Mathematically, when the combined mass flow rate to the mill was too high, the average residence time of cell z became very low, overall breakage rate dropped, causing dramatic increase in mass hold-up, which ultimately lead to an unsolvable set of DAEs at $\tau_z \approx 0$. When such a condition occurs, even a highly accurate and efficient ODE integrator like ode15s could not meet integration tolerances without reducing the step size below the smallest value allowed (~10^{-13} min) at time t = 33 min. While this gives the appearance of a numerical method failure, it reflects the physical reality of unstable operation, or operational failure

when the milling circuit is overloaded under the specific classifier–mill conditions. In general, the poorer classifier performance at the lower air flow rate also meant a dramatically higher reject rate (see **Table 4.1**) and higher feed rate of cement clinker to the mill. This operation ultimately led to overloading of the mill. The overloading of the mill in turn resulted in higher dust load and poorer classifier performance, thus feeding each other's negative impact on circuit performance, ultimately leading to the circuit failure. This finding points to the strong coupling and interplay between the classifier and the mill in the closed-circuit operation. Our findings also offer the first simulation-based evidence supporting Luckie and Austin's assertion (Luckie and Austin, 1972): "There may be a very limited range available for resetting the classifier, and in addition a simulation at a high circulation ratio may not be realistic because the classifier would overload." It should be mentioned that a previous simulation study (Kis et al., 2006) used an unsteady-state PBM with a *fixed Tromp curve* to demonstrate the operational failure due to overloading of a ball mill. They indicated that overloading occurred when the mass hold-up reached a certain value. However, this ball mill failure condition was arbitrarily set without any justification.

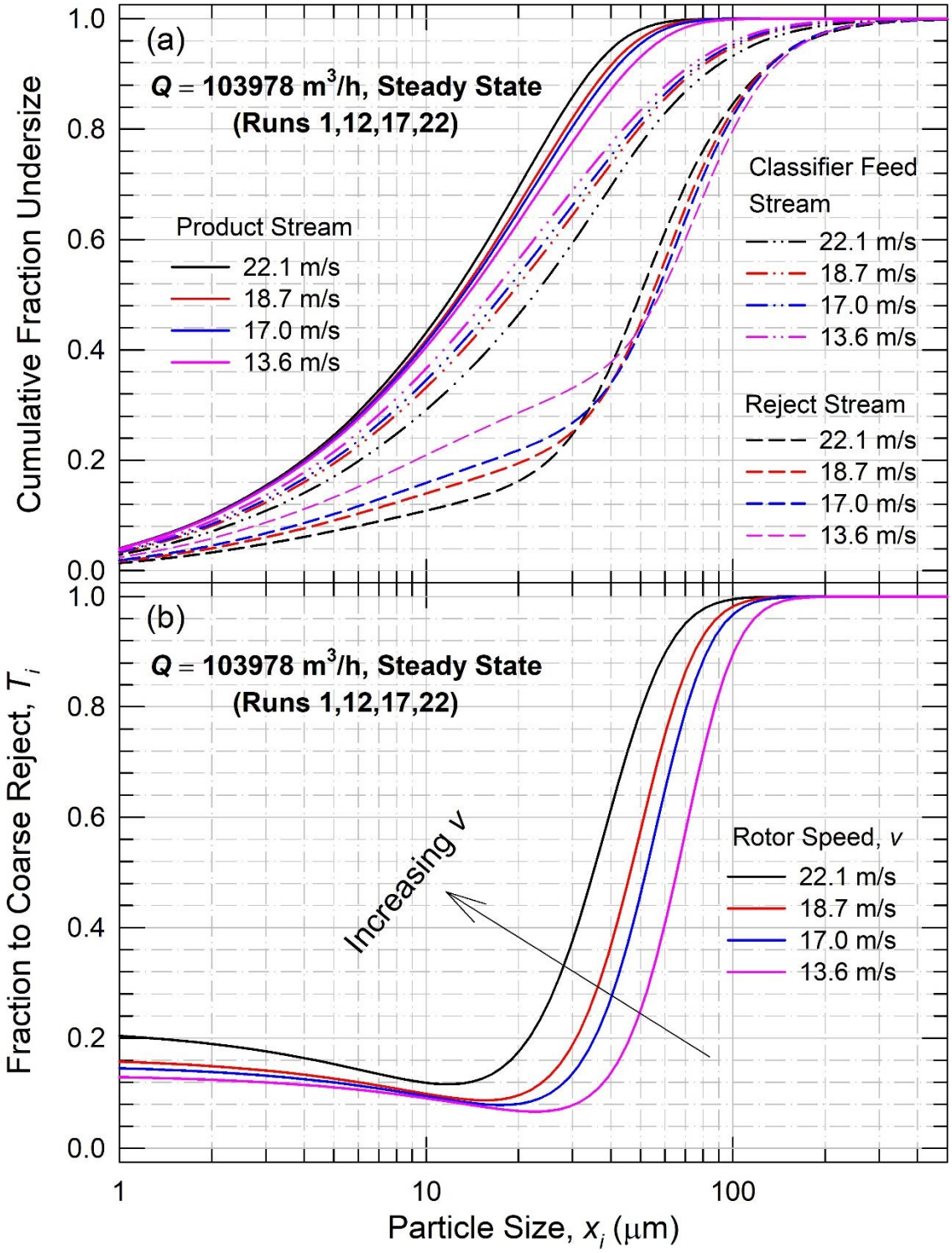

Figure 4.9 Impact of the rotor tip speed with fixed value of air flow rate through air classifier on (a) the cumulative PSD in the streams around the air classifier and (b) air classification performance (Tromp curve) at the steady state.

At a fixed air flow rate Q = 103978 m^3/h, simulation results when rotor tip speed varied from 13.6 to 22.1 m/s indicated that a faster rotor speed not only led to finer product PSD (**Figure 4.9(a)**), which is consistent with Mejeoumov (2007), but also increased the dust load of the classifier feed (see Runs 1, 12, 17, and 22 in **Table 4.1**), resulting in worsening air classification performance (**Figure 4.9(b)**), an observation in line with Brugan (1988), Ito (2000), and Yardi (2005). A similar result regarding operational failure was observed for the impact of rotor speed. Further increase in rotor speed to v = 23.8 m/s resulted in operational failure. An analysis of the simulation results with a full-factorial simulation design with the first 25 runs listed in **Table 4.1** suggests that the operating range of a closed-circuit ball mill at a fixed fresh feed rate was limited and affected by the interplay between air flow rate and rotor tip speed in view of the operational failure. Operating with a lower air flow rate could lead to failure, even at slow rotor speeds. For example, v = 18.7 m/s caused the operational failure for Q = 88381 m^3/h, while v can be up to 22.1 m/s for Q = 103978 m^3/h without any failure.

Subsequently, the impact of the air classifier's operation at a high rotor speed–high air flow rate was investigated (Runs 26–29 in **Table 4.1**). This set of simulations (Runs 26–29) is outside the domain of the original design of the simulations (Runs 1–25). Similar trends in simulation results were obtained in **Figure 4.10**. For example, for a fixed value of a rotor tip speed of v = 25.5 m/s, a higher air flow rate Q led to slightly coarser PSD in fine product and coarser reject streams, but led to a finer classifier feed PSD. Additionally, analysis of the Tromp curve in **Figure 4.10(b)** shows that lower bypass fraction δ^* and higher sharpness of classification κ were achieved by operating the classifier at a higher air flow rate. More importantly, the Blaine surface area values in **Table 4.1** for Runs 1–25

suggest that it is possible to produce cement product with a Blaine surface area of ~3600 cm^2/g by setting the operation of the air classifier at a high rotor speed–high air flow rate without any operational failure and at a relatively high sharpness ($\delta^* < 0.06$ and $\kappa > 0.60$), which cannot be achieved in Runs 1–25.

Simulated results (classification performance, cut size, and Blaine surface area) at a steady state are summarized in the last four columns of **Table 4.1** and are plotted graphically using 3D scatter in **Figure 4.11**. Note that only simulation results from 15 out of 29 runs were plotted because data were not available due to operational failures in the other 14 runs (refer to **Table 4.1**). This is why we could not plot results in 3D mesh or contours, and some trends are difficult to visualize due to missing points. To help guide the visualization of the trends, we filled some data points and use arrows. It is apparent that when the air classifier was operated at a higher air flow rate or lower rotor tip speed, sharper classification (lower δ^* and higher κ) could be achieved, albeit at a higher cut size. With a larger cut size, cement products become coarser (lower Blaine surface area), and such products might be undesirable and unacceptable in relation to end users' required specifications. Hence, overall, what matters in the end is the overall circuit performance, not the individual performance of the ball mill or the air classifier alone, and the impact on the cement quality attributes and production rate. In other words, one can manipulate the classifier's operational parameters and fresh feed rate to optimize the process, as will be discussed next.

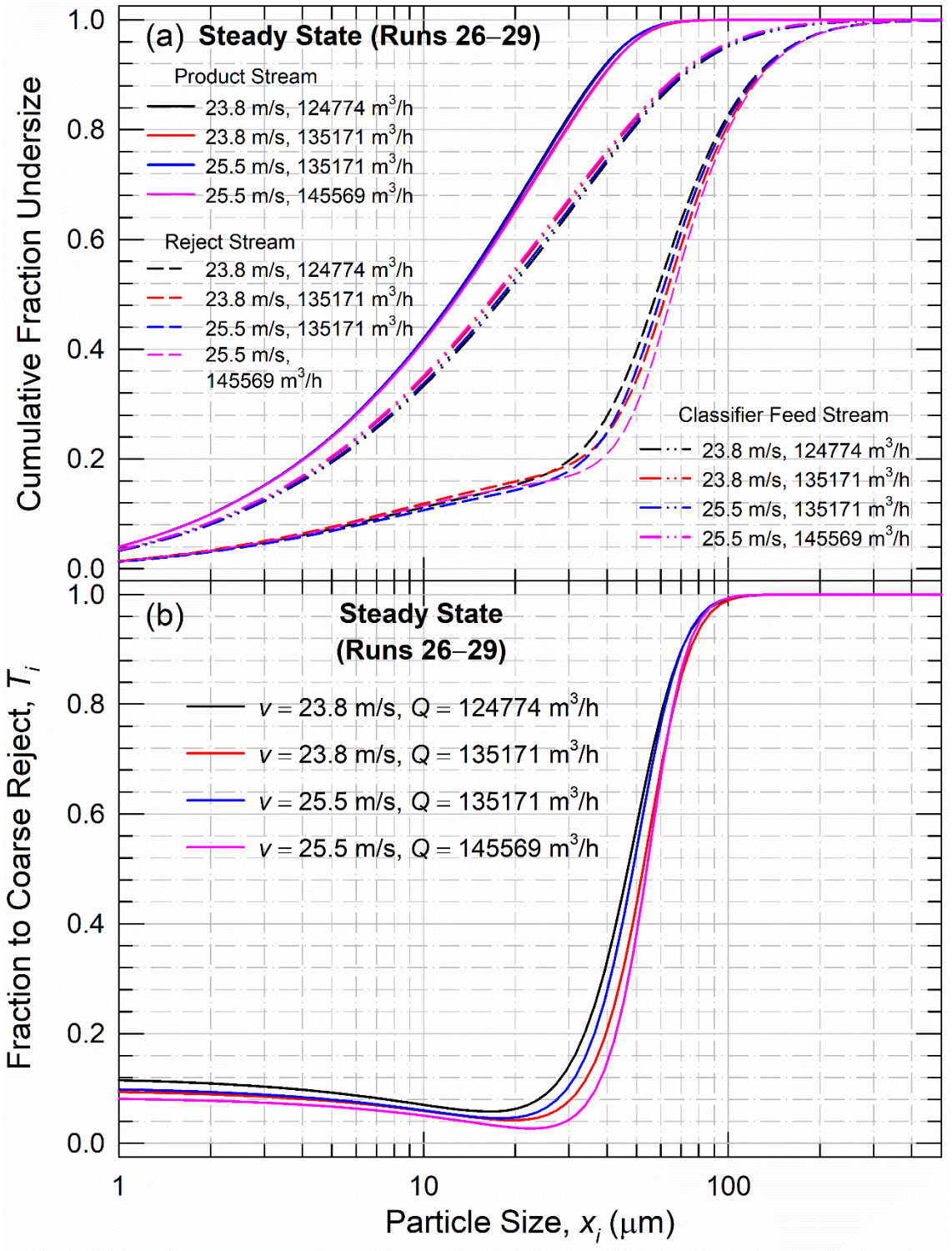

Figure 4.10 Closed-circuit operation at high rotor speed–high air flow rate: (a) the cumulative PSD in the streams around the air classifier and (b) air classification performance (Tromp curve) at the steady state.

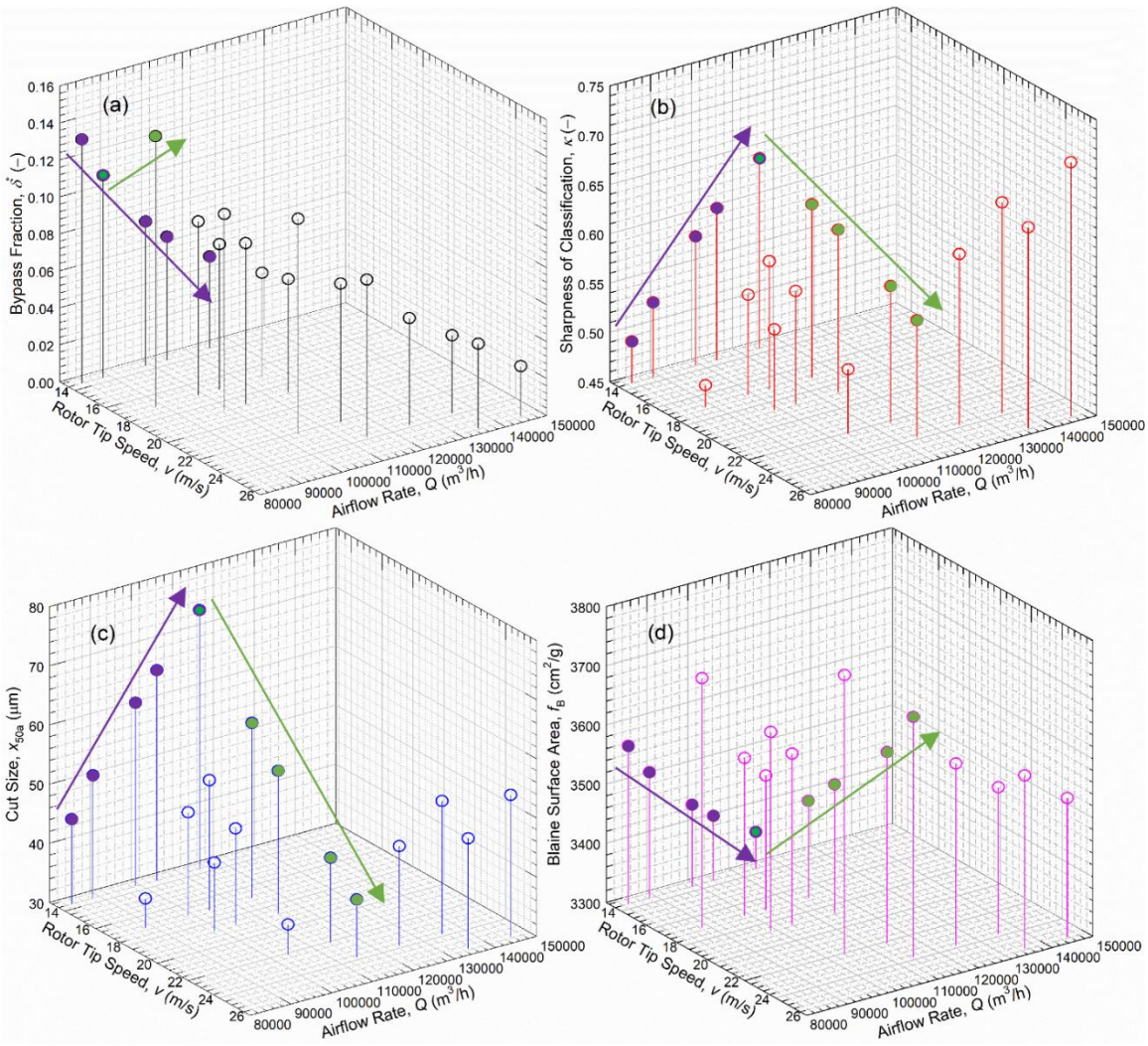

Figure 4.11 Impact of rotor tip speed and air flow rate on: (a) bypass fraction δ^*, (b) sharpness of classification κ, (c) cut size x_{50a}, and (d) Blaine surface area f_B. Filled data points and arrows are intended to highlight the general trends. Purple: varying air flow rate at constant rotor speed, Green: varying rotor speed at constant air flow rate. Runs in which operational failure has been detected are excluded from the graphs.

Table 4.3 Initial Guess and Bound Constraints for Each Parameter Used during the Global Optimizer-based Process Optimization

Process parameter	Initial guess	Constraint	
		Lower bound	Upper bound
Rotor speed, v (m/s)	20.0	12.5	30.0
Air flow rate, Q (m^3/h)	150000	100000	200000
Fresh feed rate, $\dot{m}_{FF}$ (kg/min)	1500	1000	2500

4.3.3 Identifying the optimum operational conditions for the circuit

We performed process optimization starting with the default minimum N_T = 200 (The MathWorks, 2022) and increased the N_T value to investigate whether the N_T-independent solution to the optimization problem could be obtained. **Table 4.3** lists the initial guesses and bound constraints (lower and upper limits) for each variable of optimization. Here, targeted Blaine surface area f_B^{Tar} = 3528 cm^2/g was taken from Run 1 simulation. **Table 4.4** shows the results at the steady state obtained from the global optimizer for N_T = 200, 500, 1000, and 1500. When N_T was increased from 200 to 500, the optimized v and Q varied drastically while the objection function did not decrease notably. On the other hand, a significant decrease of the objection function occurred when N_T was increased from 500 to 1000 (the default value of MATLAB), with insignificant further decrease for N_T = 1500. Most importantly, the optimized variables remained unchanged when N_T was increased from 1000 to 1500. Specifically, in comparison to the solutions obtained from the preceding value of N_T = 1000, percent relative error for all parameters and objective function was less than 10^{-1}, justifying that global minimum was obtained. We did not attempt to run an optimization with an N_T higher than 1500 because of the long computational time, requiring ~9 days for N_T = 1500. It is important to mention that the

global optimizer with N_T = 200 and 500 returned an unreasonable value of $\dot{m}_{FF}$, which is even lower than that of the baseline condition ($\dot{m}_{FF}$ = 1723 kg/min). The estimated parameters $\dot{m}_{FF}$ and Q for N_T = 200 and $\dot{m}_{FF}$ for N_T = 500 stuck around initial guess. The optimizer might have hit a local minimum or a flat parameter surface around the objective function (Kwon and Cho, 2021).

Table 4.4 Air Classifier Operation Parameters, Fresh Feed Rate, and Cement Quality Metrics Obtained by the Global Optimizer-based Process Optimization for Various Values of N_T

Process variable and cement quality metrics	Value obtained from global optimization			
	N_T = 200	N_T = 500	N_T = 1000	N_T = 1500
Rotor speed, v (m/s)	21.8	14.7	21.8	21.8
Air flow rate, Q (m^3/h)	150000	104902	126752	126752
Fresh feed rate, $\dot{m}_{FF}$ (kg/min)	1500	1502	1846	1847
Predicted cement Blaine surface area, f_B^{Mod} (cm^2/g)	3528	3528	3528	3528
Predicted cement mass fraction at 3–32 μm, M_{3-32}^{Mod}(–)	6.573×10^{-1}	6.584×10^{-1}	6.853×10^{-1}	6.854×10^{-1}
Objective function value (–)	1.009	1.007	8.564×10^{-1}	8.561×10^{-1}

Figure 4.12 demonstrates the cumulative PSDs at the steady-state optimal operation (Run 30) with desirable cement fineness identified by the global optimizer at N_T = 1500: v = 21.8 m/s, Q = 126752 m^3/h, and $\dot{m}_{FF}$ = 1847 kg/min. Based on N_T = 1500 simulation, the production rate of Run 30 was 7% higher than that of the baseline process (Run 1). Mass fraction of 3–32 μm size range of the cement product in Run 30 was 0.6854, which was slightly higher than Run 1 (M_{3-32} = 0.6769). In view of the operation of the air classifier obtained from the global optimizer, air flow rate Q and rotor tip speed v at the optimum condition (Q = 126752 m^3/h and v = 21.8 m/s) were higher than those of the

baseline (Q = 103978 m^3/h and v = 17 m/s). As can be seen from **Table 4.1**, the classifier in the optimized process provided a slightly sharper classification and a smaller cut size than that of the baseline process despite the 7% increase in production capacity.

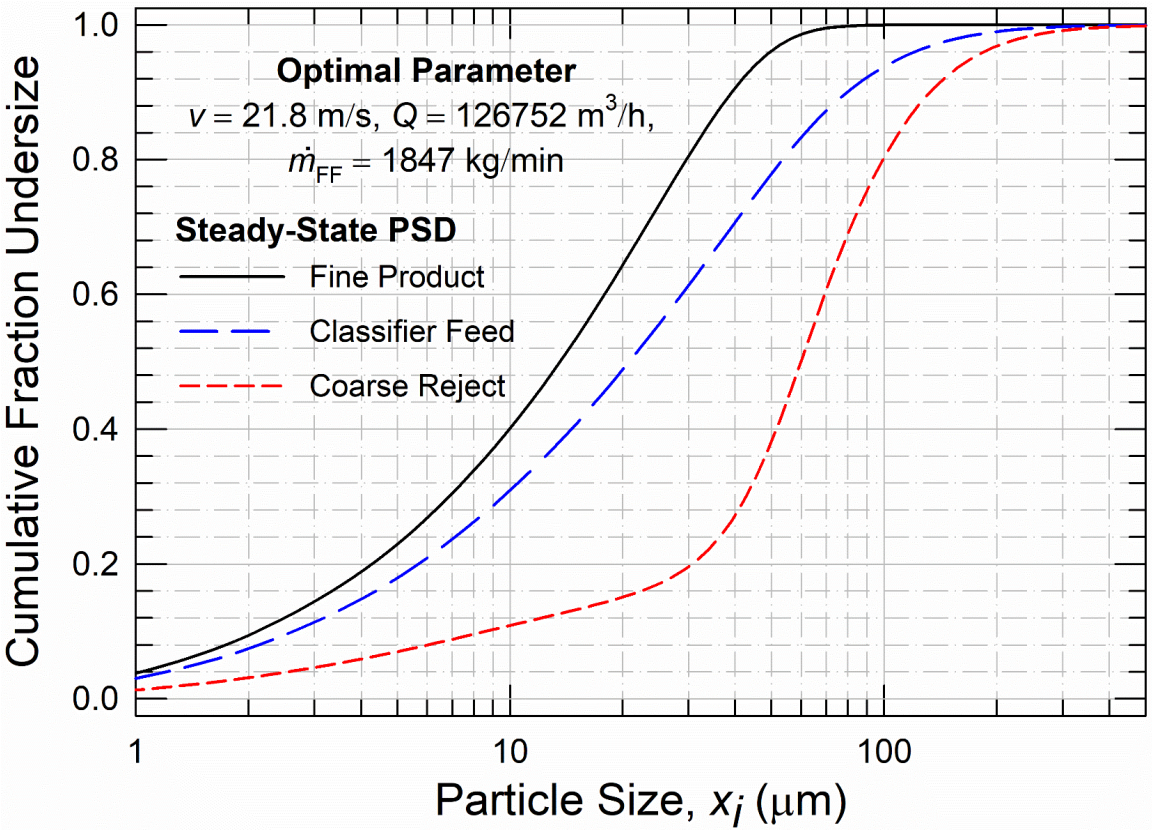

Figure 4.12 Cumulative PSDs at the optimal steady-state operation, whose operational parameters were obtained using the global optimizer: v = 21.8 m/s, Q = 126752 m^3/h, and $\dot{m}_{FF}$ = 1847 kg/min.

4.4 Conclusions

Unlike all prior PBM studies of closed-circuit cement ball milling, this study has augmented a variable Tromp curve representing external classification action with our recently developed unsteady-state, cell-based PBM simulator (TUSSIM), which accounts for mixedness degree in the mill and internal classification action by the diaphragms. Using

representative values of actual full-scale classifier parameters and continuous ball milling operational parameters from existing literature as well as actual cement clinker breakage parameters, a baseline process simulation was performed. The obtained PSDs in the circuit were similar to those obtained from actual cement mill circuits reported in the literature, giving credibility to the simulation approach and the chosen functions and parameters. Subsequently, TUSSIM was used to investigate the impact of the air classifier's operation (i.e., air flow rate and rotor tip speed). The simulation results suggested that for a fixed fresh feed rate, finer cement products could be achieved by decreasing the air flow rate and/or increasing the rotor tip speed. This study elucidated the mathematical and physical origin of the operational failure of the circuit operations. The overloading of the circuit occurs when the classifier is operated using too low an air flow rate or too fast a rotor speed. For this reason, there is a limit to product fineness adjustment at the fixed fresh feed rate by manipulating the classifier parameters.

Another novelty of this study is that TUSSIM was executed in the inverse problem framework to identify the optimum operation of the air classifier (air flow rate and rotor tip speed), along with the fresh feed rate, to produce a cement product that satisfy actual cement specifications using a global optimizer coupled with a DAE solver. We formulated an objective function considering cement quality (Blaine surface area and mass fraction of 3–32 μm) and the production capacity. The optimization results suggest that about 7% increase in circuit capacity could be achieved when higher air flow rates and rotor speeds were used in comparison to the baseline process. Overall, besides generating fundamental process insights, the use of TUSSIM augmented with a variable Tromp curve could help industrial practitioners optimize existing closed-circuit ball milling operations.

CHAPTER 5

PBM SIMULATION AND OPTIMIZATION OF CLOSED-CIRCUIT CEMENT MILLS WITH VARIOUS COMPARTMENTS AND BALL SIZE DISTRIBUTIONS

A true unsteady-state simulator (TUSSIM) for ball milling was integrated with a variable Tromp curve for classification to simulate and optimize closed-circuit, multi-compartment cement ball milling. Using realistic model–operational parameters from available literature, we first investigated the system dynamics for a two-compartment mill. Then, various simulations examined the impacts of closed-circuit vs. open-circuit operation, number of compartments, and various ball size distributions. Our results suggest that integrating an air classifier into an open-circuit ball mill can increase the production rate by 15% or increase the cement-specific surface area by 13%. A single-compartment mill entails a pre-milled feed for proper operation, whereas a two-compartment mill yields a finer cement product than a three-compartment mill. Uniform mass distribution of balls led to slightly finer product than uniform surface area or number distributions, while the impact of a classifying liner was negligibly small. Finally, we identified optimal ball mixtures in a two-compartment mill using a combined global optimizer–DAE solver, which suggests 14% capacity increase with desirable cement quality. Overall, TUSSIM's results are not only in line with limited, full-scale experimental studies and industry best practices, but also provide fundamental process insights, while enabling process optimization with tailored ball mixtures in different compartments.

5.1 Introduction

Closed-circuit tumbling ball mills with dynamic air classifiers have been commonly operated as cement mills (Labahn and Kohlhaas, 1983; Jankovic et al., 2004; Deolalkar, 2009). **Figure 5.1** shows a process flow diagram of a closed-circuit, two-compartment ball mill with an air classifier. Two-compartment mills with an intermediate diaphragm provide the flexibility to use different mixtures of ball sizes in each milling compartment. Diaphragms also retain coarse particles within the compartment for further milling and keep grinding balls from leaving the compartment. The first compartment contains a large ball mixture for coarse particle breakage. The second compartment contains a small ball mixture for fine particle breakage. For example, based on Austin et al. (1975), ~50–90 mm balls and ~20–40 mm balls were loaded in the first and second compartments in full-scale, closed-circuit ball milling of cement, respectively.

Current knowledge of the process operation of cement ball milling is largely empirical. In general, performing well-controlled, scientific experiments at full-scale mills is difficult, time-consuming, and sometimes impractical. The process know-how and expertise have been built from trial-and-error learning, suggestions from engineering companies (Shimoide, 2016; Nowack, 2022), and manuals from machine suppliers (FLSmidth, 2012; FLSmidth, 2014). Scientific studies regarding the impact of the presence of air classifiers, ball size distribution, number of compartments, and classifying liners on cement size in closed-circuit ball mills are apparently limited (Austin et al., 1976). Rather, guidance for the operation and design of closed-circuit ball mills has been widely reported in cement handbooks (Labahn and Kohlhaas, 1983; Duda, 1985; Alsop, 2007; Deolalkar, 2009) and magazines (Yardi, 2005; Fernandez and Hui, 2017). Although data from these

sources are valuable for industrial practitioners, a major issue is that details of the operation are missing, thus making reproducibility by others nearly impossible (e.g., Parkes, 1990; Van den Broeck, 1998; Fernandez and Hui, 2017). In view of all these challenges, computer simulations based on the population balance model (PBM) have been found to be a useful tool for gaining fundamental insights into cement ball milling (Austin et al., 1975; Muanpaopong et al., 2022b).

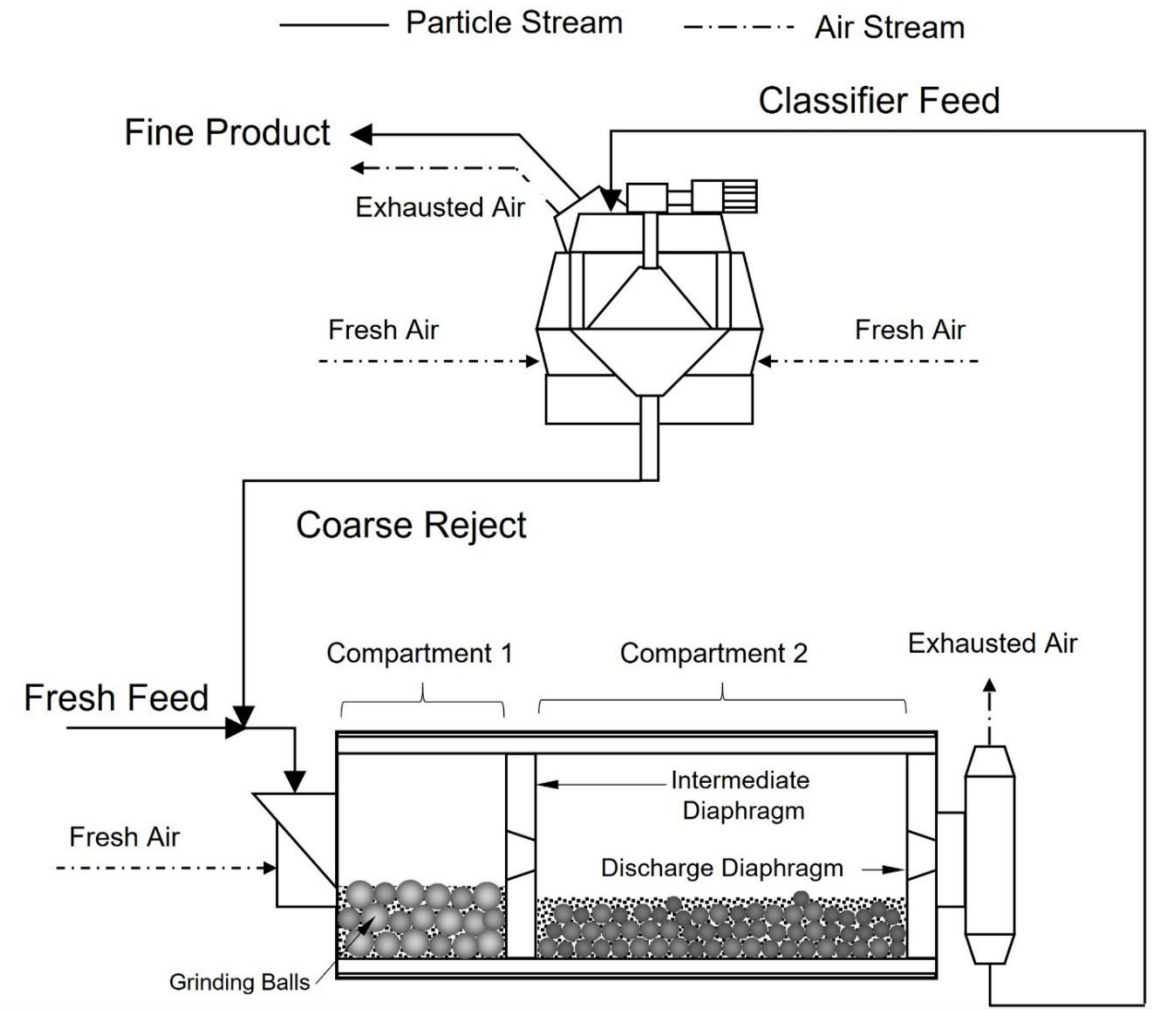

Figure 5.1 A simplified process flow diagram of a closed-circuit two-compartment ball mill with an air classifier.

It is hard to find actual experimental evidence regarding the advantages of incorporating air classifiers with ball mill circuits. In fact, only one experimental work (Parkes, 1990) reported that a 43% increase in production rate was achieved after installing an air classifier into an existing full-scale open-circuit ball mill in the UK. However, this significant improvement was partially due to the use of softer cement clinker and higher ball filling fraction after converting to a closed circuit with an air classifier. The author (Parkes, 1990) speculated that, of the 43% observed increase in production rate, 25% was due to the presence of air classifiers, but no evidence was provided to justify their speculation. Therefore, it is fair to assert that the actual advantage of air classifiers in terms of capacity improvement for open-circuit to closed-circuit operation remains unknown.

One of the most common tasks for ball milling operations is the selection of grinding ball sizes. However, only a few studies (Lynch et al., 2000; Dundar et al., 2011; Genc, 2015c) tackled the ball selection problem for closed-circuit cement ball milling in full-scale operations. For example, the actual production rate was reported to have increased in the range of 12.7–20.5% by optimizing the ball size distribution (BSD) along with modifying the slot size of the intermediate diaphragm (Dundar et al., 2011). This actual improvement agreed well with results obtained from a steady-state PBM simulation that suggested 10–17% improvement of production rate (Dundar et al., 2011). However, the details about BSD and slot size before and after optimization were not mentioned. The impact of the BSD could not be decoupled from the impact of the slot size of the diaphragm. A similar issue was found in another study that reported the combined impact of BSD and the ball-filling fraction (Genc, 2015c). Regarding PBM simulation, previous studies provide insufficient details of mathematical descriptions of steady-state PBM simulations

(Lynch et al., 2000; Dundar et al., 2011; Genc, 2015c). Specifically, approaches for translating parameters such as the ratio of specific breakage rate parameter to discharge rate parameter from one BSD to other BSDs are unclear, because none of the reported parameters was explicitly expressed as a function of ball size. Given the limitations of the currently available works, there is a need to develop a robust PBM framework for closed-circuit ball mills to comprehensively examine the impact of BSD and ball mixture.

Regarding the selection of the number of compartments to be used, a cement handbook (Deolalkar, 2009) suggests that a three-compartment mill configuration is suitable for open-circuit ball milling, while a two-compartment mill configuration is sufficient for closed-circuit ball milling with an air classifier. Although this suggestion is consistent with the current best practice (e.g., Genc, 2016; Altun, 2018), no rationale or justification was given as to why the number of compartments should be reduced for closed-circuit operation (Deolalkar, 2009). In the scientific literature, only a few studies (Genc, 2016; Muanpaopong et al., 2022b) have investigated the impact of the number of compartments on cement product fineness. However, these studies (Genc, 2016; Muanpaopong et al., 2022b) considered open-circuit ball mills without air classifiers. To the best of our knowledge, no attempts have been made to elucidate the impact of the number of milling compartments in closed-circuit ball mill operations.

A classifying liner fitted with the internal mill shell in the fine milling compartment leads to proper ball classification along the axial position of the mill length. Larger balls are retained at the entrance of the compartment. The mean ball size becomes smaller toward the discharge end of the compartment (Benzer, 2005; Altun, 2018). Classifying liners are commonly used in cement ball mills to provide a suitable spatial variation of ball sizes to

match particle sizes along the axial position (Fortsch, 2006; Altun, 2018; Ghalandari and Iranmanesh, 2020). Interestingly, only a single experimental study (Fortsch, 2006) reported that an improvement in specific power consumption at the same product fineness was not observed when classifying liners were used, based on experimental data from various closed-circuit cement mills. There is no prior PBM study that explored the impact of ball classification originating from classifying liners on the cement product fineness in closed-circuit multi-compartment mills.

PBM can simulate the temporal evolution of particle size distribution (PSD) (Austin, 1971/1972) in the full-scale milling process. PBM simulations have been commonly performed for steady-state operations of full-scale cement ball mills (e.g., Austin et al., 1975; Ergin and Ercelebi, 1999; Lynch et al., 2000; Jankovic et al., 2004; Dundar et al., 2011; Genc, 2015c; Genc, 2016; Altun, 2018). Only a few PBM studies (Boulvin et al., 2003; Huusom et al., 2005; Muanpaopong et al., 2022b) have considered the transient operation. For example, attainment of steady-state operation in terms of PSD and temporal evolution of total mass hold-up were previously examined for an open-circuit ball mill simulation (Muanpaopong et al., 2022b). Huusom et al. (2005) demonstrated the dynamic response of mass flow rate in coarse reject and fine product streams by introducing a step change in the fresh feed rate. Simulating the entire closed-circuit operation requires an external classification function of the air classifier represented by a Tromp curve model. The Tromp curve represents the fraction of particles in the classifier feed stream reporting to coarse reject stream for further ball milling (see **Figure 5.1**). Ample experimental data reported in (Onuma and Furukawa 1984; Ito, 2000; Altun and Benzer, 2014) indicate that classification performance worsens when the dust load of the

classifier feed (defined as ratio of classifier feed to air flow rate) is higher. Depending on the capability to capture the impact of dust load, the Tromp curve model can be classified as a fixed Tromp curve model (e.g., Austin et al., 1975; Ergin and Ercelebi 1999; Altun, 2018) and a variable Tromp curve model (Altun and Benzer, 2014). Here, the variable Tromp curve model is specifically referred to the Altun and Benzer model (Altun and Benzer, 2014). Unlike the fixed Tromp curve model, parameters in the variable Tromp curve model (Altun and Benzer, 2014) were obtained from various mills with wide operation conditions of dust loading during a steady state. The classification parameters were explicitly expressed as a function of dust load of the classifier feed and manipulated parameters of the air classifier (rotor tip speed and air flow rate). Therefore, the variable Tromp curve model can accurately capture the impact of dust loading on classification performance. Based on the literature review, none of the published PBM studies coupled PBM with the variable Tromp curve model.

In the context of full-scale closed-circuit ball mills for cement milling, only Austin et al. (1975) performed process optimization using an optimizer with the steady-state PBM with a fixed Tromp curve model. In their study, the air classifier's cut size and production rate were used as the variables to achieve a desirable cement specification. However, no suggestions were offered regarding how the air classifier's parameters should be set to reach that optimal condition. Moreover, Austin et al. (1975) did not consider optimization of the BSD inside the mill. To the best of our knowledge, no study has performed process optimization using an optimizer for full-scale cement ball milling to suggest the optimum ball size distribution in each compartment that maximizes production rate and improves cement quality.

This comprehensive theoretical simulation study of a full-scale ball mill with an air classifier aims to (i) elucidate the advantages of an air classifier, (ii) holistically examine the impact of ball mixture and BSD, (iii) shed light on the selection of the number of compartments, (iv) assess the impact of ball classification due to the classifying liner, and (iv) develop a process optimization scheme to identify the optimal BSD. To achieve these goals, our recently developed true unsteady-state simulator (TUSSIM) for ball milling (Muanpaopong et al., 2022b) was coupled with a variable Tromp curve model (Altun and Benzer, 2014) of classification for simulating a closed-circuit ball mill. The mathematical model of TUSSIM for closed-circuit simulation forms a set of differential algebraic equations (DAEs), which were numerically solved by a DAE solver. The comprehensive set of simulations will allow us to gain fundamental process insights into the impacts of closed-circuit vs. open-circuit operation, number of compartments, and various ball size distributions. Most importantly, for the first time in literature, the combined global optimizer–DAE solver method (Dave et al., 2022; Muanpaopong et al., 2023) will identify optimal BSD to achieve desired cement specification at maximized production rate in a full-scale closed-circuit ball mill.

5.2 Theoretical

5.2.1 Mathematical description of TUSSIM for a closed-circuit, multi-compartment ball mill

A recently developed simulator, TUSSIM (Muanpaopong et al., 2022a; Muanpaopong et al., 2022b), was coupled with the state-of-the-art variable Tromp curve model of classification (Altun and Benzer, 2014). The detailed derivation of TUSSIM can be found

in Muanpaopong et al. (2022a). **Figure 5.2** shows a model representation of a two-compartment ball mill with an air classifier.

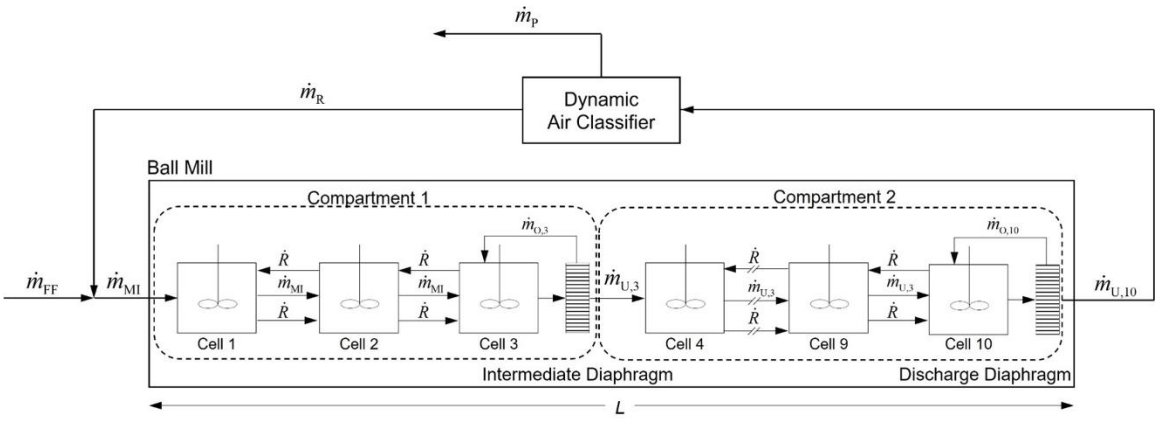

Figure 5.2 Model representation of a two-compartment ball mill in a closed-circuit operation. The ball mill is segmented into 10 perfectly mixed cells in series with axial recirculation rate $\dot{R}$ exchanging between cells.

The degree of mixedness of particles inside the ball mill can be modeled by the number of cells n and axial back-mixing ratio R. Representative values of $n = 10$ and $R = 8.01 \times 10^{-3}$ were taken from Muanpaopong et al. (2022a) and Muanpaopong et al. (2022b). These values were obtained from the best fit of the cell-based PBM without breakage terms on the experimental residence time distribution data of the full-scale two-compartment cement ball mill reported in Austin et al. (1975). A size-discrete, time-continuous form of the TUSSIM with $n = 10$ is given as follows:

$$\frac{dm_{i,z}}{dt}=\begin{cases}-S_{i,z}m_{i,z}+\sum_{j=1}^{i-1}b_{i,j}S_{j,z}m_{j,z} & \\ +\dot{m}_{\mathrm{MI},i}+\left[Rm_{i,z+1}-\left(1+R\right)m_{i,z}\right]\tau_z^{-1} & \text{for } z=1 \\ -S_{i,z}m_{i,z}+\sum_{j=1}^{i-1}b_{i,j}S_{j,z}m_{j,z} & \\ +\left[(1+R)m_{i,z-1}-\left(1+2R\right)m_{i,z}+Rm_{i,z+1}\right]\tau_z^{-1} & \text{for } z=2,5-9 \\ -S_{i,z}m_{i,z}+\sum_{j=1}^{i-1}b_{i,j}S_{j,z}m_{j,z} & \\ +\left[\left(1+R\right)m_{i,z-1}-Rm_{i,z}\right]\tau_z^{-1}-\dot{m}_{\mathrm{U},i,z} & \text{for } z=3,10 \\ -S_{i,z}m_{i,z}+\sum_{j=1}^{i-1}b_{i,j}S_{j,z}m_{j,z} & \\ +\dot{m}_{\mathrm{U},i,z-1}+\left[Rm_{i,z+1}-\left(1+R\right)m_{i,z}\right]\tau_z^{-1} & \text{for } z=4\end{cases} \tag{5.1}$$

with $m_{i,z}(0) = 0$. In Equation (5.1), i and j are size class indices ranging from 1 to N (sink size class) in geometric progression. Also, t is the milling time, z is an index used for cells ranging from 1 to n, $m_{i,z}$ is the mass of particles in size class i of cell z, $S_{i,z}$ is the specific breakage rate parameter of particles size x_i in cell z, and $b_{i,j}$ is breakage distribution parameter. Mass flow rate in size class i of mill inlet stream $\dot{m}_{\mathrm{MI},i}$ is the summation of mass flow rate in size class i of fresh feed stream $\dot{m}_{\mathrm{FF},i}$ and coarse reject stream $\dot{m}_{\mathrm{R},i}$. The mass flow rate of undersized particles in size class i passing through the diaphragm connected with cell index z is denoted as $\dot{m}_{\mathrm{U},i,z}$. The mass flow rate in size class i in the reject stream and product stream can be obtained from the Tromp curve value in size class i T_i as follows: $\dot{m}_{\mathrm{R},i} = \dot{m}_{\mathrm{U},i,10}T_i$ and $\dot{m}_{\mathrm{P},i} = \dot{m}_{\mathrm{U},i,10}(1-T_i)$, respectively.

The average residence time of cell z (τ_z) is the ratio of the total mass hold-up of cell z ($m_{\mathrm{H},z}$) to the mass flow rate through cell z, as mathematically expressed by

$\tau_z = m_{\mathrm{H},z} \Big/ \sum_{i=1}^{N} \dot{m}_{\mathrm{MI},i}$. τ_z is determined by $\tau_z = \tau/n$ with τ being total average residence time without consideration of accumulation of particles retained by diaphragm. Here, $\tau = 14$ min was taken from Austin et al. (1975) and was previously used in Muanpaopong et al. (2022b). For cells z connected to a diaphragm, the mass flow rate of oversized particles in size class i $\dot{m}_{\mathrm{O},i,z}$ can be determined from $\dot{m}_{\mathrm{O},i,z} = (1-P_{i,z})m_{i,z}/\tau_z$, where $P_{i,z}$ is the fraction of particles in size class i passing through the diaphragm connecting to cell z. In consideration of $\dot{m}_{\mathrm{O},i,z}$ that cannot pass through the diaphragm and is recycled to cell index z (see **Figure 5.2**), the definition of τ_z must be modified to King (2001):

$$\tau_z = m_{\mathrm{H},z} \Big/ \left(\sum_{i=1}^{N} \dot{m}_{\mathrm{MI},i} + \sum_{i=1}^{N} \dot{m}_{\mathrm{O},i,z} \right) \tag{5.2}$$

S_i and $b_{i,j}$ parameters must satisfy mass conservation through the following constraints: $S_N = 0$, $b_{i,i} = 0$, and $\sum_{i=j+1}^{N} b_{i,j} = 1$. The set of DAEs in Equations (5.1) and (5.2) were simultaneously solved by the DAE solver because $\dot{m}_{\mathrm{R},i}$ and $\dot{m}_{\mathrm{O},z,i}$ are time-dependent. The steady-state operation was attained when the sum of the absolute difference of PSD in cumulative form over all size classes between two subsequent time steps was less than 10^{-2} (Muanpaopong et al., 2022b). This criterion must be satisfied for all cumulative PSDs of cells connecting to the diaphragm inside the ball mill and all streams around the air classifier, i.e., classifier feed, coarse reject, and fine product. The details of the PBM simulations are provided in Appendix D.1. The simulation results are reported as full PSD in cumulative and differential forms, characteristic sizes (10% passing size x_{10}, median size

x_{50}, and 90% passing size x_{90}), specific surface area (SSA), and Blaine surface area (f_B). Readers are referred to Appendix D.2 for detailed calculations of SSA and f_B.

Besides the two-compartment configuration illustrated in **Figures 5.1 and 5.2**, three- and single-compartment configurations were also simulated. The total length of the mill was kept the same, L = 9.3 m (Genc, 2016), for all compartment configurations for a fair comparison. For the three-compartment mill, the length of each compartment was L_1 = 2.94 m, L_2 = 1.70 m, and L_3 = 4.66 m for compartments 1, 2, and 3, respectively (Genc, 2016). For the two-compartment mill, we set L_1 = 2.94 m and L_2 = 6.36 m. The same degree of mixedness (n = 10 and $R = 8.01 \times 10^{-3}$) was assumed for all compartment configurations.

5.2.2 Selected functions and values of parameters used in PBM simulations

All functions and parameters were taken from the available cement milling literature (Austin et al., 1975; Deniz, 2003; Altun and Benzer, 2014; Genc, 2016). Breakage kinetics parameters (Austin et al., 1975; Deniz, 2003) and internal classification parameters (Genc, 2016) are identical to those used in Muanpaopong et al. (2022b) for open-circuit ball milling without an air classifier. For the modeling of external air classification, the variable Tromp curve model was taken from Altun and Benzer (2014). With these purposeful selections of functions and parameters, the simulation results of the closed-circuit operation in this paper can be directly compared to those of the open-circuit operation without air classifier reported in Muanpaopong et al. (2022b) to elucidate the benefits of the air classifier.

5.2.2.1 Breakage kinetics parameters. The methodology for translating the S_i parameters obtained from lab-scale tests to full-scale ball milling has been extensively discussed in Bilgili (2023) for the integration of the Kotake–Kanda (KK) kinetics model

(Kotake et al., 2002) with the Austin's scale-up factors (Austin et al., 1984), given as follows:

$$S_i = C_1 d_{\mathrm{B}}^{C_3} x_i^{C_4} \exp\left(-\frac{C_2 x_i}{K_1 d_{\mathrm{B}}^{C_5}}\right) K_2 K_3 K_4 \tag{5.3}$$

Here, d_{B} is the ball size represented by the diameter of the grinding ball. Parameters C_1–C_5 were obtained from a lab-scale ball milling of cement clinker in Dezni (2003) as C_1 = 12.86 $\mathrm{min^{-1}\cdot mm^{-0.274}}$, C_2 = 50 $\mathrm{mm^{0.217}}$, C_3 = –0.736, C_4 = 1.01, and C_5 = 1.217. Austin's scale-up factors K_1–K_4 were used to translate S_i estimated from lab-scale data (Deniz, 2003) to full-scale ball mill operation (Genc, 2016). The current work did not address multi-component breakage; that is, only cement clinker was considered. Readers are referred to Appendix D.3 for all details of the lab-scale experimental conditions, full-scale cement ball milling operations, and calculations of the scale-up factors K_1–K_4. The above specific breakage rate parameter S_i was calculated based on a single ball size. When a mixture of P different ball sizes was used, S_i was replaced by $\bar{S}_i$, which was determined by the weighted average of individual $S_{i,p}$ (calculated from single ball size index p) and mass fraction of ball size with index p ($M_{\mathrm{B},p}$) (Austin et al., 1976), expressed as follows:

$$\bar{S}_i = \sum_{p=1}^{P} S_{i,p} M_{\mathrm{B},p} \tag{5.4}$$

Three theoretical spatially uniform BSDs were considered: uniform mass (UM), uniform number (UN), and uniform surface area (USA) of balls. $M_{B,p}$ for the UM, UN, and USA approaches was calculated using the following expressions, respectively:

$$M_{B,p} = 1/P,\ M_{B,p} = d_{B,p}^3 \Big/ \sum_{p=1}^{P} d_{B,p}^3 \text{ , and } M_{B,p} = d_{B,p} \Big/ \sum_{p=1}^{P} d_{B,p} \tag{5.5}$$

Unlike the above spatially uniform ball distribution, the use of a classifying liner causes spatially varying ball classification along the axial length of the mill. The mass fraction of each ball size varied along the mill's axial position in the compartment. All details regarding the variation of ball mass fraction caused by a classifying liner are covered in Appendix D.4.

Regarding the cumulative breakage distribution parameter $B_{i,j}$, the non-normalized form of $B_{i,j}$ expressed in Equation (5.6) was used.

$$B_{i,j} = \phi_0 \left(x_0/x_j\right)^{\theta} \left(x_{i-1}/x_j\right)^{\mu} + \left[1-\phi_0 \left(x_0/x_j\right)^{\theta}\right] \left(x_{i-1}/x_j\right)^{\nu} \tag{5.6}$$

with $b_{i,j} = B_{i,j} - B_{i+1,j}$ and $b_{N,j} = B_{N,j}$

The following values of parameters estimated from lab-scale data for cement clinker ball milling (Austin et al., 1975) were used: ϕ_0 = 0.1755, θ = 0.15, μ = 0.84, ν = 4.5, and x_0 = 26.9 mm. $B_{i,j}$ parameter was assumed to be material dependent and invariant to the operation conditions (similar to Austin et al., 1975; Austin et al., 1976; Chimwani et al., 2014).

5.2.2.2 Internal classification action by diaphragms. The Whiten model (Napier-Munn et al., 1996) has been commonly used to simulate the internal classification of particles due to the diaphragm(s) in cement ball milling (e.g., Lynch et al., 2000; Ozer et al., 2006; Altun, 2018). The fraction of particles in size class *i* passing through the diaphragm that connects to cell index *z* ($P_{i,z}$) is expressed as:

$$P_{i,z} = \left(1-\delta_{\mathrm{d},z}\right)\left\{\frac{\left(1+\beta_{\mathrm{d},z}\beta^{*}_{\mathrm{d},z}x_i/x_{50\mathrm{c,d},z}\right)\left[\exp\left(\alpha_{\mathrm{d},z}\right)-1\right]}{\exp\left(\alpha_{\mathrm{d},z}\beta^{*}_{\mathrm{d},z}x_i/x_{50\mathrm{c,d},z}\right)+\exp\left(\alpha_{\mathrm{d},z}\right)-2}\right\} \tag{5.7}$$

Here, δ is the bypass parameter, α is the sharpness parameter, β is the fish-hook parameter, and $x_{50\mathrm{c}}$ is the corrected cut size. Parameter β^{*} is introduced to satisfy the definition of corrected cut size $x_{50\mathrm{c}}$. Subscript d refers to the diaphragm. We set $\beta_{\mathrm{d}} = 0$ and $\beta_{\mathrm{d}}^{*} = 1$ (no fish-hook) and $\delta_{\mathrm{d}} = 0$ (no bypass fraction) for all diaphragms based on Genc (2016). The values of the parameters α_{d} and $x_{50\mathrm{c,d}}$ for simulating internal classification are listed in **Table 5.1**. It was assumed that the parameters for internal classification were invariant to the operation conditions.

Table 5.1 Parameters Used in the Whiten Model for Simulating Internal Classification Action due to Diaphragms

Number of compartments	Position of diaphragm	Cell index, z (–)	Corrected cut size, $x_{50c,d}$ (mm)	Sharpness parameter, α_d (–)
One	Discharge	10	0.15	2
Two	Intermediate	3	0.70	3
Two	Discharge	10	0.15	2
Three[a]	First	3	0.70	3
Three[a]	Second	5	0.16	3
Three[a]	Discharge	10	0.15	2

[a] Taken from Genc (2016).

5.2.1.3 External classification action by air classifier: A variable Tromp curve model.

A variable Tromp curve model, based on the Whiten model, was developed in Altun and Benzer (2014). The Whiten model (Napier-Munn et al., 1996) can be written in the form of the Tromp curve model using the following expression:

$$T_i = 1-(1-\delta_a)\left\{\frac{\left(1+\beta_a\beta_a^* x_i/x_{50c,a}\right)\left[\exp(\alpha_a)-1\right]}{\exp\left(\alpha_a\beta_a^* x_i/x_{50c,a}\right)+\exp(\alpha_a)-2}\right\} \tag{5.8}$$

Subscript a refers to the air classifier. In Equations (5.9) and (5.10), the variable Tromp curve model (Altun and Benzer, 2014) explicitly expressed all Whiten model parameters as a function of the air classifier's operation parameters (rotor tip speed v and air flow rate Q), dust load of classifier feed DL_{CF}, size of classifier D_c, and the mass flow rate of the classifier feed in 3–36 μm size range (F_{CF}).

$$\delta_{\mathrm{a}} = 0.10467 DL_{\mathrm{CF}}^{1.4171}, \quad \alpha_{\mathrm{a}} = 0.905\left(D_{\mathrm{c}} / DL_{\mathrm{CF}}\right)^{1.2679} \tag{5.9}$$

$$\beta_{\mathrm{a}} = 0.4417 DL_{\mathrm{CF}}^{1.4171} - 0.1293, \quad x_{50\mathrm{c,a}} = \left(Q / vF_{\mathrm{CF}}\right)^{0.7775} / 2.47 \tag{5.10}$$

Parameter β_{a}^{*} is solved at every time step during simulation by setting T_i = 1−(1−δ_{a})/2 at $x_i = x_{50\mathrm{c,a}}$. We also set the minimum value of $DL_{\mathrm{CF}} = 4.203 \times 10^{-1}$ kg/m^3 to satisfy $\beta_{\mathrm{a}} \geq 0$ based on data reported in Altun and Benzer (2014). The classification performance of the air classifier can be evaluated by the bypass fraction δ^{*} and sharpness of the classification κ. The bypass fraction is defined as the minimum Tromp curve value (Klumpar, 1992; FLSmidth, 2012). The sharpness of classification (Klumpar, 1992; FLSmidth, 2012) is defined as the ratio of the particle size corresponding to a Tromp curve value of 0.25 to the particle size corresponding to a Tromp curve value of 0.75.

A rotor tip speed of v = 17 m/s was selected considering the range of actual operations of v = 12.5–24.5 m/s (Altun and Benzer, 2014). Air flow rate Q = 45000 m^3/h was estimated from recommended value of dust load of product (defined as ratio of production rate to air flow rate) of 0.85 kg/m^3 (FLSmidth, 2012). Based on FLSmidth (2021), classifier size D_{c} = 2.36 m is suitable for Q = 45000 m^3/h. In this study, the values of rotor tip speed and air flow rate were kept constant. Readers are referred to Muanpaopong et al. (2021) for a comprehensive investigation of the impact of v and Q in the closed-circuit ball milling of cement clinker.

5.2.3 Optimization of ball milling: a combined global optimizer–DAE solver method

The objective of process optimization is to find the best ball size distribution in each milling compartment that provides the maximum production rate with improved cement product quality from a two-compartment mill circuit. A coupled global optimizer–DAE solver has

been recently developed to determine the breakage parameters and calibrate a PBM for batch milling (Dave et al., 2022; Muanpaopong et al., 2023), and it has been adapted in this study for process optimization. All details about the global optimizer-based process optimization are presented in Appendix D.1. The objective function (OF) to be minimized by the global optimizer was formulated by considering both cement quality and operational perspectives. Although the mill operator considers the Blaine surface area f_B as an indicator of cement quality (Touil et al., 2008), from the end users' point of view, cement quality, is particularly related to the actual cement performance measures such as cement compressive strength. It has been established that cement strength increases with an increase in the fraction of 3–32 μm size range in cement product (M_{3-32}) (Tsivilis et al., 1990; Tsakalakis and Stamboltzis, 2008). Therefore, the following OF was formulated to achieve the targeted Blaine surface area of cement product f_B and maximize M_{3-32} as a cement quality metric, as well as maximizing the production rate, which is equal to the fresh feed rate $\dot{m}_{FF}$ at steady-state operation:

$$\mathrm{OF} = w_1 \left| f_B^{\mathrm{Mod}} - f_B^{\mathrm{Tar}} \right| + w_2 \left| 1 - M_{3-32}^{\mathrm{Mod}} \right| + w_3 / \dot{m}_{FF} \tag{5.11}$$

The weighting factors were w_1 = 1 g/cm^2, w_2 = 1, and w_3 = 1000 kg/min. Superscripts Mod and Tar refer to the model predicted value at steady-state and targeted value, respectively. We set f_B^{Tar} = 3181 cm^2/g, referring to the Blaine surface area of the Run 1 simulation (baseline simulation). Blaine surface area of 3181 cm^2/g (Run 1 simulation) was chosen as the targeted Blaine value f_B^{Tar} for the process optimization because it is in the typical range of actual cement's Blaine (Deolalkar, 2009; Ghalandari

and Iranmanesh, 2020). Setting the value of $f_{\mathrm{B}}^{\mathrm{Tar}}$ too high will likely require an adjustment of the air classifier's parameters (rotor speed and air flow rate), which is beyond the scope of this study. Ball sizes involved in the optimization are referred to as quaternary ball mixtures (the same as Run 1). The independent search variables were the fresh feed rate and mass fraction of each ball size in the quaternary ball mixture in each of the two compartments. Therefore, the total number of variables to be searched was nine. The constraint $\sum_{p}^{P} M_{\mathrm{B},p}^{k} = 1$ must also be applied during optimization to ensure that the sum of mass fraction from all ball sizes in compartment index k is exactly 1.

The global optimizer from MATLAB's global optimization toolbox (The MathWorks, 2022) requires a number of trial points N_{T} as one of the inputs. It is important to mention that there is no guarantee that a global minimum of the objective function will be attained (The MathWorks, 2022). Our previous studies (Dave et al., 2022; Muanpaopong et al., 2023) suggest that solutions obtained from the global optimizer do not change when the number of trial points is sufficiently high. The following values of N_{T} were used: N_{T} = 200 (default minimum value), 500, 1000 (default value suggested by MATLAB (The MathWorks, 2022)), and 1500. The objective function is assumed to attain a global minimum when the absolute value of the percent relative error between two subsequent N_{T} values was less than or equal to 10^{-1} for each variable and objective function.

5.3 Results and Discussion

5.3.1 Spatio-temporal evolution of PSDs in the entire circuit

The dynamic simulation of Run 1 was performed as a baseline process simulation. The results were compared with experimental data reported in the cement milling literature to verify whether our simulation approach and the selected model parameters in Subsection 5.2.2 could lead to a reasonable cement product size at steady-state operation. The simulation was performed for 120 min, and the results were saved every 1 min. The temporal evolution of the PSDs was selectively presented at t = 10, 20, and 30 min, along with a steady-state PSD. For Run 1, a steady-state operation was attained at t = 50 min.

Figure 5.3 demonstrates the temporal evolution of cumulative PSDs inside the ball mill at the mill inlet (cell 1), in front of the intermediate diaphragm (cell 3), and in front of the discharge diaphragms (cell 10). PSDs in front of diaphragms were selected to demonstrate the possible accumulation of coarse particles retained by diaphragms. Generally, the PSD inside the ball mill shifted to a finer size along the mill axial position from the mill inlet to the mill outlet, which is in line with experimental observations in actual cement ball mills (Dundar et al., 2011; Ghalandari and Iranmanesh, 2020). The width of the PSD at the discharge end (cell 10 at L) was narrower than that of the mill inlet (cell 1 at L/10), consistent with past experimental observations (Dundar et al., 2011). In the first 10 min, PSD in the mill inlet stream was almost the same as PSD in the fresh feed stream (not shown in **Figure 5.3**) because the mass flow rate of the coarse reject stream $\dot{m}_R$ was only ~3 kg/min at t = 10 min. In cell 1 at the axial position L/10, particles were quickly broken at the initial milling time. The median size x_{50} decreased from 5.73 mm (fresh feed PSD) to ~1 mm at t = 10 min in cell 1. As milling continued, the cumulative PSD shifted

to the finer size until the steady state was reached at t = 50 min. Whereas fine particles were drastically increased at a milling time of t = 10 min until the steady state (at t = 50 min), the variation of coarse particles was relatively insensitive. For example, the 80% passing size (x_{80}) reduced from 6.21 mm at t = 10 to 4.71 mm at the steady state. As shown in **Figure 5.4**, particles less than 200 μm were recycled from the air classifier for further milling in the ball mill. The mass flow rate of the coarse reject stream increased over time and became saturated when the circuit reached a steady state: $\dot{m}_R$ = 283 kg/min at t = 50 min. Unlike the PSD in cell 1 at L/10, an opposite trend was observed for PSDs in front of the diaphragms (cell 3 at 3L/10 and cell 10 at L). In the case of the PSD in front of the intermediate diaphragm, the PSD became coarser over time until steady-state operation. Some particles coarser than 10 mm were unbroken and accumulated in the first compartment, due to classification by the intermediate diaphragm. The accumulation of coarse particles in the first compartment was also experimentally observed in actual cement ball mills (Dundar et al., 2011).

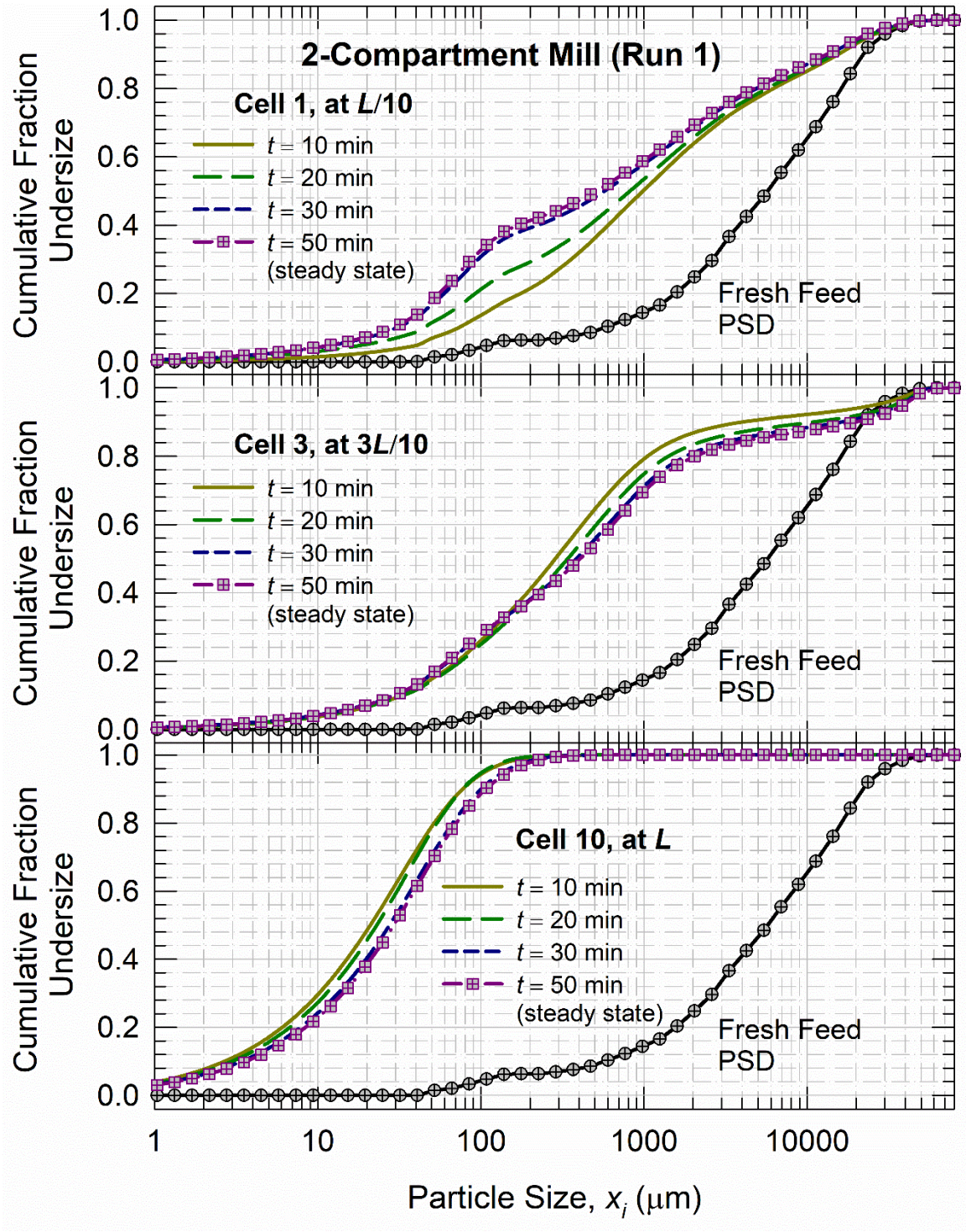

Figure 5.3 Temporal evolution of cumulative PSD in cells 1, 3, and 10 inside the ball mill corresponding to axial positions $L/10$, $3L/10$, and L, respectively, during Run 1. A steady-state operation was reached at t = 50 min.

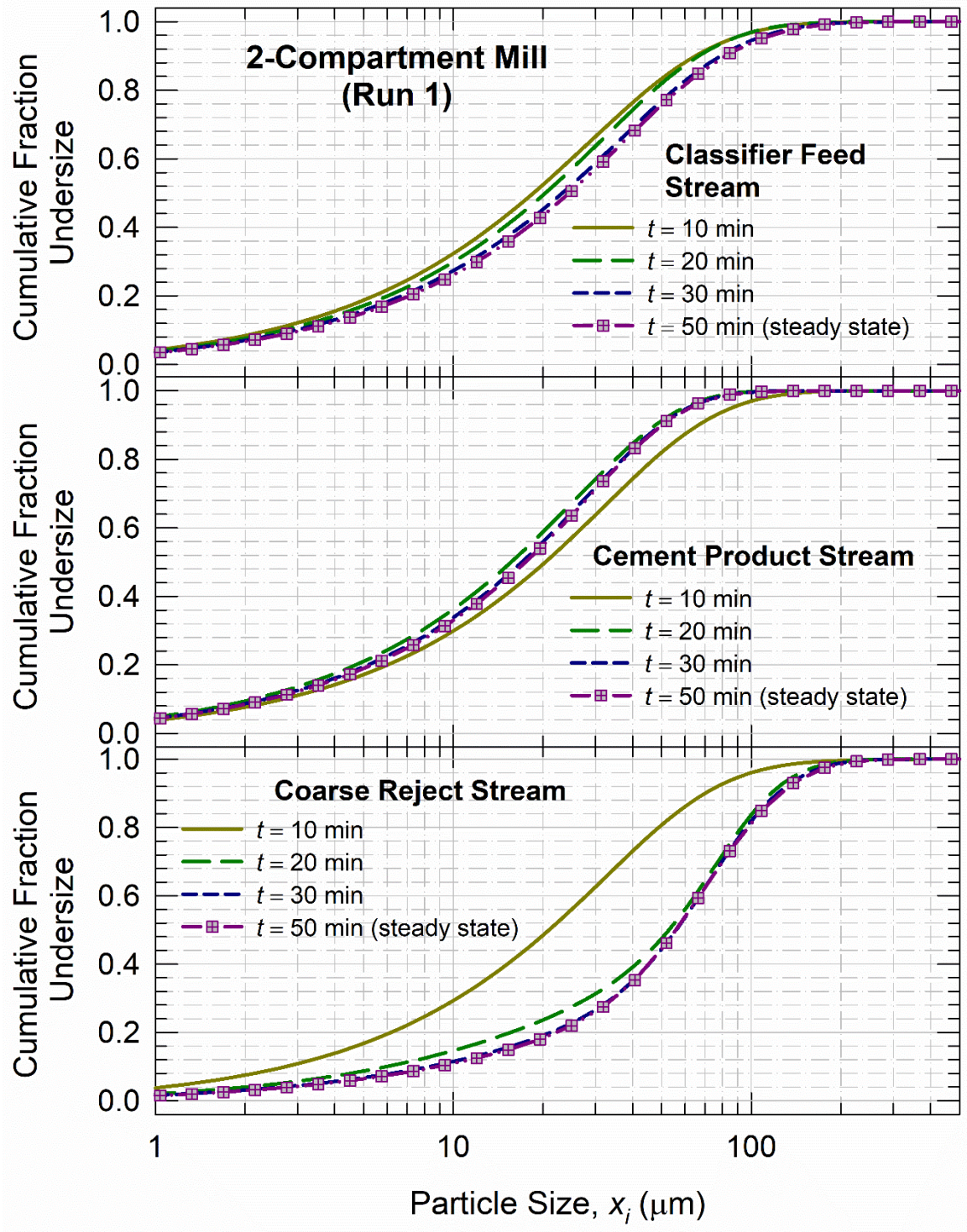

Figure 5.4 Temporal evolution of cumulative PSD in air classifier feed, cement product, and coarse reject streams during Run 1. A steady-state operation was reached at t = 50 min.

As shown in **Figure 5.3**, the simulated median size (x_{50}) of particles in cell 10 at L at the steady state was 29.2 μm, which falls within the experimentally measured median size ranging from 20 μm (Farzanegan et al., 2014) to 35 μm (Dundar et al., 2011) of cement. **Figure 5.4** demonstrates the temporal evolutions of cumulative PSD in streams around the air classifier (i.e., classifier feed, coarse reject, and fine product streams). In comparison with the PSD at cell 10 in **Figure 5.3**, the PSD in the classifier feed stream, i.e., the mill outlet stream after the discharge diaphragm, was slightly finer for $t > 10$ min until the steady state. This simulation result is consistent with experimental observations in closed circuits (Altun, 2018). Based on the simulation results depicted in **Figures 5.3 and 5.4,** the degree of internal classification action of the discharge diaphragm was remarkably smaller than that of the intermediate diaphragm.

Figure 5.5 presents the temporal evolution of the Tromp curve for the air classifier. At $t = 10$ min, classification performance evaluated by bypass fraction and sharpness of classification was relatively sharp: $\delta^* = 3.065 \times 10^{-2}$ and $\kappa = 7.465 \times 10^{-1}$. As the milling operation continued, the classification performance deteriorated, i.e., higher bypass fraction and lower sharpness of classification, until the steady state was reached. At the steady state, the classification was less sharper: $\delta^* = 1.248 \times 10^{-1}$ and $\kappa = 4.336 \times 10^{-1}$. These values are similar to the classification performance of actual full-scale circuit operation reported in Ergin and Ercelebi (1999) as $\delta^* = 9.002 \times 10^{-2}$ and $\kappa = 4.001 \times 10^{-1}$. The variable Tromp curve model's parameters in Equation (5.8) obtained from the PBM simulation at steady state were: $x_{50c,a} = 6.386 \times 10^{-2}$ mm, $\alpha_a = 2.081$, $\beta_a = 4.588 \times 10^{-1}$, $\beta_a^* = 1.354$, and $\delta_a = 1.394 \times 10^{-1}$. These values are all in the actual operating ranges reported in Altun and Benzer (2014). The classification performance worsened over time because

the dust loading of the air classifier increased over time. **Figure 5.4** also shows that the product PSD did not change significantly after t = 10 min. This insensitivity might be attributed to the presence of the air classifier. At the steady state, the product Blaine surface area f_B was 3181 cm^2/g, falling in the range of actual cement's Blaine reported in Deolalkar (2009) and Ghalandari and Iranmanesh (2020). The product median size x_{50} at the steady state was 17.5 μm (similar to x_{50} of actual cement reported by Dundar et al. (2011) and Ghalandari and Iranmanesh (2020)). Overall, these findings establish that the coupling of TUSSIM with a variable Tromp curve model with the specific functions mentioned in Subsection 5.2.2 led to reasonably realistic simulations of the PSDs in the entire closed-circuit ball milling and the quality metrics of the cement product.

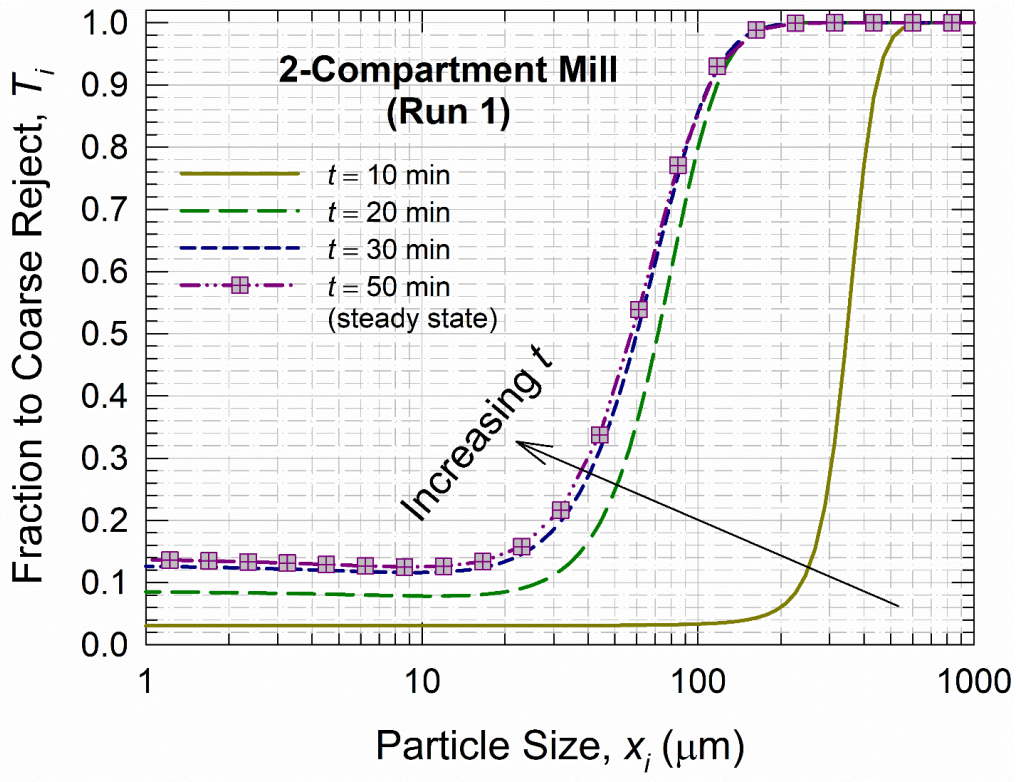

Figure 5.5 Temporal evolution of the Tromp curve of the air classifier during Run 1. A steady-state operation was reached at t = 50 min.

5.3.2 Advantages of air classifier: closed circuit vs. open circuit

We examined the advantages of incorporating an air classifier into an open-circuit ball mill from two perspectives: (a) product fineness improvement and (b) production rate (capacity) improvement. For a fixed fresh feed rate of $\dot{m}_{FF}$ = 640 kg/min, which is equal to the production rate at the steady state, **Figure 5.6(a)** demonstrates the PSDs at the steady state for three streams around the air classifier. The simulated product PSD of the open circuit was taken from Muanpaopong et al. (2022b) under identical ball mill operation conditions. Therefore, a fair comparison can be made to evaluate the actual impact of the air classifier. The simulated cement product fineness of the closed-circuit operation was quantified by SSA = 408 m^2/kg and f_B = 3181 cm^2/g. The open-circuit operation led to SSA = 361 m^2/kg and f_B = 2735 cm^2/g. That is, for a fixed fresh feed rate, fineness improvement was 13% and 16% for SSA and f_B, respectively. A similar finding was reported in a previous steady-state PBM simulation with a fixed Tromp curve (Ergin and Ercelebi, 1999), in which the cement SSA obtained from a closed circuit was higher than that of an open circuit, ranging from 3% to 15% depending on production rate. Further, as shown in **Figure 5.6(a)**, the simulated width of the product PSD for the closed circuit was smaller than that of the open circuit. This simulation observation is also consistent with those in Duda (1985), Ergin (1994), Ergin and Ercelebi (1999) and Muller-Pfeiffer et al. (2000).

To identify capacity improvement, closed-circuit simulations were performed by increasing the fresh feed rate every 1% from the baseline simulation ($\dot{m}_{FF}$ = 640 kg/min) until the simulated SSA of the product was similar to that of the open circuit (SSA = 361 m^2/kg) (Muanpaopong et al., 2022b). Based on the selected operation parameters of the air classifier (v = 17 m/s and Q = 45000 m^3/h), the fresh feed rate was increased up to 736

kg/min with an SSA of 369 m^2/kg. A further increase in the fresh feed rate to 742 kg/min would cause TUSSIM to stop, which first appears to be a purely mathematical problem. However, a detailed analysis suggests that this is an operational failure, an overload of the circuit at this fresh feed rate for the specified air classifier parameters. Specifically, the mass flow rate of the coarse reject stream increased when a higher fresh feed rate was used. This resulted in a smaller average residence time. Once the mass flow rate in the mill inlet stream reaches a certain value, τ_z will approach zero. This behavior is referred to as operation failure. Based on the above discussion, the closed-circuit operation had a 15% higher production rate than the open circuit for a similar product SSA.

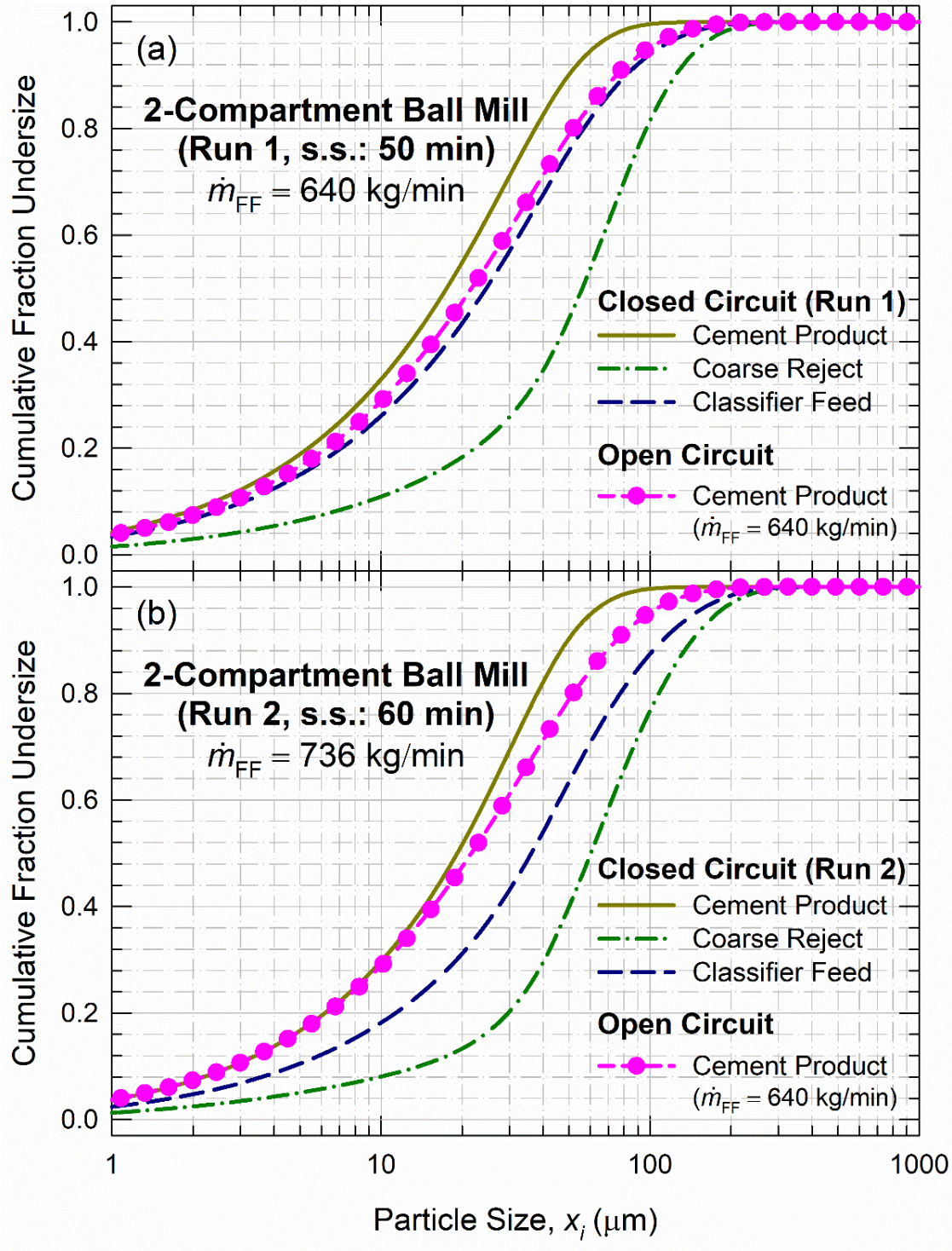

Figure 5.6 Steady-state cumulative PSD of the closed-circuit operation (this work) and open-circuit operation in two operational scenarios: (a) both operations had identical fresh feed rate at $\dot{m}_{FF}$ = 640 kg/min and (b) both operations achieved a similar cement-specific surface area but at a different $\dot{m}_{FF}$ (closed circuit: $\dot{m}_{FF}$ = 736 kg/min and open circuit: $\dot{m}_{FF}$ = 640 kg/min).

Source: Parameters adopted from Muanpaopong et al. (2022b).

Table 5.2 Ball Sizes Used in Various Compartment Configurations of the Simulated Cement Ball Milling

Run no.	Ball designation[a]	Number of compartments[b]	Ball size, d_B (mm)		
			First compartment	Second compartment	Third compartment
1	Quaternary mixture	Two	90, 80, 70, 50	30, 25, 20, 15	–
2[b]	Quaternary mixture	Two	90, 80, 70, 50	30, 25, 20, 15	–
3[b]	Quaternary mixture	Two	90, 80, 70, 50	30, 25, 20, 15	–
4	Single ball size	One	90	–	–
5	Single ball size	One	50	–	–
6	Single ball size	One	15	–	–
7	Quinary mixture	One	90, 70, 50, 30, 20	–	–
8	Ternary mixture	One	90, 70, 50	–	–
9	Ternary mixture	One	50, 30, 20	–	–
10[c]	Ternary mixture	One	50, 30, 20	–	–
11	Ternary mixture	Two	90, 70, 50	50, 30, 20	–
12	Ternary mixture–I	Two	90, 70, 50	40, 30, 20	–
13	Ternary mixture–II	Two	90, 70, 50	30, 20, 15	–
14	Binary mixture–I	Two	90, 50	40, 20	–
15	Binary mixture–II	Two	90, 50	30, 15	–
16	Single ball size	Two	90	30	–
17	Quaternary mixture	Three	90, 80, 70, 60	60, 50, 40, 30	30, 25, 20, 15
18	Ternary mixture	Three	90, 80, 70	60, 50, 40	30, 20, 15
19	Binary mixture	Three	90, 60	60, 30	30, 15
20	Single ball size	Three	90	60	30
21	Quaternary–Binary	Two	90, 80, 70, 50	30, 15[d]	–
22	Quaternary–Binary	Two	90, 80, 70, 50	30, 15	–

[a] Ball size distribution was based on uniform mass distribution, except for the compartment with a classifying liner.
[b] Fresh feed rate of 736 kg/min (Run 2) and 742 kg/min (Run 3). Other runs had a fresh feed rate of 640 kg/min (Muanpaopong et al., 2022b).
[c] Pre-milled feed.
[d] With a classifying liner.

Figure 5.6(b) presents the cumulative PSDs of these conditions. It is important to mention that the above findings are based on the selected values of Q = 45000 m^3/h and v = 17 m/s. A similar conclusion was reported by Ergin (1994) in that the closed-circuit operation has 11–18% higher capacity than the open-circuit operation.

5.3.3 Rationalizing the current best practices in the cement industry

5.3.3.1 Advantages of ball mixtures of different sizes. The next set of simulations (Runs 4–10 in **Table 5.2**) was designed to investigate the advantage of the use of a ball mixture over a single ball size. A *single-compartment mill* was considered to eliminate the influence of having multiple compartments. Three separate single ball sizes (d_B = 90, 50, and 15 mm) were considered (Runs 4–6) along with ternary ball mixtures. **Table 5.3** shows simulated cement fineness, reported as characteristic sizes (x_{10}, x_{50}, and x_{90}), Blain surface area f_B, and specific surface area SSA and **Figure 5.7(a)–5.7(c)** depict the PSDs. The cement product prepared with a ball size of d_B = 90 mm was coarser than the actual cement, based on the Blaine surface area (Deolalkar, 2009). When small ball sizes (d_B = 50 and 15 mm) were used, a steady state could not be attained. This can be explained as follows: when a single ball size of 90 mm was used, no particles coarser than 2 mm were retained in cell 10 in front of the discharge diaphragm. Unlike for 90 mm balls, a bimodal PSD with one of the peaks in the coarse size range (2–60 mm) emerged in cell 10 for 50 and 15 mm balls. This suggests continuous accumulation of the coarse cement particles and deterioration of the milling effectiveness when 50 mm and 15 mm balls were used. Although a quinary mixture of 90, 70, 50, 30, and 20 mm balls can produce a cement product at the steady-state (**Figure 5.7(d)**), the use of such a ball mixture is not feasible because of potentially high ball wear/damage with a high max. ball size to min. ball size

ratio (9:2) in the single-compartment mill (Muanpaopong et al., 2022b). In the case of the coarse ternary mixture of 90, 70, and 50 mm balls, the product Blaine surface area was smaller than the actual cement (Deolalkar, 2009) and the product PSD was coarser (**Figure 5.7(e)** vs. **Figure 5.7(d)**). A steady state was not reached when a ternary mixture of 50, 30, and 20 mm balls was used because of the accumulation of >10 mm particles in cell 10 of the mill (**Figure 5.7(f)**).

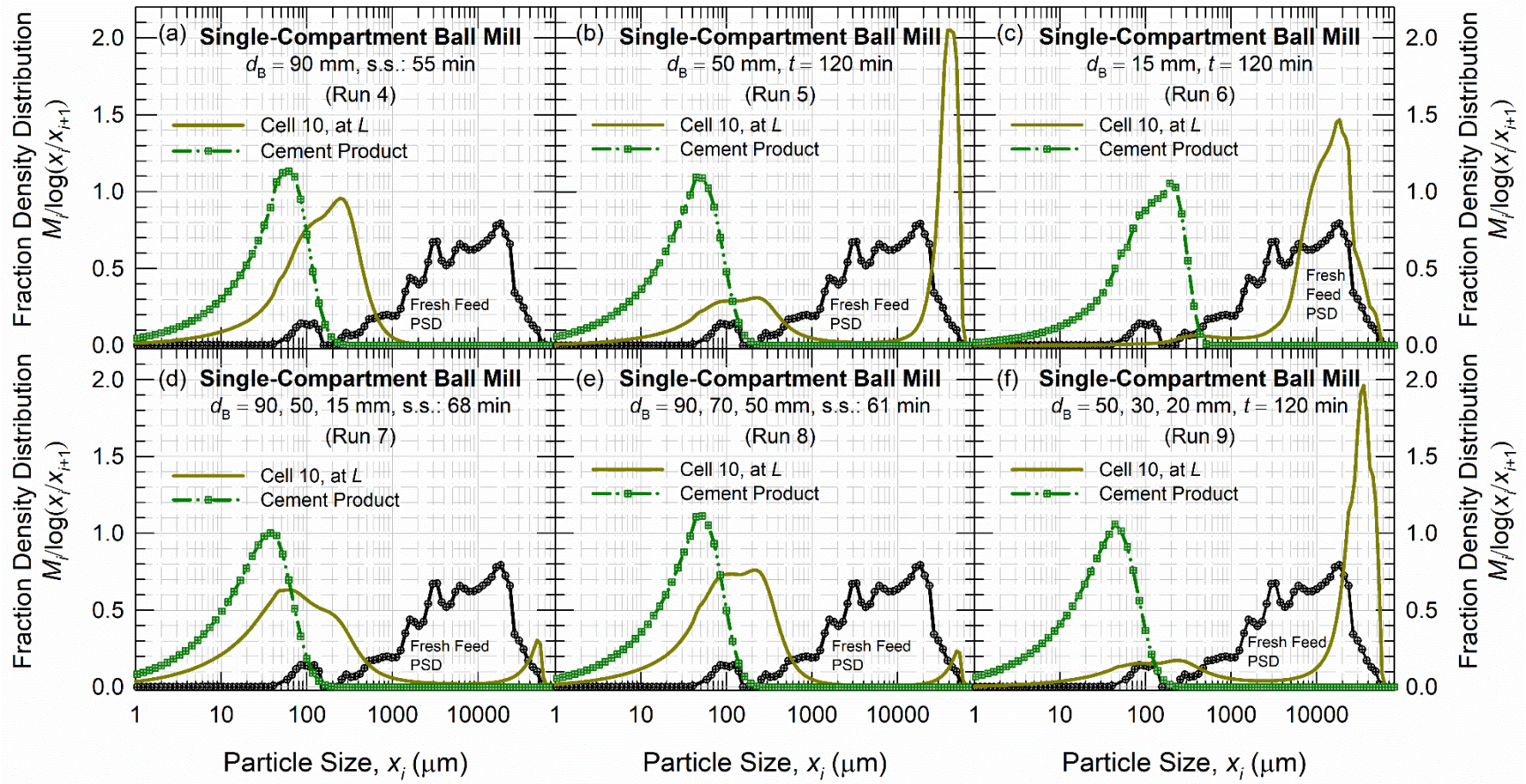

Figure 5.7 Differential PSD in cell 10 (in front of discharge diaphragm) and cement product of a single-compartment mill at steady state or at 120 min (max. operation time simulated): (a)–(c) various single ball sizes (Runs 4–6) and (d)–(f) quinary and ternary ball mixtures (Runs 7–9).

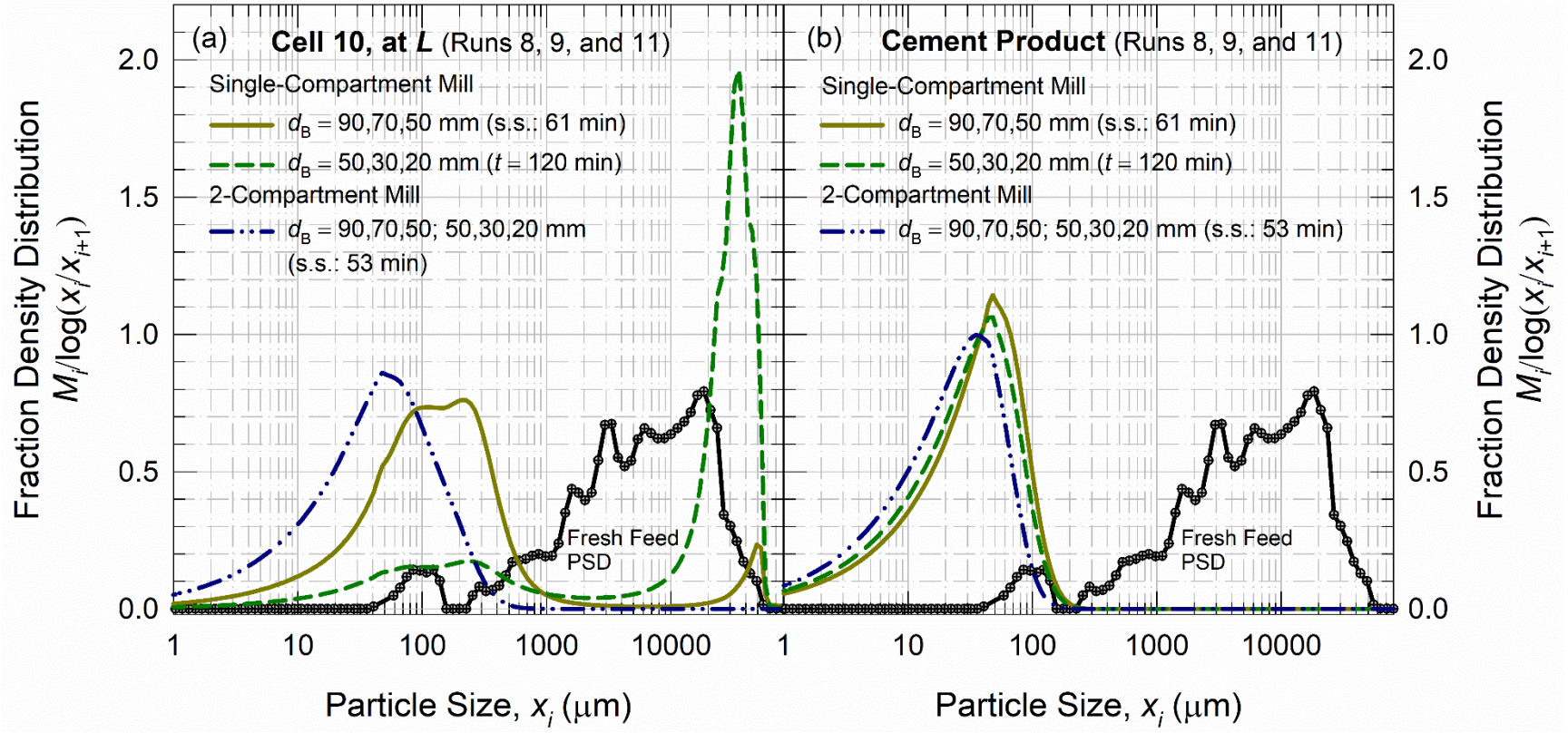

Figure 5.8 Differential PSD at steady state or at 120 min (max. operation time simulated) for a single-compartment mill (Runs 7–9) and two-compartment mill (Run 11): (a) in cell 10 (in front of discharge diaphragm) and (b) cement product after air classifier.

When a small top ball size (50 and 15 mm balls) was used, total mass hold-up continued to increase without limit. It is important to mention that the impact of total mass hold-up on S_i was addressed through the scale-up factor K_3 with the void filling fraction U (refer to Appendix D.3). When U is higher than the void filling fraction of the lab-scale test (U_T), breakage kinetics slow down. As a result, coarser particles accumulate more, and a steady state cannot be attained. In an actual mill, the ball mill will probably choke and eventually shut down. In fact, a single-compartment mill is commonly used by integrating a ball milling circuit with a pre-milling unit, such as a hydraulic roller press (HRP) (Strasser, 2002; Altun, 2016). Hence, we performed another simulation with a ternary mixture of 50, 30, and 20 mm balls, but this time, the fresh feed PSD was pre-milled by HRP, i.e., a finer fresh feed PSD (Run 10). Here, the pre-milled fresh feed PSD was taken from Genc and Benzer (2016). The simulation results show that the Blaine surface area of the cement product was 3234 cm^2/g and a steady state was attained at t = 59 min. A small portion of particles coarser than 10 mm accumulated in cell 10 at the steady state when the pre-milled fresh feed by HRP was used.

Overall, the current simulations for a single-compartment mill in a closed-circuit operation suggest a similar conclusion to that for the open-circuit operation (Muanpaopong et al., 2022b): a single-compartment mill entails a pre-milled feed for proper steady-state operation for producing a desirable cement product.

5.3.3.2 Advantages of multi-compartment mill configurations. Actual ball sizes used in industrial mills maintain a certain ratio between the largest and smallest balls to prevent damage when small balls are hit by large balls (see Muanpaopong et al. (2022b) and references therein). For example, it may not be practical to load a quinary mixture of 90,

70, 50, 30, and 20 mm balls to the same milling compartment (refer to Run 7). A multi-compartment mill provides flexibility in loading different ball combinations into different compartments while minimizing the max. ball size to min. ball size ratio, thus mitigating ball wear. In this section, a multi-compartment mill refers to a two-compartment mill, as it has been commonly used in closed-circuit operations (Deolalkar, 2009; Altun, 2018). To compare the performance of single vs. two-compartment mills, the coarser ternary ball mixture (d_B = 90, 70, and 50 mm) of Run 8 and the finer ternary ball mixture (d_B = 50, 30, and 20 mm) of Run 9 were placed into the first and second compartments of a two-compartment mill, respectively (Run 11). Note that Run 7 (single compartment) and Run 11 (two-compartment) have identical ball sizes.

Figure 5.8 compares the differential PSDs in cell 10 (in front of the discharge diaphragm) and the cement product after the air classifier. Operations using a single-compartment mill with a ternary mixture of coarse ball sizes (Run 8) could not produce a desirable cement fineness, and a ternary mixture of fine ball sizes could not attain steady-state operation (Run 9). When a ball mill has two compartments with ternary coarse and fine ball mixtures (Run 11), the ball mill operation yielded a finer product PSD than a single-compartment mill with a quinary mixture of identical ball sizes (Run 7), while producing the actual cement Blaine SSA. In the two-compartment operation, no particles coarser than 600 μm were retained in cell 10 in front of the discharge diaphragm, and a steady state was attained at t = 53 min. On the other hand, a bimodal PSD was observed in cell 10 for all single-compartment operations. These simulation results demonstrate the advantage of a two-compartment mill over a single-compartment mill: finer PSD and

flexibility to locate a wide range of ball sizes in two compartments, thus mitigating ball wear/damage significantly.

5.3.3.3 Rationales for selecting the number of compartments in a multi-compartment mill. Although a three-compartment mill is a suggested design for open-circuit operation (Deolalkar, 2009), a two-compartment mill can produce a cement product fineness similar to that of a three-compartment mill, as demonstrated by Genc (2016) and Muanpaopong et al. (2022b). The previous work (Muanpaopong et al., 2022b) highlighted that this similarity in product fineness originated from the ball sizes used. In this section, we performed simulations with various ball combinations using two- and three-compartment configurations (Runs 1, 12–20). The total length was kept the same for both mill configurations for a fair comparison. A wide range of ball mixtures (quaternary, ternary, and binary mixtures) along with a single ball size were simulated. It should be mentioned that ball mixtures in a two-compartment mill could not be designed to have the same ball sizes as those used in a three-compartment mill. For this reason, we proposed two designations of ternary and binary ball mixtures for a two-compartment mill. Ternary mixture–I and binary mixture–I had the smallest ball size of 20 mm, while ternary mixture–II and binary mixture–II had the smallest ball size of 15 mm. As shown in **Figure 5.9(a)** for the two-compartment mill and **Figure 5.9(b)** for the three-compartment mill, operation with ball mixtures produced a finer product (higher SSA and f_B) in comparison with single ball size, as expected. Considering the two-compartment mill, the ternary mixture–II with 15 mm balls yields a finer product than the ternary mixture–I with 20 mm balls. Similarly, binary mixture–II with 15 mm balls yielded a finer product than binary mixture–I with 20 mm balls. Comparing ball mixtures with 15 mm balls, the product

fineness from the binary and ternary mixtures was finer than the quaternary mixture. A similar simulation result was reported in Muanpaopong et al. (2022b).

The analysis of **Figure 5.9** and **Table 5.3** suggests that a two-compartment mill yielded a finer product than that of a three-compartment mill for all ball combinations, with the smallest ball being 15 mm. These simulation results rationalize why the design of an industry mill operating in a closed-circuit operation is suggested to be a two-compartment mill (Deolalkar, 2009). As per comprehensive simulations with various choices of ball mixtures, there is no gain in having a three-compartment mill in terms of the product fineness perspective. In view of actual operation, having a lower number of milling compartments not only leads to lower capital cost, but also lower operating cost because of lower pressure loss across the ball mill due to the presence of one less diaphragm. Overall, our simulation results with various ball combinations justify the best industry practice reported by Deolalkar (2009): closed-circuit operation is optimal with two compartments.

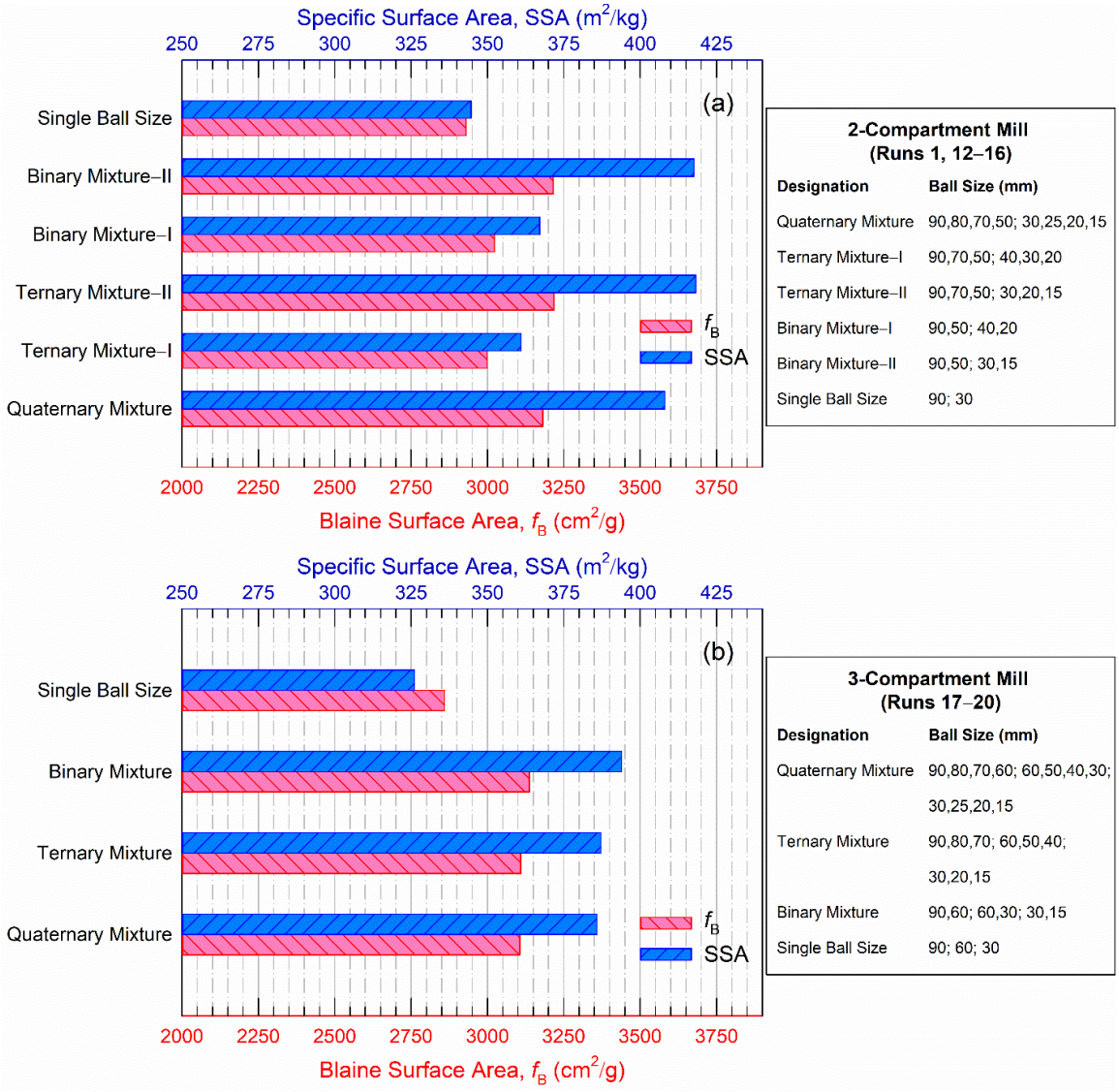

Figure 5.9 Blaine surface area and specific surface area of cement products obtained from steady-state operation of (a) a two-compartment mill and (b) a three-compartment mill with various ball mixtures in the respective compartments. Ball size distribution was based on uniform mass distribution.

Table 5.3 Characteristic Particle Sizes, Specific and Blaine Surface Areas at the Steady-State Operation

Run no.	Number of compartments	10% passing size, x_{10} (μm)	Median size, x_{50} (μm)	90% passing size, x_{90} (μm)	Specific surface area, SSA (m^2/kg)	Blaine surface area, f_B (cm^2/g)
1	Two	2.41	17.5	49.8	408	3181
2	Two	2.78	19.2	49.5	369	3155
3	Two	_[a]	_[a]	_[a]	_[a]	_[a]
4	One	5.72	39.0	93.6	212	2339
5	One	_[b]	_[b]	_[b]	_[b]	_[b]
6	One	_[b]	_[b]	_[b]	_[b]	_[b]
7	One	3.07	22.0	60.0	339	2896
8	One	4.71	32.6	81.1	245	2516
9	One	_[b]	_[b]	_[b]	_[b]	_[b]
10[c]	One	2.36	16.6	48.7	407	3234
11	Two	2.93	21.0	57.2	352	2959
12	Two	2.83	20.4	55.7	361	2999
13	Two	2.33	17.0	48.7	418	3218
14	Two	2.77	20.0	54.9	367	3023
15	Two	2.34	17.0	48.8	418	3215
16	Two	3.01	21.6	58.2	345	2930
17	Three	2.60	18.7	51.8	386	3106
18	Three	2.59	18.7	51.7	387	3109
19	Three	2.53	18.3	50.9	394	3137
20	Three	3.24	23.1	60.7	326	2859
21	Two	2.30	16.8	48.2	423	3234
22	Two	2.35	17.1	49.0	416	3208

[a] Operational failure was detected;

[b] Steady-state operation was not reached during 120 min of simulation.

[c] Pre-milled feed.

5.3.4 Impact of ball size distribution: uniform mass, number, and surface area of balls

Table 5.4 lists the design of the simulation (Runs 1, 23–30) to examine the impact of various theoretical BSDs in the two-compartment mill. A quaternary ball mixture (first compartment: d_B = 90, 80, 70, 50 mm and second compartment: d_B = 30, 25, 20, 15 mm) was used for each compartment, and only the ball mass fraction was changed based on UM, UN, and USA approaches (refer to Equation (5.5)). Generally, for a given ball mixture, UM has the smallest mean ball size, while UN has the largest mean ball size. **Figure 5.10** shows cement product fineness as characteristic sizes (x_{10}, x_{50}, and x_{90}), SSA, and the Blaine surface area. An obvious trend is that similar product fineness was obtained when the same ball distribution in the second compartment remained the same. That is, product fineness may be modulated by BSD in the second compartment. In comparison with the coarsest product (UN–UN distribution), the product obtained from the UM–UM distribution as the best BSD yielded a 9% higher product SSA. A similar result was reported in an open-circuit operation (Muanpaopong et al., 2022b). However, considering all 9 BSDs, the mean product SSA was calculated as 3124 cm^2/g with a relative standard deviation of ~2%. We note that these theoretical ball size distributions did not lead to markedly different product fineness, thus justifying optimization of ball size distributions, as will be discussed in Subsection 5.3.6.

Table 5.4 Theoretical Ball Size Distributions Used in the Simulations for the Two-Compartment Mill Configuration

Run no.	Ball size distribution[a]		Mean ball size, $d_{B,Mean}$ (mm)	
	First compartment[b]	Second compartment[c]	First compartment[b]	Second compartment[c]
1	UM	UM	72.5	22.5
23	UN	UM	80.1	22.5
24	USA	UM	75.7	22.5
25	UM	UN	72.5	26.1
26	UN	UN	80.1	26.1
27	USA	UN	75.5	26.1
28	UM	USA	72.5	23.9
29	UN	USA	80.1	23.9
30	USA	USA	75.5	23.9

[a] UM: uniform mass, UN: uniform number, and USA: uniform surface area.

[b] First compartment: d_B = 90, 80, 70, and 50 mm.

[c] Second compartment: d_B = 30, 25, 20, and 15 mm.

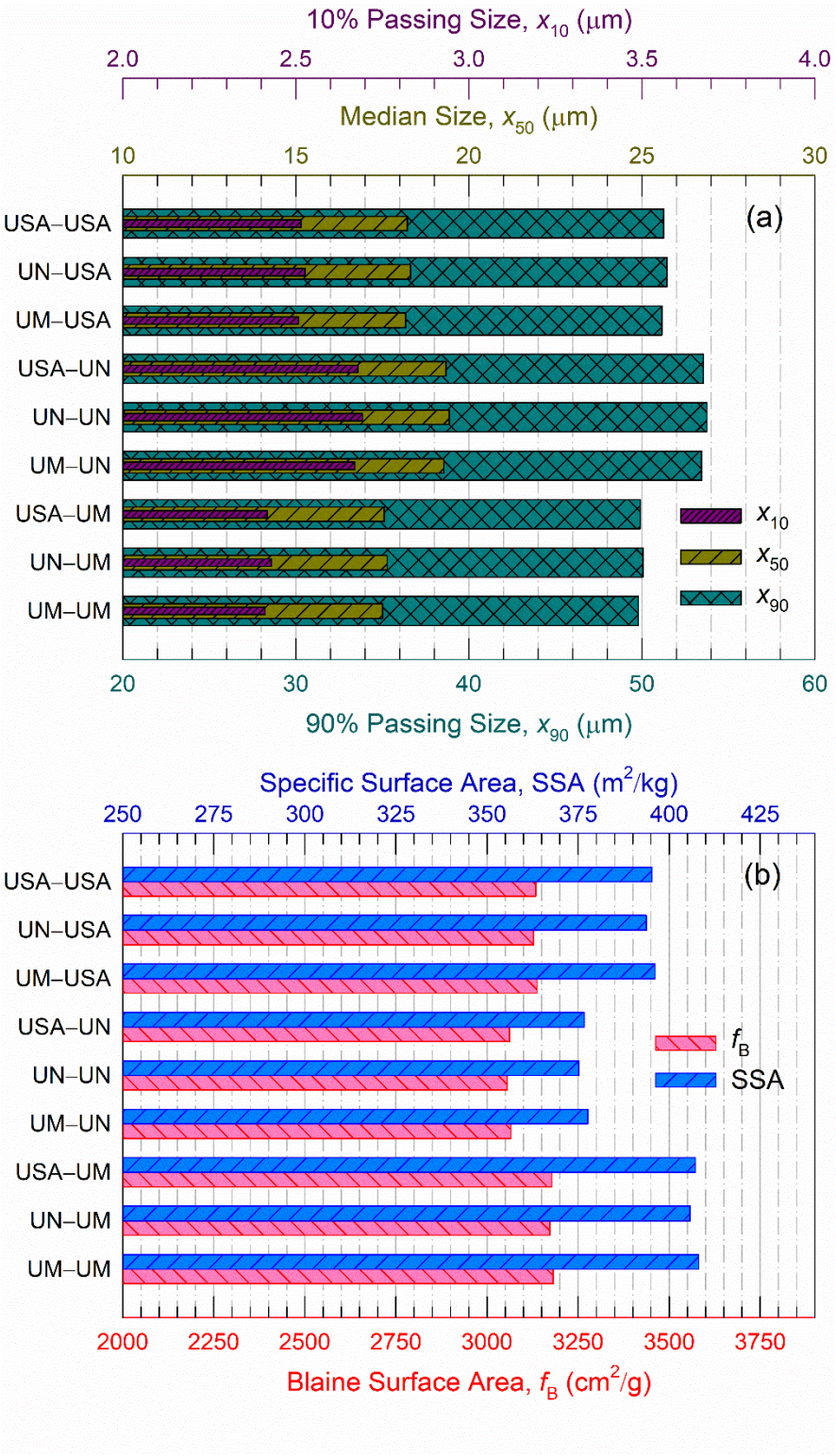

Figure 5.10 Steady-state cement products from a two-compartment ball mill with various ball size distributions (see Table 5.4): (a) characteristic particle sizes (10% passing size, median size, and 90% passing size) and (b) the Blaine surface area and specific surface area.

5.3.5 Impact of ball classification on cement fineness

Classifying liners fitted with internal mill shells have been used in the second (fine) milling compartments of cement milling (Altun, 2018; Ghalandari and Iranmanesh, 2020). This liner type leads to a spatially varying ball mixture along the axial position of the mill. In a two-compartment mill, a binary ball mixture of 15 mm and 30 mm balls was considered in the second compartment, with the quaternary mixture used in the first compartment (Run 21). A wide BSD was not considered here because of the insufficient data reported in the literature. For this reason, an additional simulation with a binary ball mixture of 15 and 30 mm based on UM (Run 22) was performed as a basis for comparison. The spatial variation pattern due to the classifying liner was kept similar to the actual data reported in Altun (2018). **Table D.2** reports the mass fractions of 30 mm and 15 mm balls in the second compartment for each axial position, taken from Muanpaopong et al. (2022b). The simulation results of the cement product fineness with a classifying liner (Run 21) were SSA = 423 m^2/kg and f_B = 3234 cm^2/g. Based on the UM distribution (Run 22), the simulated cement fineness was SSA = 416 m^2/kg and f_B = 3208 cm^2/g. Our simulation results suggest that the impact of ball classification on cement product fineness was insignificant in comparison with uniformly mixed balls based on UM. The percent improvement with a classifying liner was 1.7% and 0.81% for SSA and f_B, respectively. This result is in line with actual data obtained from a full-scale cement ball mill in a closed circuit (Fortsch, 2006).

5.3.6 Process optimization: optimal ball mixtures in the first and second compartments

Process optimization was performed using TUSSIM in the inverse problem framework. **Table 5.5** lists the initial guess, lower bound, and upper bound used during optimization for each of the nine independent search variables, along with the solution obtained from the global optimizer for various values of N_T. For all N_T values, the predicted Blaine surface area of the cement product at steady state was the same as the targeted Blaine value. It is apparent that as the value of N_T was increased, the objective function value (refer to Equation (5.11)) became smaller. By increasing N_T from 200 to 500, the mass fraction of 90 mm balls changed from 7.789×10^{-1} to 3.797×10^{-2}. In the case of N_T = 200, the obtained solution of $\dot{m}_R$ = 501 kg/min was stuck at around initial guess value of 500 kg/min. When the N_T value was high enough (N_T = 1500), the objective function value did not change in comparison to the solution obtained from the preceding N_T value, i.e., N_T = 1000. The maximum absolute value of percent relative error between solutions of N_T = 1000 and N_T = 1500 was 4.723×10^{-7}, occurring at the mass fraction of 15 mm balls. Therefore, the global minimum was deemed to be reached when N_T = 1000, according to the criterion mentioned in Subsection 5.2.3. The analysis of $\%M_B$ values in the two compartments (**Table 5.5**) suggests that the mean ball size in the first compartment was 78.2 mm (slightly finer than the value for a UN distribution of different ball sizes: 80.1 mm), while the mean ball size in the second compartment was 21.0 mm (slightly finer than the value for a UM distribution of different ball sizes: 22.5 mm). In comparison with baseline (Run 1) simulation, capacity was improved by 14% (optimum condition: 732 kg/min vs. Run 1 simulation: 640 kg/min). The mass fraction in the 3–32 um size range ($M_{3–32}$) of the

optimum condition was 0.6168, which slightly improved by ~1% in comparison with the Run 1 simulation ($M_{3–32}$ = 0.6159).

We performed the last simulation with ball mixtures from an industrial cement mill reported in Altun (2018) and compared its performance to the optimal ball mixtures identified in our study. Based on Altun (2018), in the first compartment, a quaternary mixture of 90, 80, 70, and 60 mm balls was used with mass fractions of 0.25, 0.30, 0.25, and 0.20, respectively. In the second compartment, a senary mixture of 50, 40, 30, 25, 20, and 17 mm balls was used with mass fractions of 0.08, 0.10, 0.20, 0.24, 0.23, and 0.15, respectively. For a fair comparison, the fresh feed rate was kept the same as that obtained from the global optimizer ($\dot{m}_{FF}$ = 732 kg/min). As shown in **Figure 5.11**, the product PSD simulated for the ball mixtures obtained from the global optimizer was finer than that for the ball mixtures from Altun (2018). The ball mixtures from Altun (2018) yielded product Blaine surface area f_B = 3042 cm^2/g, SSA = 343.7 m^2/kg, and $M_{3–32}$ = 0.5871), whereas the optimal ball mixtures in this work yielded Blaine surface area f_B = 3181 cm^2/g (5% higher), SSA = 380.5 m^2/kg (11% higher), and $M_{3–32}$ = 0.6212 (6% higher). Overall, our process optimization scheme using the combined global optimizer–DAE solver has clearly demonstrated the opportunity for optimizing BSD to obtain a higher production rate or a finer cement product with a higher mass fraction in 3–32 μm range at a fixed capacity.

Table 5.5 Solutions Obtained from the Global Optimizer for Various Values of the Number of Trial Points N_T along with the Predicted Cement Quality Metrics at the Steady-state Operation of a Two-compartment Ball Mill

Variable and predicted cement quality metrics	Initial guess	Bound constraint		Solution obtained from the global optimizer			
		Lower bound	Upper bound	N_T = 200	N_T = 500	N_T = 1000	N_T = 1500
%M_B of d_B = 90 mm (–)[a]	25	0	100	78.89	3.797	46.06	46.06
%M_B of d_B = 80 mm (–)[a]	25	0	100	10.75	8.897	10.21	10.21
%M_B of d_B = 70 mm (–)[a]	25	0	100	6.860	4.108	33.40	33.40
%M_B of d_B = 50 mm (–)[a]	25	0	100	3.497	83.20	10.33	10.33
%M_B of d_B = 30 mm (–)[b]	25	0	100	90.06	4.646	19.29	19.29
%M_B of d_B = 25 mm (–)[b]	25	0	100	0.7894	53.17	20.39	20.39
%M_B of d_B = 20 mm (–)[b]	25	0	100	1.300	7.818	22.09	22.09
%M_B of d_B = 15 mm (–)[b]	25	0	100	7.856	34.37	38.23	38.23
Fresh feed rate, $\dot{m}_{FF}$ (kg/min)	500	100	1500	501.0	662.8	732.0	732.0
Predicted cement Blaine surface area, f_B^{Mod} (cm^2/g)				3181	3181	3181	3181
Predicted cement mass fraction at 3–32 μm, M_{3-32}^{Mod}(–)				0.6117	0.6168	0.6212	0.6212
Objective function value (–)				2.384	1.892	1.745	1.745

[a] First compartment.

[b] Second compartment.

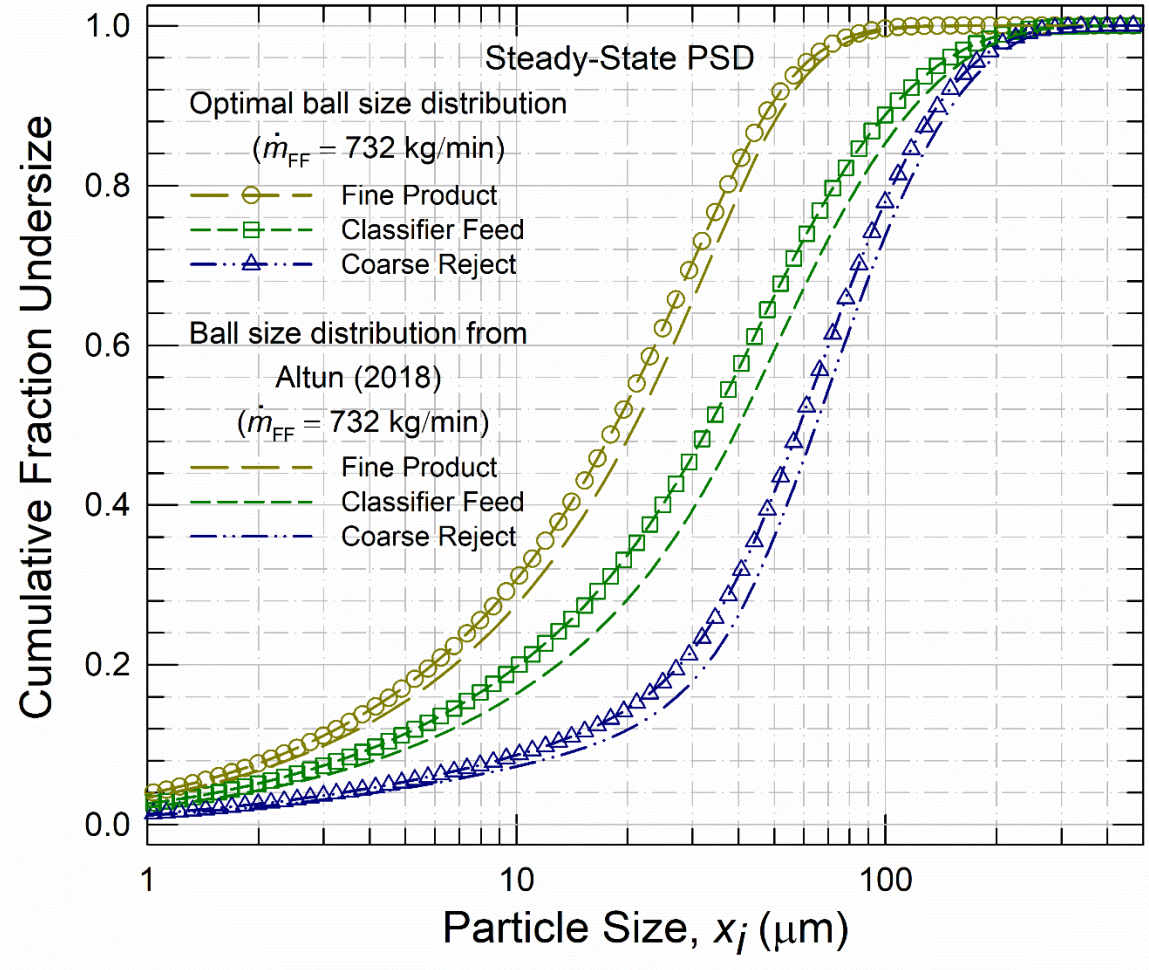

Figure 5.11 Steady-state cumulative PSDs around air classifier for a two-compartment ball mill with optimized ball mixtures in both compartments and industrial ball mixtures. Fresh feed rate $\dot{m}_{FF}$ = 732 kg/min, obtained from global optimization, was used for both simulations.
Source: Industrial ball mixtures taken from Altun (2018)

5.4 Conclusions

Simulation of full-scale closed-circuit ball milling of cement clinker was performed by TUSSIM with a variable Tromp curve model for classification. Parameters were obtained from the cement milling literature. The dynamic simulation results are not only consistent with experimental observations in full-scale operation but also provide simulation-based

evidence to explain the current best practices in the cement industry. Some of the principal results from this comprehensive simulation study include the following:

- Integrating an air classifier into a continuous ball mill can increase a product's specific surface area by ~13% at a fixed production rate. Alternatively, the production rate can be increased by 15% at a similar specific surface area of the cement product.
- A single-compartment ball mill entails a pre-milled feed for proper, steady-state operation, meeting the salient cement product quality attributes.
- In a closed-circuit operation, a two-compartment mill outperforms a three-compartment mill.
- A closed-circuit mill operation may fail due to overload especially at high fresh feed rates; hence, capacity improvement initiatives must carefully examine optimization of the ball size distributions, ball materials, and/or air classifier parameters.
- The use of different theoretical BSDs and classifying liner do not lead to significant improvement of product fineness.

As a major novelty, a combined global optimizer–DAE solver method was used to identify optimal BSD in each milling compartment that yielded a maximum production rate with desirable cement quality attributes. The production rate with optimal BSD was 14% higher than the baseline condition with a slightly higher mass fraction in 3–32 um range of cement product ($M_{3–32}$), reflecting a higher cement compressive strength. Interestingly, our optimal ball mixtures yielded a finer cement product and a much higher $M_{3–32}$ value, compared with the actual BSD used in a full-scale cement ball mill for a fixed production rate. Overall, the TUSSIM for ball milling coupled with the variable Tromp curve model for classification could help industry practitioners gain fundamental insights into the complicated behavior of their specific closed-circuit ball mills and optimize their existing operations.

CHAPTER 6

A COMPARATIVE ANALYSIS OF STEEL AND ALUMINA BALLS IN FINE MILLING OF CEMENT CLINKER VIA PBM AND DEM

This study explored the breakage kinetics of cement clinker in a lab-scale ball mill loaded with steel or alumina balls of 20, 30, and 40 mm sizes and their mixtures. The temporal evolution of the particle size distribution (PSD) was measured by sieving and laser diffraction. A global optimizer-based back-calculation method, based on a population balance model (PBM), was developed to estimate the breakage parameters. The ball motion in the mill was simulated via discrete element method (DEM). Our results show that steel balls achieved faster breakage of clinker into finer particles than alumina balls, which was explained by the higher total–mean energy dissipation rates of the steel balls. The PSD became finer as smaller balls were used. This study suggests that replacement of steel balls with alumina balls in continuous ball mills could provide significant energy savings if one accounts for the slower breakage with the alumina balls.

6.1 Introduction

Tumbling ball mill, which is a horizontally rotating cylinder that contains milling media as balls to break particles during its operation, is known as an energy-intensive and inefficient unit operation (Fuerstenau and Abouzeid, 2002). Over the past decades, considering the milling media as an integral design element of these mills, impact of ball size (Austin et al., 1976; Kotake et al., 2002; Deniz, 2003; Kotake et al., 2004), ball size distribution (BSD) (Erdem and Ergun, 2009; Oksuzoglu and Ucurum 2016; Cayirli, 2018), and ball material type (Umucu et al., 2014; Umucu and Deniz, 2015) have been investigated. In

modern cement milling plants, ball mill is not solely operated but is usually coupled with a hydraulic roller press (HRP) (Aydogan et al., 2006; Altun et al., 2011), with the latter acting as a pre-milling unit. A combined ball mill–HRP circuit results in lower total specific power consumption (Patzelt, 1992; Aydogan and Benzer, 2011). Briefly, HRP consists of two rollers with one roller being movable. During the operation of the HRP, these two rollers rotate in different directions. Hydraulic pressure is transferred to press the cement clinker from hydraulic cylinders through the moveable roller. The HRP not only reduces the size of raw materials before they are fed to the subsequent ball mill but also generates extra flaws and cracks inside particles (Fuerstenau et al., 1999; Valery and Jankovic, 2002; Celik and Oner, 2006; Yin et al., 2017; Aminalroaya and Pourghahramani, 2022) because of the high pressure it applies. As a result, pre-milled cement clinker obtained from HRP breaks more easily than raw cement clinker (Camalan and Hosten, 2015).

One of the current topics in the cement industry for reducing power consumption in cement ball milling is to properly replace conventional steel balls with alternative types of ball materials, including ceramic balls (Fernandez and Hui, 2017; Nowack, 2022). The rationale for this replacement is that, in comparison to steel balls, ceramic balls have significantly lower ball density (approximately half the density of steel balls) (Nowack, 2022) and lower wear rate (Fang et al., 2022). According to the power consumption model (Brochot et al., 2006), the power draw of a ball mill is directly proportional to the ball density. Therefore, a drastic reduction in the power draw of ball mill may be achieved with ceramic balls. Fernandez and Hui (2017) recently compared the actual performance of a full-scale cement ball mill by replacing steel balls with alumina balls in the fine milling

compartment. Based on various process configurations of cement ball mill (e.g., open circuit, closed circuit, and closed circuit with HRP), their experimental results (Fernandez and Hui, 2017) showed that the electric current of the ball mill can be reduced in the range of 20%–40%, with the production rate changing between −5% and +10%. Unfortunately, only the electric current data of the mills were reported; detailed operation conditions such as ball size, BSD, feed size, and most importantly, the product particles' sizes were not reported. Clearly, the results in this trade article cannot be reproduced or verified. Moreover, it is unclear whether the difference in performance originated from the use of alumina balls or other factors that were not even reported. Data available in the milling literature are rather limited regarding the use of ceramic balls (Umucu and Deniz, 2015), specifically alumina balls (Umucu et al., 2014; Fernandez and Hui, 2017; Rivera-Madrid et al., 2019), in dry tumbling ball milling, while most studies have widely applied ceramic balls in other types of mills, such as stirred media mills (e.g., Rule et al., 2008; Hassall et al., 2016; Zhang et al., 2021; Zhang et al., 2022; Patino et al., 2022).

A quantitative understanding of the impacts of the ball sizes and ball material type such as steel vs. ceramic during ball milling warrants the use of a population balance model (PBM). PBM has been widely used to describe the timewise evolution of particle size distribution (PSD) for various particulate processes, including ball milling (Prasher, 1987; King, 2001). It is fundamentally based on two parameters: (i) specific breakage rate parameter S_i and (ii) breakage distribution parameter $b_{i,j}$ with its cumulative form $B_{i,j}$. For a well-mixed batch ball mill, the time-continuous, size-discrete form of the PBM assuming first-order (linear) breakage is given as follows (Austin, 1971/1972):

$$\frac{dM_i}{dt} = -S_i M_i + \sum_{j=1}^{i-1} b_{i,j} S_j M_j \text{ , } N \geq i \geq j \geq 1 \text{ with } M_i(0) = M_{i,\text{ini}} \tag{6.1}$$

In Equation (6.1), i and j are size class indices that extend from size class 1, which contains the coarsest particles of size x_1, to size class N, which contains the finest particles of size x_N. t is milling time, and M_i is mass fraction in size class i. $M_{i,\text{ini}}$ is the mass fraction of feed material in size class i.

Several methods have been proposed to determine the breakage parameters, i.e., S_i and $B_{i,j}$, from experimentally obtained milling data from laboratory-scale or pilot-scale ball mills. These methods can be broadly categorized as *direct measurement method* (e.g., Kanda et al., 1999; Katubilwa and Moys, 2009; Gupta et al., 2012; Petrakis et al., 2017; Nava et al., 2021) and *back-calculation method* (Klimpel and Austin, 1977; Gupta et al., 1981; Purker et al., 1086; Capece et al., 2011a; Gupta et al., 2012), the latter of which is used in the current study. Both methods have unique disadvantages. The direct measurement method entails separate milling of multiple narrowly-sized feed samples covering the whole size range of interest; hence, it is experimentally time-consuming (Devaswithin et al., 1988). For the detailed experimental procedure of direct measurement methods, readers can refer to Austin and Bhatia (1971/1972) for the determination of S_i using the so-called one-size fraction method, and Austin and Luckie (1971/1972) for the determination of $B_{i,j}$ using multiple methods referred to as the BI, BII, and BIII. Practically, the ratio of the upper sieve size to the lower sieve size is either $2^{1/2}$ or $2^{1/4}$ (Austin and Bhatia, 1971/1972); consequently, the narrowly-sized feeds significantly deviate from ideal "monodispersed samples." Finally, narrow fractions of fine particles are hard to prepare based on commercially available sieve sizes (Jillavenkatesa et al., 2001).

Therefore, extrapolation from coarser particles to fine particles of interest is required, which may cause additional errors, especially for fine milling applications. Most of these issues have been circumvented by the back-calculation method, wherein a local optimizer along with the analytical or numerical solution of the PBM is used to estimate the PBM parameters via direct fitting to the temporal evolution of the PSD (Klimpel and Austin, 1977). However, finding a realistic set of PBM parameters has been a major challenge since the early inception of the back-calculation method (Klimpel and Austin, 1977). The local optimizer could get stuck with a local optimum, leading to an erroneous set of parameters; therefore, the use of a global optimization scheme in the back-calculation is warranted.

Our literature review revealed that the comparison of breakage kinetics between steel balls and alumina balls in ball milling within the context of PBM is rather limited and while DEM has been widely used for simulating dry tumbling ball mills (e.g., Mishra and Rajamani, 1992; Weerasekara et al., 2013; Weerasekara et al., 2016; Li et al., 2022); to the best knowledge of the authors, there exists no comparative DEM study of ball material impact in direct connection with the PBM parameters and breakage kinetics. In one study, the breakage parameters were estimated via a direct measurement method, wherein only four narrow sieve sizes were used, with the smallest sieve size of −63+45 μm, along with 30 mm balls (Umucu et al., 2014). The timewise evolution of whole PSD predicted from the PBM parameters was not compared with the experimental data. Thus, the prediction capability of PBM parameters obtained from Umucu et al. (2014) to model the timewise evolution of PSD during milling is still unknown. Raw cement clinker without pre-milling was used as a material of interest in most PBM studies of ball milling (Austin et al., 1981a;

Deniz, 2003; Deniz, 2012; Camalan, 2021b). In another study (Camalan and Hosten, 2015), breakage parameters of the raw cement clinker and pre-milled cement clinker obtained from a full-scale HRP was compared. The parameters were estimated using a direct measurement method with three narrow sieve cuts, with −850+600 μm being the smallest particle size. It is well known that specific cement quality is influenced by a specific size range. For example, mass fraction of 3–32 μm range contributes most to cement strength (Tsivilis et al., 1990). Hence, the PBM parameters obtained from Camalan and Hosten (2015) must be extrapolated to the fine particle size range of cement, which could cause errors in the actual use of PBM for predicting the evolution of PSD in cement ball milling. Our literature review suggests that none of these studies has examined the impact of the ball material–size on the breakage parameters of pre-milled cement clinker with a natural PSD, which was obtained from an industrial HRP, within the context of a global optimizer-based back-calculation method.

The aim of this study was to examine the breakage kinetics of pre-milled cement clinker in a lab-scale ball mill loaded with steel or alumina balls of 20, 30, and 40 mm sizes as well as their mixtures. In each milling experiment, samples of the milled clinker were collected at various time intervals, and the temporal evolution of the PSD was measured by a combination of sieving followed by laser diffraction. The specific breakage rate and breakage distribution parameters of the cement clinker were determined by a global optimizer-based back calculation method in which an ordinary differential equation (ODE) solver generates the model solution while the optimizer minimizes the sum-of-squared residuals. Before the actual parameter estimation, we tested the accuracy of this novel back-calculation method on synthetic (artificial) batch milling data without/with random errors.

Subsequently, as a first step to understanding the role of ball material properties and getting insights that are yet not found in the literature, we resorted to DEM simulations and determined the collisional energy spectra considering the steel and alumina balls separately and related the findings to the observed breakage kinetics. It is expected that this comprehensive, combined experimental–modeling study provides powder technologists and industry practitioners with a new global optimizer-based back–calculation methodology and will generate various insights into the impacts of ball material–sizes on the breakage kinetics of pre-milled cement clinker. In the end, we will also discuss about the feasibility of the replacement of conventional steel balls with alumina balls in full-scale continuous ball mills considering the impacts on the power consumption and breakage kinetics.

6.2 Experimental

6.2.1 Materials

Cement clinker was pre-milled by a full-scale HRP (SCG Cement, Bangkok, Thailand) and used in dry ball milling experiments. Pre-milled cement clinker, i.e., the HRP product, was taken from a ball milling circuit at a point in the conveying line before it was fed to the ball mill. Steel balls and alumina balls were purchased from Magotteaux Co., Ltd. (Saraburi, Thailand) and Hira Ceramics Co., Ltd. (Toyota, Aichi, Japan), respectively.

6.2.2 Methods

6.2.2.1 Dry ball milling. A laboratory ball mill, 30 cm in diameter and 30 cm in length, was operated batchwise with a fixed rotation speed of 71 rpm, corresponding to 92% of the critical speed (similar to Aras et al. (2012)). Its steel lining plate is smooth, without a lifter.

Steel and alumina balls of 20, 30, and 40 mm sizes were selected for our experiments because such sizes were used in the fine-milling compartment of a full-scale continuous ball mill. Each ball size was used in separate milling experiments to yield information about the ball size impact. In the experiments, total mass of steel balls and alumina balls were 29.8 and 13.4 kg, respectively, corresponding to the bulk ball filling fraction of 0.3 for both cases (same as Umucu et al., 2014; Umucu and Deniz, 2015). The mass of pre-milled cement clinker was 1.6 kg, corresponding to the bulk powder interstitial filling fraction of 0.35 (similar to Austin et al., 1981a; Kotake et al., 2002). The PSD was measured at the milling times of 0 (initial feed PSD), 2, 4, 8, 12, 20, and 28 min. As pointed out by Klimpel and Austin (1970), back-calculation from experimental data with too short milling does not provide accurate back-calculated parameters in the fine particle size domain. Here, the clinker was milled for 28 min, yielding a fine powder, which is approximately in the range of general cement product PSD.

Two model validation experiments were conducted using a mixture of 20, 30, and 40 mm ball sizes with uniform mass BSD for steel balls and alumina balls separately. Mixtures of different ball types were not considered. Feed PSD of the cement clinker was different from that used in the back-calculation procedure mentioned above. We loaded balls layer-by-layer into the mill starting with 40 mm balls followed by 30 mm and then 20 mm balls. In these two ball-mixture experiments, all other operational conditions were kept the same as those in the milling experiments with single ball sizes. The samples taken at different times were subjected to particle size analysis.

6.2.2.2 Particle size measurements. PSD of the pre-milled cement clinker was measured for various milling times using sieve opening sizes of 9.5, 4.75, 2.34, 1.18, and 0.6 mm. Sieving was performed using an AS 200 control vibratory sieve shaker (Retsch GmbH, Haan, Germany). We took the entire amount of cement clinker sample for sieving. After sieving, the cement clinker was returned to the ball mill for further milling. Five grams were taken only of particle sizes less than 0.6 mm on the pan to be measured via laser diffraction using a Malvern Panalytical particle size analyzer (model Mastersizer 3000) (Malvern, UK) in dry dispersion mode with an air pressure of 3 bar (gauge). PSD was determined based on the Mie scattering theory. A refractive index of 1.68 and imaginary refractive index (absorption index) of 0.01 were used for gray cement clinker based on data from the vendor. It is a reasonable assumption that the particles with different sizes have the same particle density. Therefore, the volume-based PSD and the mass-based PSD are assumed to be identical. With this common assumption, the PSDs obtained from the laser diffraction and the sieving were properly merged. A similar approach was used by Austin et al. (1990). Specifically, the sieve data of coarse fraction (≥0.6 mm) was combined with the laser diffraction data for <0.6 mm fraction, in which the particle size was measured down to 1.8 μm, to represent the full PSD.

6.3 Theoretical

6.3.1 Specific functional forms used in the PBM

In the back-calculation method to estimate breakage parameters, the lower the number of parameters to be estimated, the higher the accuracy of the back-calculated results (Klimpel and Austin, 1977; Kwon and Cho, 2021). Although most PBM studies have used the Austin model for the specific breakage rate parameter S_i (e.g., Austin et al., 1976; Katubilwa and Moys, 2009; Bwalya et al., 2014; Chimwani et al., 2014), we selected the Kotake–Kanda (KK) kinetic model (Kotake et al., 2002) (see Equation (6.2)) as the KK model is similar to the Austin model with the advantage of having one less parameter (Bilgili, 2023).

$$S_i = C_1 d_B^m x_i^\alpha \exp\left(-\frac{C_2 x_i}{d_B^n}\right) \tag{6.2}$$

Here, the milling operation–material dependent parameters are $C_1 > 0$ and $C_2 > 0$; m and $n > 0$ are the ball size exponents, while $\alpha > 0$ is the particle size exponent. Ball size d_B is represented by its diameter. Surprisingly, only a few studies have determined S_i via the KK model (Kotake et al., 2002; Deniz, 2003; Kotake et al., 2004). Moreover, they determined S_i by the direct measurement method; hence, as another novelty of this study, parameters of the KK model were estimated via the back-calculation method for the first time. KK model (Kotake et al., 2002; Deniz, 2003; Kotake et al., 2004) and Austin model (Bwalya et al., 2014) predict that (i) a maximum specific breakage rate S_m exists during the milling with abnormal breakage and that (ii) S_m is either monotone increasing function of d_B with or without approach to a plateau or a non-decreasing function of d_B. Within the

context of the KK model, S_m can be expressed as a function of d_B by $S_m = C_1 e^{-\alpha}(\alpha/C_2)^{\alpha} d_B^{\alpha n+m}$ (Bilgili, 2023). In view of the overwhelming experimental evidence (Kotake et al., 2002; Deniz, 2003; Kotake et al., 2004; Erdem and Ergun, 2009), we constrain the ball size exponent in the following form: $\alpha n+m \geq 0$ during back-calculation.

The following non-normalized cumulative breakage distribution parameter $B_{i,j}$ was chosen, which contains four non-negative model parameters, i.e., ϕ_0, μ, ν, and θ (see e.g. Austin and Luckie, 1971/1972; Austin et al., 1981a).

$$B_{i,j} = \phi_0 \left(\frac{x_0}{x_j}\right)^{\theta} \left(\frac{x_{i-1}}{x_j}\right)^{\mu} + \left[1 - \phi_0 \left(\frac{x_0}{x_j}\right)^{\theta}\right] \left(\frac{x_{i-1}}{x_j}\right)^{\nu} \tag{6.3}$$

We assumed that $B_{i,j}$ depends on the ball material used, but is invariant to the ball sizes although it may change with ball sizes owing to the different impact forces during collisions (Austin et al., 1982). We justified this assumption based on Deniz (2012) for the cement clinker: the $B_{i,j}$ parameter did not drastically vary in a certain range of ball sizes (d_B = 20–41 mm), which was also the range used in this study. Note that $B_{i,j}$ reduces to the commonly used, normalized (self-similar) form for $\theta = 0$. To ensure $0 \leq B_{i,j} \leq 1$ in view of $x_{i-1}/x_j \leq 1$, we invoked $0 \leq \phi_0(x_0/x_j)^{\theta} \leq 1$ and derived the following inequality constraint:

$$\theta + \frac{\ln \phi_0}{\ln\left(x_0/x_{\min}\right)} \leq 0 \tag{6.4}$$

which restricts the values of θ and ϕ_0. For example, based on Austin et al. (1975) with referenced size x_0 = 1 mm and minimum size $x_{min} = 1\times10^{-3}$ mm, θ = 0.15 and ϕ_0 = 0.288 (determined from ϕ_1 = 0.1755 with x_1 = 26.9 mm) satisfy the inequality constraint in Equation (6.4). Without going into details, we found that fitting without constraint in Equation (6.4), ϕ_0 and θ values for steel ball and ϕ_0 and ν values for alumina ball reached the upper bound and some $B_{i,j}$ values were greater than 1, which is physically implausible. By definition, the breakage distribution parameters were calculated by $b_{i,j} = B_{i,j} - B_{i+1,j}$ and $b_{N,j} = B_{N,j}$.

When a mixture of different ball sizes is used in ball milling, S_i of the ball mixture represented by $\overline{S_i}$ can be calculated by the mass fraction of individual single ball size ($M_{B,g}$) and its individual $S_{i,g}$, with g being the index for single ball size ranging from 1 to G (Austin et al., 1976). $\overline{S_i}$ is given by

$$\overline{S_i} = \sum_{g=1}^{G} M_{B,g} S_{i,g} \tag{6.5}$$

Owing to the conservation of mass, the following constraints must be imposed on S_i and $b_{i,j}$:

$$S_N = 0,\ \sum_{i=j+1}^{N} b_{i,j} = 1,\ b_{i,i} = 0 \tag{6.6}$$

6.3.2 Parameter estimation via back-calculation/optimization

The currently available back-calculation method in the context of PBM makes use of a coupled local optimizer–ODE solver with a single set of initial guesses for the parameters (e.g., Klimpel and Austin, 1977; Capece et al., 2011a). A common issue with the back-calculation method is that the obtained solution may correspond to a local optimum (Zhang and Kavetsky, 1993) or a flat surface around an objective function (Kwon and Cho, 2021). As a result, the solution obtained from back-calculation may depend on the initial guess for the parameters significantly. Our exploratory work suggested that the combined *local optimizer*–ODE solver method (Capece et al., 2011a) was not suitable when the KK model and non-normalized $B_{i,j}$ were used, which contains 9 parameters to be estimated —except when a normalized $B_{i,j}$ was justified with only 6 parameters. Specifically, the solution was strongly dependent on the particular initial guess for the parameters.

To mitigate the aforementioned issues in this study, we developed a *global optimizer*-based back-calculation method in which the optimizer is coupled with the ODE solver and coded in MATLAB using the global optimization toolbox (The MathWorks, 2022). Similar to (Capece et al., 2011a), the optimizer requires a set of initial guess and number of trial points (N_T) as an input (The MathWorks, 2022). Readers are referred to Appendix B for the details of the coupled global optimizer–ODE solver including functions used and tolerances set. The sum of squared residuals (*SSR*) was used as the objective function to be minimized. *SSR* is based on cumulative fraction undersize *F*, which is consistent with previous studies (Capece et al., 2011a; Kwon and Cho, 2021), and is

expressed as

$$SSR = \sum_{g=1}^{G} \sum_{z=1}^{Z} \sum_{k=1}^{K} \left(F_{k,z,g}^{\text{Mod}} - F_{k,z,g}^{\text{Exp}} \right)^2 \tag{6.7}$$

Here, k is the experimental size class ranging from 1 to K, and z running up to Z represents the milling time index for the sampling. Superscripts Mod and Exp denote model fitted value and experimental value, respectively. To account for the degrees of freedom for the different model fits, the standard error of the residuals (*SER*) presented in Equation (6.8) was also determined. *SER* indicates how well the model fits the experimental data.

$$SER = \sqrt{SSR / \left(D_{\text{C}} - E \right)} \tag{6.8}$$

where D_{C} is the total number of comparisons between the experimental data and the model predictions. E is the total number of model parameters.

During each iteration of the optimizer, the PBM in Equation (6.1) consisting of a set of ODEs along with the KK model for S_i in Equation (6.2), the non-normalized function for $B_{i,j}$ in Equation (6.3), and constraints in Equations (6.4) and (6.6), is solved using an ODE solver (see details in Appendix E.1). The solution of the PBM yields mass fraction, which was then converted to cumulative PSD via Equation (6.9). Subsequently, cumulative PSDs belonging to simulation size class i are interpolated to experimental size class k for the *SSR* calculation.

$$F_i = \sum_{r=i}^{N} M_r \tag{6.9}$$

6.3.2.1 Assessing the accuracy of the global optimizer-based back-calculation method. Before fitting our own experimental data, we generated synthetic data on the PSD evolution in a ball mill and fitted it using the global optimizer-based back-calculation method to assess its accuracy. Here, synthetic data were treated as experimental data during the back-calculation. First, we generated error-free synthetic PSD evolution by solving the PBM in Equation (6.1) with the KK model and the normalized $B_{i,j}$ (i.e., setting $\theta = 0$ in Equation (6.3)), along with the constraints in Equation (6.6). Specifically, parameters of S_i were taken from Bilgili (2023): $C_1 = 1.075 \times 10^2$ mm$^{0.4944}$·min^{-1}, $C_2 = 3.706 \times 10^2$ mm$^{1.364}$, $m = -1.444$, $n = 2.364$, and $\alpha = 9.496 \times 10^{-1}$, while parameters of $B_{i,j}$ were taken from Katubilwa et al. (2011): $\phi_0 = 5.100 \times 10^{-1}$, $\mu = 5.300 \times 10^{-1}$, and $\nu = 3.200$. These PBM parameters refer to the South African coal milling data reported in Katubilwa et al. (2011). For all synthetic batch ball milling data, a Gaussian PSD with a mean size of 20 mm and a standard deviation of 2 mm was used as the initial PSD, in which the Gaussian PSD was generated using the function "normpdf" in MATLAB version 9.12, which is consistent with Bilgili (2023). The timewise evolution of the PSD was generated for $t = 0.5$, 1, 2, 4, and 8 min.

We also generated synthetic batch ball milling data with two different random errors: 5% and 10%. The solution obtained from Equation (6.1) with the above-mentioned parameters for the mass fraction in size class M_i is referred to as the error-free mass fraction. The mass fraction with random error for size class i (M_i^*) at milling time t except

initial feed (t = 0) was determined via the following equation (same as Capece et al., 2011b):

$$M_i^* = M_i\left(1+\varepsilon_r r_i\right) \tag{6.10}$$

Here, r_i is the random number of particles in size class i. In this study, r_i was generated using the function "randn" in MATLAB, which provides a random number drawn from the standard normal distribution. Random error parameter ε_r of 0.05 and 0.10 were used to generate synthetic data with 5% and 10% random errors, respectively. When ε_r = 0, M_i^* is equal to M_i as in error-free data. After introduction of random error into the error-free data, M_i^* was re-normalized by the sum of M_i^* to ensure that the sum of the mass fraction for all size classes was exactly 1. The re-normalized M_i^* was subsequently converted to its cumulative form for further use in the objective function during optimization. In all model fits of synthetic data, the number of trial points N_T was set to 200 as the default minimum value, unless stated otherwise. Readers are referred to Appendix E.2 for size discretization and all back-calculation details for synthetic batch ball milling data without and with 5% and 10% random errors.

6.3.2.2 Fitting the experimental data on ball milling. Experimental data on ball milling for pre-milled cement clinker obtained for each ball material type (i.e., steel balls and alumina balls) were separately fitted using the global optimizer-based back-calculation method. The initial PSD obtained from the experiments was interpolated to the simulation size class as the initial condition of the PBM in Equation (6.1). PSDs at six milling times (t = 2, 4, 8, 12, 20, and 28 min) for three different single ball sizes (d_B = 20, 30, and 40 mm) were simultaneously fitted. The referenced particle size x_0 and minimum particle size

x_{min} were set to 1 and 1×10^{-3} mm, respectively (see Subsection 6.3.1). The optimization was executed for three different numbers of trial points N_T: 200 as the default minimum, 10^3 as the default (The MathWorks, 2022), and 10^4 to ensure a global optimum was obtained. Appendix E.3 presents details of size discretization and the back-calculation of the PBM parameters from the actual experimental data.

6.3.3 Model validation: predicting the PSD evolution for the ball mixtures

We explored whether the PBM parameters estimated could be used to predict the timewise evolution of the PSD of pre-milled cement clinker in milling conditions that were not used during the model calibration in Subsection 6.3.2.2. To this end, a separate PBM simulation was performed to predict the timewise evolution of PSD for a *mixture* of 20, 30, and 40 mm balls for an initial clinker feed PSD that was different from the one used in the model calibration. S_i associated with the ball mixture of three ball sizes (G = 3), based on the uniform mass of BSD (i.e, $M_{B,p}$ = 1/G), was determined via Equation (6.5). We chose uniform mass of BSD because it has been shown to cause faster milling than uniform number of BSD for the same ball material (Katubilwa and Moys, 2009; Muanpaopong et al., 2022b). Therefore, in the steel ball mixture, 9.93 kg of each ball size was used, whereas 4.47 kg of each ball size was used in the alumina ball mixture. So, Unlike S_i, $B_{i,j}$ was directly taken for simulation of the ball mixture based on the assumption that the $B_{i,j}$ was not sensitive to the ball sizes in the range 20–40 mm.

6.3.4 Discrete element method

DEM, as a mechanistic simulation approach, was used to study the ball motion and collisional energy spectra in the ball mill, which could give some insights about the observed impact of ball material–size. Here, the commercial software EDEM (Altair

EDEM, UK) was used. We performed a simple ball mill simulation in the absence of clinker particles (similar to Bian et al., 2017; Kime, 2017; Chimwani and Bwalya, 2020; AmanNejad et al., 2021). With the limited computational capability, the actual feed PSD of the cement clinker cannot be simulated without major simplifications and excessively long computation. Hence, in this investigation, we restricted our simulations to ball motion and ball–ball impacts only. All dimensions of the ball mill (diameter and length) and rotation speed were identical to those in the experiments (refer to Subsection 6.2.2.1). For the simulation of the ball mixture case, different ball sizes were generated layer by layer in the order of 40, 30, and 20 mm balls, consistent with the experimental procedure. Each DEM simulation was run for 20 s ball rotation, and data were logged every 10^{-1} s of ball motion. Although the balls were completely generated within the ball mill within 2 s, we did not include data in the first 5 s to eliminate data during the start-up period. The DEM simulation results in Subsection 6.4.4 were based on time-averaging between 5 and 20 s.

The Hertz–Mindlin (no slip) model (Hertz, 1882; Mindlin, 1949) was selected to resolve ball interactions because of its accurate and efficient calculation of force (DEM Solutions, 2014) and common use in simulating a ball mill (e.g., Powell et al., 2011; Li et al., 2013; Jiang et al., 2018). Readers are referred to DEM Solutions (2014) and Cundall and Strack (1979) for a detailed description of the DEM. The Hertz–Mindlin (no slip) model requires input parameters for material properties and contact coefficients. While the actual values of the material properties for both steel and alumina balls were used, all contact coefficients were taken from the available milling literature (Auerkari, 1996; Hou, 2014; Bian et al., 2017). Readers are referred to Appendix E.4 for details of the parameters used in this DEM simulation. As the calibration of all coefficients is beyond the scope of

this study, the results should be treated as a relative comparison between steel and alumina balls. Dissipation energy was used as a measure of the collision/impact energy that occurred during ball milling, in line with earlier reports (Wang et al., 2012; Capece et al., 2014).

6.4 Results and Discussion

6.4.1 Feasibility of the global optimizer-based back-calculation method

Table 6.1 shows the results of the PBM parameters that were fitted to the error-free synthetic data, along with the initial guess and bound constraints. The global optimization even with N_T = 200, which is the default minimum, converged to the same S_i and $B_{i,j}$ parameters as those taken from Bilgili (2023) and Katubilwa and Moys (2011) for South African coal milling, which were used to generate the error-free synthetic data. Practically speaking, the back-calculation method was error-free when error-free synthetic data were used in the parameter estimation. As experimental data always contain errors, a more realistic assessment of the capability of the optimizer was performed by subsequently fitting synthetic data imposed with two different levels of random errors, namely 5% and 10%. **Table 6.2** presents the results of the optimization with the synthetic data with 5% and 10% random errors. A set of initial guesses and bound constraints was identical to that for the error-free data fitting. **Table 6.2** shows that the higher the level of random error, the higher the *SSR*, and the fitting quality slightly deteriorated. The maximum absolute errors occurred for the breakage distribution exponent ν: 5.482% and 11.13% for the synthetic data with 5% and 10% random errors, respectively. Even at 10% random error added, most estimated parameters had less than 0.6% error. **Figure 6.1** illustrates the model fit to the

temporal evolution of synthetic data with 10% random error, representing a cumulative form of PSD; the small deviation between the model fit and the synthetic data with 10% random error was not even notable. The default N_T value of 10^3 was also used to in the fit to the synthetic data with 10% random error. PBM parameters obtained by the back-calculation from $N_T = 10^3$ were identical to those obtained from $N_T = 200$, indicating that there is no need for a higher value of N_T in the search for a global optimum for the estimated parameters. Overall, we proved the accuracy and feasibility of our newly developed global optimizer-based back-calculation method by showing excellent agreement between the synthetic data (without random error and with 5% and 10% random errors) and the model fit.

Table 6.1 PBM Parameters Obtained by the Back-calculation for Synthetic Batch Ball Milling Data without Random Error

Parameter	Actual parameter value[a]	Initial guess	Constraint		Back-calculated value[b]	% Absolute error
			Lower bound	Upper bound		
C_1 ($mm^{-(m+\alpha)} \cdot min^{-1}$)	1.075×10^2	1.0	0	∞	1.075×10^2	1.144×10^{-4}
C_2 (mm^{n-1})	3.706×10^2	1.0	0	∞	3.706×10^2	1.049×10^{-5}
m	–1.444	–2.0	–2.5	1.5	–1.444	7.659×10^{-6}
n	2.364	0.5	0.2	2.5	2.364	5.212×10^{-6}
α	9.496×10^{-1}	1.0	0.3	3.0	9.500×10^{-1}	4.214×10^{-2}
ϕ_0	5.100×10^{-1}	0.3	0.01	1.0	5.100×10^{-1}	4.477×10^{-5}
μ	5.300×10^{-1}	1.0	0.1	2.0	5.300×10^{-1}	8.100×10^{-6}
ν	3.200	4.0	2.0	15.0	3.200	2.936×10^{-4}
SSR					3.898×10^{-13}	
SER					1.565×10^{-8}	

[a] actual parameter values used to generate the synthetic batch ball milling data without random error. These parameter values were taken from Bilgili (2023) and Katubilwa and Moys (2011) for South African coal data.

[b] based on N_T of 200.

Table 6.2 PBM Parameters Obtained by the Back-calculation for Synthetic Batch Ball Milling Data with 5% and 10% Random Errors

Parameter	Actual parameter value[a]	Initial guess	Constraint		Data with 5% random error		Data with 10% random error	
			Lower bound	Upper bound	Back-calculated value[b]	% Absolute error	Back-calculated value[b]	% Absolute error
C_1 ($mm^{-(m+\alpha)}\cdot min^{-1}$)	1.075×10^2	1.0	0	∞	1.074×10^2	1.308×10^{-2}	1.074×10^2	3.914×10^{-2}
C_2 (mm^{n-1})	3.706×10^2	1.0	0	∞	3.706×10^2	3.450×10^{-4}	3.706×10^2	6.350×10^{-4}
m	–1.444	–2.0	–2.5	1.5	–1.443	7.480×10^{-2}	–1.442	1.282×10^{-1}
n	2.364	0.5	0.2	2.5	2.360	1.778×10^{-1}	2.356	3.176×10^{-1}
α	9.496×10^{-1}	1.0	0.3	3.0	9.506×10^{-1}	1.014×10^{-1}	9.500×10^{-1}	3.911×10^{-2}
ϕ_0	5.100×10^{-1}	0.3	0.01	1.0	5.057×10^{-1}	8.448×10^{-1}	5.005×10^{-1}	1.869
μ	5.300×10^{-1}	1.0	0.1	2.0	5.289×10^{-1}	2.166×10^{-1}	5.271×10^{-1}	5.515×10^{-1}
ν	3.200	4.0	2.0	15.0	3.025	5.482	2.844	11.13
SSR					2.250×10^{-3}		8.666×10^{-3}	
SER					1.189×10^{-3}		2.333×10^{-3}	

[a] actual parameter values used to generate the synthetic batch ball milling data without random error. These parameter values were taken from Bilgili (2023) and Katubilwa and Moys (2011) for South African coal data.

[b] based on N_T of 200.

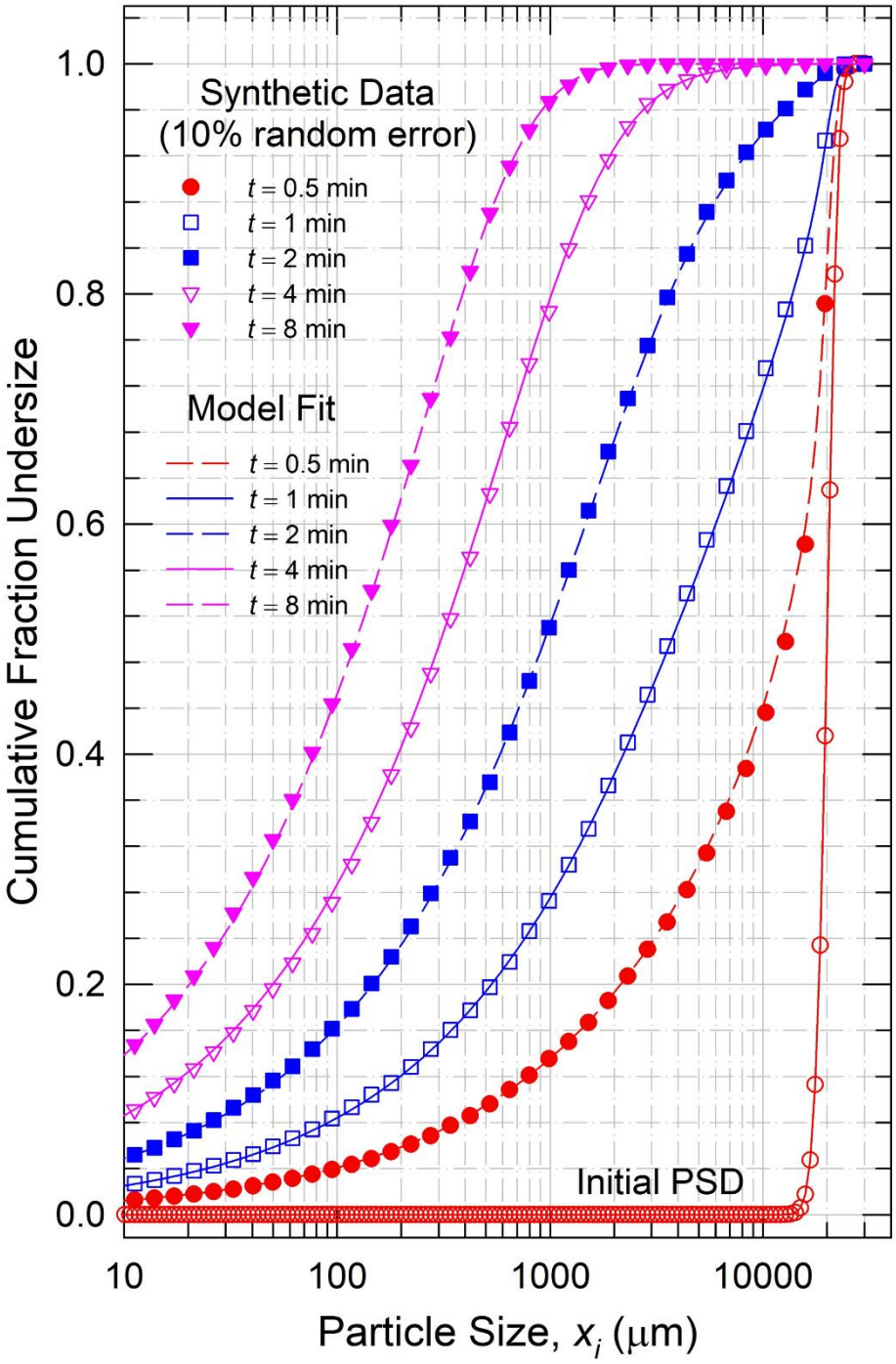

Figure 6.1 Comparison of synthetic batch ball milling data with an initial Gaussian PSD (mean size: 20 mm, standard deviation: 2 mm) augmented with 10% random error and the PBM fit to the data. The parameters estimated and fit statistics are given in the last two columns of Table 6.2.

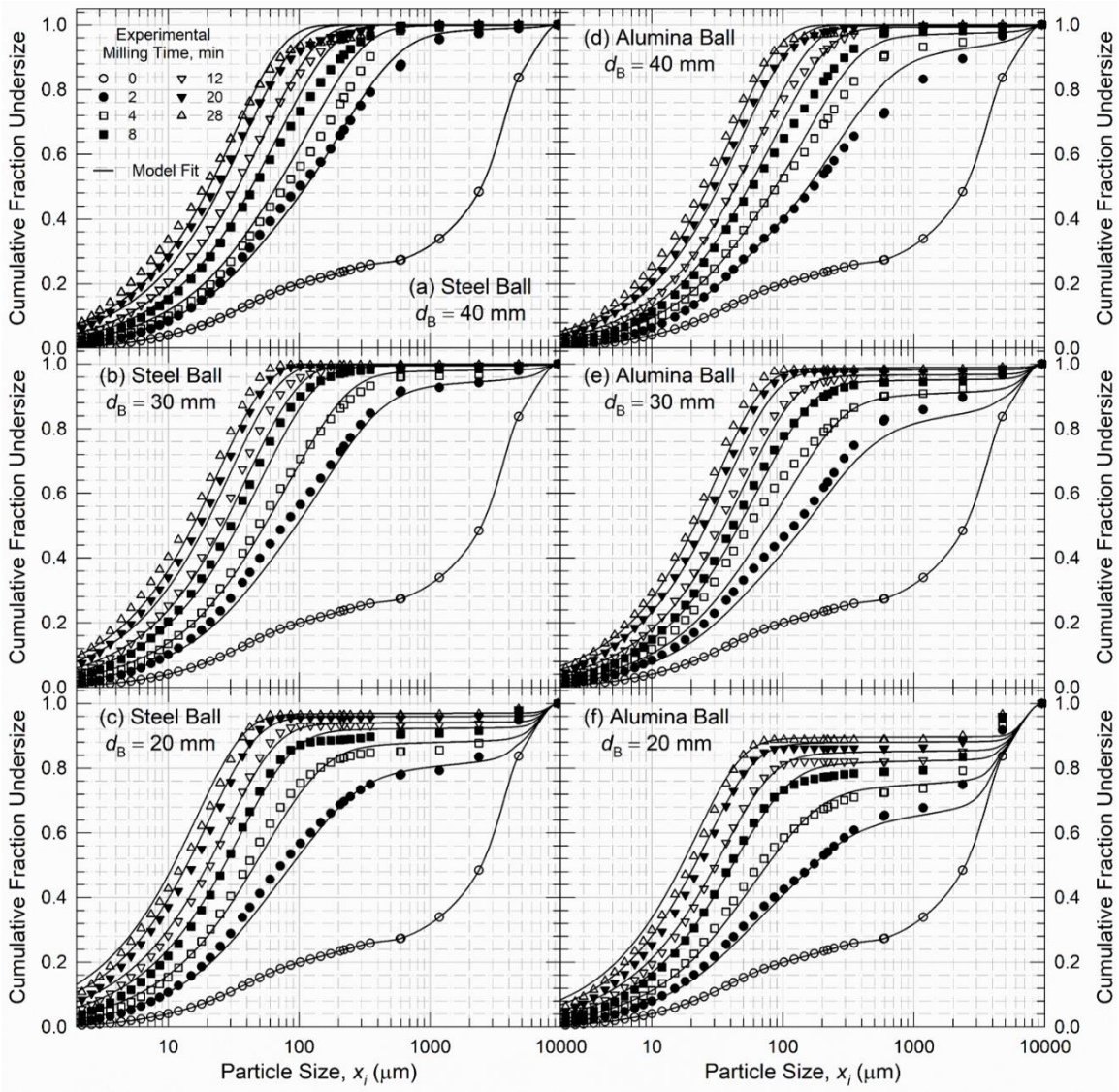

Figure 6.2 Experimental timewise evolution of the cumulative PSD of the cement clinker and its PBM fit for a single ball size: (a)–(c) steel balls and (d)–(f) alumina balls. Results are based on normalized single-term $B_{i,j}$ with $N_T = 10^4$. The parameters estimated and fit statistics are given in the last column of Tables 6.4 (steel balls) and 6.5 (alumina balls).

6.4.2 Experimental results using single ball sizes and parameter estimation

Figure 6.2 shows the timewise evolution of the cumulative PSD experimentally obtained from the laboratory batch ball mill with different single ball sizes (i.e., d_B = 20, 30, and 40 mm) using steel balls and alumina balls. As milling progressed and finer particles were generated by breakage, the PSD shifted to the left monotonically even in the fine particle size domain (1–100 μm). The median size d_{50} decreased fast within the first 5 min as the feed consisted of pre-milled, damaged cement clinker particles, which were easy to break (**Figure 6.3**). The overall breakage rate, signified by the slope of the d_{50}–t, decreased during the milling as finer clinker particles were generated, which were relatively more difficult to break and get captured by the balls. A holistic analysis of the evolution profiles in **Figures 6.2 and 6.3** suggests the following trends regarding the impact of ball materials–sizes: (i) The large beads (40 mm) led to slow breakage, but no unbroken clinker particles remained after 28 min milling; (ii) 20 mm balls yielded the finest clinker particles while this effect was more notable for the steel balls than for the alumina balls; (iii) some unbroken coarse clinker particles were observed clearly when milling with 20 mm alumina and steel balls; but the extent was higher for the alumina balls; and (iv) for a given ball size, the steel balls caused faster breakage of the cement clinker than the alumina balls. Note that Erdem and Ergun (2009) also observed unbroken, coarse cement clinker particles in dry ball milling when small balls were used.

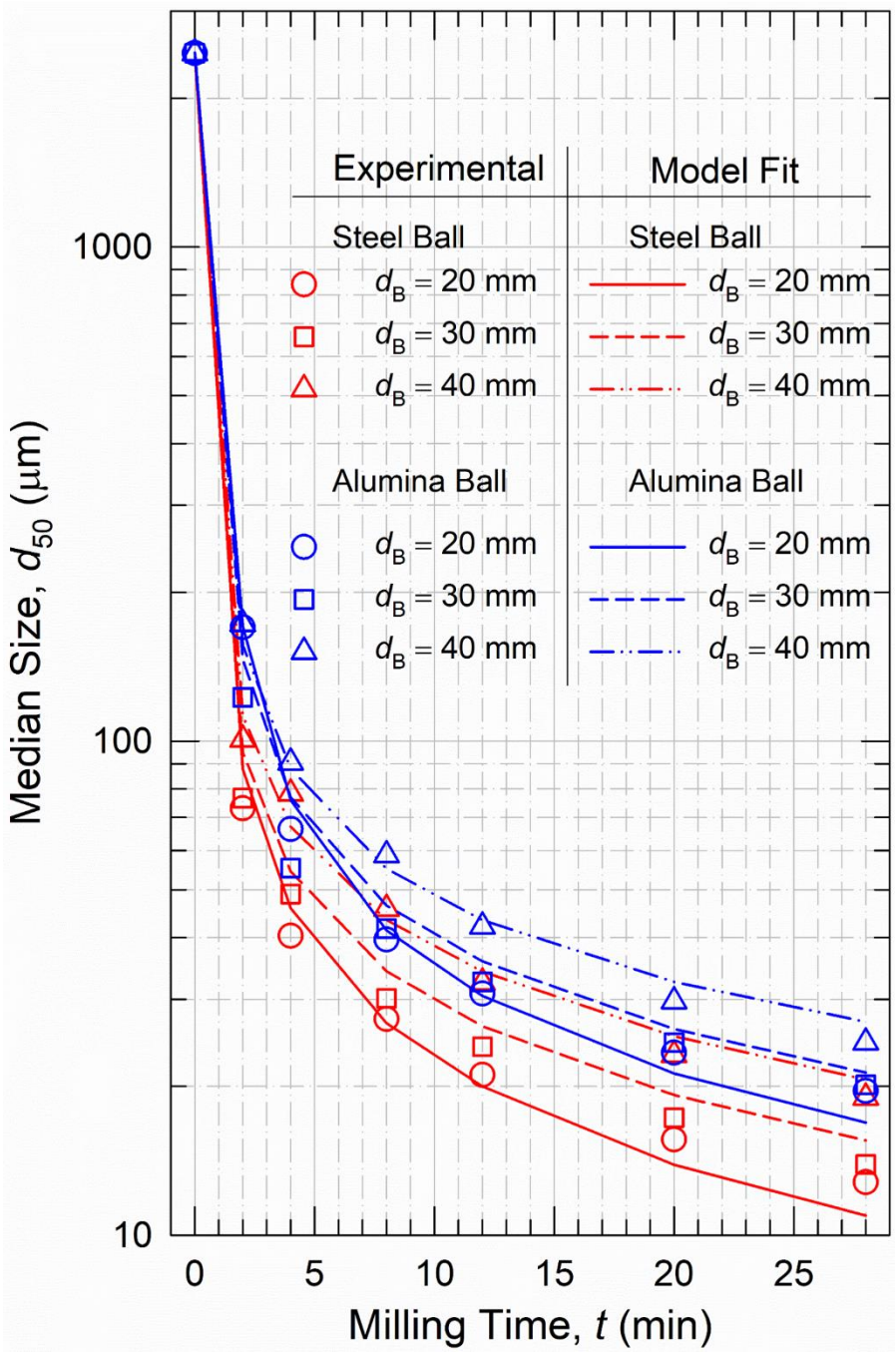

Figure 6.3 Experimental timewise evolution of the median size of the cement clinker and its PBM fit for a single ball size: (a)–(c) steel balls and (d)–(f) alumina balls. Results are based on normalized single-term $B_{i,j}$ with $N_T = 10^4$. The parameters estimated and fit statistics are given in the last column of Tables 6.4 (steel balls) and 6.5 (alumina balls).

To quantify the impact of the ball size–material on the breakage kinetics of the pre-milled cement clinker, the parameters of the PBM were estimated by the newly developed global optimizer-based back calculation method. The optimizer coupled with an ODE solver fitted the PSD evolution data obtained from the milling experiments (**Figure 6.2**). Experimental data for three single ball sizes were simultaneously fitted for each ball material type. Overall, the PBM fitted the temporal evolution of the cement clinker PSD reasonably well. The deviations of the PBM fits to the experimental profiles were most notable during the first 8 min of 28 min milling. This could be partly related to the fast, initial breakage dynamics of the pre-milled cement clinker besides the relatively crude and infrequent measurement of the PSD by sieving. The accuracy could have been improved if more frequent sampling were carried out during this period with more than 3 ball sizes.

It is important to mention that the global optimization scheme does not guarantee convergence to the global minimum of the objective function (*SSR*) (The MathWorks, 2022), which is ultimately determined by N_T and the available computational resources. **Table 6.3** lists a set of initial guesses and bound constraints used during the back-calculation. **Tables 6.4 and 6.5** report the estimated PBM parameters, along with the *SSR* values, for steel ball milling and alumina ball milling, respectively. First, we set the number of trial points N_T to 200 (default minimum). Interestingly, for both ball materials, the estimated $B_{i,j}$ parameters $\phi_0 \approx 1$ and $\theta \approx 0$ suggest that the two-term, non-normalized $B_{i,j}$ function with four parameters is too elaborate, which justifies the normalized single-term form $B_{i,j} = (x_{i-1}/x_j)^{\mu}$ and allows for a reduction of the total number of parameters to estimate from 9 to 6. Note that a single-term normalized $B_{i,j}$ has been successfully used in earlier studies (Berthiaux and Varinot, 1996; Boulvin et al., 2003; Capece, 2018). To investigate

whether the global optimizer converged to the global minimum, we then increased N_T to 10^3 and 10^4 (see the solutions in **Tables 6.4 and 6.5**). When N_T was increased from 200 to 10^3, all parameters remained unchanged within 3 significant figures, except the notable relative change in θ. But, again, we note that $\theta \approx 0$ and the absolute change to θ upon an increase in N_T was negligible. Overall, these findings give us confidence that a global minimum was obtained, and the parameters estimated are realistic. Note that with $N_T = 10^4$, a long execution (real) time was required to complete this optimization run, with the longest execution time being six days.

Table 6.3 Initial Guess and Bound Constraints for Each Parameter of the PBM Used during Back-calculation with the Experimental Data on the Ball Milling of Cement Clinker

Parameter	Initial guess	Constraint	
		Lower bound	Upper bound
C_1 ($mm^{-(m+\alpha)} \cdot min^{-1}$)	1.0	0	∞
C_2 (mm^{n-1})	1.0	0	∞
m	–2.0	–2.5	1.5
n	0.5	0.2	2.5
α	1.0	0.3	3.0
ϕ_0	0.3	0.01	1.0
μ	1.0	0.1	2.0
ν	4.0	2.0	15.0
θ	0.01	0	0.3

Table 6.4 PBM Parameters Obtained by the Back-calculation with the Experimental Data on the Ball Milling of Cement Clinker Using Steel Balls for Various N_T Values

Parameter	Back-calculated value			
	$N_T = 200$	$N_T = 10^3$	$N_T = 10^4$	$N_T = 10^4$ [a]
C_1 ($mm^{-(m+\alpha)} \cdot min^{-1}$)	1.940×10^3	1.939×10^3	1.939×10^3	1.939×10^3
C_2 (mm^{n-1})	31.46	31.45	31.45	31.45
m	−1.717	−1.717	−1.717	−1.717
n	1.101	1.101	1.101	1.101
α	1.559	1.559	1.559	1.559
ϕ_0	1.000	1.000	1.000	1[a]
μ	8.096×10^{-1}	8.097×10^{-1}	8.097×10^{-1}	8.097×10^{-1}
ν	11.42	11.37	11.36	–
θ	1.465×10^{-5}	5.844×10^{-7}	5.841×10^{-7}	0[a]
SSR	4.291×10^{-1}	4.291×10^{-1}	4.291×10^{-1}	4.291×10^{-1}
SER	2.488×10^{-2}	2.488×10^{-2}	2.488×10^{-2}	2.483×10^{-2}

[a] based on a normalized single-term $B_{i,j}$ with one fitting parameter only, i.e., μ.

Table 6.5 PBM Parameters Obtained by the Back-calculation with the Experimental Data on the Ball Milling of Cement Clinker Using Alumina Balls for Various N_T Values

Parameter	Back-calculated value			
	$N_T = 200$	$N_T = 10^3$	$N_T = 10^4$	$N_T = 10^4$ [a]
C_1 ($mm^{-(m+\alpha)} \cdot min^{-1}$)	2.849×10^3	2.849×10^3	2.849×10^3	2.849×10^3
C_2 (mm^{n-1})	36.55	36.55	36.55	36.55
m	−1.810	−1.810	−1.810	−1.810
n	1.055	1.055	1.055	1.055
α	1.715	1.715	1.715	1.715
ϕ_0	1.000	1.000	1.000	1[a]
μ	8.509×10^{-1}	8.509×10^{-1}	8.509×10^{-1}	8.509×10^{-1}
ν	11.49	11.48	11.55	–
θ	3.424×10^{-6}	6.844×10^{-7}	1.376×10^{-7}	0[a]
SSR	4.669×10^{-1}	4.669×10^{-1}	4.669×10^{-1}	4.669×10^{-1}
SER	2.596×10^{-2}	2.596×10^{-2}	2.596×10^{-2}	2.590×10^{-2}

[a] based on a normalized single-term $B_{i,j}$ with one fitting parameter only, i.e., μ.

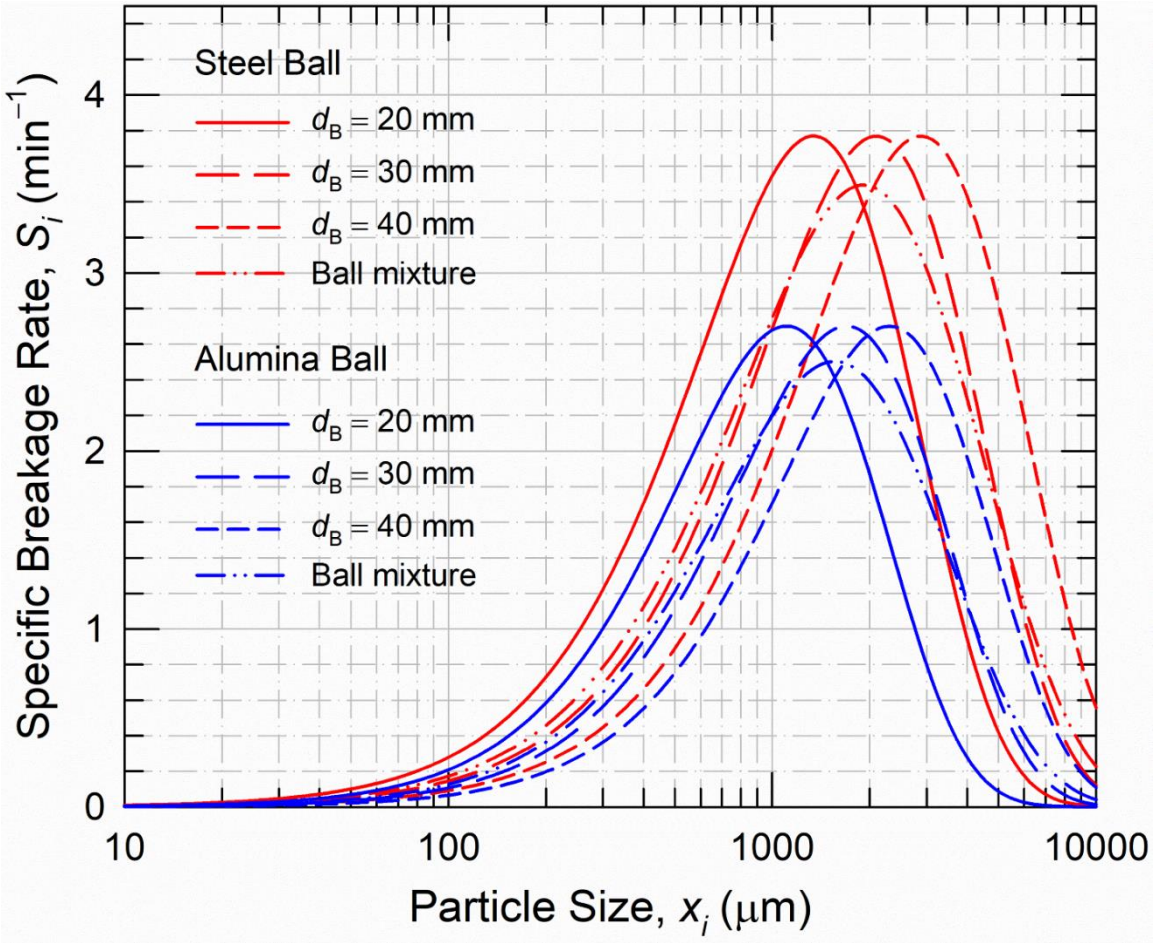

Figure 6.4 The variation of the estimated specific breakage rate with cement clinker particle size for three single ball sizes and a ball mixture (based on uniform mass distribution of 20–30–40 mm balls) when steel and alumina balls were used in the ball mill. Results are based on normalized single-term $B_{i,j}$ with $N_T = 10^4$.

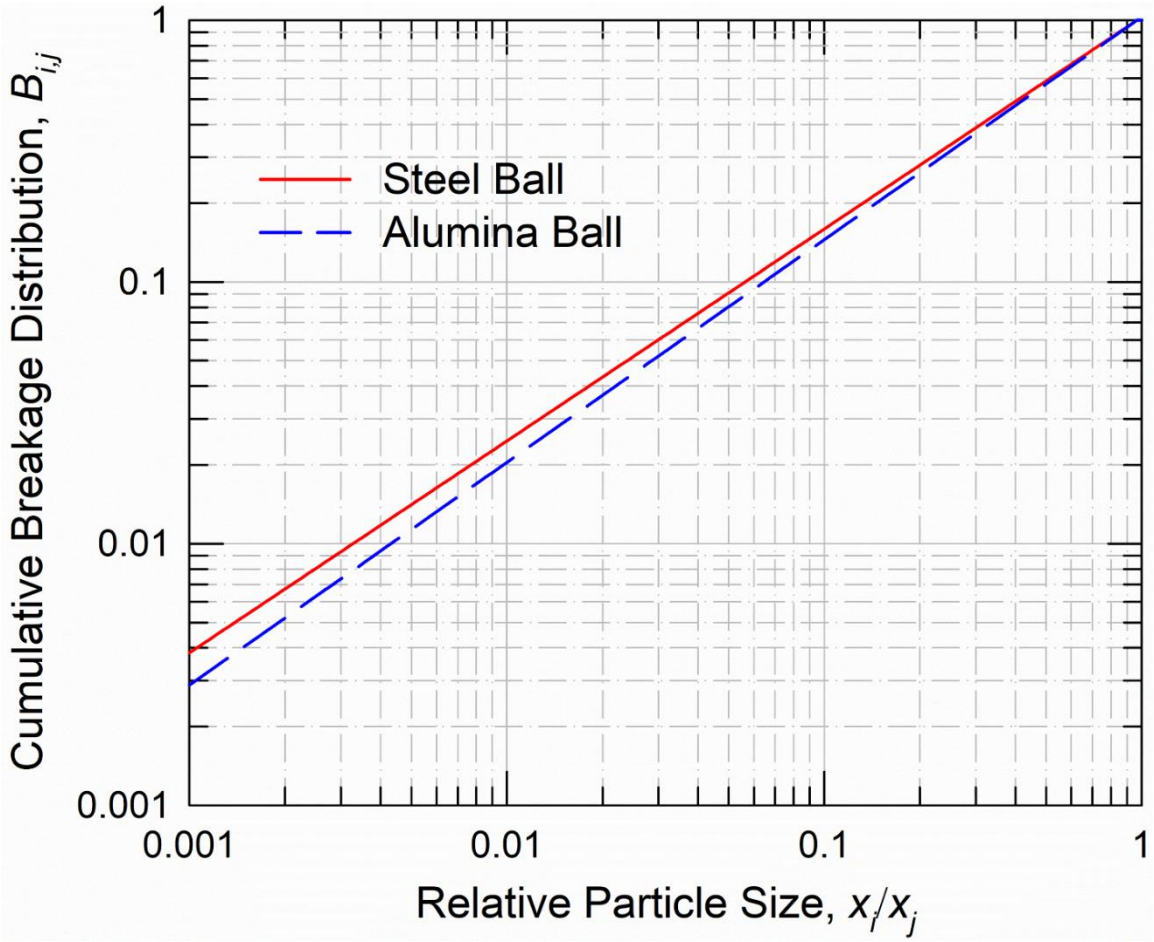

Figure 6.5 The variation of the estimated cumulative breakage distribution with relative particle size of the cement clinker for steel balls and alumina balls. Results are based on normalized single-term $B_{i,j}$ with $N_T = 10^4$.

We also ran the optimizer using $N_T = 10^4$ again, but this time we used $B_{i,j} = (x_{i-1}/x_j)^{\mu}$ with one parameter as opposed to the four-parameter $B_{i,j}$. As can be seen in **Tables 6.4 and 6.5**, there is no difference between the fitting results of the four-parameter $B_{i,j}$ and the single-term $B_{i,j}$ with a single parameter. However, the execution time with the single-term $B_{i,j}$ was significantly reduced from six days to less than one day. Note that all figures in the main text were based on normalized single-term $B_{i,j}$ with a single parameter estimated with

$N_T = 10^4$. The fitted PSDs using the normalized single-term $B_{i,j}$ with a single parameter did not differ from the non-normalized $B_{i,j}$ with four parameters.

6.4.2.1 Analysis of specific breakage rate and cumulative breakage distribution. S_i of steel balls and alumina balls for three ball sizes: d_B = 20, 30, and 40 mm were compared (**Figure 6.4**). All S_i profiles exhibited a maximum (S_m) at a cement clinker size x_m. The profile shifted right, to coarser particle size domain (higher x_m), when the ball size d_B was increased from 20 to 40 mm, which is in line with Austin et al. (1976) and Katubilwa and Moys (2009). For $x_i << d_B$, the S_i profile is governed by the traditional power law: $S_i = C_1 d_B^m x_i^\alpha$. As x_i increases, but still with $x_i < d_B$, such relatively large particles may not get nipped between the balls effectively, thus requiring much higher impact energies, and S_i starts deviating from the power-law and exhibits a maximum and fall-off behavior, which is commonly known as abnormal breakage (Austin et al., 1984).

Our comparative analysis of the S_i profiles in **Figure 6.4** suggests that for a given ball material type, the large balls (40 mm) led to higher S_i for coarser clinker particles, while the small balls (20 mm) led to higher S_i for smaller particles. This finding agrees well with Deniz (2003) and Katubilwa and Moys (2009), but contradicts with Kotake et al. (2002) and Kotake et al. (2004). It is critical to mention that the parameters related to various materials reported in Kotake et al. (2002) and Kotake et al. (2004) suggest that for some raw materials, larger balls always have higher S_i value in comparison with smaller balls for the whole particle size range. Another general trend in **Figure 6.4** is that for a given ball size, steel balls had higher S_i than alumina balls for the entire range of particle sizes, which is consistent with Umucu et al. (2014). For both steel and alumina balls, S_m is invariant with ball size d_B. Previous studies (Kotake et al., 2002; Kotake et al., 2004;

Bwalya et al., 2014) had similar findings for limestone, gypsum, talc, and coal. We also note that x_m of alumina balls is smaller than x_m of steel balls at the same ball size. The particle size x_m can be expressed as a function of d_B by $x_m=(\alpha/C_2)d_B^n$ (Bilgili, 2023). Using this equation, x_m for 20, 30, and 40 mm balls was calculated as 1.34, 2.10, and 2.88 mm, respectively, in the case of steel balls, and 1.11, 1.70, and 2.30 mm, respectively, in the case of alumina balls. **Figure 6.4** also shows the ball mixture's S_i for steel and alumina ball mixtures. The ball mixture's S_i profile was similar to the S_i profile of 30 mm balls, with two distinct differences: it is slightly wider and has a slightly lower S_m. **Figure 6.5** shows that the breakage distribution function $B_{i,j}$; the steel balls produce finer particles than the alumina balls, which is in line with Umucu and Deniz (2015) for the steel vs. ceramic ball milling of ignimbrite.

6.4.3 Model validation: prediction of timewise evolution of PSD using the ball mixture

In a separate set of experiments, pre-milled cement clinker with a smaller median size of d_{50} = 164 μm was milled with a 20–30–40 mm ball mixture, and the experimental PSD and d_{50} evolution as well as their PBM predictions are presented in **Figures 6.6 and 6.7**. Note that this finer initial feed PSD and the ball mixture were not used in the model calibration; thus, the PBM was truly used in the predictive mode here. **Figures 6.6 and 6.7** illustrate that the PBM, whose parameters were obtained from the global optimizer-based back-calculation method, predicted the temporal evolution of the PSD and d_{50} well for both the steel ball mixture and the alumina ball mixture. *SER* values of the steel ball mixture and the alumina ball mixture were 1.451×10^{-2} and 2.466×10^{-2}, respectively, which were even lower than the *SER* values for the PBM fits in the model calibration (see **Tables 6.4 and 6.5**).

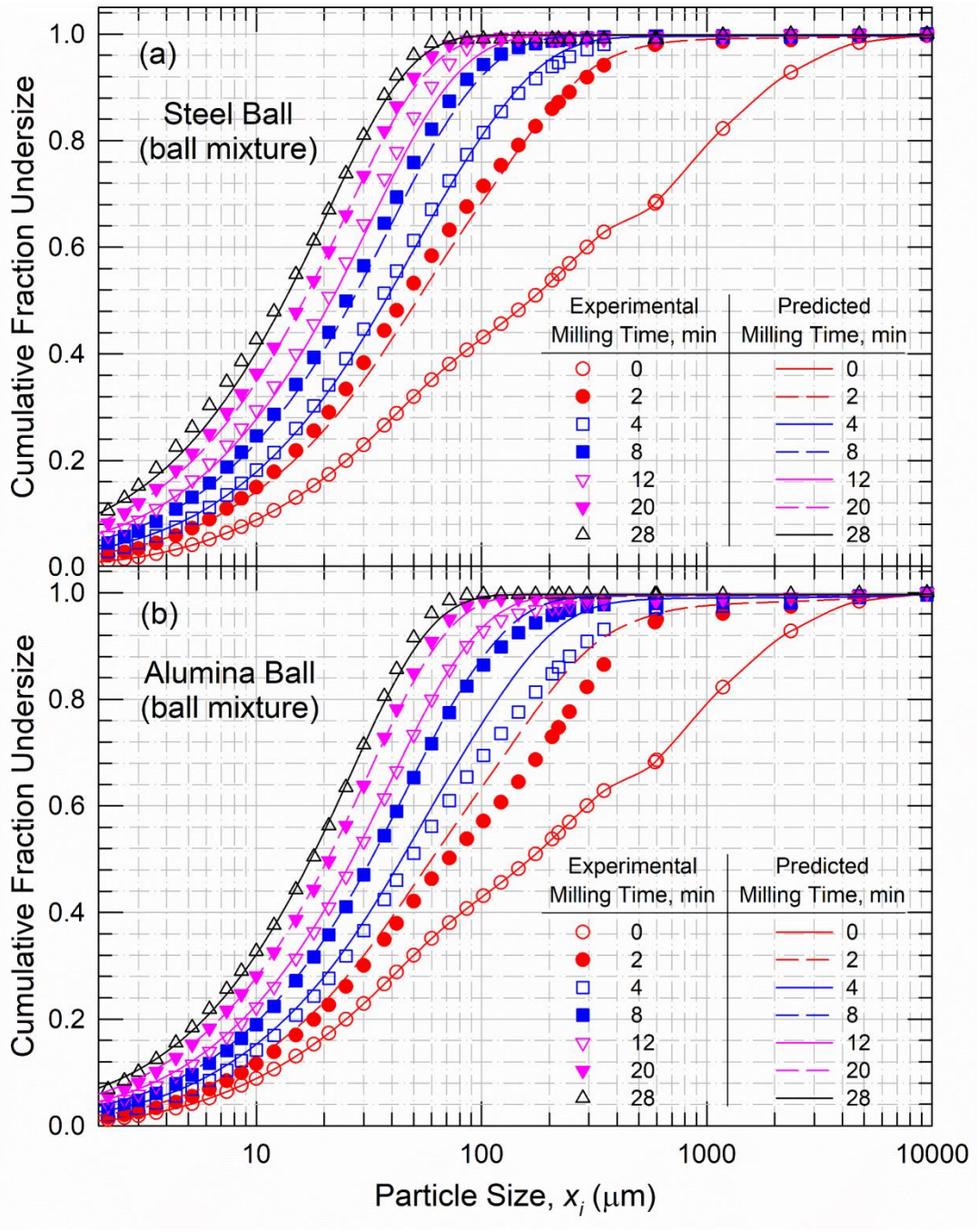

Figure 6.6 PBM prediction of the timewise evolution of the cumulative PSD of the cement clinker for a ball mixture (based on uniform mass distribution of 20–30–40 mm balls): (a) steel ball mixture and (b) alumina ball mixture. Feed PSD of the cement clinker was different from that used in the model fitting. Results are based on normalized single-term $B_{i,j}$ with $N_T = 10^4$.

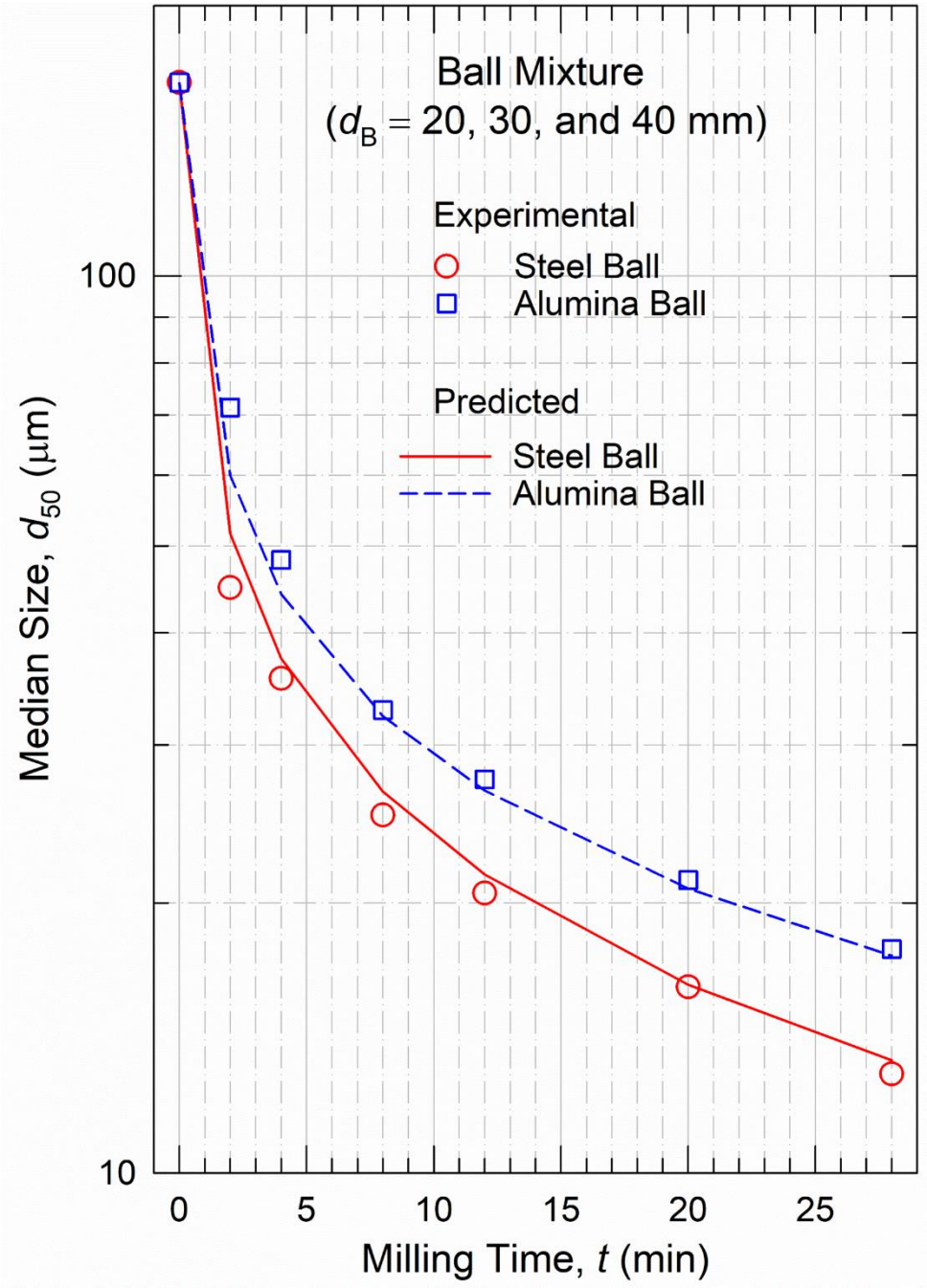

Figure 6.7 PBM prediction of the timewise evolution of the median size of the cement clinker for a ball mixture (based on uniform mass distribution of 20–30–40 mm balls). Feed PSD of the cement clinker was different from that used in the model fitting. Results are based on normalized single-term $B_{i,j}$ with $N_T = 10^4$.

Note that the initial feed PSD in the validation experiments was finer than the calibration experiments in Subsection 6.4.2. This could explain the observed lower *SER* because most deviation occurred during the initial 8 min milling in the calibration experiments. Again, the PBM with the normalized, single term $B_{i,j}$ predicted identical PSD and d_{50} evolutions (**Figures 6.6 and 6.7**) as compared with the PBM with the *non-normalized* $B_{i,j}$.

For the validation experiments, a notable deviation occurred for clinker particles coarser than 0.1 mm with alumina balls at t = 2 and 4 min. These notable deviations from the experimental data were also observed for the fitting (refer to **Figure 6.2**) when 30 mm and 40 mm alumina balls were used. Note that the PSD above 0.6 mm was experimentally obtained by sieving (5 sieves), whereas the PSD below 0.6 mm was obtained from laser diffraction with (34 size channels). Hence, the PSD of the particles above 0.6 mm were rather crudely measured by the sieving, and interpolation (refer to Appendix D) did not resolve this error. On the other hand, the PSD below 0.6 mm had 34 data points. Since most coarse particles above 0.6 mm existed during the first 4 min of ball milling, the errors during the fitting and the prediction were most prevalent during the milling times when a notable fraction of the particles were coarse (>0.6 mm). In other words, the notable deviations that occurred during the first 4 min of alumina ball milling mostly originated from the relatively crude measurement of the PSD by sieving. This sieving-related deviation was not as pronounced after 4 min. Since the steel balls milled the particles faster than the alumina balls, the coarse particles above 0.6 mm, which were measured by sieving, disappeared more quickly, and the sieving-related error was less pronounced for the steel balls. Overall, this experimental error coupled with errors associated with the calibration

of the model parameters could have been reduced by using a laser diffraction equipment that can measure particle sizes up to ~3 mm rather than 0.6 mm. However, the abrasive nature of the clinker particles could limit the use of measuring such coarser particles in laser diffraction. Finally, as mentioned in Subsection 6.4.2, the accuracy could have been improved if more frequent sampling were carried out during this initial period with more than 3 ball sizes.

6.4.3.1 Elucidating the advantage of ball mixture with various ball sizes. We rationalize the use of ball mixture commonly used in ball mills in the cement industry (e.g., Austin et al., 1975; Genc, 2008; Altun, 2018) via a separate PBM simulation with parameters obtained from the back-calculation in Subsection 6.4.2. Numerous past studies (e.g., Teke et al., 2002; Deniz, 2003; Magdalinovic et al., 2012; Mulenga et al., 2019; Haner, 2020) investigating the influence of ball size on particle breakage relied on multiple single ball sizes in their milling experiments, while only a few studies (Erdem and Ergun, 2009; Katubilwa and Moys, 2009; Oksuzoglu and Ucurum, 2016; Cayirli, 2018) used ball mixtures. Although ball mixtures are commonly used in full-scale cement ball mills (Austin et al., 1975; Genc, 2008; Altun, 2018), the role of a mixture with different ball sizes has not been thoroughly studied. Analysis of S_i values of a single ball size in Section 4.2 and earlier studies (Deniz, 2003; Katubilwa and Moys, 2009; Deniz, 2012) highlights the generally accepted notion that larger balls are effective in breaking coarser particles while smaller balls are effective in breaking finer particles. Unfortunately, when ball mixtures were studied (Erdem and Ergun, 2009; Katubilwa and Moys, 2009; Oksuzoglu and Ucurum, 2016; Cayirli, 2018), there was no attempt to elucidate why and how a ball mixture was superior to the individual single ball sizes.

For a head-to-head comparison of the ball mixture to the single balls, we performed a PBM simulation with the ball mixture. To this end, here we used the same initial feed PSD that was used during the model calibration in Subsection 6.4.2 for both single ball sizes and the ball mixture. **Figures 6.8 and 6.9** respectively illustrate the timewise evolution of the PSD and d_{50} for both steel balls and alumina balls. We represented PSD in differential form to highlight and emphasize any bimodality in the initial feed PSD and the evolving PSD. We selectively demonstrated simulation results for three milling times (i.e., t = 2, 12, and 28 min). We did not include the differential PSD of initial feed for proper scaling of **Figure 6.8**.

A cursory look at **Figure 6.8** for steel balls reveals that coarse particles (> 2 mm) were rapidly broken with large ball size (d_B = 40 mm) at t = 2 min compared to other ball sizes. With steel balls, particles coarser than 0.3 mm completely disappeared within t = 12 min for d_B of 30 and 40 mm, while in the case of 20 mm balls, some coarse particles remained unbroken. At 28 min of milling time, 20 mm balls clearly yielded finer PSD than the 30 mm and 40 mm balls. However, a portion of unbroken coarse particles remained in the product (i.e., bimodal PSD), which was not observed for 30 and 40 mm steel balls and 40 mm alumina balls. This simulation result suggests that although small balls yield finer PSD, some coarse particles cannot be properly broken by 20 mm balls. On the other hand, unlike the use of a single small ball size (20 mm), the use of the ball mixture enabled complete breakage of the coarse particles similar to the 30 and 40 mm balls alone, but the ball mixture yielded a slightly finer PSD than the 30 mm balls. Similar results were obtained for the alumina ball. **Figure 6.9** illustrates that the ball mixture was only second to 20 mm balls in yielding a fine PSD, but without any remaining unbroken cement clinker

particles. Again, the PBM with the normalized, single term $B_{i,j}$ predicted identical PSD and d_{50} evolutions (**Figures 6.8 and 6.9**) as compared with the PBM with the *non-normalized* $B_{i,j}$.

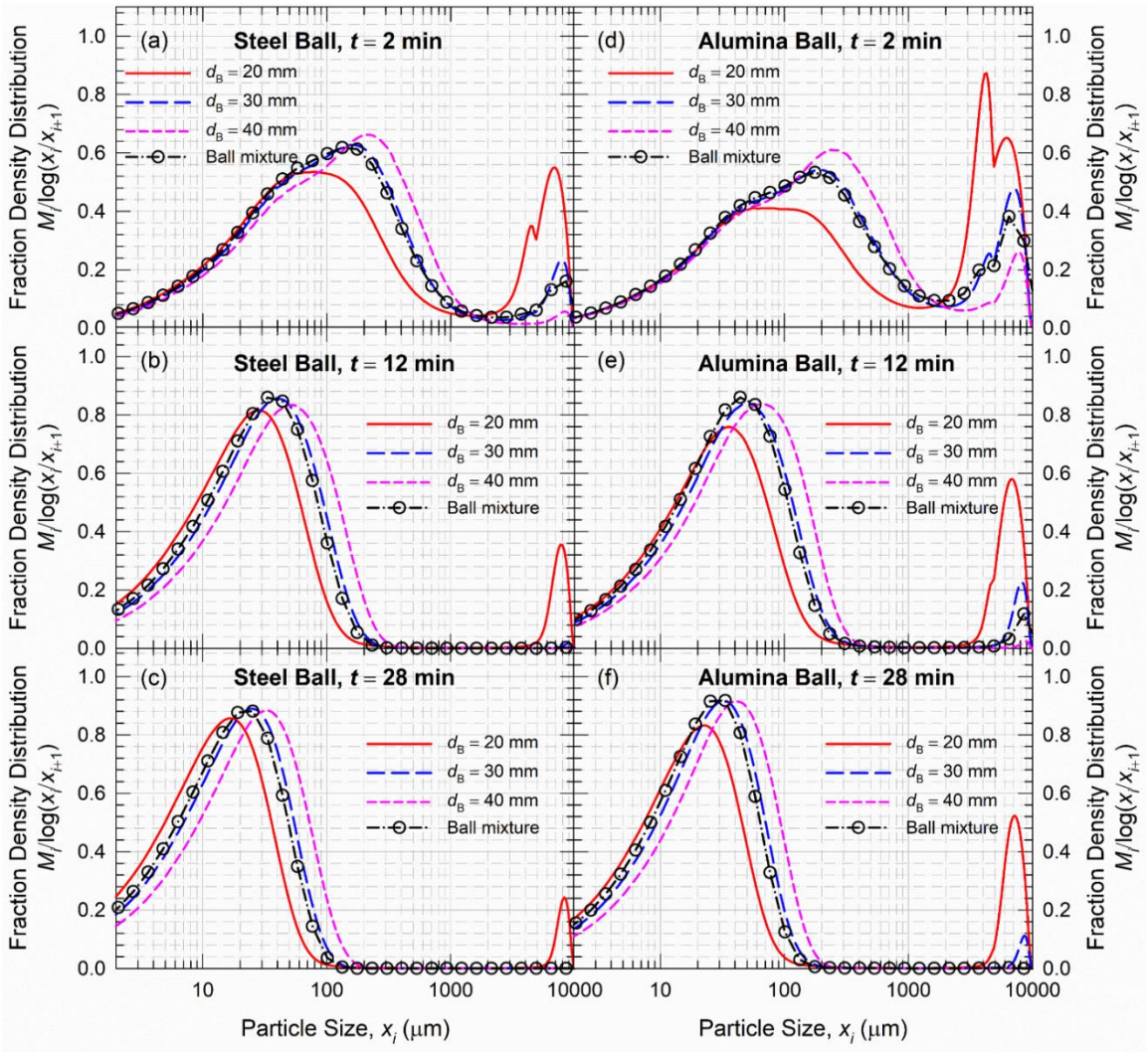

Figure 6.8 PBM simulation of the timewise evolution of the differential PSD for a single ball size and a ball mixture (based on uniform mass distribution of 20–30–40 mm balls): (a)–(c) steel balls and (d)–(f) alumina balls. Results are based on normalized single-term $B_{i,j}$ with $N_T = 10^4$. The same feed PSD of the cement clinker was used in all simulations for a head-to-head comparison.

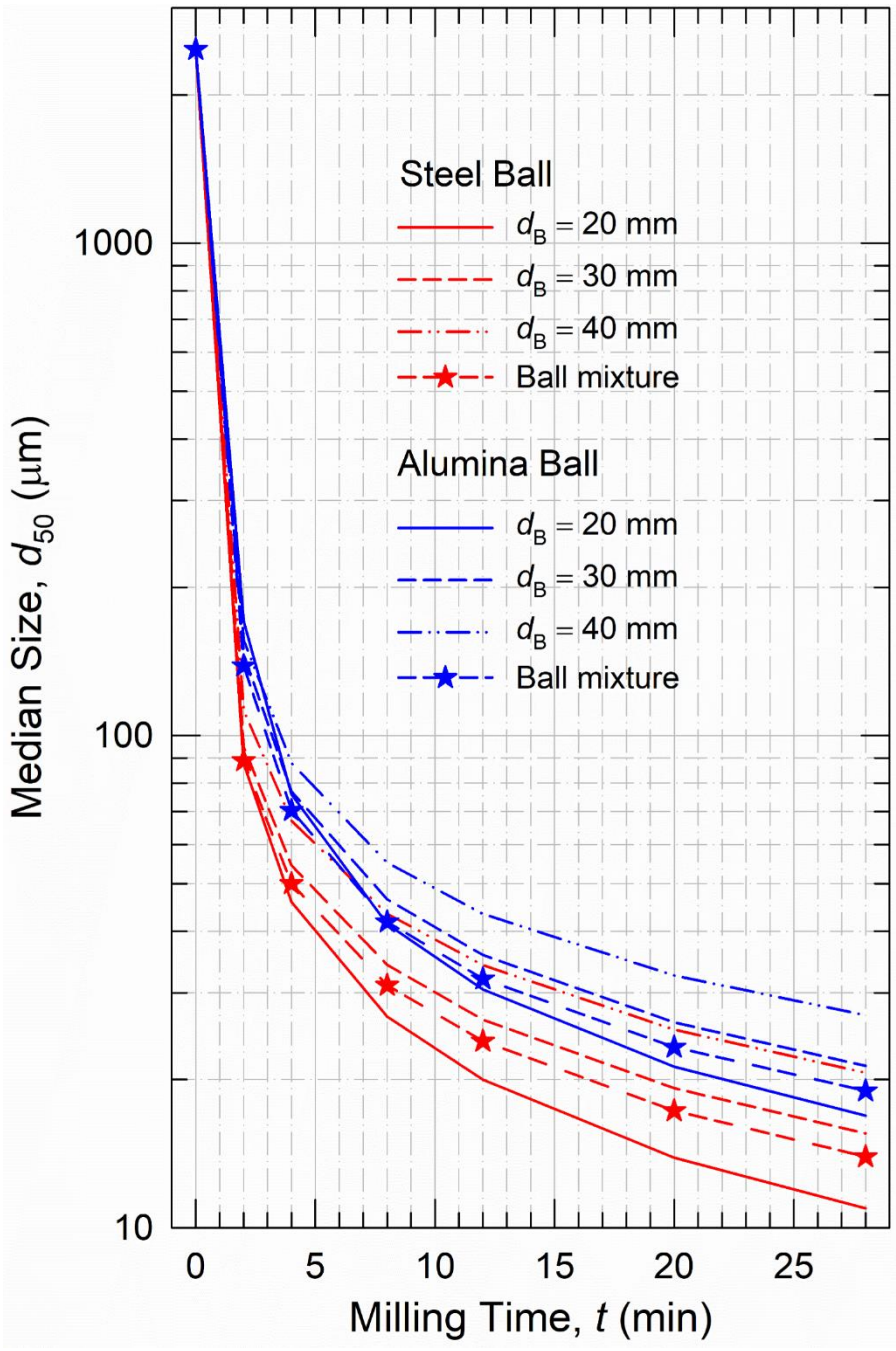

Figure 6.9 PBM simulation of the median size of the cement clinker for a single ball size and a ball mixture (based on uniform mass distribution of 20–30–40 mm balls). Results are based on normalized single-term $B_{i,j}$ with $N_T = 10^4$. The same feed PSD of the cement clinker was used in all simulations for a head-to-head comparison.

6.4.4 Some insights from the DEM simulations

DEM simulations were performed separately for the steel and alumina balls in a rotating ball mill. **Figure 6.10** illustrates the front view of the simulated ball mill and balls' position at the final simulated time of 20 s for both ball types. Color refers to different levels of dissipated energy resulting from ball collisions, with red and blue representing high and low dissipated energy levels, respectively. Analysis based on the graphical representation in **Figure 6.10** shows a cascading motion of balls inside the ball mill. A cursory look at **Figure 6.10** shows that the dissipated energy from the steel ball simulation had higher portions of the high-energy level (red) in comparison with alumina balls of the same ball size.

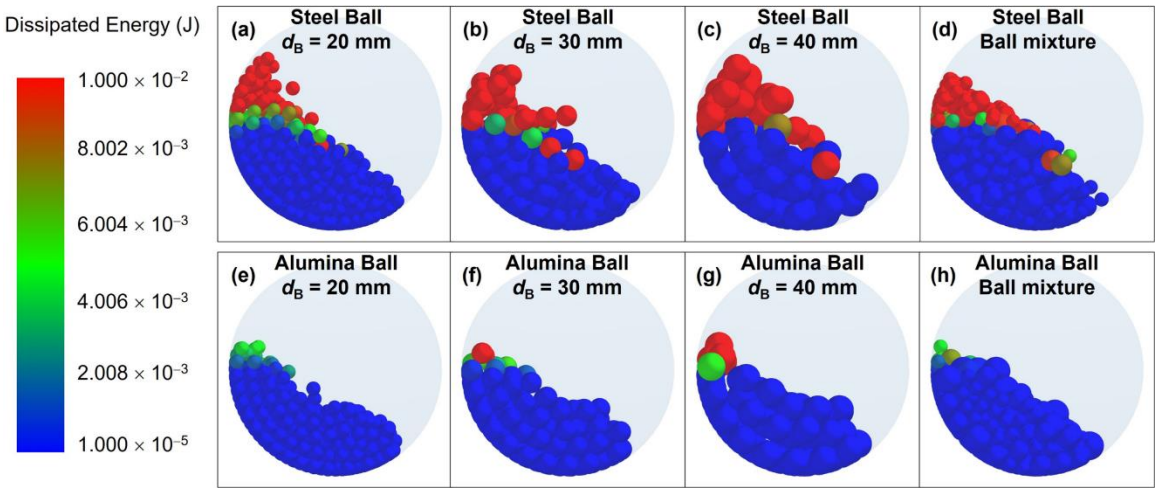

Figure 6.10 Front view of the ball mill simulated by DEM (clockwise rotation) for three single ball sizes and a ball mixture (based on uniform mass distribution of 20–30–40 mm balls): (a)–(d) steel balls and (e)–(h) alumina balls.

Table 6.6 Characteristic Information about the Collision Frequencies and Impact Energies Obtained from the DEM Simulations of the Ball Motion for Various Ball Sizes–Types

Characteristic information[a]	Steel ball milling				Alumina ball milling			
	d_B = 20 mm	d_B = 30 mm	d_B = 40 mm	Ball mixture[b]	d_B = 20 mm	d_B = 30 mm	d_B = 40 mm	Ball mixture[b]
Total collision frequency, f_{col} (s^{-1})	5.611×10^5	1.019×10^5	2.957×10^4	2.333×10^5	1.552×10^6	2.867×10^5	8.803×10^4	7.574×10^5
Collision frequency per ball, $f_{col,n}$ (s^{-1})	6.159×10^2	3.776×10^2	2.594×10^2	5.401×10^2	1.704×10^3	1.062×10^3	7.722×10^2	1.753×10^3
Specific collision frequency per unit mass of balls, $f_{col,m}$ ($s^{-1} \cdot kg^{-1}$)	1.883×10^4	3.421×10^3	9.922×10^2	7.830×10^3	1.159×10^5	2.139×10^4	6.569×10^3	5.652×10^4
Total energy dissipation rate, $\dot{E}$ ($J \cdot s^{-1}$)	95.45	89.14	84.24	144.3	12.12	10.86	9.544	14.98
Mean dissipation energy rate, $\bar{E}$ ($J \cdot s^{-1}$)	1.701×10^{-4}	8.744×10^{-4}	2.849×10^{-3}	6.183×10^{-4}	7.805×10^{-6}	3.789×10^{-5}	1.084×10^{-4}	1.978×10^{-5}

[a] Disregarded collisions with impact energies $<10^{-8}$ J.

[b] Uniform mass distribution of 20–30–40 mm balls.

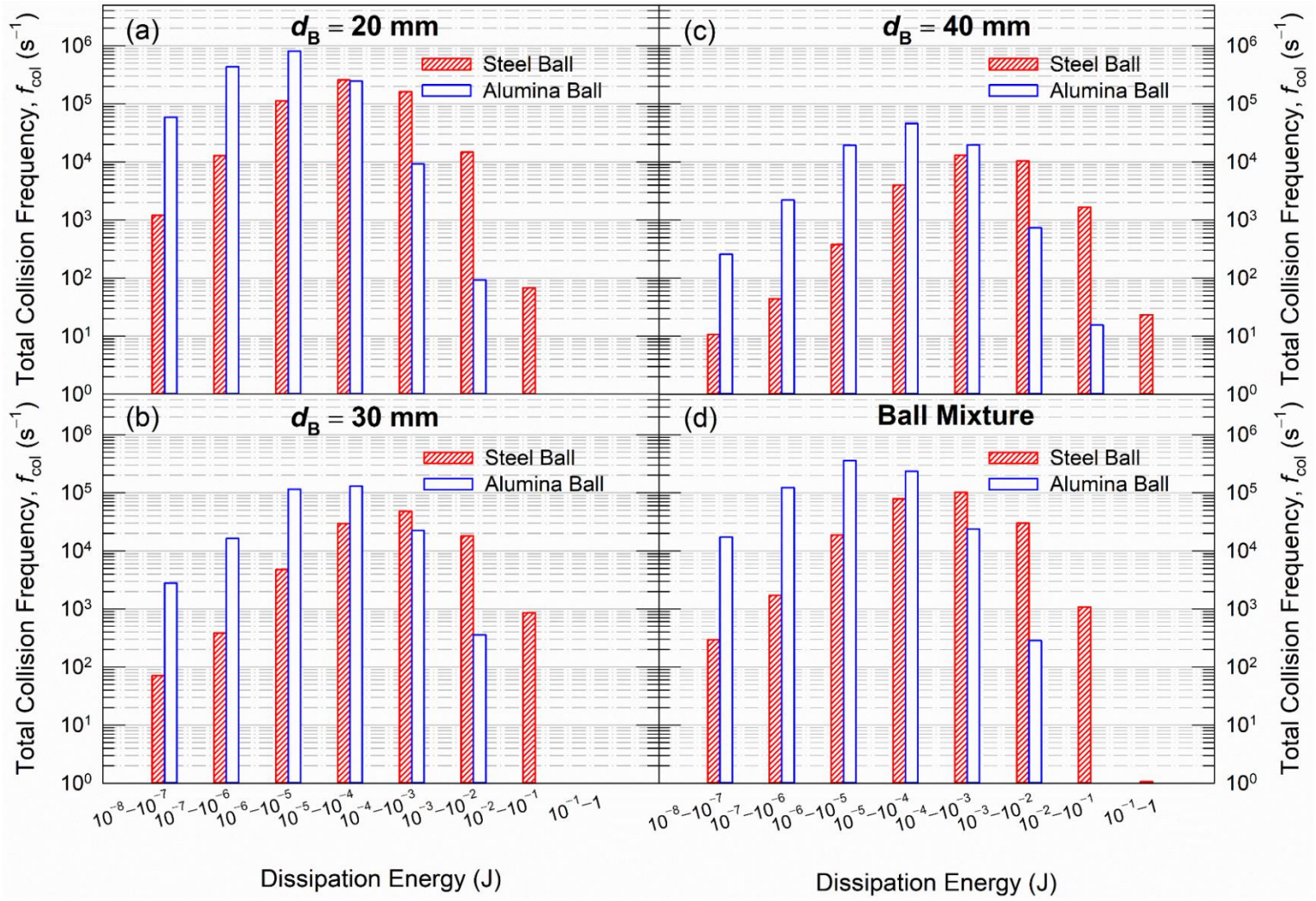

Figure 6.11. DEM-simulated dissipated energy distribution during the ball–ball collisions inside the mill with various ball sizes: (a) d_B = 20 mm, (b) d_B = 30 mm, (c) d_B = 40 mm, and (d) mixture with a uniform mass distribution of 20–30–40 mm balls.

Table 6.6 presents some characteristic information about the impact energy spectra for three single ball sizes and ball mixtures, while **Figure 6.11** presents the dissipated energy distribution as a representative measure of collisional energy spectra. The dissipation energy distribution was wide, spanning values from ~10^{-8} J to ~1 J. It is known that ball collisions that result in too low impact energies could not result in breakage due to the fact a threshold (minimum) impact energy is required to break the particles (Vogel et al., 2003; Vogel and Peukert, 2005; Capece et al., 2014). The DEM analysis presented in **Table 6.6** and **Figure 6.11** neglects the collisions with impact energies below 10^{-8} J. Obviously, a more elaborate analysis is warranted to elucidate the impact of threshold impact energy, which entails simulation of actual cement particles besides the balls. The threshold energy is material and particle size dependent; it can be determined either by single particle impact tests (see Vogel et al., 2003; Vogel and Peukert, 2005) or by fitting a combined PBM–DEM, which considers actual particles to be ground, to the experimental PSD evolution (Capece et al., 2014). In this study, we did not consider such an elaborate and computationally expensive approach; instead, we considered only the ball motion without the clinker particles, which was also adopted in other studies (Datta and Rajamani, 2002; Clearly, 2009; de Carvalho and Tavares, 2013; Bian et al., 2017). In the absence of the threshold impact energy for the cement clinker, we disregarded collisions with $<10^{-8}$ J as they may not cause any breakage, and they typically constituted much less than 1% of the collisions. A separate analysis was also conducted wherein we disregarded collisions with $<10^{-6}$ J. The microdynamic parameters obtained from this new analysis were obviously different. However, the general trends regarding the impact of the ball sizes and the ball material on the microhydrodynamic parameters remained the same in both cases.

Considering that the microdynamic information obtained from the DEM was solely used to interpret the PBM findings and breakage kinetics, we can safely conclude that the choice of $<10^{-8}$ J vs. $<10^{-6}$ J did not affect DEM-based explanation of the observed breakage kinetics.

A general trend observed in **Figure 6.11** is that the large balls (40 mm) were associated with a higher frequency of high-energy collisions ($>10^{-2}$ J) than the other balls, whereas the small balls (20 mm) yielded a much higher frequency of collisions with $<10^{-4}$ J. Apparently, the steel balls produced a greater collision frequency at the relatively high energy levels than the alumina balls for all single ball sizes and the ball mixture. DEM sensitivity analysis for balls with different density and shear modulus indicated that dissipation energy distribution was mainly affected by the ball density, and to a lesser extent by the shear modulus; so, the different collisional energy spectra and breakage kinetics associated with the steel vs. alumina balls are mainly determined by the higher density of the steel balls as compared with the alumina balls.

For a given ball material, the total collision frequency f_{col}, the collision frequency per ball $f_{\text{col,n}}$, and the specific collision frequency per unit mass of balls $f_{\text{col,m}}$ increased when smaller balls (higher in number) were used, whereas the mean energy dissipation rate $\bar{\dot{E}}$ increased when coarser balls were used (**Table 6.6**). These two counteracting effects of the ball size on the collision frequency and the impact energy somewhat balanced each other, leading to a higher, albeit to a much smaller extent, increase in the total energy dissipation rate $\dot{E}$ when smaller balls were used, which could explain the "overall" faster breakage with the smaller balls (refer to **Figures 6.2 and 6.3**). The S_i profiles in **Figure 6.4** and the exponents $m < 0$ (governing $x_i << d_B$) and $n > 0$ (governing $x_i < d_B$) suggest that

the smaller balls were more effective breaking the smaller clinker particles and the bigger balls were more effective breaking the coarser clinker particles, causing a rightward shift of x_m when the coarser balls were used. This could be explained as follows: a high collision frequency could be important for the breakage of relatively small clinker particles while a high impact energy could be important for breaking the coarse clinker particles. While the mass-specific threshold impact energy of the particles to be ground inversely varies with particle size x_i (Vogel et al., 2003; Vogel and Peukert, 2005), the threshold impact energy increases with the square of the particle size (Capece et al., 2014). In view of these considerations, the drastically higher f_{col}, $f_{col,n}$, and $f_{col,m}$ make small balls (20 mm) advantageous for breaking the finer clinker particles, while the higher $\overline{\dot{E}}$ of the large balls (40 mm) make them advantageous for breaking the coarser clinker particles. This could fundamentally explain the S_i profiles in terms of the ball size impact (refer to Figure 4). As expected intuitively, when a ball mixture (uniform mass) of 20–30–40 mm balls were used, the f_{col} and $\overline{\dot{E}}$ fell in between those of 20 mm and 30 mm balls, which could explain the S_i profiles in **Figure 6.4**. Interestingly, the ball mixtures had higher $\dot{E}$ than 20 mm and 30 mm balls alone. This finding could explain why the ball mixture performed second to the 20 mm balls alone in terms of producing the finest clinker particles, albeit without any unbroken cement clinker particles (refer to **Figures 6.2 and 6.8**) and rationalize the practice of ball mixtures vs. mono-sized balls in industrial applications.

Finally, **Figure 6.11** and **Table 6.6** data show that for the same ball size, the steel balls had 22–26-fold higher $\overline{\dot{E}}$ than the alumina balls, whereas the alumina balls had about 3-fold higher f_{col} than the steel balls. Overall, the steel balls had about 8–9-fold higher $\dot{E}$ than the alumina balls, which could explain the higher S_i values (refer to **Figure 6.4**),

generation of finer cement clinker upon primary breakage (refer to **Figure 6.5**), and faster milling with the steel balls (refer to **Figures 6.2 and 6.3**) as compared with the alumina balls.

6.4.5 On the replacement of steel balls with alumina balls in full-scale continuous ball mills

One of the drivers for this study was to assess the feasibility of the replacement of the traditional media, i.e., steel balls of density ρ_B = 7800 kg/m^3, with ceramic balls such as alumina of ρ_B = 3500 kg/m^3 in continuous ball mills during the production of cement clinker. As can be seen from Equation (6.11) (Brochot et al., 2006), the power consumption P in a continuous ball mill is proportional to the ball density ρ_B and $J(3.2–3J)$ with J denoting fractional ball loading; hence, the direct replacement with the same J may lead to a 55% reduction in power and energy consumption.

$$P = 4.879\left(\frac{\pi}{4}D^{2.3}L\right)0.6J\rho_B\left(3.2-3J\right)\phi_C\left(1-\frac{0.1}{2^{9-10\phi_C}}\right) \tag{6.11}$$

Here, D, L, and ϕ_C denote the mill diameter, the mill length, and the fraction of operating rotation speed compared to the critical speed. However, as established in this study, due to the slower breakage kinetics associated with the alumina balls as compared with the steel balls, such a power/energy reduction is impossible to achieve if the product fineness and the fresh feed rate (equals production rate at the steady-state) to the continuous ball mill are to be kept the same. In this context, one can increase J of the alumina balls with the goal of increasing S_i and keeping the same product fineness. To examine the

potential improvement in S_i when alumina balls are used, let us consider a typical set of operating conditions of full-scale continuous ball mill operation, based on Genc (2008), Altun (2018), and Nomura (2020): J = 0.27, fractional powder loading f_c = 0.097, porosity ε = 0.40, and interstitial powder filling fraction U = 0.90 (note: $U = f_c/J\varepsilon$). This selected operating condition is in the common range of full-scale cement ball mills operating in the closed-circuit mode (Nomura, 2020). These values were taken as the base case, and then J was increased from 0.27 to 0.30, 0.34, and 0.37 keeping the same f_c and ε, which we refer to new cases. By using the celebrated scaling rules of Austin (Austin et al., 1984), one can find the ratio of S_i in the new case to that in the base case:

$$\frac{S_{i,\text{new}}}{S_{i,\text{base}}} = K_3 = \frac{1+6.6J_{\text{base}}^{2.3}}{1+6.6J_{\text{new}}^{2.3}} \exp\left[-1.2\left(U_{\text{new}} - U_{\text{base}}\right)\right] \tag{6.12}$$

The ratio K_3 was calculated, and the results are presented in **Table 6.7**. The K_3 values suggest that up to 7% increase in S_i is possible upon an increase in J from 0.27 to 0.34, corresponding to a 26% increase in alumina ball loading. In the absence of any scale-up work with alumina balls for the pre-milled cement clinker, it is difficult to know if this 7% increase in S_i at the full-scale would be able to compensate for the drop in S_i observed at the lab-scale when the steel balls were replaced with the alumina balls (refer to **Figure 6.4**). More importantly, with this increase in J from 0.27 to 0.34, even the total replacement of the steel balls with the alumina balls could only reduce power/energy consumption by 48%, not 55%, per Equation (6.11).

Table 6.7 Potential Improvements to the Specific Breakage Rate S_i at Typical Full-scale Continuous Ball Milling Conditions upon an Increase in Fractional Ball Loading J

Operation condition and improvement in S_i	Base case	New case 1	New case 2	New case 3
Fractional ball loading, J (–)	0.27	0.30	0.34	0.37
Fractional powder loading, f_c (–)	0.097	0.097	0.097	0.097
Interstitial powder filling fraction, U (–)	0.90	0.81	0.72	0.66
Ratio of $S_{i,new}$ to $S_{i,base}$, K_3 (–)	–	1.04	1.07	1.06

Another important consideration is that in a full-scale two-compartment continuous ball mill operating in the closed-circuit mode, for an unmilled cement clinker feed, it is customary to load ~50–90 mm steel balls in the first compartment with length L_1 and ~20–40 mm steel balls in the second (fine milling) compartment with length L_2 (Austin et al., 1975; Clearly, 2009). In our study, due to their lower impact energies (refer to Subsection 6.4.4), the 20–30–40 mm alumina ball mixture led to slower breakage than the 20–30–40 mm steel ball mixture, with unbroken coarse particles in the mill at 12 min even for a pre-milled cement clinker unlike the steel ball mixture (refer to **Figure 6.8**). This fact and along with the concern about potential breakage of large alumina balls (50–90 mm) inform engineers to keep 50–90 mm steel balls in the first compartment and replace the 20–40 mm steel balls in the second compartment by the 20–40 mm alumina balls, with ensuing partial replacement of the steel balls. Having steel balls in the first compartment along with an increase in J from 0.27 to 0.34 as well as additional potential adjustments to the external classifier parameters will likely compensate for the slower breakage associated with the partial replacement of the steel balls and help to keep a similar product fineness. Obviously, full-scale testing is required to confirm this aspect. Based on Equation (6.11) and representative values of L_1 = 3.9 m and L_2 = 8.4 m (Altun, 2018), we find that the partial

replacement of the steel balls with the alumina balls in the second compartment along with an increase in J from 0.27 to 0.34 will reduce the power/energy consumption by 28%. An alternative approach is to utilize the novel concept of mixtures of different ball materials demonstrated for a stirred ball mill (Guner et al., 2021). A mixture of steel and alumina balls in the second compartment of the continuous ball mill can also reduce the power consumption, albeit to a smaller extent than the full replacement, but potentially without causing significant drop of the breakage rate associated with the alumina balls. This approach warrants further experimental and modeling investigation.

6.5 Conclusions

This study demonstrated the impacts of ball material type (steel vs. alumina) and ball size on the breakage kinetics of a pre-milled cement clinker in a lab-scale ball mill. The newly developed global optimizer-based back-calculation method was proven accurate and reliable. Predicted timewise evolution of PSD with the ball mixture demonstrated reasonably good agreement with the experimental data for both steel and alumina balls, showing the prediction capability of the PBM. The estimated S_i and $B_{i,j}$ suggest that the feed clinker particles were broken into coarser particles slowly when the alumina balls were used as the media in lieu of the steel balls. For the same ball material, the estimated S_i values suggest that the smaller balls were more effective for breaking the smaller clinker particles, while the bigger balls were more effective milling the coarser clinker particles. Hence, the ball mixture of 20 mm, 30 mm, and 40 mm balls was the most effective overall: it was ranked second to the 20 mm balls in generating the finest PSD, but without having any unbroken particles in the milled product unlike the case for the 20 mm balls. The

preliminary DEM study considered only the ball motion, without the clinker particles, and yielded the dissipated energy spectra of the balls. The DEM provided significant physical insights into the observed breakage kinetics when various ball sizes and ball materials were used. We have also assessed the feasibility of power reduction and potential energy savings by replacing the conventional steel balls with the alumina balls in full-scale continuous ball mills. Our analysis suggests that (i) the reduction in power consumption is limited by the slower breakage associated with the alumina balls and the need to use the alumina balls in the fine milling compartment, and (ii) it is possible to make significant power/energy reduction with partial replacement of the conventional steel balls with the alumina balls; however, it is unrealistic to expect more than ~30% in energy savings.

CHAPTER 7

SIMULATION OF A VERTICAL ROLLER MILL

Our recently developed true unsteady-state simulator (TUSSIM) for continuous milling was used to model a full-scale vertical roller mill (VRM) for cement milling. TUSSIM is based on a cell-based population balance model with internal classification. Its mathematical model consists of a set of differential algebraic equations. TUSSIM can be modified to model closed circuits by incorporating an external classification model (Tromp curve model) of air classifiers. Constructing a Tromp curve requires particle size distribution (PSD) of three streams—classifier feed, coarse reject, and fine product streams. VRM combines particle breakage and classification in a single-unit operation. Thus, the PSDs of coarse reject and classifier feed streams cannot be sampled. It is challenging to obtain a credible Tromp curve that represents particle classification by an air classifier. In this work, two different models with particle classification were tested to determine whether they could represent VRM operation realistically. The first model (Model A) treated VRM as an open-circuit continuous mill with internal classification, whereas the second, more elaborate model (Model B) treated it as a closed-circuit continuous mill with external classification. A realistic degree of mixedness of the particles inside the mill was used based on the residence time distribution data. Model fitting was performed using a global optimizer-based back-calculation method to determine the unknown model parameters of breakage kinetics and classification. Our results suggest that both models could be used to simulate the product PSD during VRM of cement clinker. The cut size of classification, 1.6 μm, is somewhat unrealistic, which could explain the

high specific breakage rate parameter (Model A: the open-circuit model with internal classification). In the case of the closed circuit with an external classification model (Model B), a decent value for the specific breakage parameter was obtained, which aligned well with the realistic cut size of 34 µm for air classifier. Model B requires a credible Tromp curve, which is hard to obtain since particle classification takes place inside the VRM.

7.1 Introduction

Vertical roller mills (VRM) have been used for cement milling since the 1980s (Tamashige et al., 1991). It has been reported that the specific energy consumption of VRMs is lower than that of traditional ball mills (Tamashige et al., 1991; Xu et al., 2015). A VRM combines particle breakage and classification processes into a single-unit operation. **Figure 7.1** presents a general flow diagram of the VRM milling process. **Figure 7.2** presents a detailed view of VRM operations (Strohmeyer, 2013).

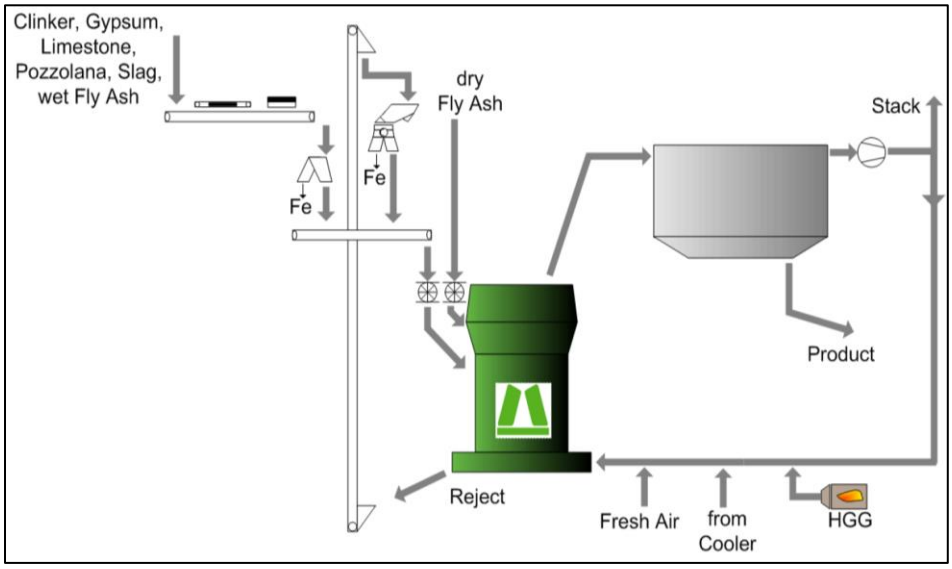

Figure 7.1 A general schematic of VRM operations.
Source: Strohmeyer (2013)

A simplified process operation can be briefly explained as follows. First, fresh particles are continuously fed to the VRM by a feeder. These fresh feed particles are mixed with coarse particles on the milling table, which are recycled from the built-in air classifier on top of the VRM. The milling pressure is transferred from the hydraulic cylinder to rollers for particle breakage. The particles retained on the rotating table due to the dam ring at the table's edge are broken by rollers. The rollers are rotated according to the motion of the rotating table. Therefore, both compression and shear forces from the rollers are applied for particle breakage. Sufficiently fine particles are lifted to the air classifier by air flow induced by an external mill fan, and fine products passing through the air classifier are collected as the final product. Finally, coarse particles are recycled back to the table and mixed with fresh feed particles. This process takes place continuously inside the VRM.

Constructing a Tromp curve for classification requires particle size distributions (PSDs) of three streams around the air classifier—classifier feed, coarse reject, and fine product streams. Unlike ball milling in closed-circuit operations, the PSDs of classifier feed and coarse reject streams could not be sampled separately because the PSDs of these streams are mixed inside the mill. Recent works (Aydogan, 2015; Altun et al., 2017) have demonstrated a mass balance method to determine the PSDs of the classifier feed and coarse reject streams that cannot be experimentally sampled. In Altun et al. (2017), the PSD in front of the roller was assumed to be the PSD of the mill inlet, which is the combination of fresh feed and coarse reject PSDs. The PSD after roller was assumed to be the PSD of the mill outlet. With these assumptions, the PSDs of all streams can be estimated. As a result, the Tromp curve of the air classifier of the VRM can be

approximated. However, the Tromp curve reported in Altun et al. (2017) was not coupled with the PBM to simulate the evolution of PSD during the milling of full-scale VRM.

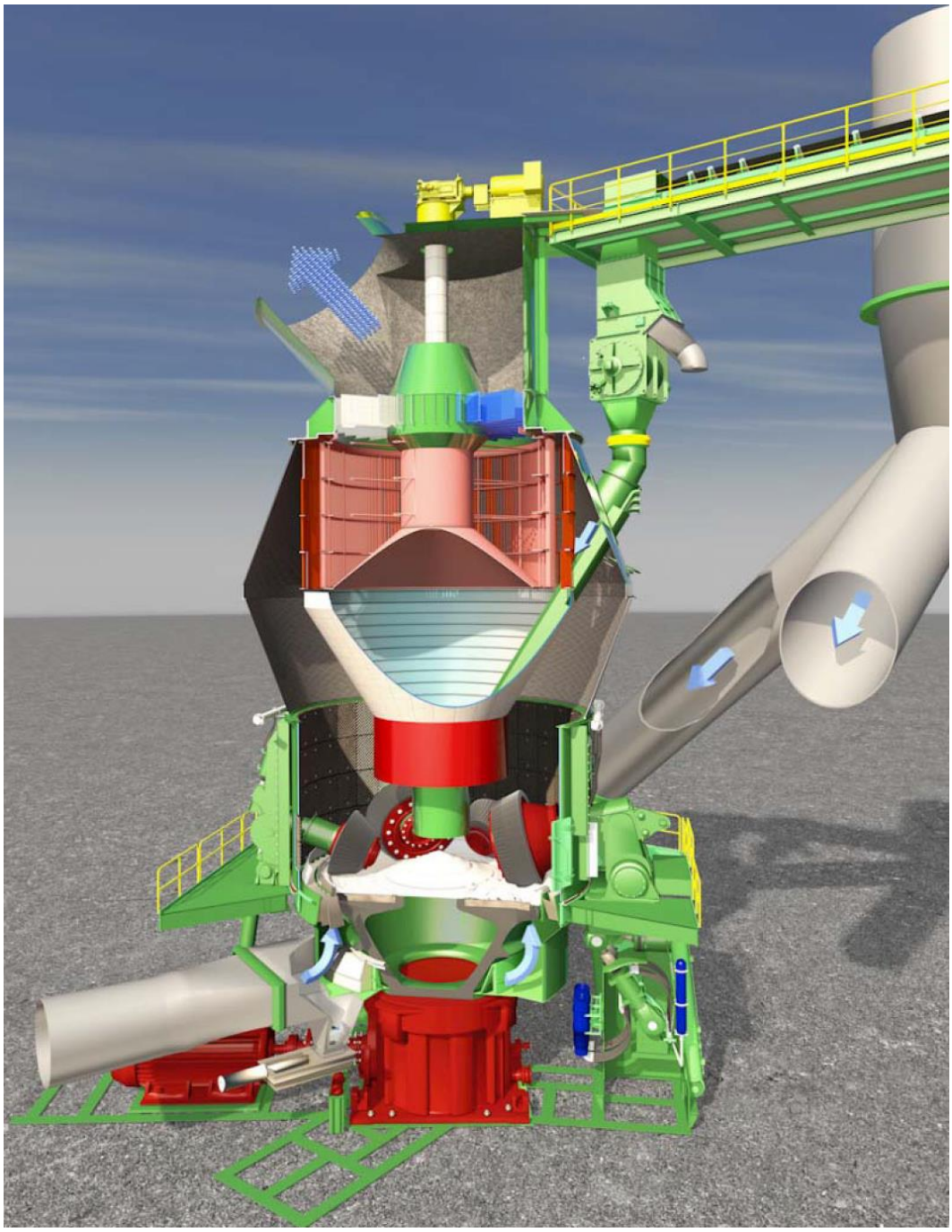

Figure 7.2 A detailed view of VRM operations.

Source: Strohmeyer (2013)

In the context of the population balance model (PBM), only a limited number of studies on VRM for cement milling (Shahgholi et al., 2017; Fatahi and Barani, 2020; Fatahi et al., 2022) are available in the literature. All these works were conducted by the research group in Iran. The modeling approach from this group can be summarized as follows. Cumulative breakage distribution parameters used in the PBM were obtained from lab-scale data using a compression piston (Shahgholi et al., 2017), where the shear force could not be accounted for. The cumulative breakage distribution parameter was assumed to be material dependent and did not vary with the operation conditions. The experimentally obtained residence time distribution (RTD) data of full-scale VRM for cement mills was fitted with various RTD models. Their results (Fatahi and Barani, 2020) showed that the 5-tanks-in-series model could be accurately fitted with the experimental RTD of VRM. The average residence time (space time) was reported to be 1.12 min. However, when their PBM simulation was performed, they assumed ideal perfect mixing (i.e., one tank), which contradicts their RTD study (Fatahi and Barani, 2020). These previous modeling studies applied a steady-state, perfect mixing PBM for a continuous mill to fit the experimental cement product PSD at steady state. Their model considered only breakage kinetics while disregarding particle classification in the VRM. Neglecting classification could lead to an erroneous interpretation of the breakage kinetics and erroneous specific breakage rate parameters (falsified kinetics). Given the limitations of prior work, there is a need to develop a robust model of VRM that accounts for particle classification.

As advanced from the currently available models, our recently developed true unsteady-state simulator (TUSSIM) with two different approaches for particle classification was used to fit the steady-state cement product PSD of the VRM using a

global optimizer-based back-calculation method. All the parameters used in the simulation were taken from the VRM literature. We first tested whether the VRM circuit could be represented by open-circuit milling with internal classification (Model A). Subsequently, a more elaborate model (Model B) representing closed-circuit milling with external classification requiring a Tromp curve model was assessed. While this was our first attempt to simulate VRM, the model structure was obviously advanced from all prior studies as particle classification in the VRM was explicitly accounted for.

7.2 Theoretical

7.2.1 Model description

TUSSIM was developed based on cell-based PBM, where the degree of mixedness can be modulated by the number of cells n and the axial back-mixing ratio R. The derivation of TUSSIM can be found in Muanpaopong et al. (2022a). Based on Fatahi and Barani (2020), the 5-tanks-in-series model accurately represented the experimental RTD of full-scale VRM. Therefore, $n = 5$ and $R = 0$ were used to represent the realistic mixing of the VRM in TUSSIM. Two representation models (Models A and B) were tested to determine whether they could represent particle classification and overall VRM operation well.

7.2.1.1 Model A: Continuous open-circuit mill with internal classification. The first model treats VRM as a continuous open-circuit mill with an internal classification action (discharge screen). A schematic of Model A is shown in **Figure 7.3**. A size-discretized, time-continuous PBM for five cells with discharge screen is expressed by

$$\frac{dm_{i,z}}{dt} = \begin{cases} -S_i m_{i,z} + \sum_{j=1}^{i-1} b_{i,j} S_j m_{j,z} \\ +\left(Rm_{i,z+1} - m_{i,z} - Rm_{i,z} \right) \tau_z^{-1} + \dot{m}_{i,\mathrm{FF}} & \text{for } z = 1 \\ -S_i m_{i,z} + \sum_{j=1}^{i-1} b_{i,j} S_j m_{j,z} \\ +\left(m_{i,z-1} + Rm_{i,z-1} + Rm_{i,z+1} - m_{i,z} - 2Rm_{i,z} \right) \tau_z^{-1} & \text{for } z = 2-4 \\ -S_i m_{i,z} + \sum_{j=1}^{i-1} b_{i,j} S_j m_{j,z} \\ +\left(m_{i,z-1} + Rm_{i,z-1} - Rm_{i,z} \right) \tau_z^{-1} - \dot{m}_{i,\mathrm{out}} & \text{for } z = 5 \end{cases} \tag{7.1}$$

with $m_{i,z}(0) = 0$. Here, i and j are size class indices. The size classes ranged from size class 1 (containing the coarsest particles of size x_1 = 80 mm) to size class N = 160 (containing the finest particle of size x_N) with a geometric progression of $2^{1/8.5}$. The particle size in each size class was represented by the upper edge of the size class. t is the milling time. $\dot{m}_{i,\mathrm{FF}}$ and $\dot{m}_{i,\mathrm{out}}$ denote the inlet mass flow rate and outlet mass flow rate, respectively, of the particles in size class i. z is the index used for the cell. S_i is the specific breakage rate parameter of particle size x_i. The breakage distribution parameter is denoted as $b_{i,j}$ with the cumulative form of $B_{i,j}$.

The average residence time of cell z is denoted as τ_z, defined as the ratio of the mass in cell z ($m_{\mathrm{H},z}$) to the total mass flow rate through that cell, and τ_z was determined from $\tau_z = \tau/n$. Here, τ = 1.12 min was taken from Fatahi and Barani (2020) based on their RTD data. The production rate equals the rate of discharge through the discharge screen, as modulated by the screen's classification function P, i.e., $\dot{m}_{i,\mathrm{P}} = \dot{m}_{i,\mathrm{out}} P_i$. The coarser particles that are prevented from leaving the mill by the discharge screen are recycled to the last cell (King, 2001). This relationship was mathematically expressed as $\dot{m}_{i,\mathrm{oversize}} =$

$\dot{m}_{i,\text{out}}(1-P_i)$. Unlike that of the first and intermediate cells, the average residence time in the last cell ($z = n$) connecting to the discharge screen was expressed by:

$$\tau_n = \frac{m_{\text{hold-up},n}}{\sum_{i=1}^{N} \dot{m}_{i,\text{FF}} + \sum_{i=1}^{N} \dot{m}_{i,\text{oversize}}} \tag{7.2}$$

where $m_{\text{hold-up},n}$ is the total mass of material in cell n. Note that $\dot{m}_{\text{oversize},i}$ is time-dependent and unknown during a transient operation. Therefore, Equation (7.2) was solved simultaneously with Equation (7.1), forming a set of differential algebraic equations (DAEs). A steady state was attained when the sum of the absolute difference between the cumulative PSDs of the subsequent time steps for all size classes was equal to or less than 10^{-2}. This criterion must be satisfied for all PSDs inside the mill and product streams. The conservation of mass dictates that the S_i and $b_{i,j}$ parameters must satisfy mass conservation through the following constraints: $S_N = 0$, $b_{i,i} = 0$, and $\sum_{i=j+1}^{N} b_{i,j} = 1$.

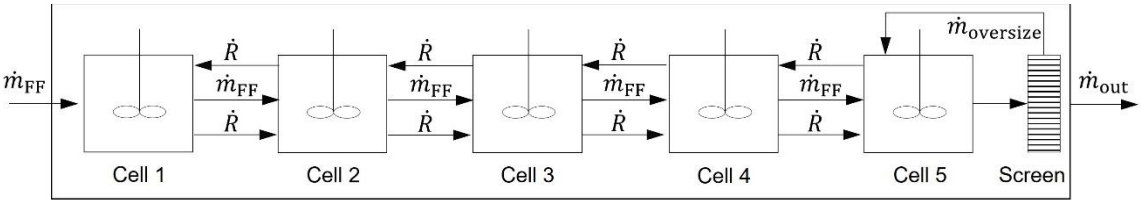

Figure 7.3 Schematic of Model A: Open-circuit mill with internal classification. Mill is represented by five perfect mixing cells in a series. The axial recirculation rate $\dot{R}$ is exchanged between adjacent cells.

7.2.1.2 Model B: Continuous closed-circuit mill with external classification. The second model represents the VRM as a continuous closed-circuit mill with an external

classification action. A schematic of Model B is shown in **Figure 7.4**. Here, the internal classification was neglected, i.e., $P_i = 1$ for all i size classes. In the case of closed-circuit milling with external classification, $\dot{m}_{i,\mathrm{FF}}$ in Equations (7.1) and (7.2) was replaced by the mass flow rate of the mill inlet stream of size class i ($\dot{m}_{i,\mathrm{MI}}$), which is the combination of $\dot{m}_{i,\mathrm{FF}}$ and the mass flow rate of the coarse reject stream in size class i ($\dot{m}_{i,\mathrm{R}}$). In correlation with the Tromp curve value of particles in size class i (T_i), the mass flow rates of product ($\dot{m}_{i,\mathrm{P}}$) and reject ($\dot{m}_{i,\mathrm{R}}$) streams were determined from $\dot{m}_{i,\mathrm{P}} = \dot{m}_{i,\mathrm{out}}(1-T_i)$ and $\dot{m}_{i,\mathrm{R}} = \dot{m}_{i,\mathrm{out}}T_i$, respectively.

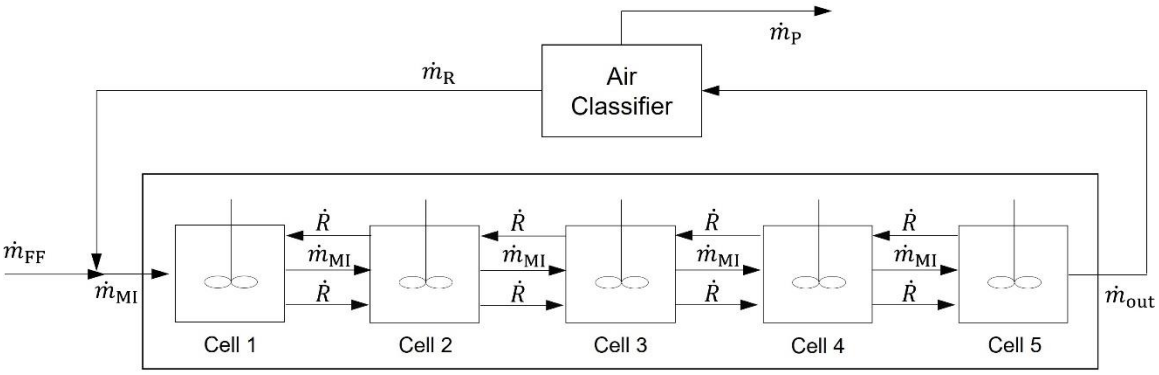

Figure 7.4 Schematic of Model B: closed-circuit mill with external classification. Mill is represented by five perfect mixing cells in a series. The axial recirculation rate $\dot{R}$ is exchanged between adjacent cells. The coarse particles rejected from the dynamic air classifier are returned to the mill, whereas the fine particles are obtained as the final product.

7.2.2 Selected functional forms used in the PBM

A power-law function was selected for the specific breakage rate parameter S_i, and the one-parameter normalized function was selected for the cumulative breakage distribution parameter $B_{i,j}$, as expressed by

$$S_i = Ax_i^{\gamma},\ B_{i,j} = \left(x_{i-1}/x_j\right)^{\mu} \text{ with } b_{i,j} = B_{i,j} - B_{i+1,j} \tag{7.3}$$

In Equation (7.3), A is the breakage rate constant, γ is the breakage rate exponent, and μ is the breakage distribution exponent. In the case of discharge screen for Model A, internal classification parameter P_i, based on the Whiten model (Napier-Munn et al., 1996) in Equation (7.4), assumes absence of bypass and fish hook effects.

$$P_i = \left[\exp\left(\alpha_{\mathrm{d}}\right) - 1\right]\left\{\exp\left(\alpha_{\mathrm{d}}\frac{x_i}{x_{50\mathrm{c,d}}}\right) + \exp\left(\alpha_{\mathrm{d}}\right) - 2\right\}^{-1} \tag{7.4}$$

Here, α is the sharpness parameter and x_{50c} is the corrected cut size. The subscript d refers to the discharge screen. In the case of the Tromp curve for external particle classification in Model B, the Whiten model (Napier-Munn et al., 1996) was also used for external classification, as expressed by:

$$T_i = 1 - \left(1 - \delta_{\mathrm{a}}\right)\left(1 + \beta_{\mathrm{a}}\beta_{\mathrm{a}}^{*}\frac{x_i}{x_{50\mathrm{c,a}}}\right)\left[\exp\left(\alpha_{\mathrm{a}}\right) - 1\right]\left\{\exp\left(\alpha_{\mathrm{a}}\frac{x_i}{x_{50\mathrm{c,a}}}\right) + \exp\left(\alpha_{\mathrm{a}}\right) - 2\right\}^{-1} \tag{7.5}$$

where δ is the bypass parameter, β is the fish–hook parameter, and β^* is a parameter that preserves the definition of x_{50c}. The subscript a refers to the air classifier. Note that different models for particle classification, Equations (7.4) and (7.5), were used in Models A and B, respectively. Model A used Equation (7.4) with two parameters only because it would be impossible to calibrate the model if it had more parameters in the absence of PSD data from a reject stream. Model B used Equation (7.5) with 4 adjustable parameters as the fitting of Model B entails consideration of two different PSDs, as will be elaborated below.

7.2.3 Model fit and parameter estimation

The combined global optimizer–DAE solver was used to estimate unknown breakage kinetic parameters and classification parameters. The number of trial points was set to 200 as the minimum default from MATLAB. The objective function to be minimized by the global optimizer was the sum of the square residuals (*SSR*) between the experimental and simulation results of steady-state PSDs in cumulative form. The MATLAB function "GlobalSearch" was used to generate a set of initial guesses for the next trial point using the scatter method (Glover, 1998). The stopping criteria of the optimizer were taken from Capece et al. (2011), where termination tolerances on constraint violation, function value, and parameter were all set to 10^{-9}. For the DAE solver, relative and absolute tolerances of 10^{-4} and 10^{-6}, respectively, were also taken from Capece et al. (2011).

7.3 Results and Discussion

We began by performing the model fitting of the open-circuit mill with internal classification (Model A). The parameters to be estimated were breakage kinetics parameters (3 parameters: A, γ, and μ) and classification parameters (2 parameters: α_d and

$x_{50c,d}$). Here, fresh feed PSD was taken from Fatahi and Barani (2020). For Model A, only the cement product PSD was considered in the objective function. **Table 7.1** lists the upper bound and lower bound along with the initial guess value of each parameter and the solution returned from the global optimizer. As shown in **Figure 7.5**, the simulated PSD using parameters obtained from the global optimizer was almost identical to the experimental cement product PSD taken from Fatahi and Barani (2020). As can be seen in **Figure 7.6**, S_i values were very high—up to ~4800 min^{-1} at a particle size of 40 mm and S_i dropped dramatically with decreasing particle size. A similarly high value of S_i was reported in Fatahi and Barani (2020), where classification was disregarded during fitting. Although almost identical results of simulated cement product PSD at steady state were obtained in comparison with experimental product PSD, we suspect that this high value of S_i may be caused by improper modeling of the air classifier as a discharge screen (internal classification). Note that $x_{50c,d}$ = 1.59 μm is highly realistic for particle classification in the VRM, and such a value suggests that there is no classification of particles with a size above a few microns. Considering the fact that the product PSD had ~80% particles above ~4 μm, majority of the particles were not even subjected to particle classification. As the fitting of Model A did not consider any PSD other than of the product stream, it was not possible to identify a good classification model, which probably led to the extremely high S_i values.

Table 7.1 Parameters Obtained from the Global Optimizer

Parameter	Initial guess	Constraint		Solution from global optimizer	
		Lower bound	Upper bound	Model A	Model B
A (min^{-1})	5	0	40	14.2	1.67
γ	0.1	0	5	1.58	4.43×10^{-1}
μ	0.5	0	5	7.26×10^{-1}	7.46×10^{-2}
α_d	0.5	0	10	1.06×10^{-2}	–
$x_{50c,d}$ (mm)	0.5	0	1	1.59×10^{-3}	–
SSR				2.36×10^{-3}	1.01×10^{-1}

The next model fitting was performed for the closed-circuit mill with external classification (Model B). Before performing the model fitting of the PSDs in the VRM circuit, we first fitted Equation (7.5) with the experimental Tromp curve reported in Altun et al. (2017) by minimizing the *SSR* between the experimental Tromp curve value and the fitted Tromp curve value. In other words, particle classification was decoupled and fitted separately. The obtained parameters for simulating the Tromp curve were $\alpha_a = 1.28$, $\beta_a = 2.92$, $\delta_a = 0.704$, and $x_{50c,a} = 33.5$ μm (see **Figure 7.7**). The $x_{50c,a} = 33.5$ μm is quite realistic considering the typical air classifiers used in cement manufacturing. In Altun et al. (2017), the PSD and mass flow rates of cement clinker, gypsum, and limestone were reported individually. In our study, we estimated the fresh feed stream PSD to be fed to the VRM by weighted average using the reported PSD and mass flow rate of each component. Unlike Model A, where only cement product PSD at steady state was considered, steady-state PSDs of the cement product and mill inlet were considered in the objective function for Model B. **Table 7.1** also lists the solution of model fitting using Model B. **Figure 7.8** depicts a comparison between experimental PSDs (Altun et al., 2017) and fitted PSDs performed by this work, showing reasonably good agreement. As can be seen in **Figure**

7.9, a value of ~12 min^{-1} for S_i at a particle size of 80 mm was obtained, which is in the same range as full-scale ball milling. As signified by the low exponent (μ = 0.07) in Model B (**Table 7.1)**, the $B_{i,j}$ parameter was slightly dependent on the particle size ratio, suggesting a relatively uniform distribution of broken particles' masses. As mentioned earlier, prior work (Shahgholi et al., 2017) determined the $B_{i,j}$ parameter by compression piston, which disregards shear forces. However, both compression and shear forces are imposed on the particle bed during milling using the VRM.

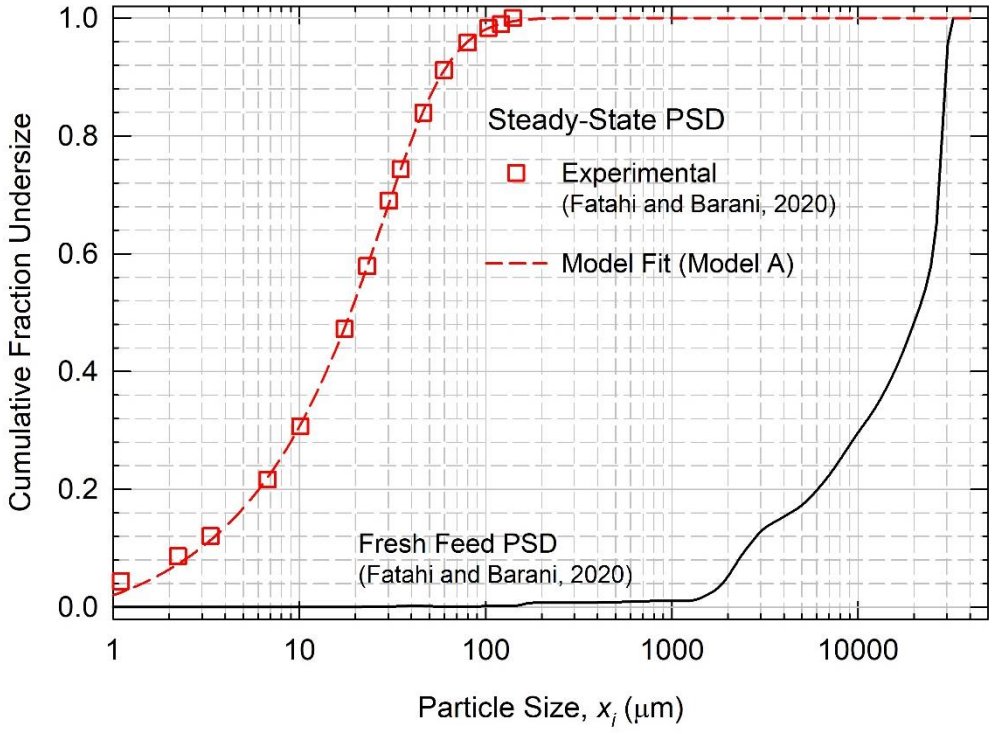

Figure 7.5 A comparison of cement products at steady state between experimental and fitted Model A.

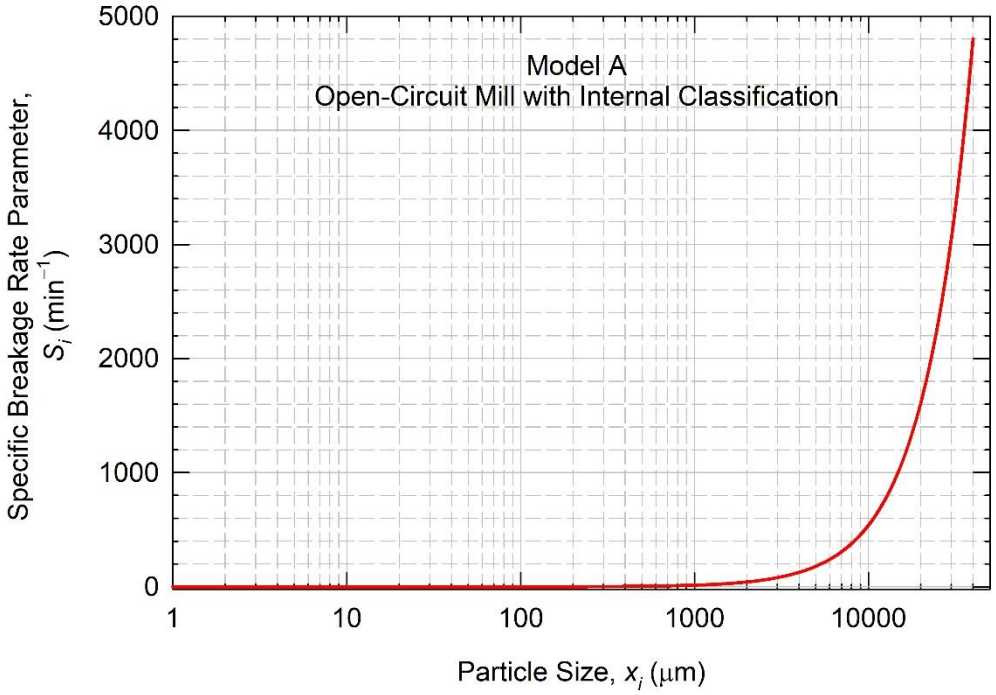

Figure 7.6 Specific breakage rate parameter of Model A: A = 14.2 mm$^{-1.58}$·min^{-1} and γ = 1.58.

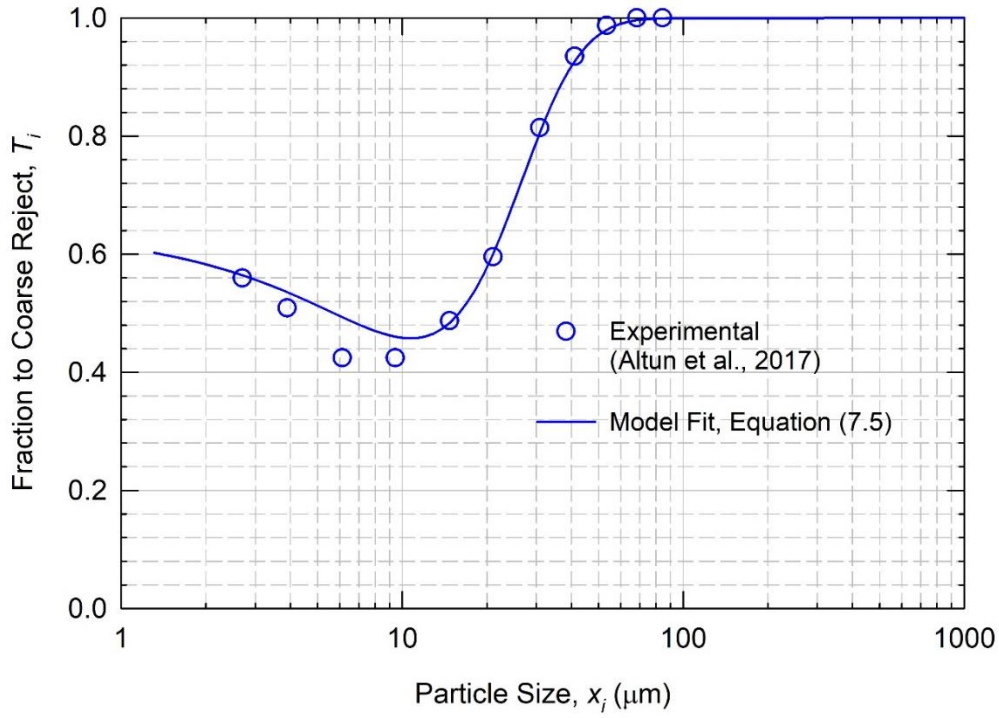

Figure 7.7 Experimental Tromp curve and fitted Tromp curve (α_a = 1.28, β_a = 2.92, δ_a = 0.704, and $x_{50c,a}$ = 33.5 μm).

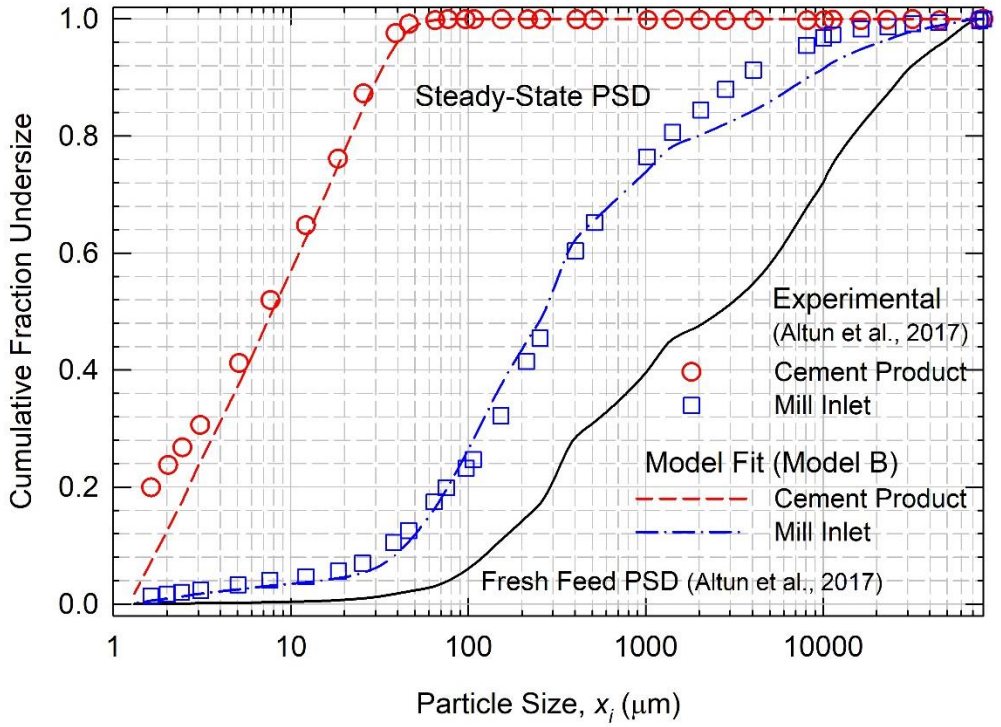

Figure 7.8 A comparison of various PSDs at steady state between experimental and fitted Model B.

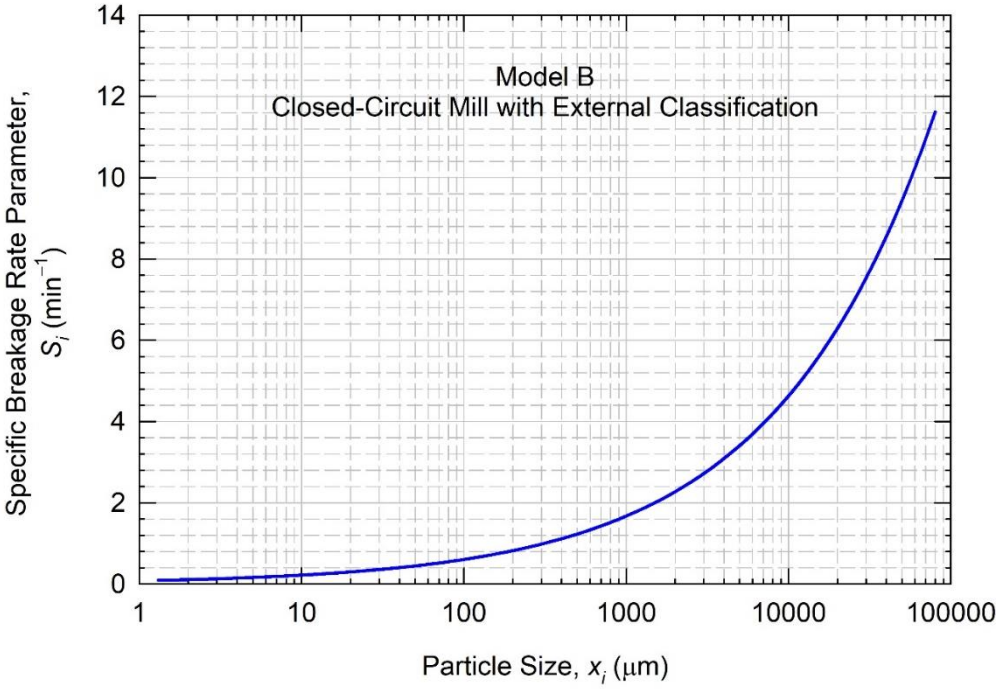

Figure 7.9 Specific breakage rate parameter of Model A: A = 1.67 mm$^{-0.443}$·min^{-1} and γ = 4.43 × 10^{-1}.

7.4 Conclusions

TUSSIM was used to represent a full-scale VRM for cement milling, where particle breakage and particle classification were combined in a single-unit operation. Unlike previous PBM studies in which particle classification was disregarded, we assessed the feasibility of using two representative models of particle classification to simulate VRM at steady state—(i) an open-circuit mill with internal classification (Model A) and (ii) a closed-circuit mill with external classification (Model B). A realistic degree of mixedness of particles inside the VRM was used during the simulation, based on experimental RTD data in full-scale operation. The simulation results suggest that both models mentioned above could be used to represent VRM. Although the open circuit with internal classification provided an almost perfect model fit with experimental cement product PSD at steady state, its particle classification function appears to be unrealistic, leading to an erroneous interpretation of specific breakage rate parameters. The obtained value of the specific breakage rate parameter is similar to those estimated from a prior PBM study that neglected particle classification. On the other hand, a more elaborated closed circuit with external classification (Model B) provides decent values for the particle classification and specific breakage kinetics. However, a realistic Tromp curve is required for external classification. Overall, we successfully demonstrated the capability of TUSSIM to represent VRM operation using two different models incorporating the classification of particles, which is advanced from the currently available literature.

CHAPTER 8

CONCLUSIONS AND FUTURE WORK

8.1 Conclusions

In this dissertation, a true unsteady-state simulator (TUSSIM) was developed for continuous dry milling. TUSSIM is based on a cell-based population balance model (PBM) that can address the degree of nonideal mixedness of particles inside the mill and the internal classification of particles. TUSSIM's mathematical model consists of a set of differential algebraic equations (DAEs), which were numerically solved. In Chapter 2, TUSSIM was used to simulate the spatio-temporal evolution of the particle size distribution (PSD) in the mill and the product stream of continuous open-circuit dry milling with a discharge screen. The simulation results suggest that a smaller screen opening not only delayed the attainment of the steady state but also increased the total mass hold-up and led to a finer product PSD. The cushioning action of fines resulted in a coarser product PSD. However, a smaller opening of the discharge screen mitigated this effect.

Subsequently, in Chapters 3–5, TUSSIM was employed to perform comprehensive parametric studies for full-scale ball milling of cement clinker to gain a fundamental process understanding. All parameters were obtained from the available literature on cement clinker. In Chapter 3, TUSSIM was used to model a full-scale open-circuit ball milling. The simulation results suggest that milling with a ball mixture outperformed milling with a single ball size. Single-compartment milling produced desirable product fineness when the feed was pre-milled. A two-compartment mill performed similarly to or better than a three-compartment mill, depending on the ball sizes used. For a given set of

ball sizes, a theoretical distribution with a uniform mass of balls, as opposed to that with a uniform number of balls, achieved an 8% increase in the cement product's specific surface area. The use of a classifying liner achieved a negligibly finer cement product compared to a uniform mass of balls.

In Chapters 4 and 5, TUSSIM was modified to model full-scale closed-circuit cement ball milling. Unlike all prior works, the PBM for the mill was coupled with a dust load-dependent variable Tromp curve for the air classifier. In Chapter 4, the impact of the air classifier's operation parameters was investigated. The simulation results suggest that a lower air flow rate or higher rotor speed of the classifier not only led to a finer product but also increased the dust load of the classifier feed. When the dust loading of the classifier feed was too high, operational failure due to overloading of the whole circuit was detected. For the first time, TUSSIM was used for process optimization with a global optimizer–differential algebraic equation (DAE) solver to identify the air classifier's parameters that yielded desirable cement quality while maximizing production rate. At optimum operation conditions, the production rate could be increased by 7% compared to the baseline process.

In Chapter 5, the impact of ball mill's operation was investigated, similar to Chapter 2, but this chapter considers closed-circuit operation. The simulation results suggest that a single-compartment mill entailed a pre-milled feed for proper operation, whereas a two-compartment mill yielded a finer cement product than a three-compartment mill. The uniform mass distribution of balls led to a slightly finer product than uniform surface area or number distributions, while the impact of a classifying liner was negligibly small. In comparison to the simulation results in Chapter 2, integrating an air classifier into an open-

circuit ball mill increased the production rate by 15% or the cement-specific surface area by 13%. Finally, optimal ball mixtures in a two-compartment mill were identified using a combined global optimizer–DAE solver, suggesting that 14% production rate increase with desirable cement quality was feasible.

In Chapter 6, the breakage kinetics parameters of the pre-milled cement clinker were explored via experiments and PBM–DEM simulations. A global optimizer-based back-calculation method based on PBM was newly developed to estimate the breakage parameters of cement clinker in a lab-scale ball mill loaded with steel or alumina balls of 20, 30, and 40 mm and their mixtures. The ball motion in the mill was simulated using the discrete element method (DEM). The experimental–modeling results show that steel balls achieved faster breakage of clinker into finer particles than alumina balls, which was explained by the higher total–mean energy dissipation rates of the steel balls. The PSD became finer as smaller balls were used. The ball mixture of 20, 30, and 40 mm balls was the most effective overall. It was ranked second to the 20 mm balls in generating the finest PSD; however, the mixture did not result in any unbroken particles in the milled product, unlike the case for the 20 mm balls.

In the last chapter (Chapter 7), efforts were made to model a vertical roller mill (VRM). It must be mentioned that VRM simulation is complicated since milling and classification processes take place within the VRM. Two model structures (open circuit with internal classification and closed circuit with external classification) were evaluated to determine whether they could be fitted with cement produced from a full-scale VRM. The simulation results showed that both model structures successfully fit the product PSD at the steady state of the VRM operation.

8.2 Future Work

8.2.1 Breakage kinetics parameters for multicomponent formulations

In actual cement milling operations, various raw materials such as cement clinker, gypsum, limestone, and fly ash are milled to produce cement powder. However, simulation studies for full-scale ball milling in Chapters 3–5 only considered cement clinker, which is the main component of ordinary Portland cement, which is the most widely used cement type. Future studies should treat breakage of multicomponent formulations as each material can break at different rates and they can accelerate/decelerate the breakage of the other materials, which cannot be treated by the currently available PBMs rigorously.

8.2.2 Modification of Austin's scale-up rule for specific breakage rate parameters

A credible Austin's scale-up rule was used in Chapters 3–5 to translate specific breakage rate parameters estimated from lab-scale data to full-scale operation. The Austin's scale-up factors are based on various experimental data. However, as for any scale-up rule with particulate systems, they are far from excellent. The accuracy of the scale-up factor could be improved by introducing a correction factor that can specifically consider the energy dissipation rates of the colliding balls at different scales. Future studies should focus on modifying Austin's scale-up factors by incorporating information at the particle ensemble scale (e.g., energy dissipation during ball collisions) obtained from mechanistic DEM simulations for different mill scales.

8.2.3 Determination of total mass hold-up

Total mass hold-up is directly reflected in the average residence time, which is one of the input parameters in PBM. In Chapters 4 and 5, the total mass hold-up was assumed to be invariant with the fresh feed rate, within the range studied. The available model for

estimating mass hold-up is apparently limited (e.g., Nomura's transport model). Future studies should focus on developing a robust modeling framework for determining variations in mass hold-up with process operations.

8.2.4 Mixture of different types of grinding balls

A mixture of different materials of balls (beads) was used in a lab-scale wet stirred media mill successfully demonstrated. However, such an approach has not been adopted in dry tumbling ball milling. In Chapter 6, the breakage kinetics of traditional steel balls and alternative alumina steels were explored. To compensate for the slower breakage of the alumina ball, a mixture of alumina balls and steel balls could be used. Future studies should focus on determining the proper operation conditions for this mixture of different ball types. A caveat is that alumina balls could be damaged by collisions with steel balls during dry ball milling; however, considering the significant energy savings, such investigation of such ball mixtures is warranted.

8.2.5 Elucidation of nonlinear effects in batch and continuous milling of cement

Unfortunately, there is no information about nonlinear effects in cement milling. Chapter 2 has already mentioned how to characterize the nonlinear kinetics in continuous ball milling. Moreover, in Chapter 6, batch milling of cement clinker in a lab-scale ball mill has been performed with 3 different sizes of alumina and steel balls. The purpose was to mainly compare alumina and steel balls; nonlinear kinetics was not studied. To this end, batch milling experiments with multiple feed size distributions (at least three widely different PSDs) and multitude of ball sizes (at least 5 different sizes) with prolonged milling (down to a cement clinker media particle size below 10 μm) should be carried out. This will enable

one to generate a dense data set, which in turn will allow for estimation of the nonlinear breakage parameters accurately.

8.2.6 DEM simulations with cements clinker particles

In Chapter 6, DEM simulations were performed considering the balls without the cement clinker particles. A more rigorous simulation, albeit computationally expensive and time-consuming, entails considering the actual cement clinker particles and their size evolution during the milling. Such simulations will enable estimation of size-dependent minimum impact energy and a thorough analysis of the impact energy spectrum of the cement clinker particles. They will also enable to assess energy utilization during milling with alumina vs. steel balls.

8.2.7 Physics of particle classification

In this report, particle classification has been described by a Tromp curve model, which provides a phenomenological description of classification within the context of PBM. On the other hand, a coupled CFD–PBM could help to identify the roles of dust loading, rotor speed, and air flow rate on the classification selectivity and bypass fraction.

8.2.8 Process optimization with economic considerations

Our process optimization in this report has factored in quality metrics of the cement product as well as production capacity, but without considering the operational costs. To the extent realistic cost estimations can be formulated, the objective function of the optimizer can include operational costs.

APPENDIX A

SUPPLEMENTARY DATA FOR CHAPTER 2

The supplementary materials of Chapter 2 are shown in this section.

A.1 Convection–Dispersion PBM

The size- and time-continuous convective dispersion PBM for continuous milling (Mihalyko et al., 1998) is

$$\frac{\partial m_{\mathrm{d}}(x,y,t)}{\partial t} = -k(x)m_{\mathrm{d}}(x,y,t) + \int_{x}^{x_{\max}} b(x,l)k(l)m_{\mathrm{d}}(l,y,t)\mathrm{d}l + D\frac{\partial^2 m_{\mathrm{d}}(x,y,t)}{\partial y^2} - u\frac{\partial m_{\mathrm{d}}(x,y,t)}{\partial y} \tag{A.1}$$

$$m_{\mathrm{d}}(x,y,0) = m_{\mathrm{d},0}(x,y)\,,\ \dot{m}_{\mathrm{in,d}}(x,t) = um_{\mathrm{d}}(x,0,t) - D\frac{\partial m_{\mathrm{d}}(x,0,t)}{\partial y}\,,\ \text{and}\ \frac{\partial m_{\mathrm{d}}(x,L,t)}{\partial y} = 0$$

where m_{d} and t are the mass density and the milling time, respectively. The specific breakage rate function is k, and the breakage distribution function is b. D and u denote the dispersion coefficient and the average velocity, respectively. The left-hand side of Equation (A.1) refers to the accumulation rate of the mass density $m_{\mathrm{d}}(x,y,t)$ of size x particles at longitudinal location y and time t. The first term on the right-hand side represents the death rate due to the breakage of the size x particles, whereas the second term describes the birth rate of size x particles due to the transport of broken particles from size l particles. The third term refers to the dispersive transport of particles due to their random motion, and the fourth term corresponds to the convective bulk transport of the size x particles. The initial

condition specifies that the mill contains mass density $m_{d,0}$ at $t = 0$. The first boundary condition assumes that the mass flow density $\dot{m}_{in,d}$, which is fed to the mill—a flow that is characterized by convective flow—, is equal to the mass flow density at the mill inlet ($y = 0$), which is driven by convective flow and dispersion. The second boundary condition states that the mass density does not change at the mill outlet ($y = L$). Both boundary conditions were formulated by Danckwerts (1953).

A.2 Details of the Cell-based PBM

The derivation of cell-based PBM equations is based on the conservation of mass for particles in each cell *z*, the rate of particle transport between cells and the rate of appearance–disappearance of particles in size class *i* in each cell. To construct the model equations, each cell is considered to be the control volume (CV). For the sake of brevity, only the generic equation for intermediate cells is derived and explained step by step. Consider cell *z* for all integer *z* ($1 < z < n$) as CV; the equation for the mass balance in size class *i* in the CV is expressed as Equation (A.2):

$$\underbrace{\frac{dm_{i,z}}{dt}}_{\substack{\text{Accumulation rate}\\ \text{of mass in size class } i}} = \overbrace{-k_i F_i [\ ] m_{i,z}}^{\substack{\text{Death rate of}\\ \text{mass in size class } i}} \underbrace{+\sum_{j=1}^{i-1} b_{i,j} k_j F_j [\ ] m_{j,z}}_{\substack{\text{Birth rate of}\\ \text{mass in size class } i}}$$

$$\overbrace{+\dot{m}_{\text{in}} \frac{m_{i,z-1}}{m_{\text{cv}}} + \dot{R} \frac{m_{i,z-1}}{m_{\text{cv}}} + \dot{R} \frac{m_{i,z+1}}{m_{\text{cv}}}}^{\substack{\text{Mass flow rate of particles with size } x_i\\ \text{into the CV from the neighboring cells}}}$$

$$\underbrace{-\dot{m}_{\text{in}} \frac{m_{i,z}}{m_{\text{cv}}} - \dot{R} \frac{m_{i,z}}{m_{\text{cv}}} - \dot{R} \frac{m_{i,z}}{m_{\text{cv}}}}_{\substack{\text{Mass flow rate of particles with size } x_i\\ \text{out of the CV into the neighboring cells}}} \qquad \text{(A.2)}$$

where m_{cv} represents the mass hold-up in the CV. The left-hand side of Equation (A.2) refers to the accumulation rate of the mass in size class *i* in the CV. On the right-hand side of Equation (A.2), the first and second terms express the death rate and birth rate of the particles in size class *i* in the CV, respectively. The third group of terms expresses the mass flow rate of particles with size x_i into the CV from the neighboring cells, whereas the fourth group of terms expresses the mass flow rate of particles with size x_i out of the CV into the neighboring cells. By definition, the average residence time τ is the ratio of the total mass hold-up to the mass flow rate (i.e., $\tau = n m_{\text{cv}} / \dot{m}_{\text{in}}$) and the back-mixing ratio *R* is the ratio of the mass back-flow rate to the bulk mass flow rate (i.e., $R = \dot{R} / \dot{m}_{\text{in}}$). With the variables τ and *R*, Equation (A.2) can be rewritten as Equation (A.3).

$$\frac{dm_{i,z}}{dt} = -k_i F_i[\ ]m_{i,z} + \sum_{j=1}^{i-1} b_{i,j} k_j F_j[\ ]m_{j,z} + \frac{n}{\tau}\left(m_{i,z-1} + Rm_{i,z-1} + Rm_{i,z+1} - m_{i,z} - 2Rm_{i,z}\right) \quad \text{(A.3)}$$

At time t = 0 min, the mass hold-up in the mill was assumed to be zero (empty mill). The initial condition is $m_{i,z}(0) = 0$. Model equations for the first cell (z = 1) and the last cell (z = n) can be derived using the same approach as formulated for the intermediate cells. The final form of equations is expressed in Equations (2.2) and (2.4) of the main text.

It should be noted if one considers only one cell, removes the last term, sets $F_i[\ ]$ = 1, and replaces time t with contact time $t^* = y/u$ for any axial position y in the mill, while making use of $M_{i,z} = m_{i,z} \Big/ \sum_{i=1}^{N} m_{i,z}$, then Equation (A.3) turns into the classical PFTM model with the linear breakage kinetics:

$$\frac{dM_i}{dt^*} = -k_i M_i + \sum_{j=1}^{i-1} b_{i,j} k_j M_j \quad \text{(A.4)}$$

Solving Equation (A.4) gives the steady-state product PSD at $t^* = \tau = L/u$ for the feed PSD $M_{i,0}$.

APPENDIX B

SUPPLEMENTARY DATA FOR CHAPTER 3

The supplementary materials of Chapter 3 are shown in this section.

B.1 Scale-up of Specific Breakage Rate

Scale-up factors K_1, K_2, K_3, and K_4 depend on the diameter and operation parameters of the full-scale mill and the small-scale test mill (T), as expressed by Equations (B.1) and (B.2) (Austin et al., 1984).

$$K_1 = \left(\frac{D}{D_\mathrm{T}}\right)^{N_2},\ K_2 = \begin{cases} \left(\dfrac{D}{D_\mathrm{T}}\right)^{N_1} & \text{if } D \le 3.81\,\mathrm{m} \\ \left(\dfrac{3.81}{D_\mathrm{T}}\right)^{N_1}\left(\dfrac{D}{3.81}\right)^{N_1-N_3} & \text{if } D > 3.81\,\mathrm{m} \end{cases} \tag{B.1}$$

$$K_3 = \frac{1+6.6J_\mathrm{T}^{2.3}}{1+6.6J^{2.3}}\exp\left[-1.2\left(U-U_\mathrm{T}\right)\right],$$

$$K_4 = \left(\frac{\phi_\mathrm{C}-0.1}{\phi_{\mathrm{C,T}}-0.1}\right)\left\{\frac{1+\exp\left[15.7\left(\phi_{\mathrm{C,T}}-0.94\right)\right]}{1+\exp\left[15.7\left(\phi_\mathrm{C}-0.94\right)\right]}\right\} \tag{B.2}$$

A recent study (Bilgili, 2023) established that (i) the Kotake–Kanda kinetic model and the traditional Austin kinetic model provide similar PSD evolution upon scale-up, (ii) the modification of the Austin's scale-up exponents N_1 and N_2 is not warranted, and (iii) the Austin's scale-up methodology is applicable to the Kotake–Kanda model as well as the

Austin model. Hence, N_1 and N_2 were taken as 0.5 and 0.2, respectively, along with N_3 = 0.2. Here, subscript T is the test condition in the laboratory mill. D is the diameter of the ball mill. J is the ball filling ratio, which is defined as the fraction of the mill volume filled by balls. For any cell z, the powder filling U was calculated using

$$U_z = m_{\mathrm{H},z} \big/ \rho_{\mathrm{c}} \left(1-\varepsilon_{\mathrm{c}}\right) J_z \varepsilon_{\mathrm{b}} V_z \tag{B.3}$$

where the total mass hold-up of the cement clinker in cell z ($m_{\mathrm{H},z}$) can be determined by summation of mass in cell z over all N size classes, i.e., $m_{\mathrm{H},z} = \sum_{i=1}^{N} m_{i,z}$. V_z is the mill volume in cell z. ε_{c} and ε_{B} denote the void fraction of cement clinker and steel balls, respectively, which were taken as 0.4, similar to Deniz (2012). ϕ_{c} is the fraction of actual rotation speed compared to the critical speed N_{c}, which is defined as the theoretical rotation speed where the centrifugal force of the ball is equal to the gravitational force of the ball at the mill shell. N_{c} was determined using

$$N_{\mathrm{c}} = 42.3\left(D - d_{\mathrm{B}} \big/ 10^3\right)^{-1/2} \tag{B.4}$$

For a mixture of ball sizes, the ball size d_{B} (in mm) was replaced by the maximum ball size $d_{\mathrm{B,Max}}$ (Kasim et al., 1996).

B.2 Details of the Size-discretization and the Solution of the DAEs

In all simulations, the size class is represented by its upper edge progressing downward according to a geometric progression ratio. The number of size classes N was set to 320, and the geometric progression ratio was set to $2^{1/17}$, which yields grid-independent simulation results. The upper edge of the topmost size class x_1 was set to 80 mm according to the natural feed PSD taken from Genc (2016). While the evolution of PSD was recorded every minute over a total milling time of 120 min, PSDs at various milling times were sampled to assess attainment of steady-state operation. The operation was deemed to reach a steady state when the summation of absolute difference of cumulative product PSDs over all 320 size classes between two subsequent time points was less than or equal to 10^{-2}. Simulated product fineness at steady state was described by characteristic PSD values such as d_{10}, d_{50}, and d_{90}, span calculated from $(d_{90}-d_{10})/d_{50}$, and SSA. The mass fraction of particles in size class i of the product passing the discharge diaphragm connected to cell n ($M_{\text{out},i}$), the Sauter mean diameter d_{32}, and the SSA were calculated by

$$M_{\text{out},i} = \dot{m}_{\text{out},i,n} \Big/ \sum_{i=1}^{N} \dot{m}_{\text{out},i,n}\,, \quad d_{32} = 1 \Big/ \sum_{i=1}^{N} \frac{M_{\text{out},i}}{\bar{x}_i}\,, \text{ and } \text{SSA} = \left(6/\rho_{\text{c}}\right) \Big/ \left(d_{32}/10^{3}\right) \tag{B.5}$$

where $\bar{x}_i$ is the geometric average size of particles in size class i. The set of DAEs in Equations (3.1), (3.3), and (3.4) was solved simultaneously using the function “ode15s” in MATLAB version 9.9, which is a highly accurate, variable order–step-size ordinary differential equation (ODE) solver that can efficiently handle DAEs (Shampine et al.,

2003). The relative error tolerance was set to 10^{-4}, and the absolute error tolerance was set to 10^{-6}.

APPENDIX C

SUPPLEMENTARY DATA FOR CHAPTER 4

The supplementary materials of Chapter 4 are shown in this section.

C.1 Details of the Numerical Solutions of the DAE and the Optimization Problem

The topmost size class x_1, representing the coarsest particles, was set to 50 mm, according to the fresh feed size taken from Altun (2018). A geometric discretization of particle size was employed with a progression ratio of $2^{1/9.5}$. The number of size classes N was set to 160. The set of DAEs was numerically solved using the MATLAB function ode15s (Shampine et al., 2003) with the relative error tolerance and the absolute error tolerance taken from Capece et al. (2011a) as 10^{-4} and 10^{-6}, respectively.

Optimized values were obtained from the global optimizer-based process optimization written in MATLAB version 9.12. The optimizer, fmincon, within the global optimization toolbox (The MathWorks, 2022) via the function GlobalSearch, was used to minimize the objective function and find the global minimum. At each iteration of the optimizer, the objective function was evaluated by finding the solution of the PBM using the MATLAB function ode15s. GlobalSearch generates a set of trial points using the scatter search method (Glover, 1998). The optimizer's stopping criteria, i.e., tolerances for function values and parameters were all set to 10^{-9} (Capece et al., 2011a). The number of size classes, geometric progression, and tolerances of the solver for each iteration were kept the same as in the forward simulations reported above. All simulations and

optimizations were executed by a Dell Precision 7820 Tower Workstation with Intel(R) Xeon(R) Gold 6254 CPU @ 3.10 GHz and 3.09 GHz.

C.2 Referenced Full-scale and Laboratory-scale Cement Ball Mills and Scale-up

The mill dimensions and operation conditions of the full-scale cement ball mill were taken from Altun (2018). The ball mill consisted of two milling compartments. Ball mill diameter D was 4.0 m, and the length of ball mill L was 12.3 m, with the first and the second compartment lengths of 3.9 and 8.4 m, respectively. Ball filling fractions J were 0.267 and 0.301 for compartments 1 and 2, respectively. Ball sizes used in compartment 1 were 90, 80, 70, and 60 mm, with mass fractions of 0.25, 0.30, 0.25, and 0.20, respectively. In compartment 2, the ball sizes used were 50, 40, 30, 25, 20, and 17 with mass fractions of 0.08, 0.10, 0.20, 0.24, 0.23, and 0.15, respectively.

In the case of a laboratory ball mill for cement clinker milling, the mill dimensions and operation data were taken from Deniz (2003). The ball mill's diameter D_T was 0.2 m, and the length L_T was 0.2 m. Ball filling fraction J_T was 0.2, and void filling fraction U_T was 0.525. The ball mill rotated at a fractional speed $\phi_{C,T}$ of 0.75. Note that since the mill speed of the referenced full-scale mill ϕ_C was not mentioned in Altun (2018), it was assumed to be identical to a laboratory ball mill ($\phi_C = \phi_{C,T}$).

The scale-up factors K_1, K_2, K_3, and K_4 translate S_i obtained from the lab-scale ball mill into the industrial-scale ball mill of interest. These scale-up factors are related to the mill dimensions and the operating conditions. The scale-up of S_i from the lab-scale test (with subscript T) to the full-scale mill of interest was performed using the following K_1, K_2, K_3, and K_4 expressions (Austin et al., 1984):

$$K_1 = \left(\frac{D}{D_T}\right)^{N_2}, \; K_2 = \begin{cases} \left(\frac{D}{D_T}\right)^{N_1} & \text{if } D \le 3.81\,\text{m} \\ \left(\frac{3.81}{D_T}\right)^{N_1}\left(\frac{D}{3.81}\right)^{N_1-N_3} & \text{if } D > 3.81\,\text{m} \end{cases} \tag{C.1}$$

$$K_3 = \frac{1+6.6J_T^{2.3}}{1+6.6J^{2.3}}\exp\left[-1.2\left(U-U_T\right)\right],$$
$$K_4 = \left(\frac{\phi_C - 0.1}{\phi_{C,T} - 0.1}\right)\left\{\frac{1+\exp\left[15.7\left(\phi_{C,T}-0.94\right)\right]}{1+\exp\left[15.7\left(\phi_C-0.94\right)\right]}\right\} \tag{C.2}$$

According to Bilgili (2023), the S_i values obtained with the Kotake–Kanda model (Kotake et al., 2002) at the lab-scale can be scaled up using N_1 = 0.5, N_2 = 0.2, and N_3 = 0.2 in the above Austin's scale-up factors (Austin et al., 1984).

C.3 Variable Tromp Curve Model

The parameters used in the variable Tromp curve in Equation (4.8) were obtained from Altun and Benzer (2014). All air classification parameters were correlated with the operating conditions of the classifier and the continuous ball mill, i.e., air flow rate of air classifier Q, rotor tip speed v, dust load of the classifier feed DL_{CF}, and mass flow rate of classifier feed at 3–36 μm fraction F_{CF}. These correlations were obtained from various full-scale cement ball mills operating in the closed-circuit mode at the steady state. The parameters for the variable Tromp curve model are given by

$$\alpha_{\mathrm{a}} = 0.905\left(D_{\mathrm{c}}/DL_{\mathrm{CF}}\right)^{1.2679},\ \beta_{\mathrm{a}} = 0.4417DL_{\mathrm{CF}}{}^{1.4171} - 0.1293 \tag{C.3}$$

$$\delta_{\mathrm{a}} = 0.10467DL_{\mathrm{CF}}{}^{1.4171},\ x_{50\mathrm{c,a}} = \left[Q/\left(\nu F_{\mathrm{CF}}\right)\right]^{0.7775}/2.47 \tag{C.4}$$

By definition of the corrected cut size, the function "fsolve" was used to determine β_{a}^{*} (refer to Equation (4.8)) at each time step while solving the set of DAEs. We set $\beta_{\mathrm{a}} \geq 0$ based on published data (Altun and Benzer, 2014)); hence, a minimum value of DL_{CF} was set to 4.203×10^{-1} kg/m^3 to satisfy $\beta_{\mathrm{a}} \geq 0$. Setting the minimum value of DL_{CF} also resolved the problem of singularity of α_{a} at the initial simulation (refer to Equation (C.3)) because of $DL_{\mathrm{CF}} = 0$ kg/m^3 at $t = 0$ min.

C.4 Approximation of Blaine Surface Area

An empirical correlation of Blaine surface area f_{B} (in cm^2/g) with 80% passing size of the cement product x_{80} is expressed by (Shimoide, 2016):

$$f_{\mathrm{B}} = \begin{cases} -2105\ln\left(x_{80}\right) + 10614 & \text{if } x_{80} \leq 28\ \mu\mathrm{m} \\ -1489\ln\left(x_{80}\right) + 8573.4 & \text{if } 28 < x_{80} \leq 45.7\ \mu\mathrm{m} \\ -1156\ln\left(x_{80}\right) + 7298.2 & \text{if } 45.7 < x_{80} \leq 550\ \mu\mathrm{m} \\ 0 & \text{if } x_{80} > 550\ \mu\mathrm{m} \end{cases} \tag{C.5}$$

Equation (C.5) was assessed in comparison with the experimental data available in the literature. Based on published experimental data (Tsakalakis and Stamboltzis, 2008), $x_{80} = 41$ μm corresponds to $f_{\mathrm{B}} = 3000$ cm^2/g. Substituting $x_{80} = 41$ μm to Equation (C.5)

results in f_B = 3044 cm^2/g, showing good approximation with a deviation of roughly 1% compared to the experimentally obtained results.

APPENDIX D

SUPPLEMENTARY DATA FOR CHAPTER 5

The supplementary materials of Chapter 5 are shown in this section.

D.1 Details of the PBM Simulation and Optimization

The number of size classes N was set to 160, providing grid-independent results. The topmost size x_1 was 80 mm, as per the fresh feed PSD (Genc, 2016). Geometric progression ratio for the size classes was $2^{1/8.5}$. The PBM was coded in MATLAB version 9.12. A set of DAEs in Equations (5.1) and (5.2), along with the selected functions and parameters in Section 2.2, were solved using the function ode15s. The values of relative error and absolute error tolerances were 10^{-4} and 10^{-6}, respectively (Muanpaopong, 2022b).

In the case of process optimization, the function GlobalSearch, as part of the global optimization toolbox of MATLAB, was used to generate a set of trial points. The function fmincon was used as a nonlinear optimizer. The function ode15s was used as a DAE solver. Optimizer's stopping criteria as tolerances on the functions, constraints, and parameters were taken from Capece et al. (2011a) as 10^{-9}. Dell Precision 7820 Tower Workstation with Intel(R) Xeon(R) Gold 6254 CPU @ 3.10 GHz and 3.09 GHz was used to perform all PBM simulations and optimizations.

D.2 Calculation of the Specific Surface Area and the Blaine Surface Area

Sauter mean diameter d_{32} and specific surface area SSA (m^2/kg) of cement product at steady state are, respectively, expressed as

$$d_{32} = 1 \Big/ \sum_{i=1}^{N} \frac{M_{\mathrm{P},i}}{\bar{x}_i} \text{ and } \mathrm{SSA} = \frac{6}{\rho_{\mathrm{c}} \left(d_{32} / 10^3 \right)} \tag{D.1}$$

In Equation (D.1), $\bar{x}_i$ is the geometric average size of particles in size class i. $M_{\mathrm{P},i}$ is the mass fraction of cement product in size class i at the steady state. The density of cement clinker ρ_{c} was taken from Deniz (2003) as 3000 kg/m^3. The above SSA calculation assumes spherical particles.

Blaine surface area f_{B} (cm^2/g) of cement product can be empirically approximated from 80% passing size x_{80} (μm) of the cumulative PSD of cement product at steady state (Shimoide, 2016), as given by

$$f_{\mathrm{B}} = \begin{cases} -2105 \ln\left(x_{80}\right) + 10614 & \text{if } x_{80} \le 28\ \mu\mathrm{m} \\ -1489 \ln\left(x_{80}\right) + 8573.4 & \text{if } 28 < x_{80} \le 45.7\ \mu\mathrm{m} \\ -1156 \ln\left(x_{80}\right) + 7298.2 & \text{if } 45.7 < x_{80} \le 550\ \mu\mathrm{m} \\ 0 & \text{if } x_{80} > 550\ \mu\mathrm{m} \end{cases} \tag{D.2}$$

The predictive capability of the empirical Blaine surface area of Equation (D.2) was assessed using a wide range of x_{80}–f_{B} pairs reported in the cement handbook (Deolalkar, 2009). Table D.1 presents a comparison of the Blaine surface area values reported by Deolalkar (2009) and those calculated by Equation (D.2). Accurate prediction of the Blaine surface area using x_{80} value by Equation (D.2) was demonstrated, with the maximum absolute value of the relative error is less than 0.8%.

Table D.1 Assessment of Empirical Correlation Between 80% Passing Size of Cement Product and Blaine Surface Area of Cement Product

80% passing size, x_{80} (μm)[a]	Blaine surface area, f_B (cm^2/g)		Absolute value of the percent relative error
	Corresponding Blaine value[a]	Calculated Blaine value[b]	
62.4	2520	2520	7.994×10^{-3}
53.6	2700	2696	1.656×10^{-1}
45.7	2880	2882	7.971×10^{-2}
40.7	3060	3055	1.691×10^{-1}
37.6	3150	3173	7.235×10^{-1}
28.2	3600	3601	3.193×10^{-2}

[a] Taken from Deolalkar (2009).

[b] Calculated from Equation (D.2).

D.3 Details of the Laboratory Ball Mill, Full-scale Ball Mill, and Scale-up Factors

The specific breakage rate parameter S_i for cement clinker was obtained from a laboratory tumbling ball mill (Deniz, 2003) operating in the batch mode. The mill diameter D_T was 0.2 m, and the mill length L_T was 0.2 m. Experimental conditions were as follows: ball filling fraction $J_T = 0.2$, void filling fraction $U_T = 0.525$, and fraction of operating rotation to critical speed $\phi_{c,T} = 0.75$.

Mill size, along with the operating condition of a full-scale, continuous tumbling ball mill for cement milling, was taken from Genc (2016). This ball mill with a total length $L = 9.3$ m was operated in an open circuit without an air classifier. The length of each compartment was $L_1 = 2.94$ m, $L_2 = 1.70$ m, and $L_3 = 4.66$ m for compartments 1, 2, and 3, respectively. Mill diameter D was 3.5 m. Ball filling fraction J was 0.318, 0.318, and 0.290 for compartments 1, 2, and 3, respectively. The ball mill was rotated at 16.55 rpm. A

theoretical critical speed N_c was calculated from $N_c = 42.3(D–d_B/10^3)^{–1/2}$. When a mixture of different ball sizes was used, d_B was replaced by $d_{B,Max}$ (Kasim et al., 1996). Based on the prior work for a three-compartment mill (Muanpaopong et al., 2022b), two intermediate diaphragms were removed to simulate a single-compartment mill. The second intermediate diaphragm was removed to simulate the two-compartment mill.

Austin's scale-up factors K_1–K_4 (Austin et al., 1984) were used to translate S_i obtained from the lab test condition (with subscript T) to the full-scale operation (without subscript), and are expressed as

$$K_1 = \left(D/D_T\right)^{N_2}, \quad K_2 = \begin{cases} \left(D/D_T\right)^{N_1} & \text{if } D \le 3.81\,\text{m} \\ \left(3.81/D_T\right)^{N_1}\left(D/3.81\right)^{N_1-N_3} & \text{if } D > 3.81\,\text{m} \end{cases} \tag{D.3}$$

$$\begin{aligned} K_3 &= \frac{1+6.6J_T^{2.3}}{1+6.6J^{2.3}}\exp\left[-1.2\left(U-U_T\right)\right], \\ K_4 &= \left(\frac{\phi_c-0.1}{\phi_{c,T}-0.1}\right)\left\{\frac{1+\exp\left[15.7\left(\phi_{c,T}-0.94\right)\right]}{1+\exp\left[15.7\left(\phi_c-0.94\right)\right]}\right\} \end{aligned} \tag{D.4}$$

Based on the analysis presented in Bilgili (2023), it was established that the scale-up exponents $N_1 = 0.5$, $N_2 = 0.2$, and $N_3 = 0.2$ of Austin's scale-up factors are suitable for use with the KK kinetic model.

D.4 Calculations Regarding the Classifying Liner

An empirical model was developed in Muanpaopong et al. (2022b) to determine mean ball size ($d_{B,Mean}$) for axial position l in the second compartment of a ball mill with a classifying liner as follows:

$$d_{B,Mean} = d_{B,Min}/A_3 + \left(d_{B,Max}/A_1 - d_{B,Min}/A_3\right)\exp\left(-A_2 l\right) \tag{D.5}$$

Maximum and minimum ball sizes of the ball mixture used in the classifying liner compartment are denoted as $d_{B,Max}$ and $d_{B,Min}$, respectively. Based on Run 21, $d_{B,Max}$ = 30 mm and $d_{B,Min}$ = 15 mm. The parameters used to characterize ball classification patterns were taken from Muanpaopong et al. (2022b) as A_1 = 1.10, A_2 = 0.215 m^{-1}, and A_3 = 0.899. These values of A_1–A_3 provide a similar ball pattern as experimentally observed in Altun (2018).

The mean ball size for axial position l ($d_{B,Mean,l}$) calculated from Equation (D.5) was used to determine the mass fraction of balls in the binary ball mixture using the following equation:

$$d_{B,Max} M_{B,Max,l} + d_{B,Min} M_{B,Min,l} = d_{B,Mean,l} \tag{D.6}$$

Using the correlation $M_{B,Min,l} = 1 - M_{B,Max,l}$ and rearranging to determine the mass fraction of 30 mm balls $M_{B,Max,l}$, the following equation was obtained:

$$M_{\mathrm{B,Max},l} = \left(d_{\mathrm{B,Mean},l}/15\right) - 1 \tag{D.7}$$

The mass fraction of 15 mm balls at axial position l ($M_{\mathrm{B,Min},l}$) can be calculated via $M_{\mathrm{B,Min},l} = 1 - M_{\mathrm{B,Max},l}$. Table D.2 lists the mass fraction of each ball size at each axial position, taken from Muanpaopong et al. (2022b). Table D.2 clearly shows the gradient of 30 mm balls along the axial direction in the second compartment: highest near the entry of second compartment to minimum near the outlet, whereas 15 mm balls exhibit vice versa.

Table D.2 Mass Fraction of 30 mm Balls ($M_{\mathrm{B,Max}}$) and Mass Fraction of 15 mm Balls ($M_{\mathrm{B,Min}}$) for Each Axial Position l of the Second Compartment with a Classifying Liner

Axial position, l (m)	Ball mass fraction	
	$M_{\mathrm{B,Max}}$ (–)	$M_{\mathrm{B,Min}}$ (–)
0.909	0.697	0.303
1.82	0.594	0.406
2.73	0.508	0.492
3.63	0.438	0.562
4.54	0.380	0.620
5.45	0.333	0.667
6.36	0.294	0.706

Source: Muanpaopong et al., (2022b)

APPENDIX E

SUPPLEMENTARY DATA FOR CHAPTER 6

The supplementary materials of Chapter 6 are shown in this section.

E.1 Details of the Global Optimizer-based Back-calculation Method

A newly developed code was written in MATLAB version 9.12. Nonlinear constrained optimizer "fmincon" was coupled with ODE solver "ode15s" within the global optimization toolbox (The MathWorks, 2022), which minimizes *SSR* as the objective function. The MATLAB function "GlobalSearch" was used to generate the next set of initial guesses for the next trial point using the scatter method (Glover, 1998). The stopping criteria of the optimizer were taken from Capece et al. (2011a), where termination tolerances on constraint violation, function value, and parameter were all set to 10^{-9}. For the ODE solver, relative and absolute tolerances of 10^{-4} and 10^{-6}, respectively, were also taken from Capece et al. (2011a). The optimization was run by a Dell Precision 7820 Tower with Intel(R) Xeon(R) Gold 6254 CPU @ 3.10 GHz and 3.09 GHz.

E.2 Details of the Use of the Back-calculation Method with the Synthetic Milling Data

The number of size classes N and geometric progression ratio were taken from Bilgili (2023) as 320 and $2^{1/13}$, respectively. The synthetic data were regarded as experimental data during the back-calculation; hence, the total number of experimental size classes K (refer to Equation (6.7)) was 320 (i.e., $K = N$). The topmost size x_1 was 30 mm, which was taken from Bilgili (2023). The particle size was represented by its upper edge. Synthetic

data were generated for five milling times (i.e., t = 0.5, 1, 2, 4, and 8 min) with d_B = 38 mm. A Gaussian feed with a mean size of 20 mm and a standard deviation of 2 mm was used as the initial feed at t = 0, as explained in Subsection 6.3.2.1. In each iteration of the global optimizer, the PBM solution, which is the mass fraction, was converted to the cumulative PSD (see Equation (6.9)). The simulated cumulative PSD obtained from the ODE solver was subsequently compared with the synthetic (experimental) cumulative PSD to determine *SSR*.

E.3 Details of the Use of the Back-calculation Method with the Experimental Cement Clinker Ball Milling Data

The number of size classes N and geometric progression were set to 160 and $2^{1/10}$, respectively. The topmost size x_1 was 25 mm. Here, a lower number of size classes, compared to the synthetic data fit, was chosen to reduce execution time because 480 ODEs must be simultaneously solved for three ball sizes (d_B = 20, 30, and 40 mm). Additionally, a number of trial points N_T up to 10^4 was chosen, resulting in a long execution time.

Experimental initial feed data, in cumulative PSD form with 39 sizes (K = 39), were first interpolated into simulation size classes (N = 160) using the function “pchip” in MATLAB. Subsequently, cumulative PSD with 160 size classes was converted to mass fraction, in which the mass fraction with 160 size classes was used as the initial condition at t = 0 for the ODE solver. Once the PBM solution, which is the mass fraction in each simulation size class (N = 160), was obtained, the cumulative PSD could then be calculated (refer to Equation (6.9)). Using the function “pchip,” the cumulative PSD under the simulation size class was then again interpolated into the experimental size classes (K =

39) to determine *SSR*.

E.4 Details of the DEM Simulation Setup

Table E.1 lists the parameters used in the DEM simulation. For the material properties, the shear modulus was 7.8×10^{10} Pa for steel balls (Hou, 2014) and 1.3×10^{11} Pa for alumina balls (Auerkari, 1996), while the Poisson's ratio was 0.28 for steel balls (Hou, 2014) and 0.25 for alumina balls (Auerkari, 1996). A simulation time step corresponding to 20% of the Rayleigh time step, which depends on the ball material type and ball size, was chosen (similar to Capece et al. (2014)).

Table E.1 Coefficients Used in the DEM Simulations

Parameter	Contact type		
	Steel–Steel[a]	Steel–Ceramic[b]	Ceramic–Ceramic[b]
Coefficient of restitution	0.5	0.5	0.5
Coefficient of static friction	0.5	0.2	0.5
Coefficient of rolling friction	0.01	0.01	0.01

[a] taken from Bian et al. (2017); [b] taken from Hou (2014).

REFERENCES

A.-Z.M. Abouzeid, D.W. Fuerstenau, K.V.S. Sastry, Transport behavior of particulate solids in rotary drums: scale-up of residence time distribution using the axial dispersion model, Powder Technology, 27 (1980) 241−250.

A.-Z.M.A. Abouzeid, T.S. Mika, K.V. Sastry, D.W. Fuerstenau, The influence of operating variables on the residence time distribution for material transport in a continuous rotary drun, Powder Technology, 10 (1974) 273–288.

P.A. Alsop, The Cement Plant Operations Handbook for Dry-Process Plants, 5th ed., 2007, Dorking, United Kingdom: Tradeship Publications Ltd, 2007.

O. Altun, Simulation aided flow sheet optimization of a cement grinding circuit by considering the quality measurements, Powder Technology, 301 (2016) 1242−1251.

O. Altun, Energy and cement quality optimization of a cement grinding circuit, Advanced Powder Technology, 29 (2018) 1713−1723.

D. Altun, N.A. Aydogan, O. Altun, A.H. Benzer, Performance evaluation of vertical roller mill in cement ginding: case study ESCH Cement Plant, European Symposium on Comminution Classification, Izmir, Turkey, 11–14 September 2017.

O. Altun, H. Benzer, Selection and mathematical modelling of high efficiency air classifiers, Powder Technology, 264 (2014) 1–8.

D. Altun, A.H. Benzer, O. Altun, Modelling of component behaviour around a cement grinding circuit, ZKG International, 70 (2017) 58−67.

O. Altun, H. Benzer, H. Dundar, N.A. Aydogan, Comparison of open and closed circuit HPGR application on dry grinding circuit performance, Minerals Engineering, 24 (2011) 267−275.

O. Altun, H. Benzer, E. Karahan, S. Zencirci, A. Toprak, The impacts of dry stirred milling application on quality and production rate of the cement grinding circuits, Minerals Engineering, 155 (2020) 106478.

O. Altun, A. Toprak, H. Benzer, O. Darilmaz, Multi component modelling of an air classifier, Minerals Engineering, 93 (2016) 50−56.

M. AmanNejad, K. Barani, Effects of ball size distribution and mill speed and their interactions on ball milling using DEM, Mineral Processing and Extractive Metallurgy Review, 42 (2021) 374–379.

A. Aminalroaya, P. Pourghahramani, Investigation of particles breakage and weakening behaviors in multi-component feed grinding by high pressure grinding rolls (HPGR), Mineral Processing and Extractive Metallurgy Review, 43 (2022) 217–232.

A. Aras, A. Ozkan, S. Aydogan, Correlations of Bond and breakage parameters of some ores with the corresponding point load index, Particle and Particle Systems Characterization, 29 (2012) 1–7.

ASTM C-204, Standard Test Methods for Fineness of Hydraulic Cement by Air-Permeability Apparatus, Annual Book of ASTM Standards, West Conshohocken, PA: ASTM International, 2019.

P. Auerkari, Mechanical and physical properties of engineering alumina ceramics, Espoo, Finland: VTT Technical Research Centre of Finland, 1996.

L.G. Austin, A review introduction to the mathematical description of grinding as a rate process, Powder Technology, 5 (1971/1972) 1–17.

L.G. Austin, P. Bagga, An analysis of fine dry grinding in ball mills, Powder Technology, 28 (1981) 83–90.

L.G. Austin, P. Bagga, M. Celik, Breakage properties of some materials in a laboratory ball mill, Powder Technology, 28 (1981a) 235–243.

L.G. Austin, D. Bell, R.S.C. Rogers, Incorporation of the slowing down effect into a mill model, Particulate Science and Technology, 2 (1984) 135–145.

L.G. Austin, V.K. Bhatia, Experimental methods for grinding studies in laboratory mills, Powder Technology, 5 (1971/1972) 261–266.

L.G. Austin, R.R. Klimpel, An improved method for analyzing classifier data, Powder Technology, 29 (1981) 277–281.

L.G. Austin, R.R. Klimpel, P.T. Luckie, R.S.C. Rogers, Simulation of grinding circuits for design, in: A.L. Mular, G.V. Jergensen (Eds.), Design and Installation of Comminution Circuits, New York, NY: American Institute of Mining, Metallurgical, and Petroleum Engineers (AIME), 1982, pp. 301–324.

L.G. Austin, R.R. Klimpel, P.T. Luckie, Process Engineering of Size Reduction: Ball Milling, Littleton, CO: Society of Mining Engineers of the American Institute of Mining, Metallurgical, and Petroleum Engineers (AIME), 1984.

L.G. Austin, P.T. Luckie, Methods for determination of breakage distribution parameters, Powder Technology, 5 (1971/1972) 215–222.

L.G. Austin, P.T. Luckie, The estimation of non-normalized breakage distribution parameters from batch grinding tests, Powder Technology, 5 (1972) 267–271.

L.G. Austin, P.T. Luckie, A simulation model for an air-swept ball mill grinding coal, Powder Technology, 38 (1984) 255–266.

L.G. Austin, P.T. Luckie, B.G. Ateya, Residence time distributions in mills, Cement and Concrete Research, 1 (1971) 241–256.

L.G. Austin, P.T. Luckie, D. Wightman, Steady-state simulation of a cement-milling circuit, International Journal of Mineral Processing, 2 (1975) 127–150.

L.G. Austin, Z. Rogovin, R.S.C. Rogers, T. Trimarchi, The axial mixing model applied to ball mills, Powder Technology, 36 (1983) 119–126.

L.G. Austin, J. Shah, J. Wang, E. Gallagher, P.T. Luckie, An analysis of ball-and-race milling. Part I. The Hardgrove mill, Powder Technology, 29 (1981b) 263–275.

L.G. Austin, K. Shoji, P.T. Luckie, The effect of ball size on mill performance, Powder Technology, 14 (1976) 71–79.

L.G. Austin, M. Yekeler, T.F. Dumm, R. Hogg, The kinetics and shape factors of ultrafine dry grinding in a laboratory tumbling ball mill, Particle and Particle Systems Characterization, 7 (1990) 242–247.

N.A. Aydogan, A simple sampling method for VRMs, ZKG International, (2015) 50–55.

N.A. Aydogan, H. Benzer, Comparison of the overall circuit performance in the cement industry: high compression milling vs. ball milling technology, Minerals Engineering, 24 (2011) 211–215.

N.A. Aydogan, L. Ergun, H. Benzer, High pressure grinding rolls (HPGR) applications in the cement industry, Minerals Engineering, 19 (2006) 130–139.

D. Barrasso, S. Oka, A. Muliadi, J.D. Litster, C. Wassgren, R. Ramachandran, Population balance model validation and prediction of CQAs for continuous milling processes: toward QbD in pharmaceutical drug product manufacturing, Journal of Pharmaceutical Innovation, 8 (2013) 147–162.

B. Beke, Grinding Body Charge and Wear, in: The Process of Fine Grinding, Developments in Mineral Science and Engineering Volume 1, Dordrecht, Netherlands: Springer, 1981.

D.P. Bentz, G. Sant, J. Weiss, Early-age properties of cement-based materials. I: Influence of cement fineness, Journal of Materials in Civil Engineering, 20 (2008) 502–508.

H. Benzer, Modeling and simulation of a fully air swept ball mill in a raw material grinding circuit, Powder Technology, 150 (2005) 145–154.

H. Benzer, L. Ergun, A.J. Lynch, M. Oner, A. Gunlu, I.B. Celik, N. Aydogan, Modelling cement grinding circuits, Minerals Engineering, 14 (2001a) 1469–1482.

H. Benzer, L. Ergun, M. Oner, A.J. Lynch, Simulation of open circuit clinker grinding, Minerals Engineering, 14 (2001b) 701–710.

H. Berthiaux, D. Heitzmanns, J.A. Dodds, Validation of a model of a stirred bead mill by comparing results obtained in batch and continuous mode grinding, International Journal of Mineral Processing, 44–45 (1996) 653–661.

H. Berthiaux, C. Varinot, Approximate calculation of breakage parameters from batch grinding tests, Chemical Engineering Science, 51 (1996) 4509–4516.

X. Bian, G. Wang, H. Wang, S. Wang, W. Lv, Effect of lifters and mill speed on particle behaviour, torque, and power consumption of a tumbling ball mill: experimental study and DEM simulation, Minerals Engineering, 105 (2017) 22–35.

E. Bilgili, On the similarity of Austin model and Kotake–Kanda model and implications for tumbling ball mill scale-up, KONA Powder and Particle Journal, 40 (2023) 250–261.

E. Bilgili, M. Capece, A. Afolabi, Modeling of milling processes via DEM, PBM, and microhydrodynamics, in: P. Pandey, R. Bharadwaj (Eds.), Predictive Modeling of Pharmaceutical Unit Operations, Cambridge, MA: Woodhead Publishing, 2017, pp. 159–203.

E. Bilgili, B. Scarlett, Population balance modeling of non-linear effects in milling processes, Powder Technology, 153 (2005a) 59–71.

E. Bilgili, B. Scarlett, Numerical simulation of open-circuit continuous mills using a non-linear population balance framework: incorporation of non-first-order effects, Chemical Engineering and Technology, 28 (2005b) 153–159.

E. Bilgili, J. Yepes, B. Scarlett, Formulation of a non-linear framework for population balance modeling of batch grinding: beyond first-order kinetics, Chemical Engineering Science, 61 (2006) 33–44.

F.C. Bond, Grinding ball size selection, Mining Engineering, 10 (1958) 592−595.

M. Boulvin, A.V. Wouwer, R. Lepore, C. Renotte, M. Remy, Modeling and control of cement grinding processes, IEEE Transactions on Control Systems Technology, 11 (2003) 715−725.

S. Brochot, R.L. Wiegel, S. Ersayin, S. Touze, Modeling and simulation of comminution circuits with USIM PAC, in: S.K. Kawatra (Ed.), Advances in Comminution, Littleton, CO: Society for Mining, Metallurgy, and Exploration, Inc. (SME), 2006, pp. 495–511.

J.M. Brugan, High efficiency separators − problems and solutions, ZKG International, 41 (1988) 350−355.

M.M. Bwalya, M.H. Moys, G.J. Finnie, F.K. Mulenga, Exploring ball size distribution in coal grinding mills, Powder Technology, 257 (2014) 68−73.

M. Camalan, A pseudo-matrix model coupled to a particle selection algorithm for simulating batch grinding, Minerals Engineering, 170 (2021a) 106993.

M. Camalan, A computational algorithm to understand the evolution of size distribution with successive breakage events at grinding, Environmental Sciences Proceedings, 6 (2021b) 7.

M. Camalan, C. Hosten, Ball-mill grinding kinetics of cement clinker comminuted in the high-pressure roll mill, Mineral Processing and Extractive Metallurgy Review, 36 (2015) 310−316.

M. Capece, Population balance modeling applied to the milling of pharmaceutical extrudate for use in scale-up, Advanced Powder Technology, 29 (2018) 3022–3032.

M. Capece, E. Bilgili, R. Dave, Identification of the breakage rate and distribution parameters in a non-linear population balance model for batch milling, Powder Technology, 208 (2011a) 195–204.

M. Capece, E. Bilgili, R.N. Dave, Emergence of falsified kinetics as a consequence of multi-particle interactions in dense-phase comminution processes, Chemical Engineering Science, 66 (2011b) 5672–5683.

M. Capece, E. Bilgili, R.N. Dave, Formulation of a physically motivated specific breakage rate parameter for ball milling via the discrete element method, AIChE Journal, 60 (2014) 2404–2415.

M. Capece, R.N. Davé, E. Bilgili, A pseudo-coupled DEM–non-linear PBM approach for simulating the evolution of particle size during dry milling, Powder Technology, 323 (2018) 374–384.

M. Capece, R.N. Davé, E. Bilgili, On the origin of non-linear breakage kinetics in dry milling, Powder Technology, 272 (2015) 189–203.

R.M. de Carvalho, L.M. Tavares, Predicting the effect of operating and design variables on breakage rates using the mechanistic ball mill model, Minerals Engineering, 43–44 (2013) 91–101.

S. Cayirli, Influences of operating parameters on dry ball mill performance, Physicochemical Problems of Mineral Processing, 54 (2018) 751–762.

I.B. Celik, The effects of particle size distribution and surface area upon cement strength development, Powder Technology, 188 (2009) 272–276.

I.B. Celik, M. Oner, The influence of grinding mechanism on the liberation characteristics of clinker minerals, Cement and Concrete Research, 36 (2006) 422–427.

T.W. Chenje, Development and validation of a model for steel grinding media wear in tumbling mills, PhD Thesis. McGill University, Quebec, Canada, 2007.

N. Chimwani, M.M. Bwalya, Using DEM to investigate how shell liner can induce ball segregation in a ball mill, Minerals Engineering, 151 (2020) 106311.

N. Chimwani, F.K. Mulenga, D. Hildebrandt, D. Glasser, M.M. Bwalya, Scale-up of batch grinding data for simulation of industrial milling of platinum group minerals ore, Minerals Engineering, 63 (2014) 100–109.

H. Cho, L.G. Austin, The equivalence between different residence time distribution models in ball milling, Powder Technology, 124 (2002) 112–118.

P.W. Cleary, Ball motion, axial segregation and power consumption in a full scale two chamber cement mill, Minerals Engineering, 22 (2009) 809–820.

P.A. Cundall, O.D.L. Strack, A discrete numerical model for granular assemblies, Geotechnique, 29 (1979) 47–65.

P.V. Danckwerts, Continuous flow systems: distribution of residence times, Chemical Engineering Science, 2 (1953) 1–13.

P.K. Das, Use of cumulative size distribution to back-calculate the breakage parameters in batch grinding, Computer and Chemical Engineering, 25 (2001) 1235–1239.

A. Datta, R.K. Rajamani, A direct approach of modeling batch grinding in ball mills using population balance principles and impact energy distribution, International Journal of Mineral Processing, 64 (2002) 181–200.

R. Dave, N. Muanpaopong, E. Bilgili, Modeling the impact of ball size–material on the fineness of cement clinker particles prepared by dry ball milling, Keynote Speech, Proceedings 9th World Congress on Particle Technology (WCPT9), Madrid, Spain, 18–22 September 2022.

DEM Solutions Ltd., EDEM 2.6 Theory Reference Guide, Edinburgh, UK, 2014.

V. Deniz, A study on the specific rate of breakage of cement materials in a laboratory ball mill, Cement and Concrete Research, 33 (2003) 439–445.

V. Deniz, The effect of mill speed on kinetic breakage parameters of clinker and limestone, Cement and Concrete Research, 34 (2004) 1365–1371.

V. Deniz, Influence of interstitial filling on breakage kinetics of gypsum in ball mill, Advanced Powder Technology, 22 (2011) 512–517.

V. Deniz, A study on the effect of ball diameter on breakage properties of clinker and limestone, Indian Journal of Chemical Technology, 19 (2012) 180–184.

V. Deniz, T. Onur, Investigation of the breakage kinetics of pumice samples as dependent on powder filling in a ball mill, International Journal of Mineral Processing, 67 (2002) 71–78.

S.P. Deolalkar, Handbook for Designing Cement Plants, 1st ed., Hyderabad, Telangana: BS Publications, 2009.

A. Devaswithin, B. Pitchumani, S.R. de Silva, Modified back-calculation method to predict particle size distributions for batch grinding in a ball mill, Industrial and Engineering Chemistry Research, 27 (1988) 723–726.

R.B. Diemer, Application of the linear mass-sectional breakage population balance to various milling process configurations, American Association of Pharmaceutical Scientists PharmSciTech, 22:86 (2021).

R.B. Diemer, J.H. Olson, A moment methodology for coagulation and breakage problems: part 3—generalized daughter distribution functions, Chemical Engineering Science, 57 (2002) 4187–4198.

W.H. Duda, Cement Data Book, Volume One: International Process Engineering in the Cement Industry, 3rd ed., Wiesbaden und Berlin, Hesse: Bauverlag GmbH, 1985.

H. Dundar, H. Benzer, N.A. Aydogan, O. Altun, N.A. Toprak, O. Ozcan, D. Eksi, A. Sargin, Simulation assisted capacity improvement of cement grinding circuit: case study cement plant, Minerals Engineering, 24 (2011) 205–210.

A.S. Erdem, S.L. Ergun, The effect of ball size on breakage rate parameter in a pilot scale ball mill, Minerals Engineering, 22 (2009) 660–664.

H. Ergin, The simulation of an air-swept cement grinding mill, PhD Thesis, University of Leeds, Leeds, England, 1994.

H. Ergin, S.G. Ercelebi, Optimisation of cement grinding circuit through simulation, 11th European Simulation Symposium, Erlangen, Germany, 1999, pp. 379–383.

H.B. Fadhel, C. Frances, A. Mamourian, Investigations on ultra-fine grinding of titanium dioxide in a stirred media mill, Powder Technology, 105 (1999) 362–373.

X. Fang, C. Wu, N. Liao, C. Yuan, B. Xie, J. Tong, The first attempt of applying ceramic balls in industrial tumbling mill: a case study, Minerals Engineering, 180 (2022) 107504.

A. Farzanegan, E.G. Ardi, A. Valian, V. Hasanzadeh, Simulation of clinker grinding circuits of cement plant based on process models calibrated using GA search method, Journal of Central South University, 21 (2014) 799–810.

R. Fatahi, K. Barani, Modeling and simulation of vertical roller mill using population balance model, Physicochemical Problems of Mineral Processing, 56 (2020) 24–33.

R. Fatahi, A. Pournazari, M.P. Shah, A cement vertical roller mill modeling based on the number of breakages, Advanced Powder Technology, 33 (2022) 103750.

C. Fernandez, Z. Hui, Benefits of ceramic grinding, International Cement Review (2017) 56–57.

J.A. Finch, Modelling a fish-hook in hydrocyclone selectivity curves, Powder Technology, 36 (1983) 127–129

FLSmidth, Comminution Manual, Denmark, 2012.

FLSmidth, Grinding Technology Course, Ball Mill Grinding Media, Copenhagen, Denmark, 23–27 June 2014.

FLSmidth, SEPAX separator, 2021 [Brochure].

H.S. Fogler, Elements of Chemical Reaction Engineering, 4th ed., Englewood Cliffs, NJ: Prentice Hall, 2006.

D.S. Fortsch, Ball charge loading – Impact on specific power consumption and capacity. IEEE Cement Industry Technical Conference Record, 62–72, 2006.

C. Frances, On modelling of submicronic wet milling processes in bead mills, Powder Technology, 143–144 (2004) 253–263.

D.W. Fuerstenau, A.-Z.M. Abouzeid, Effect of fine particles on the kinetics and energetics of grinding coarse particles, International Journal of Mineral Processing, 31 (1991) 151–162.

D.W. Fuerstenau, A.-Z.M. Abouzeid, The energy efficiency of ball milling in comminution, International Journal of Mineral Processing, 67 (2002) 161–185.

D.W. Fuerstenau, A.-Z.M. Abouzeid, S.H.R. Swaroop, Material transport in ball mills: effect of discharge-end design, Powder Technology, 46 (1986) 273–279.

D.W. Fuerstenau, A. De, P.C. Kapur, Linear and nonlinear particle breakage processes in comminution systems, International Journal of Mineral Processing, 74S (2004) S317–S327.

D.W. Fuerstenau, J.J. Lutch, A. De, The effect of ball size on the energy efficiency of hybrid high-pressure roll mill/ball mill grinding, Powder Technology, 105 (1999) 199–204.

D.W. Fuerstenau, A. Shukla, P.C. Kapur, Energy consumption and product size distributions in choke-fed, high-compression roll mills, International Journal of Mineral Processing, 32 (1991) 59–79.

M. Furuya, Y. Nakajima, T. Tanaka, Theoretical analysis of closed-circuit grinding system based on comminution kinetics, Industrial & Engineering Chemistry Process Design and Development, 10 (1971) 449–456.

L. Gao, Y. Yu, J. Liu, Study on the cut size of a turbo air classifier, Powder Technology, 237 (2013) 520–528.

R.P. Gardner, R.S. Rogers, K. Verghese, Short-lived radioactive tracer methods for the dynamic analysis and control of continuous comminution processes by the mechanistic approach, The International Journal of Applied Radiation and Isotopes, 28 (1977) 861–871.

R.P. Gardner, K. Sukanjnajtee, A combined tracer and back-calculation method for determining particulate breakage functions in ball milling. Part III. Simulation of an open-circuit continuous milling system, Powder Technology, 7 (1973) 169–179.

T. Gelpe, F. Flament, D. Hodouin, Computer design of grinding circuit flowsheets – application to cement and ore processing, Mining Engineering, 37 (1985) 241–248.

O. Genc, An investigation on the effects of design and operational parameters on grinding performance of multi-compartment ball mills used in the cement industry, PhD Thesis, Hacettepe University, Ankara, Turkey, 2008.

O. Genc, Analysis of grinding media effect on specific breakage rate function of particles in a full-scale open circuit three-compartment cement ball mill, Minerals Engineering, 81 (2015a) 10–17.

O. Genc, Optimization of a fully air-swept dry grinding cement raw meal ball mill closed circuit capacity with the aid of simulation, Minerals Engineering, 74 (2015b) 41–50.

O. Genc, Effect of ball load and size distribution on grinding and classification performance, ZKG International, 68 (2015c) 40–51.

O. Genc, Optimization of an industrial scale open circuit three-compartment cement grinding ball mill with the aid of simulation, International Journal of Mineral Processing, 154 (2016) 1–9.

O. Genc, A.H. Benzer, Effect of high pressure grinding rolls (HPGR) pre-grinding and ball mill intermediate diaphragm grate design on grinding capacity of an industrial scale two-compartment cement ball mill classification circuit, Minerals Engineering, 92 (2016) 47–56.

O. Genc, S.L. Ergun, A.H. Benzer, The dependence of specific discharge and breakage rate functions on feed size distributions, operational and design parameters of industrial scale multi-compartment cement ball mills, Powder Technology, 239 (2013) 137–146.

V. Ghalandari, A. Irananesh, Energy and exergy analyses for a cement ball mill of a new generation cement plant and optimizing grinding process: a case study, Advanced Powder Technology, 31 (2020) 1796–1810.

F. Glover, A template for scatter search and path relinking, in: J.K. Hao, E. Lutton, E. Ronald, M. Schoenauer, D. Snyers (Eds.), Artificial Evolution, Lecture Notes in Computer Science vol. 1363., Heidelberg, Baden-Wurttemberg: Springer, 1998, pp. 13–54.

G. Guner, M. Kannan, M. Berrios, E. Bilgili, Use of bead mixtures as a novel process optimization approach to nanomilling of drug suspensions, Pharmaceutical Research, 38 (2021) 1279–1296.

V.K. Gupta, D. Hodouin, M.A. Berube, M.D. Everell, The estimation of rate and breakage distribution parameters from batch grinding data for a complex pyritic ore using a back-calculation method, Powder Technology, 28 (1981) 97–106.

V.K. Gupta, A. Tripathi, J.P. Patel, An experimental and computational methodology for estimation of breakage rate and distribution parameters for batch ball milling operation, Proceedings 26th IMPC, New Delhi, India, 2012, pp. 1800–1810.

O. Gutsche, D.W. Fuerstenau, Fracture kinetics of particle bed comminution – ramifications for fines production and mill optimization, Powder Technology, 105 (1999) 113–118.

S. Haner, The effects of ball size on the determination of breakage parameters of nepheline syenite, Journal of Mining Science, 56 (2020) 848–856.

P. Hassall, E. Nonnet, V. Keikkala, T. Komminaho, L. Kotila, Ceramic bead behavior in ultra fine grinding mills, Minerals Engineering, 98 (2016) 232–239.

S.L.A. Hennart, W.J. Wildeboer, P. van Hee, G.M.H. Meesters, Identification of the grinding mechanisms and their origin in a stirred ball mill using population balances, Chemical Engineering Science, 64 (2009) 4123–4130.

J.A. Herbst, D.W. Fuerstenau, Scale-up procedure for continuous grinding mill design using population balance models, International Journal of Mineral Processing, 7 (1980) 1–31.

H. Hertz, On the contact of elastic solids, Journal fur die Reine und Angewandte Mathematik, 92 (1882) 156–171.

W.E. Horst, Mathematical description of a comminution process, PhD Thesis, The University of Arizona, Tucson, Arizona, United States, 1967.

Y. Hou, DEM simulation and analysis of operating parameters on grinding performance of a vertical stirred mill, MS Thesis, The University of British Columbia, Vancouver, British Columbia, Canada, 2014.

M.J. Hounslow, The population balance as a tool for understanding particle rate processes, KONA, 16 (1998) 179–193.

J.K. Huusom, A.D. Jensen, S.B. Jorgensen, M. Michelsen, J. Knudsen, B. Recke, J.B. Jorgensen, Modelling of cement grinding circuits for predictive control, IFAC Proceedings Volumes, 38 (2005) 350–355.

International Energy Agency (IEA) and World Business Council for Sustainable Development (WBCSD), Cement Technology Roadmap 2009 Carbon emissions reductions up to 2050, Atar Roto Presse SA, Switzerland, 2009.

M. Ito, Effect of kinetic comminution parameters and classification efficiency on output during closed-circuit cement grinding, part 1, ZKG International, 53 (2000) 186–194.

A. Jankovic, W. Valery, E. Davis, Cement grinding optimisation, Minerals Engineering, 17 (2004) 1075–1081.

S. Jiang, Y. Ye, Y. Tan, S. Liu, J. Liu, H. Zhang, D. Yang, Discrete element simulation of particle motion in ball mills based on similarity, Powder Technology, 335 (2018) 91–102.

A. Jillavenkatesa, S.J. Dapkunas, L.-S.H. Lum, NIST Recommended Practice Guide: Particle Size Characterization, Special Publication 960-1, Washington, DC: U.S. Government Printing Office, 2001.

Y. Kanda, K. Simodaira, N. Kotake, Y. Abe, Experimental study on the grinding rate constant of a ball mill: effects of feed size and ball diameter, KONA, 17 (1999) 220–225.

N.H.A. Kasim, D.T. Millett, J.F. McCabe, The ball mill as a means of investigating the mechanical failure of dental materials, Journal of Dentistry, 24 (1996) 117–124.

F.M. Katubilwa, M.H. Moys, Effect of ball size distribution on milling rate, Minerals Engineering, 22 (2009) 1283–1288.

F.M. Katubilwa, M.H. Moys, D. Glasser, D. Hildebrandt, An attainable region analysis of the effect of ball size on milling, Powder Technology, 210 (2011) 36–46.

K.K. Kiangi, M.H. Moys, Particle filling and size effects on the ball load behaviour and power in a dry pilot mill: experimental study, Powder Technology, 187 (2008) 79–87.

S. Kim, E. Bilgili, R.N. Davé, Impact of altered hydrophobicity and reduced agglomeration on dissolution of micronized poorly water-soluble drug powders after dry coating, International Journal of Pharmaceutics, 606 (2021) 120853.

M.B. Kime, Using the discrete-element method to investigate ball milling power draw, load behaviour, and impact energy profile, Canadian Institute of Mining, Metallurgy and Petroleum (CIM) Journal, 8 (2017) 59–66.

R.P. King, Modeling and Simulation of Mineral Processing Systems, Oxford, United Kingdom: Butterworth-Heinemann, 2001.

P.B. Kis, C. Mihalyko, B.G. Lakatos, Mathematical models for simulation of continuous grinding process with recirculation, Acta Cybernetica 15 (2002) 529–545.

P.B. Kis, C. Mihalyko, B.G. Lakatos, Optimising design of continuous grinding mill-classifier systems, Chemical Engineering and Processing, 44 (2005) 273–277.

P.B. Kis, C. Mihalyko, B.G. Lakatos, Discrete model for analysis and design of grinding mill-classifier systems, Chemical Engineering and Processing, 45 (2006) 340–349.

R.R. Klimpel, L.G. Austin, Determination of selection-for-breakage functions in the batch grinding equation by nonlinear optimization, Industrial and Engineering Chemistry Fundamentals, 9 (1970) 230–237.

R.R. Klimpel, L.G. Austin, The back-calculation of specific rates of breakage and non-normalized breakage distribution parameters from batch grinding data, International Journal of Mineral Processing, 4 (1977) 7–32.

I.V. Klumpar, Measuring and optimizing air classifier performance, Separations Technology, 2 (1992) 124–135.

J. Kolacz, K.L. Sandvik, Ultrafine grinding in an air-swept ball mill circuit, International Journal of Mineral Processing, 44–45 (1996) 361–371.

N. Kotake, K. Daibo, T. Yamamoto, Y. Kanda, Experimental investigation on a grinding rate constant of solid materials by a ball mill—effect of ball diameter and feed size, Powder Technology, 143–144 (2004) 196–203.

N. Kotake, K. Suzuki, S. Asahi, Y. Kanda, Experimental study on the grinding rate constant of solid materials in a ball mill, Powder Technology, 122 (2002) 101–108.

A. Kwade, J. Schwedes, Wet comminution in stirred media mills, KONA, 15 (1997) 91–102.

A. Kwade, J. Schwedes, Wet grinding in stirred media mills, in: A.D. Salman, M. Ghadiri, M.J. Hounslow (Eds.), Handbook of Powder Technology, vol. 12: Particle Breakage, Amsterdam, The Netherlands: Elsevier, 2007, pp. 251–382.

J. Kwon, H. Cho, Investigation of error distribution in the back-calculation of breakage function model parameters via nonlinear programming, Minerals, 22 (2021) 425.

O. Labahn, B. Kohlhaas, Cement Engineers' Handbook, 4th ed., Wiesbaden and Berlin, Hesse: Bauverlag GmbH, 1983.

H. Li, W. Dong, X. Xie, Analysis of mill performance of industrial scale ball mill using DEM simulation, Advanced Materials Research, 634–638 (2013) 3732–3736.

Y. Li, Y. You, D. Gou, A. Yu, R. Yang, A DEM based scale-up model for tumbling ball mills, Powder Technology, 409 (2022) 117854.

B.B. Lira, A. Kavetsky, Applications of a new model-based method of ball mill simulation and design, Minerals Engineering, 3 (1990) 149–163.

P.T. Luckie, L.G. Austin, A review introduction to the solution of the grinding equations by digital computation, Minerals Science and Engineering, 4 (1972) 24–51.

A.J. Lynch, M. Oner, H. Benzer, Simulation of a closed cement grinding circuit, ZKG International, 53 (2000) 560–567.

A.J. Lynch, C.A. Rowland, The History of Grinding, Littleton, CO: Society for Mining, Metallurgy, and Exploration, Inc., 2005.

J.M. Lytle, K.A. Prisbrey, Material-dependent non-linear modeling of fine coal grinding, Powder Technology, 38 (1984) 93–97.

N. Magdalinovic, M. Trumic, M. Trumic, L. Andric, The optimal ball diameter in a mill, Physicochemical Problems of Mineral Processing, 48 (2012) 329−339.

J.C. Marchand, D. Hodouin, M.D. Everell, Residence time distribution and mass transport characteristics of large industrial grinding mills, Proceedings 3rd IFAC Symposium on Automation in Mining, Mineral and Metal Processing, Montreal, Canada, 18−20 August 1980.

G.G. Mejeoumov, Improved cement quality and grinding efficiency by means of closed mill circuit modeling, PhD Thesis, Texas A&M University, College Station, Texas, United States, 2007.

M.J. Meulendyke, J.D. Purdue, Wear of grinding media in the mineral processing industry: an overview, Minerals and Metallurgical Processing, 6 (1989) 167−172.

C. Mihalyko, T. Blickle, B.G. Lakatos, A simulation model for analysis and design of continuous grinding mills, Powder Technology, 97 (1998) 51–58.

T.S. Mika, A solution to the distributed parameter model of a continuous grinding mill at steady state, Chemical Engineering Science, 31 (1976) 257–262.

R.D. Mindlin, Compliance of elastic bodies in contact, Journal of Applied Mechanics, 16 (1949) 259–268.

B.K. Mishra, A review of computer simulation of tumbling mills by the discrete element method: part I—contact mechanics, International Journal of Mineral Processing, 71 (2003) 73−93.

B.K. Mishra, R.K. Rajamani, The discrete element method for the simulation of ball mills, Applied Mathematical Modelling, 16 (1992) 598−604.

Y. Mori, G. Jimbo, M. Yamazaki, On the residence time distribution and mixing characteristics of powders in open-circuit ball mill, Kagaku Kogaku Ronbunshu, 28 (1964) 204–213.

S. Morrell, Y.T. Man, Using modelling and simulation for the design of full scale ball mill circuits, Minerals Engineering, 10 (1997) 1311–1327.

N. Muanpaopong, R. Dave, E. Bilgili, Modeling of full-scale cement ball milling using a new simulator: TUSSIM-BM, 12th International Comminutuin Symposium (Comminution ’21), MEI Conferences, 19−22 April 2021.

N. Muanpaopong, R. Dave, E. Bilgili, Unsteady-state simulation of cement milling in closed-circuit operation: a fully coupled ball mill–air classifier model, American Institute of Chemical Engineers (AIChE) Annual Meeting, Paper No: 724e, Virtual, 13–14 November 2021.

N. Muanpaopong, R. Davé, E. Bilgili, A cell-based PBM for continuous open-circuit dry milling: impact of axial mixing, nonlinear breakage, and screen size, Powder Technology, 397 (2022a) 117099.

N. Muanpaopong, R. Davé, E. Bilgili, Impact of ball size distribution, compartment configuration, and classifying liner on cement particle size in a continuous ball mill, Minerals Engineering, 189 (2022b) 107912.

N. Muanpaopong, R. Davé, E. Bilgili, A comparative analysis of steel and alumina balls in fine milling of cement clinker via PBM and DEM, Powder Technology, 421 (2023) 118454.

F.K. Mulenga, Sensitivity analysis of Austin's scale-up model for tumbling ball mills – part 1. effects of batch grinding parameters, Powder Technology, 311 (2017) 398–407.

F.K. Mulenga, H.H. Gharehgheshlagh, S. Chehreghani, Assessing the dependency of selection function parameters with batch mill design, Advanced Powder Technology, 30 (2019) 2042–2051.

M. Muller-Pfeiffer, H.-G. Ellerbrock, S. Sprung, Controlling the particle size distribution of cement during grinding, ZKG International, 53 (2000) 549–559.

T.J. Napier-Munn, S. Morrell, R.D. Morrison, T. Kojovic, Mineral Comminution Circuits Their Operation and Optimisation, Julius Kruttschnitt Mineral Research Centre, Brisbane, Queensland: The University of Queensland, 1996.

J.V. Nava, A.L. Coello-Velazquez, J.M. Menendez-Aguado, Grinding kinetics study of tungsten ore, Metals, 11 (2021) 71.

J.V. Nava, T. Llorens, J.M. Menendez-Aguado, Kinetics of dry-batch grinding in a laboratory-scale ball mill of Sn–Ta–Nb minerals from the Penouta Mine (Spain), Metals, 10 (2020) 1687.

S. Nomura, Analysis of holdups in continuous ball mills, Powder Technology, 235 (2013) 443–453.

S. Nomura, A scale-up and design basis of continuous tube mills in cement industries, Powder Technology, 363 (2020) 717–734.

T. Nowack, Cement grinding is changing – trends towards decarbonisation, Optimising the Grinding Process, 2022 Live Webinar Series, 2 March 2022.

A.L.R. de Oliveira, L.M. Tavares, Modeling and simulation of continuous open circuit dry grinding in a pilot-scale ball mill using Austin's and Nomura's models, Powder Technology, 340 (2018) 77–87.

B. Oksuzoglu, M. Ucurum, An experimental study on the ultra-fine grinding of gypsum ore in a dry ball mill, Powder Technology, 291 (2016) 186–192.

E. Onuma, T. Furukawa, O–SEPA a new high-performance air-classifier, World Cement, 15 (1984) 13–24.

E. Onuma, M. Ito, Productivity increase by high-efficiency separators, World Cement, 26 (1995) 43–48.

C.E. Ozer, S.L. Ergun, A.H. Benzer, Modeling of the classification behavior of the diaphragms used in multi-chamber cement mills, International Journal of Mineral Processing, 80 (2006) 58–70.

A. Ozkan, M. Yekeler, M. Calkaya, Kinetics of fine wet grinding of zeolite in a steel ball mill in comparison to dry grinding, International Journal of Mineral Processing, 90 (2009) 67–73.

P.F. Parkes, Energy saving by utilisation of high efficiency classifier for grinding and cooling of cement on two mills at Castle Cement (Ribblesdale) Limited, Clitheroe, Lancashire, UK, in: J. Sirchis (Ed.), Energy Efficiency in the Cement Industry, 1st ed., UK: Taylor & Francis, 1990.

F. Patino, D. Talan, Q. Huang, Optimization of operating conditions on ultra-fine coal grinding through kinetic stirred milling and numerical modeling, Powder Technology, 403 (2022) 117394.

N. Patzelt, High-pressure grinding rolls, a survey of experience, IEEE Cement Industry Technical Conference, (1992) 149–181.

E. Petrakis, E. Stamboliadis, K. Komnitsas, Identification of optimal mill operating parameters during grinding of quartz with the use of population balance modeling, KONA Powder and Particle Journal, 34 (2017) 213–223.

M.S. Powell, N.S. Weerasekara, S. Cole, R.D. LaRoche, J. Favier, DEM modelling of liner evolution and its influence on grinding rate in ball mills, Minerals Engineering, 24 (2011) 341–351.

C.L. Prasher, Crushing and Grinding Process Handbook, Chichester, United Kingdom: Wiley, 1987.

P. Purker, R. Agrawal, P.C. Kapur, A G–H scheme for back-calculation of breakage rate functions from batch grinding data, Powder Technology, 45 (1986) 281–286.

K.J. Reid, A solution to the batch grinding equation, Chemical Engineering Science, 20 (1965) 953–963.

I.E. Rivera-Madrid, M. Rincon-Fulla, A. Osorio-Correa, L. Chica-Osorio, O. Bustamante-Rua, J.M. Menendez-Aguado, Comparison of alumina ball size distribution in two white cement grinding units using Swebrec function, DYNA 86 (2019) 25–29.

R.S.C. Rogers, L.G. Austin, K.A. Brame, Mill sizing for phosphate grinding in mills of 0.2 to 5 meters in diameter, Minerals and Metallurgical Processing, 3 (1986) 240–246.

R.S.C. Rogers, R.P. Gardner, Use of a finite-stage transport concept for analyzing residence time distribution of continuous processes, AIChE Journal, 25 (1979) 229–240.

Z. Rogovin, A. Casali, J.A. Herbst, Tracer study of mass transport and grinding in a rod mill, International Journal of Mineral Processing, 22 (1988) 149–167.

B.R. Rohrs, G.E. Amidon, R.H. Meury, P.J. Secreast, H.M. King, C.J. Skoug, Particle size limits to meet USP content uniformity criteria for tablets and capsules, Journal of Pharmaceutical Sciences, 95 (2006) 1049−1059.

C.M. Rule, L. Knopjes, B. Clermont, C. Philippe, Fine grinding−developments in ceramic media technology and resulting improved plant performance at Anglo Platinum, Third International Platinum Conference, Sun City, South Africa, 2008, pp. 53−62.

H.M. Saleh, R.O.A. Rahman, Introductory Chapter: Properties and Applications of Cement-Based Materials, in: H.E.-D.M. Saleh, R.O.A. Rahman (Eds.), Cement Based Materials, London, United Kingdom: IntechOpen, 2018, pp. 3–12.

S. Sander, D. Droop, Current trends in air classification of fine powders, Book of Extended Abstracts for 16th European Symposium on Comminution & Classification (ESCC 2019), Leeds, UK, 2−4 September 2019, pp. 15−16.

H.M. von Seebach, E. Neumann, L. Lohnherr, State-of-the-art of energy-efficient grinding systems, ZKG International, 49 (1996) 61–67.

M.V. Seebach, L. Schneider, Update on finish grinding with improved energy efficiency, IEEE Transactions on Industry Applications, IA-23 (1987) 397−403.

H. Shahgholi, K. Barani, M. Yaghobi, Application of perfect mixing model for simulation of vertical roller mills, Journal of Mining and Environment, 8 (2017) 545–553.

L.F. Shampine, I. Gladwell, S. Thompson, Solving ODEs with MATLAB, New York City, NY: Cambridge University Press, 2003.

K. Shimoide, Design and Operation of Cement Grinding Plant KS Text Book No. 5, 2016.

K. Shoji, L.G. Austin, A model for batch rod milling, Powder Technology, 10 (1974) 29–35.

K. Shoji, L.G. Austin, F. Smaila, K. Brame, P.T. Luckie, Further studies of ball and powder filling effects in ball milling, Powder Technology, 31 (1982) 121–26.

K. Shoji, R. Hogg, L.G. Austin, Axial mixing of particles in batch ball mills, Powder Technology, 7 (1973) 331–336.

K. Shoji, S. Lohrasb, L.G. Austin, The variation of breakage parameters with ball and powder loading in dry milling, Powder Technology, 25 (1980) 109–114.

L. Sottili, D. Padovani, Effect of grinding admixtures in the cement industry, part 1, ZKG International, 53 (2000) 568−575.

S. Strasser, Existing mill capacity doubled developments in grinding process, IEEE Cement Industry Technical Conference Record, (2002) 213−227.

D. Strohmeyer, Cement Grinding with Loesche Vertical Roller Mills – History and Global Market Trends, Presented at the technical meeting with SCG, Bangkok, Thailand, 5 April 2013.

T.-L. Su, D.Y.-L. Chan, C.-Y. Hung, G.-B. Hong, The status of energy conservation in Taiwan's cement industry, Energy Policy, 60 (2013) 481–486.

S.H.R. Swaroop, A.-Z.M. Abouzeid, D.W. Fuerstenau, Flow of particulate solids through tumbling mills, Powder Technology, 28 (1981) 253–260.

T. Tamashige, H. Obana, M. Hamaguchi, Operational results of OK series roller mill, IEEE Transactions on Industry Applications, 27 (1991) 416–424.

L.M. Tavares, R.M. de Carvalho, Modeling breakage rates of coarse particles in ball mills, Minerals Engineering, 22 (2009) 650–659.

E. Teke, M. Yekeler, U. Ulusoy, M. Canbazoglu, Kinetics of dry grinding of industrial minerals: calcite and barite, International Journal of Mineral Processing, 67 (2002) 29–42.

The MathWorks, Inc., Global Optimization Toolbox User's Guide (R2022a), 2022.

N.A. Toprak, O. Altun, N. Aydogan, H. Benzer, The influences and selection of grinding chemicals in cement grinding circuits, Construction and Building Materials, 68 (2014) 199–205.

N.A. Toprak, A.H. Benzer, C.E. Karahan, E.S. Zencirci, Effects of grinding aid dosage on circuit performance and cement fineness, Construction and Building Materials, 265 (2020) 120707.

D. Touil, S. Belaadi, C. Frances, The specific selection function effect on clinker grinding efficiency in a dry batch ball mill, International Journal of Mineral Processing, 87 (2008) 141–145.

G.E. Troxell, H.E. Davis, J.W. Kelly, Composition and Properties of Concrete, 2nd ed., New York, NY: McGraw Hill, 1968.

M. Trumic, N. Magdalinovic, G. Trumic, The model for optimal charge in the ball mill, Journal of Mining and Metallurgy, 43 A (2007) 19–31.

K.G. Tsakalakis, G.A. Stamboltzis, Correlation of the Blaine value and the d80 size of the cement particle size distribution, ZKG International, 61 (2008) 60–68.

S. Tsivilis, S. Tsimas, A. Benetatou, E. Haniotakis, Study on the contribution of the fineness on cement strength, ZKG International, 43 (1990) 26–29.

Y. Umucu, M.Y. Altinigne, V. Deniz, The effects of ball types on breakage parameters of barite, Journal of the Polish Mineral Engineering Society, (2014) 113–117.

Y. Umucu, V. Deniz, The effect of ball type in fine particles grinding on kinetic breakage parameters, Journal of the Polish Mineral Engineering Society, (2015) 197–203.

W. Valery, A. Jankovic, The future of comminution, Proceedings 34th IOC on Mining and Metallurgy, Bor Lake, Yugoslavia, 2002, pp. 287–298.

M. Van den Broeck, A SD100 Sturtevant high-efficiency classifier for Origny-Rochefort, International Cement Journal, (1998) 39–45.

A. Vanarase, R. Aslam, S. Oka, F. Muzzio, Effects of mill design and process parameters in milling dry extrudates, Powder Technology, 278 (2015) 84–93.

C. Varinot, H. Berthiaux, J. Dodds, Prediction of the product size distribution in associations of stirred bead mills, Powder Technology, 105 (1999) 228–236.

C. Varinot, S. Hiltgun, M.-N. Pons, J. Dodds, Identification of the fragmentation mechanisms in wet-phase fine grinding in a stirred bead mill, Chemical Engineering Science, 52 (1997) 3605–3612.

R. Verma, R.K. Rajamani, Environment-dependent breakage rates in ball milling, Powder Technology, 84 (1995) 127–137.

P.J. Vikesland, A.M. Heathcock, R.L. Rebodos, K.E. Makus, Particle size and aggregation effects on magnetite reactivity toward carbon tetrachloride, Environmental Science and Technology, 41 (2007) 5277–5283.

L. Vogel, W. Peukert, Breakage behaviour of different materials—construction of a mastercurve for the breakage probability, Powder Technology, 129 (2003) 101–110.

L. Vogel, W. Peukert, From single particle impact behaviour to modelling of impact mills, Chemical Engineering Science, 60 (2005) 5164–5176.

T. Vuk, V. Tinta, R. Gabrovsek, V. Kaucic, The effects of limestone addition, clinker type and fineness on properties of Portland cement, Cement and Concrete Research, 31 (2001) 135–139.

X. Wang, Y. Wang, C. Yang, D. Xu, W. Gui, Hybrid modeling of an industrial grinding-classification process, Powder Technology, 279 (2015) 75–85.

M.H. Wang, R.Y. Yang, A.B. Yu, DEM investigation of energy distribution and particle breakage in tumbling ball mills, Powder Technology, 223 (2012) 83–91.

D.M. Weedon, A perfect mixing matrix model for ball mills, Minerals Engineering, 14 (2001) 1225–1236.

N.S. Weerasekara, L.X. Liu, M.S. Powell, Estimating energy in grinding using DEM modelling, Minerals Engineering, 85 (2016) 23–33.

N.S. Weerasekara, M.S. Powell, P.W. Cleary, L.M. Tavares, M. Evertsson, R.D. Morrison, J. Quist, R.M. Carvalho, The contribution of DEM to the science of comminution, Powder Technology, 248 (2013) 3–24.

W.J. Whiten, A matrix theory of comminution machines, Chemical Engineering Science, 29 (1974) 589–599.

W.J. Whiten, A. Kavetsky, Studies on scale-up of ball mills, Minerals and Metallurgical Processing, (1984) 23–28.

D. Xu, Y. Cui, H. Li, K. Yang, W. Xu, Y. Chen, On the future of Chinese cement industry, Cement and Concrete Research 78 (2015) 2–13.

R.Y. Yang, R.P. Zou, A.B. Yu, Microdynamic analysis of particle flow in a horizontal rotating drum, Powder Technology, 130 (2003) 138–146.

J. Yardi, Separator technology, World Cement, 36 (2005) 87–104

K. Yildirim, H. Cho, L.G. Austin, The modeling of dry grinding of quartz in tumbling media mills, Powder Technology, 105 (1999) 210–221.

W. Yin, Y. Tang, Y. Ma, W. Zuo, J. Yao, Comparison of sample properties and leaching characteristics of gold ore from jaw crusher and HPGR, Minerals Engineering, 111 (2017) 140–147.

Y. Yu, J. Liu, K. Zhang, Establishment of a prediction model for the cut size of turbo air classifiers, Powder Technology, 254 (2014) 274–280.

Y.M. Zhang, T.J. Napier-Munn, Effects of particle size distribution, surface area and chemical composition on Portland cement strength, Powder Technology, 83 (1995) 245–252.

H. Zhang, Building Materials in Civil Engineering, Cambridge, UK: Woodhead Publishing Limited, 2011.

Y.M. Zhang, A. Kavetsky, Investigation of particle breakage mechanisms in a batch ball mill using back-calculation, International Journal of Mineral Processing, 39 (1993) 41–60.

Y.M. Zhang, A. Kavetsky, T.J. Napier-Munn, D.S. Rapson, Effects of separator efficiency on clinker grinding circuits – a computer simulation study, ZKG International, 41 (1988) 501–505.

X. Zhang, Y. Qin, Y. Han, Y. Li, P. Gao, G. Li, S. Wang, A potential ceramic ball grinding medium for optimizing flotation separation of chalcopyrite and pyrite, Powder Technology, 392 (2021) 167–178.

X. Zhang, Y. Qin, J. Jin, Y. Li, P. Gao, High-efficiency and energy-conservation grinding technology using a special ceramic-medium stirred mill: a pilot-scale study, Powder Technology, 396 (2022) 354–365.

H.P. Zhu, Z.Y. Zhou, R.Y. Yang, A.B. Yu, Discrete particle simulation of particulate systems: a review of major applications and findings, Chemical Engineering Science, 63 (2008) 5728–5770.